The Physical and Chemical Origins of Amyloid at Interfaces

Thesis submitted in accordance with the requirements of the

University of Liverpool

for the degree of

Doctor of Philosophy

by

Nathan Cumberbatch

March 2021

University of Liverpool

Abstract

Amyloidosis is of serious concern within the modern world with an ageing global population, there is a significant drive to understand how amyloid forms in order to research and develop new therapeutics to combat this threat. This thesis proposes using a cross-disciplinary collaborative approach to determine multiple aspects within the amyloid-like fibrillation pathway for human insulin (HI) at acidic and neutral pH conditions.

Chapter 2 uses Reflection Anisotropy Spectroscopy to obtain fibrillar orientation information with the goal to investigate whether structural morphology can direct fibril growth. Lack of reproducibility at the surfaces and the observation of a 'blue-haze' on the silicon wafers led to the method development in Chapter 3.

Chapter 4 uses conventional biophysical techniques, fluorescence spectroscopy and electron microscopy to study hydrophobic functionalised mesoporous silica microparticles provides a scaffold for human insulin fibrillation to occur. These results show that the microparticles induced fibril morphology changes and inhibited or enhanced the fibrillation process, with respect to the human insulin control.

Chapter 5 explores the mass and structural changes of adsorbed human insulin at a hydrophobic surface, by QCM-D and Raman spectroscopy. The results of which showed variable human insulin adsorption to the two differing hydrophobically functionalised surfaces at pH 2 and pH 7 conditions.

Chapter 6 is the result of a collaboration with the Department of Physics and provides the first images obtained from infrared scanning near-field optical microscopy in reflection with a quantum cascade laser source of human insulin adsorbed to gold surfaces to obtain both structural and locational information. These preliminary results provide exciting opportunities for future development of this technique at other surfaces and proteins.

Chapter 7 uses fluorescence excitation – emission matrices to uncover the origin of the deep-blue autofluorescence phenomenon, with human insulin, α-synuclein and other peptides.

Contents

Figures

Tables

Acknowledgements

Where to begin? Throughout these eight years in Liverpool, I have been lucky enough to have met some incredible people and without their support this thesis would not have been possible, but to thank everyone would be a thesis within itself!

Firstly, I would like to thank my collaborators, the Weightman group in Physics, although words aren't enough to describe my gratitude. Peter, Caroline, Steve, Paul H, Paul U, Conor and Safaa, every one of you have gone above and beyond. The long days, nights and weekends to see this project through and I am grateful for your hard work and dedication.

Secondly, to all those on the 4th floor Organic Chemistry labs, which I called my home for the past three years, particularly thanks to; Shirley, Sean, Gina, Mike, Rachel, Nada, Chris, Sophie, Josh, Monika, Chris, Jack, Charlie and Liqun. Who would have thought I would learn so much synthetic organic / medicinal chemistry! A special thanks to Gita, Cate, Helen, Debbie, Jackie and Sam for the various opportunities I have had, such as; Outreach, Teaching activities, industrial collaborations and many more. The central teaching hub (CTL) team, particularly; Chris, Ann, Lynne, Emma, Josh and Steve who provided so much support throughout the last eight years in Liverpool.

Thirdly, to the biologists (Hannah, Mahmoud, James, Kieran, Kiani and Jill) who have guided my understanding of biology specifically amyloidosis and α-synuclein!

Finally, and most importantly, my family; Mum, Dad, Brother and Sister for being there – your unwavering support, making me strive to better myself.

I am and always will be grateful and appreciative to each and every one of you, see you all in the future.

Nathan

Abbreviations

1-D	One-dimensional
2-D	Two-dimensional
3-D	Three-dimensional
aa	amino acid
Ab	Amyloid-β peptide
Abs	Absorbance
AC	Alternating Current
AFM	Atomic Force Microscope
αS	α-Synuclein
ATR	Attenuated Total Reflection
BLG	β-Lactoglobulin
BSA	Bovine Serum Albumin
CD	Circular Dichroism
CE	Chemical Enhancement
CHN	Carbon, Hydrogen, Nitrogen
CR	Congo Red
Cryo-EM	Cryogenic Electron Microscopy
dbAF	Deep Blue Autofluoresence
DC	Direct Current
DLS	Dynamic Light Scattering
DNA	Deoxyribonucleic Acid
DTPA	Diethylenetriaminepentaacetic acid
EEM	Excitation and Emission Matrix
EM	Electromagnetic
eV	Electron Volt
fcc	Face Centered Cubic
FTIR	Fourier Transform Infrared
HEWL	Hen Egg White Lysozyme
HFIP	Hexafluoroisopropanol
HI	Human Insulin
hIAPP	Human Islet Amyloid Polypeptide
HOMO	Highest Occupied Molecular Orbital
HPLC	High Performance Liquid Chromatography
IDP	Intrinsically Disordered Protein
IF	Intrinsic Fluorescence
IFE	Inner Filter Effect
IR	Infrared
LD	Linear Dichroism
l_{EM}	Emission Wavelength
l_{EX}	Excitation Wavelength
LUMO	Lowest Unoccupied Molecular Orbital

mRNA	messenger Ribonucleic Acid
MS	Mass Spectrometry
NAC	Non-Amyloid-β Component
NMR	Nuclear Magnetic Resonance
NTIL	Non-Traditional Intrinsic Luminescence
PBS	Phosphate Buffered Saline
PD	Parkinson's Disease
PDB	Protein Data Bank
PDI	Polydispersity index
PDMS	Polydimethylsiloxane
PEM	Photoelastic Modulator
PES	Polyethersulfone
PTFE	Polytetrafluoroethylene
QCM	Quartz Crystal Microbalance
QCM-D	Quartz Crystal Microbalance with Dissipation
RAS	Reflection Anisotropy Spectroscopy
RSA	Random Sequential Adsorption
SAM	Self-Assembled Monolayer
SDS	Sodium Dodecyl Sulfate
SEM	Scanning Electron Microscope
SERS	Surface Enhanced Raman Spectroscopy
SNOM	Scanning Near-field Optical Microscope
SPR	Surface Plasmon Resonance
TEM	Transmission Electron Microscope
TERS	Tip Enhanced Raman Spectroscopy
TFA	Trifluoroacetic acid
ThT	Thioflavin-T
TMPS	Trimethoxypropylsilane
UHV	Ultra-High Vacuum
UV	Ultra-Violet
UV-Vis	Ultraviolet-Visible
VMD	Visual Molecular Dynamics
WT	Wild Type

Chapter 1: Introduction

1.1. Introduction

Amyloid proteins are clinically important since the accumulations of amyloid fibrils, termed amyloid plaques,[1,2] are hallmarks of 'amyloidosis diseases';[3] Alzheimer's,[4] Parkinson's[5] and Type II diabetes.[6] Treating these diseases is a growing worldwide problem for social welfare and the associated financial expenditure.[7,8] For example, Alzheimer's, which is often diagnosed late in life, is becoming endemic as life expectancy increases, leading to a greater demand on social welfare for ageing populations. Unfortunately, there is currently no cure for amyloidosis, but rather therapeutics have been designed to reduce disease progression[9] or symptomatic alleviation.[10,11] There are a whole host of reasons as to why there is no cure, such as variations between associated diseases,[12] genetic diversity,[13] diagnostic issues,[14] but fundamentally the necessity to gain a better understanding of the disease is paramount.[10]

Amyloidosis is the misfolding of proteins, from their native states, into insoluble fibril-like supramolecular structures. Understanding how these proteins misfold into fibril structures is critical in pharmaceutical development, which has so far been plagued with clinical trial failures.[15] These failures indicate more research is necessary to understand the various fibrillation mechanisms, which are important for medicinal drug targets.[16] An immediate consideration is to tackle this fibrillation problem by investigation of; the bulk solution and surface adsorption, as these can give rise to varying fibrillation pathways.[17–19]

Human insulin (HI), a key physiological hormone for glucose regulation, is a model protein that can be used for amyloid research. Firstly, HI is highly prone to form amyloid-like fibrils *in vitro* (outside the living organism), which are termed amyloid-like as the fibrils are formed *in vitro* as opposed to *in vivo*, and are therefore able to be studied within laboratory conditions. Secondly, induced-amyloidosis at injection sites, has been reported as a long-term effect of insulin therapy.[20] Thirdly, HI is widely available and insulin analogues have been extensively studied due to the clinical importance of insulin as a drug for diabetes treatment. The high propensity

for insulin fibrillation *in vitro*, whilst beneficial in this work, is detrimental to the drug delivery system in regard to storage and logistical concerns.[21,22] Issues arising from these concerns are insulin aggregation, which affects the controlled therapeutic dosage to the patient, or physical obstruction and restriction within the flow devices.

Investigating amyloid-like fibrillation from an interdisciplinary perspective is exciting, as the use of biological and chemical techniques can provide a coherent assessment of fibrillation pathways. These techniques are important since current research suggests that whilst mature fibrils are markers of disease pathology, the clinical toxicity is driven in the pre-fibrillar oligomeric phase.[23,24] There is a growing need in amyloid research for therapeutic development and earlier clinical detection, but first understanding how fibrillation is affected by surface architecture is important for medical treatment design. Hydrophobic surfaces are known to induce fibrillation, but how does this interface affect typical fibrillation pathways? Is it possible to reduce amyloid toxicity through interfacial architecture? This thesis uses chemical principles to alter the interfacial composition of the surface to investigate whether the biological components are affected by utilising a range of biophysical techniques. These spectroscopic techniques will be used to investigate any effect that hydrophobic functionalisation has on HI fibrillation pathways from bulk solution to adsorption and rearrangement, through to desorption and fibrillation events.

The primary objective for this thesis was to study the effect of hydrophobic functionalised interfaces on HI fibrillation under measurable conditions using an ensemble of spectroscopic techniques, to gain insight into structural and kinetic properties of HI fibrillation. Particular attention will be given to the pre-fibrillar events because protein adsorption at the surface can induce fibrillation through an autocatalytic effect[17] into the bulk solution, which participates in primary nucleation events by a seeded-growth mechanism.[19] A secondary objective is to consider how the physical and chemical composition of amyloid-like fibrils are affected by the hydrophobic modifications of the surface interface hence a range of spectroscopic techniques are utilised.

1.2. What are proteins?

To be able to understand amyloid mechanics, the biophysical properties of proteins / peptides and their fundamental chemistry should first be considered.

Proteins and peptides are biochemical assemblies composed of amino acid (aa) residues linked together through peptide bonding, which is termed the peptide backbone. The specific terminology used to describe the architecture, protein or peptide, is classified by the specific assembly size. A protein consists of fifty or more amino acid residues, whereas a peptide ranges between two to fifty amino acid residues. Furthermore, a peptide can also be designated as an 'oligo-' or 'poly-' peptide, whereby the prefix refers to; 'oligo-' a small (less than twenty residues) or 'poly-' any length peptide but of a single-linear chain. The species studied in this thesis; Insulin and α-synuclein (αS) are proteins, since their assemblies are larger than fifty residues, at 51 and 140 amino acid residues respectively.

Peptides and proteins are biologically critical in physiology, whereby their functions are typically regulation and maintenance of cellular systems.[25] An important physiological protein is HI, which is a human metabolic hormone essential for blood sugar regulation.[26] A protein's functionality is influenced by its overall three-dimensional (3D) structure and the exhibited biophysical properties, which are attributed to the amino acid residue side chains diverging from the backbone.[27]

1.2.1. What are amino acids?

There are twenty-one known essential proteinogenic amino acid residues, which occur naturally and can be incorporated within a protein. Chemically, an amino acid is an organic molecule comprised of three distinct regions; amine, carboxyl and side chain, which are illustrated in Figure 1. The amino acid side group (R-group), gives rise to the residue's biophysical properties, which are distinct for each of the twenty-one known proteinogenic residues. Whilst each of these residues have their own distinct biophysical properties, when encoded into a larger assembly, the properties give rise to both a localised and overall ensemble effect.

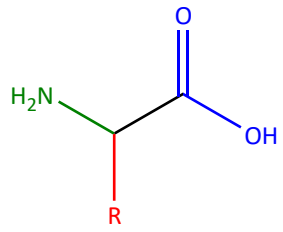

Figure 1: A chemical schematic showing a generalised amino acid residue, with functional groups colour-coded; (green) amine, (blue) carboxyl and (red) side chain.

Figure 2 shows the four different classes of the amino acid residues, these are; electronically charged, hydrophobic, polar and miscellaneous (stated in Figure 2 as "special cases"). The electronically charged class is subdivided into positively charged (basic) and negatively charged (acidic) for example; arginine (Arg, R) and glutamic acid (Glu, E). Hydrophobic is also subdivided into aliphatic and aromatic for example; alanine (Ala, A) and phenylalanine (Phe, F). The polar category represents residues with hydrophilic side chain groups, whereas the miscellaneous category refers to four residues, which do not conform to the other categories.

The four amino acid residues categorised as miscellaneous are; glycine (Gly, G), proline (Pro, P), cysteine (Cys, C) and selenocysteine (Sec, U). Glycine is unique since the side chain is a proton and as such this residue is not sterically hindered and can be found anywhere within a polypeptide chain. Conversely, proline is structurally hindered because the amino functionality is part of the side chain group, thus restricting the spatial orientation of the residue within the polypeptide chain. Cysteine can also modify the structural arrangement of the polypeptide chain, since it is able to form disulfide bridges with another cysteine residue through its terminal sulfhydryl group. Selenocysteine, an uncommon residue, is an analogue of cysteine where selenium is substituted for sulfur.[28]

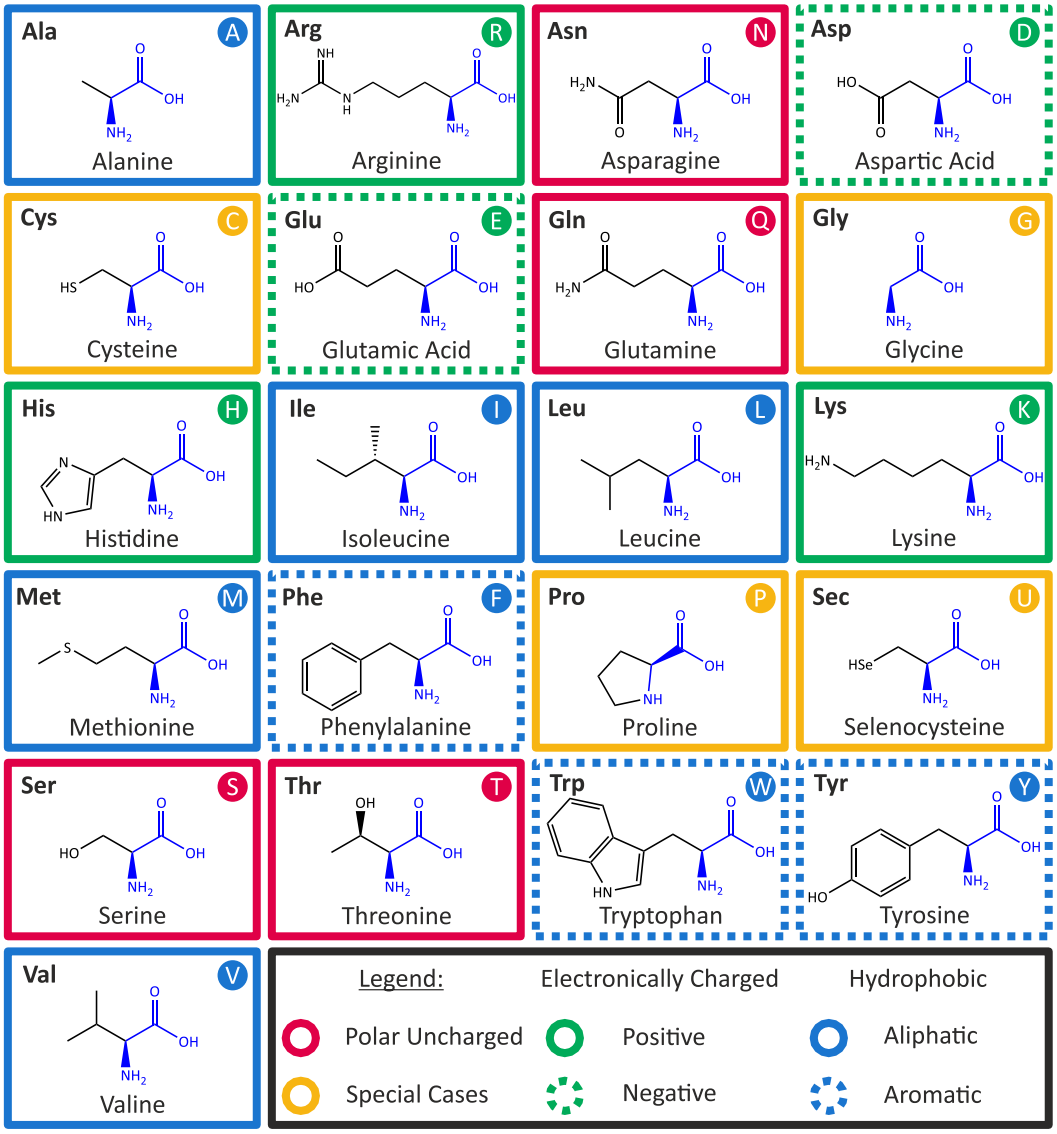

Figure 2: The 21 proteinogenic amino acid residues are arranged alphabetically, the colours are coordinated to the amino acid class; (red) polar uncharged, (yellow) special cases, (green) electronically charged and (blue) hydrophobic. The electronically charged and hydrophobic classes are further subdivided into (solid green) positively or (dashed green) negatively charged and either (solid blue) aliphatic or (dashed blue) aromatic. The amino acid abbreviations in three letter and one letter forms are displayed in the top left and right corners, respectively. Adapted from Cooper et al.[29]

Each of the residues are designated a full name and two abbreviated forms; consisting of one or three letters. This thesis will utilise the one letter code. The biophysical properties of these residues are critical in determining the overall properties of the protein.

1.2.2. How are proteins formed?

The polypeptide chain can lead to numerous protein configurations both structurally and chemically because of their amino acid residue makeup. Proteins are formed through a polymerisation reaction, which links the differing amino acid residues together through the peptide backbone into a singular linear chain.

This reaction scheme, Figure 3, is a reversible condensation / dehydration reaction, whereby the leading residue's hydroxy (-OH) group in the carboxyl (-COOH) region reacts with a proton from the lagging residue's amine ($-NH_2$) group. A covalent bond is therefore formed between the carbonyl carbon and the nitrogen of the amine, with the loss of one water molecule. This covalent bond is termed a 'peptide bond' because it is the central bond within the amide group.

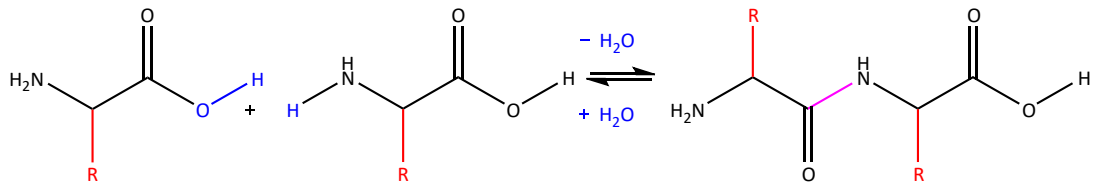

Figure 3: A generalised reversible condensation / dehydration reaction, showing the removal of (blue) water, formation of (purple) peptide bond and the (R, red) side chain groups.

The singular uninterrupted chain from the N-terminus through amide groups to the C-terminus, is defined as the protein backbone and is the core of the protein. The spatial arrangement of the protein backbone is dependent upon the biophysical properties of the side chain groups.

1.2.3. What is the protein structure?

A protein can have up to four levels of structure; primary, secondary, tertiary and quaternary as demonstrated by HI in Figure 4, HI will be discussed further (1.4. Human insulin: The model protein for amyloid research, page 45). The primary structure is defined as the linear amino acid sequence, which is read from nitrogen- to carbon-termini. The secondary structure is how the protein residues are arranged locally with the main features such as; α-helical, β-sheet, β-turns and random coil. These features are particularly important for biochemical spectroscopic analysis because the constructs give rise to unique spectroscopic profiles. The

tertiary structure is how these secondary structural components are spatially arranged within the protein, as determined through structural analysis such as; crystallography, nuclear magnetic resonance (NMR) and cryogenic electron microscopy (cryo-EM). The final level is quaternary, which is not present in all proteins because it is the spatial arrangement of two or more non-bonded protein strands.[30]

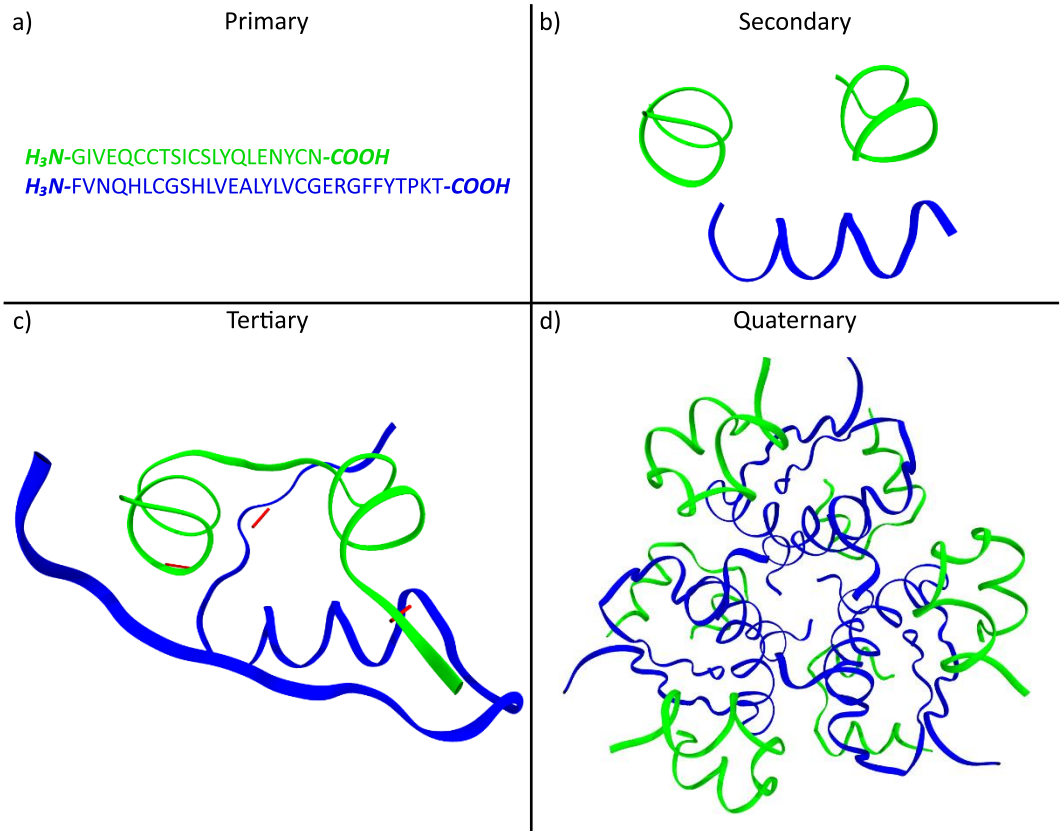

Figure 4: Levels of protein structure, as represented by human insulin (HI) showing (green) chain A and (blue) chain B. (a) The primary amino acid sequence of both chains drawn in the conventional method. (b) Secondary structure illustrates the three α-helices. (c) Tertiary structure illustrates how the three α-helices are connected, by random coils / turns and three (red) disulfide bridges. (d) Quaternary structure shows the hexameric configuration of how the six insulin monomers interact. Adapted from protein data bank (PDB) files; monomeric (PDB: 2JV1)[31] and hexameric (PDB: 3AIY),[32] using visual molecular dynamics (VMD).[33]

Figure 4 shows the primary, secondary and tertiary levels of the monomeric state and for the quaternary level the hexamer oligomeric state of HI. HI is a 51 amino acid globular protein consisting of two strands, Chains A and B, which consist of 21 and 30 amino acid residues respectively. In Figure 4 the chains are coloured green

and blue for A and B respectively. The primary sequence gives residue designations within the peptide chain and can deduce their absolute biophysical properties but does not illustrate the spatial arrangement of the residues within the protein. The other three levels; secondary, tertiary and quaternary, are represented here using a ribbon graphic, which renders the peptide backbone only. This representation is used to improve visibility of the protein's spatial arrangement, which is determined by the side-groups (not shown). The secondary structure is the local arrangement of residues within the protein, which is structurally stabilised by extensive hydrogen bonding between the peptide backbone. There are three main types of secondary structure architecture; α-helix, β-sheet and random coils.

Helices are coiled structures, and contain three sub-groups; α-, π- and 3_{10}-helices. The most common class is the α-helix, shown in Figure 5, which is moderately sized containing approximately 3.6 aa residues per turn.[34] The 3_{10}-helix is often located at the termini to the α-helix, and has been considered as an intermediate structural feature due to its smaller size (~3 aa residues per turn).[35] The π-helix is the rarest, due to its much larger size (~4.4 aa residues per turn) and is often only partially observed within protein structures.[36]

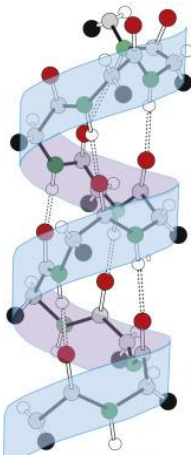

Figure 5: Illustration of hydrogen bonding within an α-helix, showing the (black bonds) backbone of (black) carbon atoms, (red) oxygen atoms and (green) nitrogen atoms involved in (dashed black lines) hydrogen bonding within the helical structure. Reproduced from Feher et al.[37]

The β-sheet structural features, as illustrated in Figure 6, are derived from at least two adjacent β-strands and are typically parallel or anti-parallel which arises

from the peptide backbone directionality. The parallel arrangement leads to staggered hydrogen bonding interactions, whereas the anti-parallel leads to planar interactions, which has the greatest stability.[38] These features are important for amyloid research for two reasons; firstly, due to the steric zipper effect[39] (see 1.3.1. What is protein fibrillation?, page 40), which is an assumed spontaneous assembly process for amyloid fibrils, and secondly since it is an essential component of a cross-β structure which defines amyloid.[40]

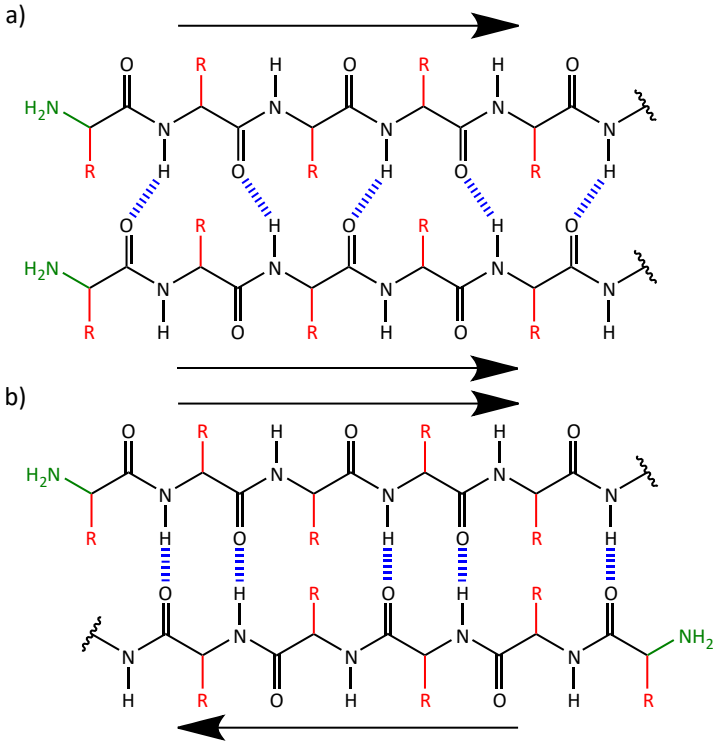

Figure 6: Illustration of hydrogen-bonding within different ß-sheet secondary structure orientations composed of; (a) parallel and (b) anti-parallel ß-strands. The various functional groups are represented; (green) amine group, (red) side chains, (blue) hydrogen bonds and (black wavy bond) the repeater unit.

The final structural element and possibly the most widespread are random coils. This component category is defined as random, since there is no conformation to regular structural characteristics or hydrogen bonding networks. These features are often found linking various constructs, which are termed loops, or at the termini of chains.

In the secondary structure example (Figure 4b), HI is represented with three disjointed α-helices within the protein. There are two α-helices in chain A and these are arranged parallel to each other, whilst the α-helix in chain B is arranged perpendicular to the other two. This fails to address how the isolated structural features are connected to the rest of the protein. As shown in Figure 4c, the tertiary representation shows the entirety of the peptide backbone's spatial arrangement and also the three disulfide bridges (red) are drawn, which highlight that there are two inter- and one intra-chain (A_7:B_7, A_{20}:B_{19} and A_6:A_{11}).

Figure 4d is a quaternary representation showing the HI hexamer formed from six monomer subunits, which are firstly associated into dimers by hydrogen bonding between chain B's C-termini. These dimer components associate together to form a hexameric complex in the presence of zinc ions.[41]

Protein structure is a critical part of amyloid research, since the native protein becomes denatured and misfolds during amyloid fibrillation events. The protein misfolding often affects the native structure, by inducing structural change to allow for the wider assembly of the protein into a supramolecular structure.

1.3. What is amyloid?

Amyloid is commonly recognised for its pathological inherency, known as amyloidosis,[3] which is a group of diseases such as; Alzheimer's,[4] Parkinson's,[5] and Type II diabetes.[6] A general hallmark of these diseases are amyloid plaques,[1,2] which are a build-up of amyloid fibrils. Amyloid fibrils are formed when soluble native proteins misfold, and through propagation, result in insoluble fibrillar structures.[42,43] This abridged description of fibrillation is not entirely correct since non-amyloidogenic proteins can also accumulate into aggregates,[44,45] therefore what characterises a protein as 'amyloidogenic'?

Proteins can only be described as amyloidogenic,[1] if the resulting aggregates fulfil the following criteria; exhibition of cross-β structure[45] and histological Congo-red (CR) staining, resulting in apple-green birefringence under cross polarised microscopy.[46] Historically Geddes *et al*[47] reported the amyloid structure was naturally present within the silk of a lacewing fly.

Amyloid is investigated by the formation of cross-β structures, which are the result of amyloidogenic protein fibrillation. A cross-β structure (Figure 7) is a highly organised assembly of two or more β-sheets, which are orientated perpendicular to the fibril axis. There are two dyes, termed amyloid-specific molecules; Congo-red (CR) and thioflavin-T (ThT), which bind to the grooves and ridges of the cross-β structure.[48–50]

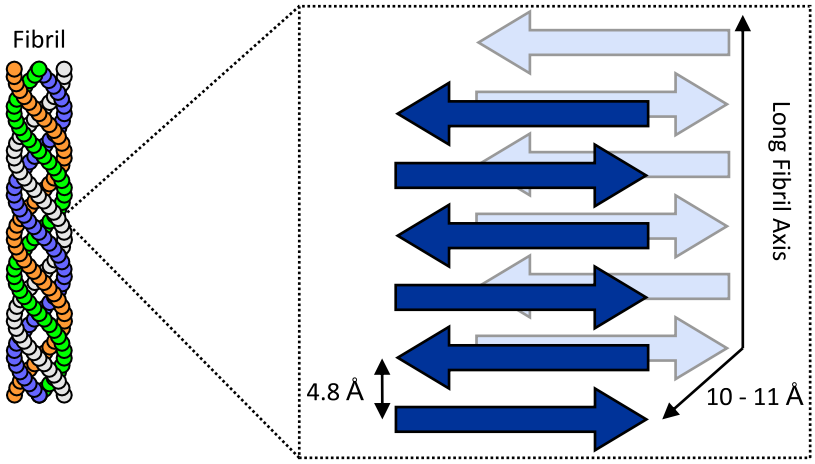

Figure 7: Schematic of the amyloid cross-ß structure showing the ß-sheets composed of anti-parallel ß-strands, adapted from Biancalana et al.[51]

The cross-β structure, shown in Figure 7, has been represented with β-sheets composed of anti-parallel β-strands but parallel β-strands are also possible.[52] In either case, the β-sheets are assembled by the formation of a dehydrated β-sheet bilayer whereby the associated side chain groups are interdigitated, leading to both backbone and side chain hydrogen bonding, binding the sheets together in a steric zipper mechanism along the fibril axis.[40,53,54] Ivanova *et al*[55] previously reported an amyloidogenic sequence (LVEALYL) situated in HI chain B, which forms structurally similar amyloid-like fibrils in isolation to HI through the steric zipper mechanism (1.3.1. What is protein fibrillation?, page 40) and suggested that this segment is central to the fibrillation pathway.

1.3.1. What is protein fibrillation?

Protein fibrillation is termed as the process for which proteins misfold from their native state into large linear aggregates.[56] Investigation of the fibrillation pathway is important for amyloid studies since the large insoluble fibrillar assemblies

are hallmarks of amyloidosis. However questions were raised on how these fibrils incite toxicity within the proposed amyloid cascade hypothesis.[4] Recent advances have re-evaluated the cascade perspective,[57,58] and stipulated the pre-fibrillar mobile oligomeric species are the likely source of pathological toxicity.[59,60]

The fibrillation process is a nucleated self-assembly reaction[61] and can be generalised to a three-phase kinetic model, represented by a sigmoidal curve as shown in Figure 8, comprised of the; lag-, elongation- or growth- and finally saturation phase. Kinetically these phases correspond to; an increasing exponential growth rate (lag), linear maximum growth rate (elongation) and a decreasing asymptotic rate (saturation). Amyloid fibrillation kinetics are quantified using ThT fluorescence assays, which monitor the fibrillation pathway whereby fluorescence emission intensity is correlated to increasing fibrillation state, which will be discussed further in Chapter 4 (4.3.3. Measuring the amyloid-like fibrillation kinetics, page 144).

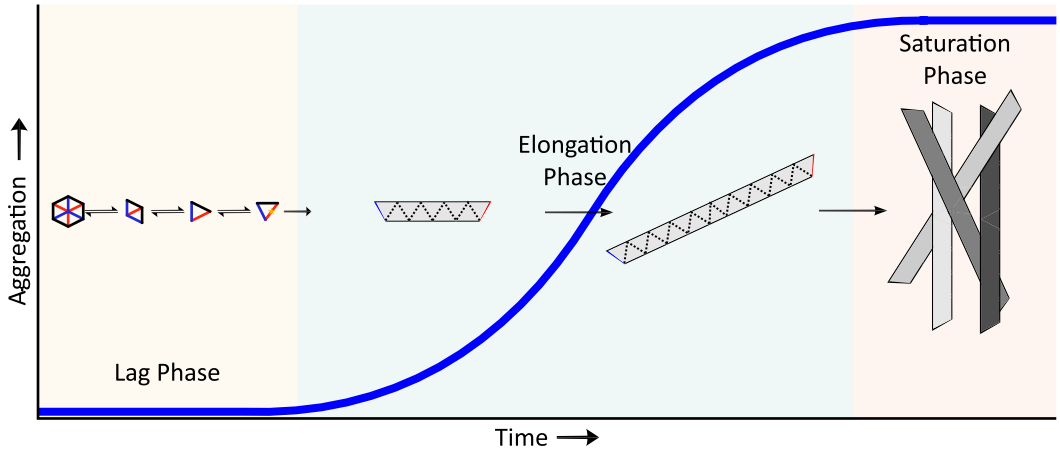

Figure 8: The three-phase kinetic amyloid fibrillation pathway model, showing a (blue sigmoidal curve) fibrillation proceeding through the (yellow) lag-, (green) elongation- and (pink) saturation- phases as a function of time (x-axis) and aggregation (y-axis).

The lag phase, shown as yellow background in Figure 8, consists of nuclei formation, which are stable states that allow growth and addition events to occur, and generate a critical concentration for detection within bulk assays.[61] Formation of nuclei in the lag phase occurs by the misfolding of protein monomers either in the

bulk solution (homogeneous) or at a surface (heterogeneous), which is termed as primary (*de novo*) nucleation and is shown in Figure 9.[62]

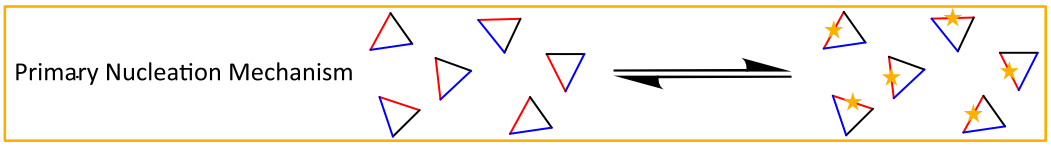

Figure 9: Schematic of the homogeneous primary nucleation mechanism, showing the soluble monomers as triangles with a (red) hydrophobic and (blue) hydrophilic domain and the (orange star) nucleation site. Adapted from Almeida et al.[63]

The primary nucleation mechanism (Figure 9), shows the HI monomers existing in an equilibrium with the nuclei. In the case of HI, the monomers also exist in an equilibrium, which will be discussed further (1.4.1. Oligomer Equilibrium, page 47), therefore the primary nucleation equilibrium necessitates the dissociation of hexamer species through dimeric to monomeric first.[64] Changes in the lag phase have been directly correlated to fibrillation kinetics, where decreased lag times have been associated with increased fibrillation.[65–67] For HI, Nielsen *et al*[68] have reported that increasing HI concentration or fibrillation in acidic conditions leads to a decreased lag time and accelerated fibrillation.

The elongation phase, also termed growth phase, is the linear propagation of aggregates formed by the addition of monomers to the nucleation sites at the fibril ends,[69,70] eventually resulting in a fibrillar structure as shown in Figure 10.[3] In Figure 10a, this is shown by the addition of soluble monomers (triangles) to the preformed fibrillar species (black trapezoid). In addition to the elongation mechanism, this phase also consists of two secondary nucleation pathways; fragmentation and surface-catalysed, shown in Figure 10b and c. Fibril fragmentation (Figure 10b) generates an increased number of nucleation sites through which elongation can proceed, therefore accelerating fibrillation rate within the system.[71] Surface-catalysed nucleation (Figure 10c) occurs on the surface of preformed fibrils, whereby transient adsorption of monomers results in templated fibrillation.[72,73]

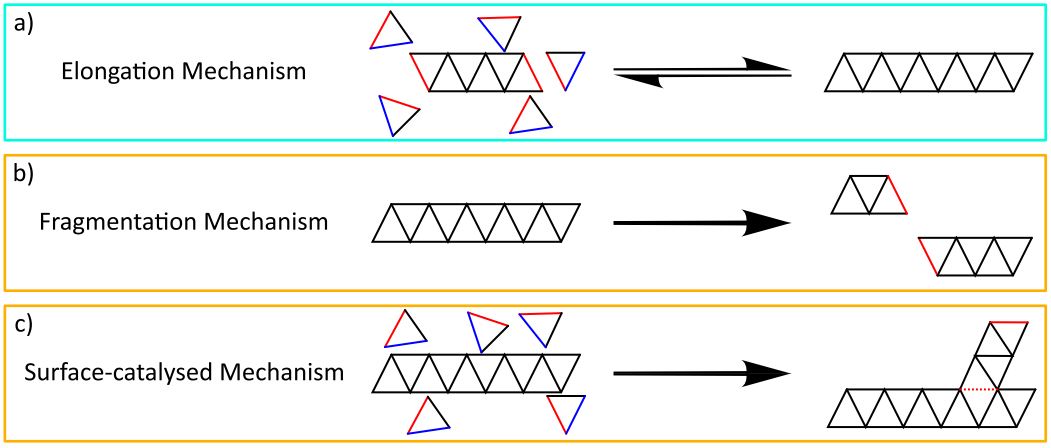

Figure 10: Schematic showing the elongation phase which consists of the (blue border) growth and (orange border) nucleation states. The associated fibrillation mechanisms; (a) Elongation, (b) Fragmentation and (c) Surface-catalysed mechanisms. The soluble monomers are represented as triangles with a (red) hydrophobic and (blue) hydrophilic domain. Adapted from Almeida et al.[63]

The surface-catalysed mechanism shown in Figure 10, can disrupt an amyloidogenic fibrillation pathway, because fibrillation can occur at nucleation sites on preformed aggregate surfaces therefore resulting in statistically variable reaction rates.[74] The nucleation arising from aggregate surfaces is termed seeded-growth, which has been shown to significantly affect the fibrillation pathway,[69,75] and accelerated kinetics for HI have been reported.[55,76] This mechanism is described here for nucleation on protein species, but it can also occur at physical surfaces, which will be discussed further (1.5.1. Protein interaction at the liquid-solid interface, page 52).

Khurana *et al*[77] describe fibrillation as a hierarchal assembly model, whereby the nucleated polymerisation firstly results in a linear aggregate structure termed a protofilament. A protofilament is formed, by two β-sheets (green and pink) interlocking together in a steric zipper mechanism, as shown in Figure 11a, forming a dehydrated β-sheet bilayer which runs along the fibril axis, shown in Figure 11b. In the case of HI, association of two protofilaments (pink / green and purple / orange) through intertwined or associated side-by-side processes results in the formation of a protofibril (green / purple), shown in Figure 11c.[78,79] Finally, two protofibrils interweave resulting in a mature insulin fibril (green / purple and grey / orange) shown in Figure 11d.[80] A recent investigation by Dolui *et al*[81] has shown the increasing diameter size and morphological changes of HI as fibrillation proceeds by

atomic force microscopy (AFM), from 3 – 4 nm for protofilaments[82] to 5 – 8 nm for protofibrils[81] through to 10 nm for fibrils.[78]

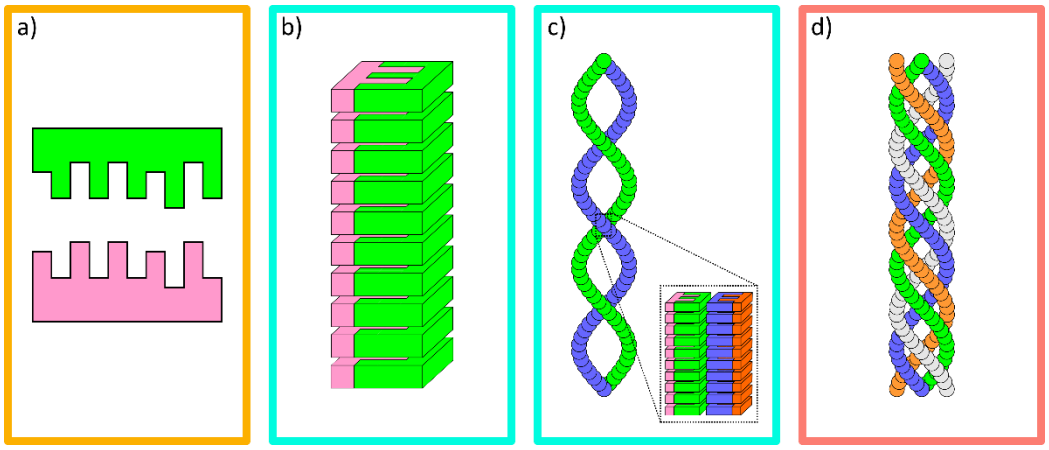

Figure 11: A schematic showing the hierarchal assembly of a fibril, (a) steric zipper mechanism between two ß-sheets, (b) protofilament between the two zippers along a fibril axis, (c) Protofibril with inset showing the association of two protofilaments along the axis and (d) a fibril formed by two protofilaments. The coloured borders are indicative of the three-phase kinetic model, (orange) nucleation, (blue) lag and (red) saturation. Adapted from Khuruna et al.[77]

The elongation phase (Figure 8) has received significant interest recently because current research reports amyloid toxicity is derived from the pre-fibrillar species as opposed to the mature fibrils, which are categorised as hallmarks of amyloidosis diseases due to their aggregation into plaques.[24] The saturation phase (Figure 8), which is the association of fibrillar species into mature fibrils, is dependent upon the arrangement of protofibrils, which twist around each other, giving rise to differing fibril morphologies. The fibrillation process is affected by factors such as; temperature,[83] agitation,[84] pH,[85] concentrations[64] and denaturation additives[86] as a function of time, which construct fibrils of differing morphologies. In the case of HI, fibrils formed in neutral conditions are significantly shorter than those in acidic conditions as shown in Figure 12.[87] The chirality and morphology are also affected by slight variations in acidic conditions, where left-handed intertwined fibrils (~8 nm) are observed at pH 2.4 – 3.2 but become shorter (~2 nm) and aggregated right-handed fibrils at increased acidity (pH 1.1 – 2.1).[79]

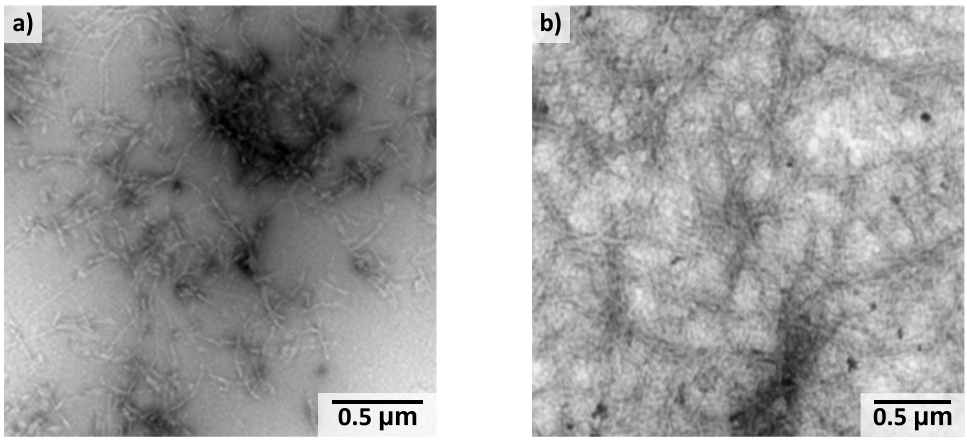

Figure 12: Transmission Electron Microscopy (TEM) images of human insulin (HI) fibrillation showing fibril morphology differences with respect to fibrillation in (pH 7.0, a) neutral and (pH 1.8, b) acidic conditions. Adapted from Iannuzzi et al.[87]

1.4. Human insulin: The model protein for amyloid research

The primary protein of interest within this thesis is human insulin (HI), which is a metabolic hormone physiologically important for the regulation of blood sugar. Insulin is a model protein for amyloid-fibrillation events, for two main reasons; its significance as a therapeutic for managing both Type I and II diabetes, and the high propensity to form amyloid-like fibrils *in vitro*.[88] Globally, it is estimated 415 million people live with diabetes, which is set to rise to 642 million by 2040.[89]

In both diabetic types, the condition can be managed by insulin treatments administered by transdermal injections.[90] However, both diseases differ significantly in the onset of disease. Type I diabetes is an autoimmune disease, whereby the patient's body is attacking and destroying insulin synthesising cells, β-cells, which are located within the pancreas. Conversely, Type II diabetes is insulin resistance, where the β-cells are becoming resistant to insulin therefore causing the pancreas to increase insulin production.[91] Unfortunately, the excessive demand upon the pancreas to increase insulin production, damages the β-cells thus reduces production which leads to a diminished physiological insulin response over time as the cell damage increases. In both types the ability to regulate and maintain blood sugar levels effectively is reduced, therefore both conditions are treated by introduction of physiologically-active insulin.[92,93] It is therefore of paramount importance to

understand the insulin fibrillation pathway in order to increase efficiency of the drug delivery systems, whilst reducing the risk of induced amyloidosis at the injection site.

The key focus for why this thesis focuses on HI rather than other amyloidogenic proteins, in addition to clinical importance, is the *in vitro* capability, specifically the ability to investigate HI fibrillation under laboratory conditions within a measurable timeframe. This thesis investigates how hydrophobic variability at the interface affects HI fibrillation, with the attention on surfaces which come into contact with insulin outside of the human body but are still important, such as; downstream processing, drug delivery systems and pharmaceutical storage. HI is globular protein, a class of proteins defined by their spherical architecture and sensitivity to changes in the local environment such as; temperature or pH, which allows for various conditions to be studied.

Chemically, HI is a 51 amino-acid residue polypeptide consisting of two chains (A and B) containing 21 and 30 amino acids respectively. There are three disulfide bonds present within the molecule which provide structural support for both chains; one intra-chain (A_6:A_{11}) and two inter-chain (A_7:B_7 and A_{20}:B_{19}), which are illustrated as orange bonds in Figure 13.

The three-dimensional representation of an NMR resolved HI monomer[31] in Figure 13, was rendered from the protein data bank (PDB) file using the Visual Molecular Dynamics (VMD) software.[33] HI consists of three α-helical secondary structure elements, two α-helices in chain A (green) and one in chain B (blue). The cyan and red colouration (Figure 13) denotes the C-termini at chains A and B respectively. The termini locations are also utilised for the single-point mutations observed for insulin analogues (as shown in 1.4.2. Mutations of insulin, page 48). Formation of an anti-parallel β-sheet, to stabilise the HI dimer, occurs at the B-chain C-termini from residues B_{24}.[94]

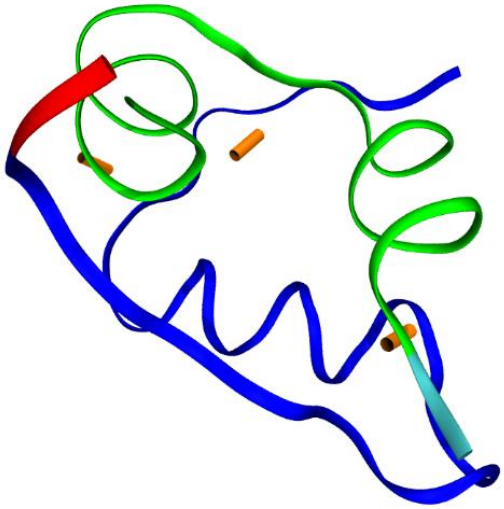

Figure 13: Visual Molecular Dynamics (VMD)[33] representation of human insulin (HI, PDB: 2JV1),[31] illustrating; (green) chain A, (blue) chain B, (orange) disulfide bonding, point mutation (cyan) A_{21} and mutation region for point mutations (red) B_{31} and B_{32}.

1.4.1. Oligomer Equilibrium

Insulin can exist in various oligomeric states (Figure 14); monomer, dimer and hexamer, dependent upon the environmental conditions present.[95,96] This equilibrium is important and has been exploited in the pharmaceutical industry. As the hormone is active in its monomeric state, but its stability is inversely proportional to the oligomeric state as fibrillation occurs more rapidly,[97] therefore the hexameric state is preferential for logistical purposes as the hexamer reduces chemical degradation and toxic aggregation from occurring during storage.[98] The physiological dissociation of hexamer to monomer state, upon injection, gives rise to the various pharmacodynamic analogues,[99,100] which will be discussed further (1.4.2. Mutations of insulin, page 48).

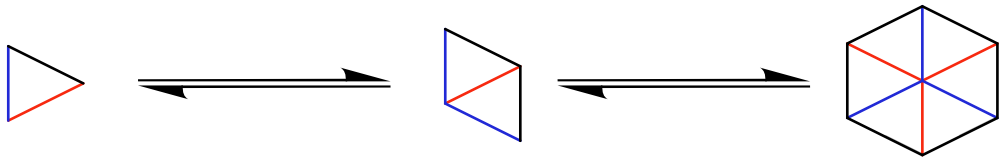

Figure 14: Human insulin (HI) oligomeric states represented (left to right); monomer, dimer and hexamer. The colour denotes the (red) hydrophobic and (blue) hydrophilic domains.

The oligomeric states exist in an equilibrium, which is mediated by pH and HI concentration. In general, low pH (acidic) promotes monomeric state, whilst increasing the insulin concentration leads to a greater preference for higher order oligomeric species. Attaining the hexameric state requires zinc ion stabilisation, whereby the dimeric species co-ordinate to the zinc ion. In pH 2 conditions, acetic acid (20%) and reduced HI concentration, the monomeric state is preferred.[68,101] Ideally, amyloid-like fibrillation investigations should aim to study and contrast both oligomeric-dominant extreme conditions.[96,101,102] The manipulation of oligomeric equilibrium is critical in this thesis, as both monomeric (pH 2, 20% acetic acid) and predominantly higher order oligomeric species (pH 7, phosphate-buffered saline, PBS) are studied to observe the differences posed at the hydrophobic interfaces.

The monomeric state is both pharmaceutically active and has also been reported to most readily adsorb to hydrophobic surfaces.[21,68,88,103] This activity is derived from the monomeric structure, since it has an exposed hydrophobic region, which drives the surface adsorption to minimise exposure to the hydrophilic solution. Meanwhile, the oligomeric states are formed by two monomeric hydrophobic regions joining together (dimerising), thus burying this interface and reducing preference for surface adsorption through the hydrophobic interactions. If an insulin monomer adsorbs to the hydrophobic surface, this involves structural rearrangement leading to disordering and thus misfolding events at the bulk interface allowing for amyloid-like fibrillation to occur.[104]

1.4.2. Mutations of insulin

The importance of insulin as a model protein for amyloid research has led to a lot of literature for the insulin fibrillation pathway, however the main concern attributed to this is the lack of clarity or consistency surrounding the insulin variant

studied. Historically, the management of diabetic conditions was with animal derived insulin, specifically bovine (cow) or porcine (pig). It was not until the 1980s that a human insulin variant was commercially available.[105] HI was an issue for patients due to the associated pharmacokinetic and pharmacodynamic drug profiles, therefore pharmaceutical analogues were developed. These new pharmaceutical analogues, with significantly improved biostatistics, such as potency and drug lifetime, have resulted in five categorisations of medicinal-grade insulin, which are classified by drug activity lifetime; rapid-, short-, intermediate-, long- and ultra-long-acting. HI is categorised as a short-term drug, whereas a synthetic variant, insulin glargine, is a long-term drug due to its longer activity period, up to 24 hours.[106,107]

Insulin derivatives and analogues exist by means of amino acid mutations within the primary peptide sequence, where a single-point mutation can result in vastly different pharmacodynamics. A brief comparison of the single-point mutations present in the pharmaceutical insulin analogue glargine, and historic derived bovine and porcine, compared to HI is shown Table 1.

Table 1: Analogues of insulin showing the mutated amino acid residue sites for each analogue; Human (HI), Glargine, Bovine, and Porcine. Only the mutated sites are displayed, and those which differ from HI are shown in bold. Glargine is the most mutated sequence for these analogues consisting of three residues across both chains at sites A_{21}, B_{31} and B_{32}, with the latter two residues additional to the HI sequence. Bovine also consists of three mutation sites across both chains, but with no additional residues, situated at A_8, A_{10} and B_{30}. Porcine is the least mutated analogue shown here, with only one mutation situated within the B-chain at B_{30}.

Insulin variant	**Amino acid mutation (chain, residue number)**					
	A_8	**A_{10}**	**A_{21}**	**B_{30}**	**B_{31}**	**B_{32}**
Human	Threonine	Isoleucine	Asparagine	Threonine	-	-
Glargine	Threonine	Isoleucine	**Glycine**	Threonine	**Arginine**	**Arginine**
Bovine	**Alanine**	**Valine**	Asparagine	**Alanine**	-	-
Porcine	Threonine	Isoleucine	Asparagine	**Alanine**	-	-

Table 1 highlights that overall there are six possible single-point mutation sites, three in each chain, including two additional residue sites at chain B, which result in differing pharmacodynamics apparent for; glargine, bovine, or porcine insulin. The pharmaceutically designed analogue, insulin glargine, consists of three mutations; one at the A-chain carbon terminus (A_{21}) and the addition of two residues at the B-chain carbon terminus (B_{31}, B_{32}). In terms of historic insulin analogues, similarly to glargine, bovine consists of three mutations; two within the A-chain ($A_{8, 10}$), and one at the B-chain carbon terminus (B_{30}), whereas porcine has the least mutations with only one which is situated at the B-chain carbon terminus (B_{30}),[99,108] neither historic analogue contains any additional residues.

It is important to consider the effect of single-point mutations on the HI sequence, as mutations result in vastly different protein properties either intentionally or otherwise, which are pharmaceutically beneficial because the associated pharmacopeia / kinetic / efficacy properties can be adapted as required. For example, insulin glargine was designed with the inclusion of the two additional arginine residues, which are both positively charged, at the B-chain termini and leads to a larger structural effect; isoelectric precipitation.[109] This effect shifts the isoelectric point of insulin to neutral pH, which is critical from a pharmaceutical perspective. Injection of glargine into the human body, at physiological pH, leads to precipitation of the drug, which is a desired process as this prolongs the adsorption of glargine into the bloodstream resulting in a controlled long-term release.[110]

Overall, the effect of mutations in the wider context of amyloid research, leads to questioning the validity of utilising protein analogues, since the biophysical properties of the peptide differ and thus may aggregate and fibrillate differently. A slight modification of the primary sequence can have major ramifications regarding the protein output as observed with single-point mutations and the resulting analogues. A mutation at a hydrophobic region, or the inclusion of hydrophobicity could affect the oligomeric equilibrium of insulin and thus enhance or inhibit the aggregation propensity thereof.

1.4.3. Fibrillation pathway

The previous section, (1.3.1. What is protein fibrillation?, page 40), has already presented the amyloid fibrillation pathway using HI as the exemplar protein to discuss the three-phase fibrillation kinetic model. A prerequisite for insulin to undergo the fibrillation process, is the dissociation of insulin oligomers within the oligomeric equilibrium (Figure 14) into the active fibrillation component, monomeric state. It has been reported that the fibrillation pathway is triggered at the monomeric state by a structural change resulting in partial unfolding and exposure of the hydrophobic domain to the environment.[55,97,111] The unfolding event occurs at the A-chain N-termini, which exposes a hydrophobic domain,[97] this unfolding is important for both surface adsorption and fibrillation to occur because of the hydrophobic interactions.[112] These interactions result in a β-sheet formation, whereby disulfide bonds are retained,[78,113] which gives rise to a protofilament through the steric zipper mechanism.[114]

In this thesis both acidic and neutral pH conditions are studied to manipulate the oligomeric equilibrium. Acidic conditions are used to study amyloid-like fibrillation within a reasonable timeframe for measurements, whereby neutral pH is used for comparison to physiological conditions.

1.5. Why are surfaces important?

A surface or interface is defined as a boundary between two phases, whereby there is an abrupt change in properties with distance.[115,116] Molecularly, surface atoms located at the outermost layer, have different chemical and physical properties to those in the bulk material because of a lack of neighbouring atoms.[117] Interfaces are often used in surface science studies to facilitate chemical or biological processes, such as electrochemical or heterogeneous catalytic reactions.[118] The presence of a surface can influence a biological system; therefore, it is important to consider the effect of a substrate surface on a liquid suspension for various reasons ranging from storage to logistics or processing events, whereby the suspension is in contact with a high surface area.

1.5.1. Protein interaction at the liquid-solid interface

Research targeting the interaction of proteins at surfaces is of increasing importance, to understand the implications on processes such as; clinical, medicinal and industrial. These processes could range from biomaterials for implants, to drug delivery, through to downstream processing in industrial environments. This thesis is principally interested in the implications which arise from the formation of fibrillar structures by amyloidogenic proteins, specifically the impact of surfaces on HI in respect to the long-term storage and logistical issues for the drug delivery system.

Protein adsorption to the surface is a spontaneous process which occurs through chemisorption or physisorption processes.[17,119] The protein's structural state is dependent upon its classification, Norde *et al*[120] classified proteins according to their structural stability. Low internal stability termed "soft" and thus likely to undergo structural rearrangement upon adsorption at the surface, whereas high internal stability termed "rigid" where limited structural rearrangement occurs.[120] HI is a structurally labile globular protein and thus has been defined as 'soft' using the Norde classification,[121] which infers structural rearrangement occurs upon adsorption to the surface. Adsorption to a surface is a complex phenomenon and can occur through various mechanisms, dependent upon the properties of both the surface and protein. There are many possible mechanisms for protein adsorption to a surface, as shown in Figure 15. However these are simplified adsorption models based on generalised assumptions of both the surface and protein.[122]

The nine protein adsorption models shown in Figure 15, have been grouped into; specific site adsorption (Figure 15a, b, c), clustering adsorption (Figure 15d, e) and change in adsorbed protein state (Figure 15f, g, h, i). In the specific site adsorption models the protein (purple circle) initially adsorbs (shaded lilac) to an available site (green dashed line) on the surface (shaded grey). In the Langmuir model (Figure 15a) the protein adsorbs at discrete sites, whilst in the Random Sequential Adsorption model (RSA, Figure 15b) arbitrary adsorption to any site occurs and finally for the Tracking model (Figure 15c) the adsorption is facilitated by the pre-adsorbed protein. Pre-adsorbed species are also key in the clustering processes (Figure 15d and e); in the exchange model (Figure 15d) a monomer initially

adsorbs to the surface, but can then be replaced through dimer association from the bulk solution. Whilst in the surface clustering model (Figure 15e) adlayer adsorption or diffusion can occur. Adsorption of a soluble protein monomer to a pre-adsorbed species can occur either in a multi-layer form directly above or adjacent to the gathered species, which can result in diffusion of the species across the surface leading to surface clustering. The final models result in a protein state change upon adsorption to the surface, which are the; (f) rollover, (g) two-states, (h) three-states and (i) multi-state models. In regards to HI, all the models are valid but are dependent on the HI oligomeric state, suspension and surface properties.[124]

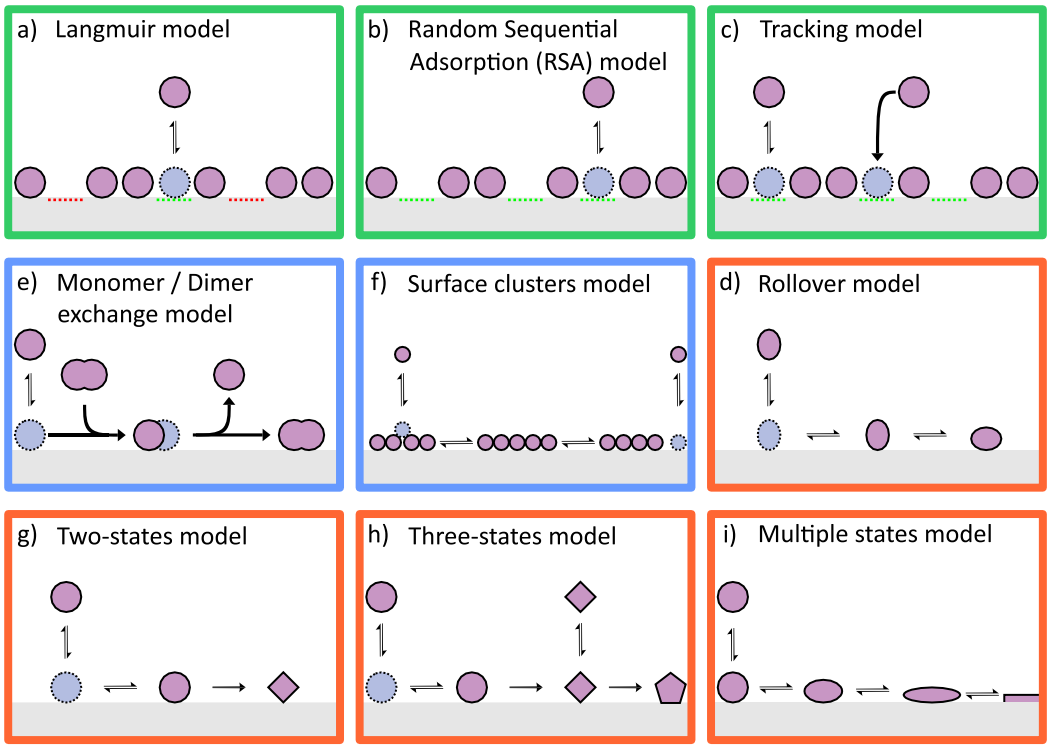

Figure 15: Schematic showing the various possible (purple circles) protein adsorption events, with the (lilac) initial adsorption state onto a (grey) generalised surface mechanisms. (green borders) Specific site adsorption model are; (a) Langmuir, (b) Random Sequential Adsorption and (c) Tracking, with (dashed) possible adsorption sites shown as either (green) available or (red) unavailable. (blue borders) The clustering models are; (d) Monomer / Dimer exchange and (e) Surface clusters. (orange borders) A change in adsorbed protein state results in the following models; (f) Rollover, (g) Two-states, (h) Three-states and (i) multiple states, as shown by the shape change from circular to diamond or pentagon. Adapted from Rabe et al.[123]

Arnebrant *et al*[125] have reported that soluble HI monomers adopt a close packed layer on adsorption[126] to metal surfaces. In the presence of gold, insulin

monomers have been reported to adsorb through chemisorption processes via the insulin disulfide bridges, as shown in Figure 16, which result in degradation of the insulin structure to accommodate formation of gold-sulfur bonds (Au-S).[127] Welinder *et al*[127] proposed the structurally labile insulin monomer (or dimer) species becomes increasingly unfolded on adsorption to the gold surface due to sequential Au-S bonding.

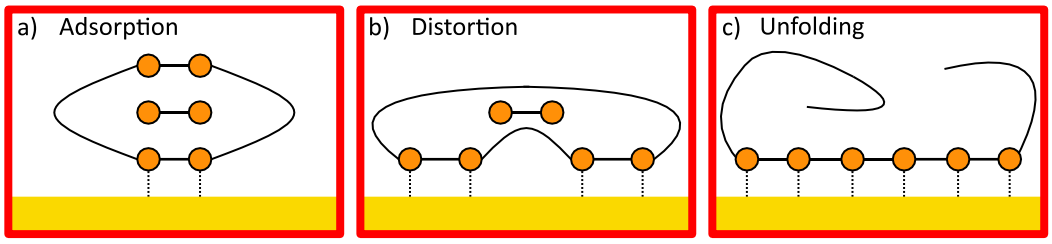

Figure 16: Schematic of an insulin monomer adsorption process to a (yellow) gold surface illustrating the effect of adsorption through the (orange) internal cysteine residues by various disulfide bonds. (a) adsorption to one disulfide bond, (b) distortion for two disulfide bonds and (c) unfolding resulting in three disulfide bonds to gold. Adapted from Welinder et al.[127]

Initially insulin adsorbs to a bare gold surface by chemisorption with formation of two Au-S bonds through one of insulin's intra-disulfide bonds shown in Figure 16a. Insulin is structurally labile therefore distortion processes lead to adsorption through two intra-disulfide bonds resulting in four Au-S bonds formed shown in Figure 16b. The insulin monomer then becomes increasingly distorted, which results in unfolding processes, as all disulfide bonds adsorb to the surface thus formation of six Au-S bonds (Figure 16c). The formation of the strong Au-S bond occurs because gold has a high affinity for sulfur and is the driving force for the establishment of self-assembled monolayers (SAMs) through thiol and disulfide chemistry.[128] After adsorption to the gold surface (Figure 16a), as HI is structurally labile, it undergoes a conformational change leading to the autocatalytic effect.

The autocatalytic effect, as described by Hammarstrom *et al,*[129,130] occurs when the adsorbed insulin layer undergoes a conformational change which results in self-replication as adsorption to the layer proceeds, through the secondary nucleation surface-catalysed mechanism (Figure 10c).[19] Firstly, the soluble insulin monomers adsorb to the surface substrate, resulting in a conformational change at

the adsorbed insulin layer. Continued adsorption initiates the nucleation phase thereby generating nucleation sites for which fibrillation can proceed. At a critical point, the nucleated insulin molecules dissociate from the adsorbed layer, thereby resulting in fibril seeds which propagate within the media through a seeded-growth approach. The loss of the insulin fibril seeds results in regeneration of the adsorbed layer, therefore allowing for further insulin adsorption at this layer and continuation of the autocatalytic cycle. Fibrillation of HI through the autocatalytic effect is further compounded by its classification as a "soft" protein as it is structurally labile on adsorption to hydrophobic and hydrophilic surfaces.

1.5.2. Why is hydrophobicity key?

A surface can be described by its wetting ability, which is the amount of contact a water droplet has at a surface interface defined as hydrophobic or hydrophilic character. This terminology is derived from Latin meaning; 'hydro-' (water), '-phobic' (repel) and '-philic' (attract). Hydrophobicity has been observed in nature, the noteworthy example of a lotus leaf, which utilises hydrophobic character as a self-cleaning mechanism, whereby the water droplet rolls off the leaf removing dirt particulates from the leaf's surface.[131] The hydrophobicity of a material is determined by the contact angle of a water droplet at the surface, as shown in Figure 17. A surface is described as hydrophobic if the contact angle is greater than or equal to 90°. Conversely, a surface is classified as hydrophilic if it possesses a contact angle less than 90°, thus the surface is wetting. Recent scientific interests include superhydrophobicity (contact angle greater than 150°) and superhydrophilicity (contact angle equal to 0°), which are proposed for separation sciences.[132]

Hydrophobicity is not a specific phenomenon attributed to surfaces but is attributed to the overall charge of a molecule. A molecule with no regions of charge is non-polar, thus does not dissolve in water and is termed hydrophobic, whilst a molecule with partial positive or negative charges is hydrophilic. Molecules which consist of both hydrophobic and hydrophilic regions are termed amphiphilic, an example of such is a surfactant with a hydrophobic tail and hydrophilic head. In aqueous colloidal conditions and above a certain concentration, the individual

surfactants aggregate together, with the hydrophobic tails creating a hydrophobic core and the head groups interacting with the suspension, which forms a three-dimensional supramolecular assembly termed micelle. Aggregation is driven here by entropic factors, the loss of solvation shells surrounding the surfactants hydrophobic tail groups is greater than the loss of entropy as a result of the micelle's hydrophobic core.[133]

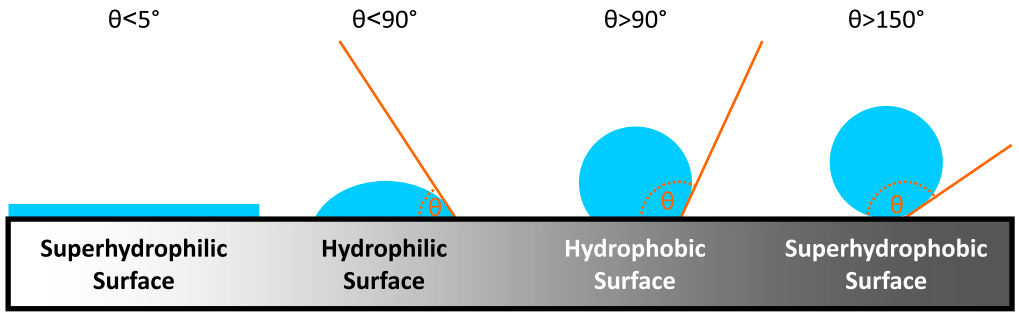

Figure 17: Characterising surface hydrophobicity, shown by changes in the (θ, orange) contact angle between the (blue) water droplet and (grey / black) surface. The increasing (θ) contact angle corresponds to increasing hydrophobicity, surface dewetting and reduction in surface adhesion and surface free energy.

Proteins are complex amphiphilic constructs comprised of various hydrophobic and hydrophilic amino acid residue side groups. The amphiphilic character is an integral feature for many structural features, such as α-helices with hydrophobic groups orientated towards the centre and hydrophilic on the outside forming a hydrophobic core. Proteins adsorb to hydrophobic surfaces because of this entropic effect, by increasing entropy resulting from loss of a solvation shell around each protein molecule.[134] A soft protein such as HI, adsorbs strongly to hydrophobic and hydrophilic surfaces because of the entropy gained from structural rearrangement, which overcomes electrostatic concerns.

Adsorption at a hydrophobic surface presents an additional concern for amyloidogenic proteins, as proteins adsorb to a hydrophobic surface as a cluster, which can then spread across the surface because of their innate high surface mobility.[123] The generalised protein (green shaded circles) adsorption pathway for hydrophobic (red border) and hydrophilic (blue border) surfaces are shown in Figure 18. In the hydrophobic pathway (Figure 18a, b, c) the protein cluster firstly

adsorbs onto the surface by anchoring to the surface substrate, diffusing the pre-adsorbed species, thus allowing the protein cluster to disperse across the surface. In contrast, for the hydrophilic pathway (Figure 18 d, e, f), the protein cluster fails to adsorb, resulting in no anchoring mechanisms, thus detaches from the hydrophilic surface.

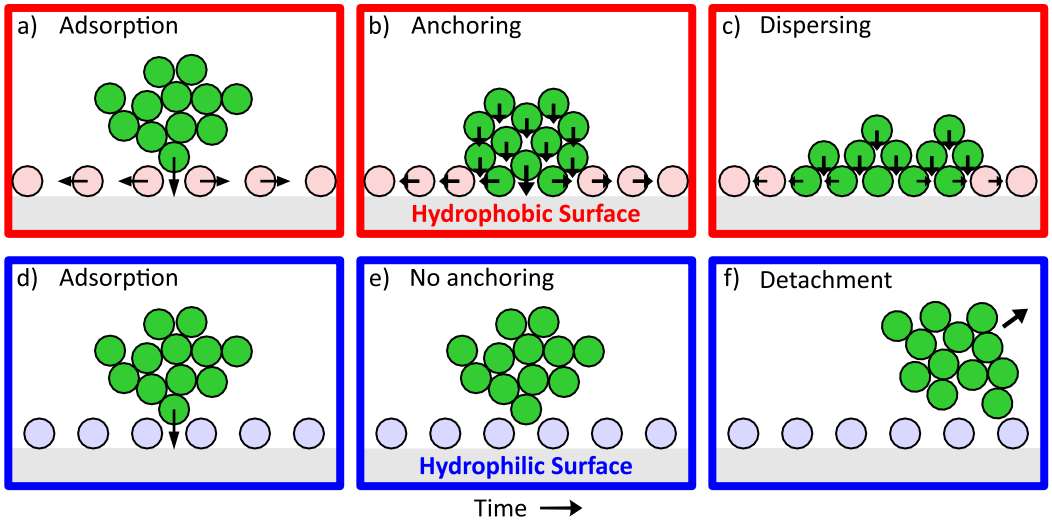

Figure 18: Schematic of a (green) generalised protein cluster adsorption mechanism to a (red) hydrophobic or (blue) hydrophilic surface. Adapted from Rabe et al.[123]

Previous studies have reported that hydrophobicity affects the HI fibrillation pathway, in the presence of hydrophobic Teflon particles (~0.2 µm) the fibrillation kinetics are increased.[96] It has been shown that the HI monomers undergo conformational changes on adsorption to thiol-functionalised gold surfaces which allow further HI binding.[135] HI monomers have been shown to adsorb to hydrophobic surfaces preferentially, with one of the monomers hydrophobic interfaces orientated towards the surface.[125,136] Nayak *et al*[137] proposed it is the confinement of protein molecules on hydrophobic surfaces, which increased localised protein concentrations, that attributed to the enhanced fibrillation kinetics for insulin.

There are benefits to hydrophobic materials, for example their increasing usage in clinical applications because of the advantages such as; anti-corrosion, anti-fouling and self-cleaning.[138] An emerging clinical application for superhydrophobic materials are medical implants, as the hydrophobicity can reduce biofilm formation, an accumulation of bacterial communities, which are attributed

to bacterial infections within the patient.[139] Pharmaceutically, hydrophobic materials may present advances in drug delivery systems from utilising nanostructures,[140] to polymer drug conjugates,[141] through to 3D superhydrophobic cages,[142] or for syringe needle coatings to reduce patient discomfort during transdermal injections.[143]

1.5.3. Changing surface properties by functionalisation techniques

The primary aim of this thesis is to investigate how varying surface hydrophobicity affects HI fibrillation, for comparability purposes it is therefore advantageous to maintain the same bulk substrate and only change the surface functionality. This thesis investigates two bulk substrates, silicon and gold, because they are both used in medicinal applications, are of spectroscopic interest, but most importantly can be hydrophobically functionalised using standard methodology.

Silicon is increasingly used from diagnostics[144] to biomedical applications,[145,146] through to amyloid research as a spectroscopic substrate.[130] This thesis utilises silicon for the latter, as a substrate for which hydrophobic functionalisation can occur, its use as a substrate is ideal due to its spectroscopic potential. Surface-sensitive spectroscopic studies require a highly reflective surface, for which silicon when polished can attain, whilst the material itself has isolated Raman vibrational band characteristics (520 cm^{-1}).[147] Silicon can be easily modified through silane chemistry, which functionalises the interface with the desired modification as shown in Figure 19.

The silanisation process resulting in SAMs, shown in Figure 19, firstly requires a clean hydroxylated silicon surface, this surface undergoes hydrolysis in the presence of a silane resulting in the loss of an alcohol group. The silanisation process can propagate further with silane molecules hydrolysing at the surface or polymerising with other silane groups. The silanisation process is ineffective and on termination results in residual hydroxyl sites, also known as silanol groups, which could lead to unintended chemical reactions or degradation of the silicon substrate. In applications such as chromatography, it is vital to limit the silanol availability as the functionalised interface dictates specific binding to the analyte.[149] A process

termed end-capping shown in Figure 19d, is often used which functionalises the remaining silanol sites with a smaller silane functional group.

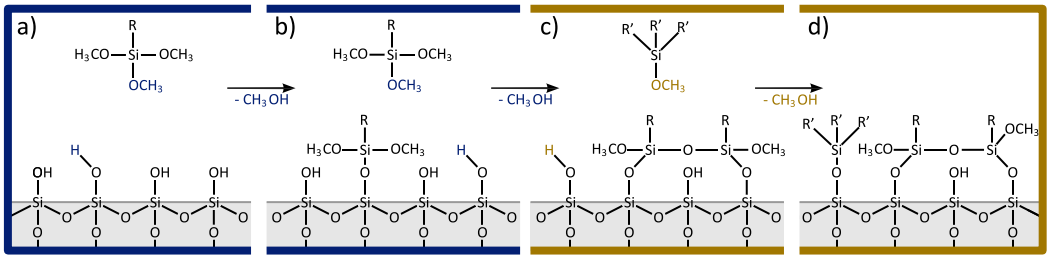

Figure 19: Schematic for the formation of self-assembled monolayers (SAMs) using silane chemistry on a (grey) hydroxylated silicon surface. (blue border) The silanisation process commences with (a) hydrolysis of a silane molecule and hydroxyl group resulting in loss of methanol, (b) additional silane molecules can hydrolysis with both the surface and adsorbed silane methoxy group resulting in loss of methanol molecules. (gold border) The end-capping process (c) introduces a smaller functional silane to the remaining silanol groups and through hydrolysis results in loss of methanol molecule, providing (d) an end-capped silane functionalised silicon surface. Adapted from Ratner et al.[148]

Gold, an inert metal, is a widely utilised material due in large parts to its biological compatibility and historical usage, with applications ranging from medical devices to anti-inflammatory and anti-microbial purposes.[150] A bare gold substrate is also spectroscopically advantageous as it is reflective and thus can be utilised in surface-sensitive techniques. Similarly to silicon, a gold surface can be functionalised using SAMs with chemistry analogous to silanisation, utilising thiol and disulfide chemistry.[151–156] It is important to note that while gold is spectroscopically an ideal material, as previously shown in Figure 16, the bare gold surface can associate to HI through the formation of Au-S bonds, which are detrimental to the structural stability of HI. The use of gold nanoparticles has been shown to inhibit bovine insulin fibrillation and affect its fibrillar morphology.[157] Functionalised gold surfaces have previously been used in amyloidogenic studies from autocatalytic fibrillation of amyloid-β (Aβ),[158] to seeded-fibrillation growth studies of bovine insulin by quartz crystal microbalance (QCM).[159]

The work in this thesis designated an interface as the boundary between a hydrophobically functionalised solid substrate and a protein suspension, which is titled *The Physical and Chemical Origins of Amyloid at Interfaces.* The specific

objective of this work was to study the effect of hydrophobic functionalised interfaces, silicon and gold, on HI fibrillation under measurable conditions using an ensemble of spectroscopic techniques, to gain an insight into structural and kinetic properties particularly the pre-fibrillar state.

1.6. Outline of thesis

1.6.1. Chapter 2: Directed Human Insulin Fibrillation on Hydrophobic Silane Functionalised Silicon Surfaces

Reflection anisotropy spectroscopy is used to determine how adsorbed HI and its pharmaceutical analogue aligned with the underlying architecture of the Si surfaces. The initial promise of this methodology showing differing alignment for these proteins was abandoned when irreproducibility issues prevailed, and this goal was unfortunately not achieved.

1.6.2. Chapter 3: The Importance of Protein Pre-Treatment

This chapter develops a new methodology for the preparation and storage of the HI suspensions to ensure the reproducibility of the results in subsequent work.

1.6.3. Chapter 4: The Co-incubation Effect of Functionalised Mesoporous Silica Microparticles with Human Insulin, on Amyloid-like Fibrillation

Silica mesoporous microparticles are used in this study to investigate the effect of hydrophobic functionalised mobile surfaces on HI fibrillation using adsorption, kinetics and morphology techniques. The results showed that HI incubation with particles at pH 2 inhibited whilst at pH 7 enhancement of the typical sigmoidal curve occurred and these results were correlated to the transmission electron microscopy (TEM) images of the fibrils.

1.6.4. Chapter 5: Hydrophobic Functionalisation of Gold Surfaces on Human Insulin Fibrillation

The effect of the surface hydrophobic functionalisation on the thickness of an adsorbed HI monolayer is investigated and correlated to pH and degree of hydrophobicity. These monolayers were probed with Raman spectroscopy to

determine the structural composition of the HI adlayer, specifically as structural rearrangement of HI had occurred upon adsorption to the hydrophobic surface.

1.6.5. Chapter 6: Interrogating Human Insulin Adsorption on Hydrophobically Functionalised Gold Interfaces with Infrared-Scanning Near-field Optical Microscopy (IR-SNOM)

This chapter uses the novel technique of scanning infrared near-field optical microscopy (IR-SNOM) in a preliminary investigation to determine the effect of hydrophobic functionalised gold surfaces on the secondary structure of HI. The results presented are the first results obtained from an IR-SNOM in reflection mode (with the quantum cascade laser as the mid-IR source), of adsorbed protein at a hydrophobic interface. These results showed that the IR-SNOM is able to determine variations in the HI secondary structure contributions within the Amide I band.

1.6.6. Chapter 7: Utilising Intrinsic Fluorescence to Probe a Potential Amyloid-like Signature

Deep-blue autofluorescence, is a fluorescence phenomenon that has recently been associated as an amyloidogenic property. In this chapter fluorescence excitation – emission matrices are used to probe the origin of this phenomenon using HI, α-synuclein and other peptides. The results did not determine the origin, however did provide further information into the applicability of this technique for amyloid-like fibrillation.

1.6.7. Chapter 8: Future Work

This chapter summarises the work of the thesis and provides ideas for future work for instrument development and experiments to elucidate more information on HI fibrillation.

Bibliography

1. Eisenberg, D. & Jucker, M. The Amyloid State of Proteins in Human Diseases. *Cell* **148**, 1188–1203 (2012).
2. Jucker, M. & Walker, L. C. Self-propagation of pathogenic protein aggregates in neurodegenerative diseases. *Nature* **501**, 45–51 (2013).
3. Rambaran, R. N. & Serpell, L. C. Amyloid fibrils. *Prion* **2**, 112–117 (2008).
4. Hardy, J. & Higgins, G. Alzheimer's disease: the amyloid cascade hypothesis. *Science* **256**, 184–185 (1992).
5. Polymeropoulos, M. H. *et al.* Mutation in the α-synuclein gene identified in families with Parkinson's disease. *Science* **276**, 2045–2047 (1997).
6. Marzban, L., Park, K. & Verchere, C. B. Islet amyloid polypeptide and type 2 diabetes. *Exp. Gerontol.* **38**, 347–351 (2003).
7. Quock, T. P., Yan, T., Chang, E., Guthrie, S. & Broder, M. S. Healthcare resource utilization and costs in amyloid light-chain amyloidosis: A real-world study using US claims data. *J. Comp. Eff. Res.* **7**, 549–559 (2018).
8. Quock, T. P., Yan, T., Tieu, R., D'Souza, A. & Broder, M. S. Untangling the clinical and economic burden of hospitalization for cardiac amyloidosis in the United States. *Clin. Outcomes Res.* **Volume 11**, 431–439 (2019).
9. Sayed, R. H., Hawkins, P. N. & Lachmann, H. J. Emerging treatments for amyloidosis. *Kidney Int.* **87**, 516–526 (2015).
10. Merlini, G. & Palladini, G. Amyloidosis: Is a cure possible? *Ann. Oncol.* **19**, 63–66 (2008).
11. Comenzo, R. L. How I treat amyloidosis. *Blood* **114**, 3147–3157 (2009).
12. Glabe, C. G. Common mechanisms of amyloid oligomer pathogenesis in degenerative disease. *Neurobiol. Aging* **27**, 570–575 (2006).
13. Selkoe, D. J. Amyloid β-Protein and the Genetics of Alzheimer's Disease. *J. Biol. Chem.* **271**, 18295–18298 (1996).
14. Picken, M. M. New insights into systemic amyloidosis: The importance of diagnosis of specific type. *Curr. Opin. Nephrol. Hypertens.* **16**, 196–203 (2007).
15. Mullane, K. & Williams, M. Alzheimer's therapeutics: Continued clinical failures question the validity of the amyloid hypothesis - But what lies beyond? *Biochem. Pharmacol.* **85**, 289–305 (2013).
16. Ankarcrona, M. *et al.* Current and future treatment of amyloid diseases. *J. Intern. Med.* **280**, 177–202 (2016).
17. Zhu, M., Souillac, P. O., Ionescu-Zanetti, C., Carter, S. A. & Fink, A. L. Surface-catalyzed Amyloid Fibril Formation. *J. Biol. Chem.* **277**, 50914–50922 (2002).
18. Sharp, J. S., Forrest, J. A. & Jones, R. A. L. Surface Denaturation and Amyloid Fibril Formation of Insulin at Model Lipid−Water Interfaces. *Biochemistry* **41**, 15810–15819 (2002).
19. Törnquist, M. *et al.* Secondary nucleation in amyloid formation. *Chem. Commun.* **54**, 8667–8684 (2018).
20. Shikama, Y. *et al.* Localized Amyloidosis at the Site of Repeated Insulin Injection in a Diabetic Patient. *Intern. Med.* **49**, 397–401 (2010).
21. Sluzky, V., Tamada, J. A., Klibanov, A. M. & Langer, R. Kinetics of insulin aggregation in aqueous solutions upon agitation in the presence of hydrophobic surfaces. *Proc. Natl. Acad. Sci. U. S. A.* **88**, 9377–9381 (1991).
22. Frokjaer, S. & Otzen, D. E. Protein drug stability: A formulation challenge. *Nat. Rev. Drug Discov.* **4**, 298–306 (2005).
23. Stefani, M. & Dobson, C. M. Protein aggregation and aggregate toxicity: new insights into protein folding, misfolding diseases and biological evolution. *J. Mol. Med.* **81**, 678–699 (2003).
24. Glabe, C. G. Structural Classification of Toxic Amyloid Oligomers. *J. Biol. Chem.* **283**, 29639–29643 (2008).
25. Berg, J. M., Tymoczko, J. L., Gatto Jr., G. J. & Stryer, L. *Biochemistry.* (W.H. Freeman, 2015).
26. Wilcox, G. Insulin and Insulin Resistance. *Clin. Biochem. Rev.* **26**, 19–39 (2005).
27. Uzman, A. *Molecular Cell Biology*. *Biochemistry and Molecular Biology Education* **29**, (2001).
28. Lodish, H. F. *et al. Molecular cell biology.* (Macmillan Science & Educ. USA, 2016).
29. Cooper, S. & Sanderfoot, A. Primary Structure. in *Molecular Life Sciences* (ed. Bell, E.) 1–3 (Springer New York, 2014). doi:10.1007/978-1-4614-6436-5_2-3
30. Ouellette, R. J. & Rawn, J. D. Amino Acids, Peptides, and Proteins. in *Principles of Organic Chemistry* 371–396 (Elsevier,

2015). doi:10.1016/B978-0-12-802444-7.00014-8

31. Bocian, W. *et al.* Structure of human insulin monomer in water/acetonitrile solution. *J. Biomol. NMR* **40**, 55–64 (2008).

32. O'Donoghue, S. I., Chang, X., Abseher, R., Nilges, M. & Led, J. J. Unraveling the symmetry ambiguity in a hexamer: calculation of the R6 human insulin structure. *J. Biomol. NMR* **16**, 93–108 (2000).

33. Humphrey, W., Dalke, A. & Schulten, K. VMD: Visual molecular dynamics. *J. Mol. Graph.* **14**, 33–38 (1996).

34. Boyle, A. L. Applications of de novo designed peptides. in *Peptide Applications in Biomedicine, Biotechnology and Bioengineering* 51–86 (Elsevier, 2018). doi:10.1016/B978-0-08-100736-5.00003-X

35. Choudhuri, S. Additional Bioinformatic Analyses Involving Protein Sequences. in *Bioinformatics for Beginners* 183–207 (Elsevier, 2014). doi:10.1016/B978-0-12-410471-6.00008-6

36. Weaver, T. M. The π-helix translates structure into function. *Protein Sci.* **9**, 201–206 (2008).

37. Feher, J. Protein Structure. in *Quantitative Human Physiology* 130–141 (Elsevier, 2017). doi:10.1016/B978-0-12-800883-6.00012-4

38. Merkel, J. S., Sturtevant, J. M. & Regan, L. Sidechain interactions in parallel β sheets: The energetics of cross- strand pairings. *Structure* **7**, 1333–1343 (1999).

39. Vitagliano, L., Stanzione, F., De Simone, A. & Esposito, L. Dynamics and stability of amyloid-like steric zipper assemblies with hydrophobic dry interfaces. *Biopolymers* **91**, 1161–1171 (2009).

40. Nelson, R. *et al.* Structure of the cross-β spine of amyloid-like fibrils. *Nature* **435**, 773–778 (2005).

41. Kosinová, L. *et al.* Insight into the structural and biological relevance of the T/R transition of the N-terminus of the B-chain in human insulin. *Biochemistry* **53**, 3392–3402 (2014).

42. L. Lyubchenko, Y. Amyloid misfolding, aggregation, and the early onset of protein deposition diseases: insights from AFM experiments and computational analyses. *AIMS Mol. Sci.* **2**, 190–210 (2015).

43. Chuang, E., Hori, A. M., Hesketh, C. D. & Shorter, J. Amyloid assembly and disassembly. *J. Cell Sci.* **131**, jcs189928 (2018).

44. Hwang, Y. M. *et al.* Nonamyloid aggregates arising from mature copper/zinc superoxide dismutases resemble those observed in amyotrophic lateral sclerosis. *J. Biol. Chem.* **285**, 41701–41711 (2010).

45. Astbury, W. T., Dickinson, S. & Bailey, K. The X-ray interpretation of denaturation and the structure of the seed globulins. *Biochem. J.* **29**, 2351-2360.1 (1935).

46. Sipe, J. D. & Cohen, A. S. Review: History of the amyloid fibril. *Journal of Structural Biology* **130**, 88–98 (2000).

47. Geddes, A. J., Parker, K. D., Atkins, E. D. T. & Beighton, E. 'Cross-β' conformation in proteins. *J. Mol. Biol.* **32**, 343–358 (1968).

48. Wu, C., Wang, Z., Lei, H., Zhang, W. & Duan, Y. Dual Binding Modes of Congo Red to Amyloid Protofibril Surface Observed in Molecular Dynamics Simulations. *J. Am. Chem. Soc.* **129**, 1225–1232 (2007).

49. Greenwald, J. & Riek, R. Biology of Amyloid: Structure, Function, and Regulation. *Structure* **18**, 1244–1260 (2010).

50. Cao, Y. & Mezzenga, R. Food protein amyloid fibrils: Origin, structure, formation, characterization, applications and health implications. *Adv. Colloid Interface Sci.* **269**, 334–356 (2019).

51. Biancalana, M. & Koide, S. Molecular mechanism of Thioflavin-T binding to amyloid fibrils. *Biochim. Biophys. Acta - Proteins Proteomics* **1804**, 1405–1412 (2010).

52. Sirangelo, I., Borriello, M., Irace, G. & Iannuzzi, C. Intrinsic blue-green fluorescence in amyloyd fibrils. *AIMS Biophys.* **5**, 155–165 (2018).

53. Sawaya, M. R. *et al.* Atomic structures of amyloid cross-β spines reveal varied steric zippers. *Nature* **447**, 453–457 (2007).

54. Park, J., Kahng, B. & Hwang, W. Thermodynamic Selection of Steric Zipper Patterns in the Amyloid Cross-β Spine. *PLoS Comput. Biol.* **5**, e1000492 (2009).

55. Ivanova, M. I., Sievers, S. A., Sawaya, M. R., Wall, J. S. & Eisenberg, D. Molecular basis for insulin fibril assembly. *Proc. Natl. Acad. Sci.* **106**, 18990–18995 (2009).

56. Dobson, C. M. Protein folding and misfolding. *Nature* **426**, 884–890 (2003).

57. Klein, W. Targeting small Aβ oligomers: the solution to an Alzheimer's disease conundrum? *Trends Neurosci.* **24**, 219–224 (2001).

58. Hardy, J. The Amyloid Hypothesis of Alzheimer's Disease: Progress and Problems on the Road to Therapeutics. *Science* **297**, 353–356 (2002).

59. Gong, Y. *et al.* Alzheimer's disease-affected brain: Presence of oligomeric A ligands (ADDLs) suggests a molecular basis for reversible memory loss. *Proc. Natl. Acad. Sci.* **100**, 10417–10422 (2003).

60. Baglioni, S. *et al.* Prefibrillar amyloid aggregates could be generic toxins in higher organisms. *J. Neurosci.* **26**, 8160–8167 (2006).

61. Arosio, P., Knowles, T. P. J. & Linse, S. On the lag phase in amyloid fibril formation. *Phys. Chem. Chem. Phys.* **17**, 7606–7618 (2015).

62. Linse, S. Monomer-dependent secondary nucleation in amyloid formation. *Biophys. Rev.* **9**, 329–338 (2017).

63. Almeida, Z. L. & Brito, R. M. M. Structure and Aggregation Mechanisms in Amyloids. *Molecules* **25**, 1195 (2020).

64. Librizzi, F. & Rischel, C. The kinetic behavior of insulin fibrillation is determined by heterogeneous nucleation pathways. *Protein Sci.* **14**, 3129–3134 (2005).

65. Ahmad, A., Millett, I. S., Doniach, S., Uversky, V. N. & Fink, A. L. Partially Folded Intermediates in Insulin Fibrillation †. *Biochemistry* **42**, 11404–11416 (2003).

66. Ahmad, A., Millett, I. S., Doniach, S., Uversky, V. N. & Fink, A. L. Stimulation of Insulin Fibrillation by Urea-induced Intermediates. *J. Biol. Chem.* **279**, 14999–15013 (2004).

67. Ahmad, A. DnaK/DnaJ/GrpE of Hsp70 system have differing effects on α-synuclein fibrillation involved in Parkinson's disease. *Int. J. Biol. Macromol.* **46**, 275–279 (2010).

68. Nielsen, L. *et al.* Effect of environmental factors on the kinetics of insulin fibril formation: Elucidation of the molecular mechanism. *Biochemistry* **40**, 6036–6046 (2001).

69. Lorenzen, N. *et al.* Role of Elongation and Secondary Pathways in S6 Amyloid Fibril Growth. *Biophys. J.* **102**, 2167–2175 (2012).

70. Vahdat Shariat Panahi, A., Hultman, P., Öllinger, K., Westermark, G. T. & Lundmark, K. Lipid membranes accelerate amyloid formation in the mouse model of AA amyloidosis. *Amyloid* **26**, 6–8 (2019).

71. Xue, W.-F., Hellewell, A. L., Hewitt, E. W. & Radford, S. E. Fibril fragmentation in amyloid assembly and cytotoxicity. *Prion* **4**, 20–25 (2010).

72. Foderà, V., Librizzi, F., Groenning, M., Van De Weert, M. & Leone, M. Secondary nucleation and accessible surface in insulin amyloid fibril formation. *J. Phys. Chem. B* **112**, 3853–3858 (2008).

73. Tian, J. *et al.* Tannic Acid-Induced Surface-Catalyzed Secondary Nucleation during the Amyloid Fibrillation of Hen Egg-White Lysozyme. *Int. J. Mol. Sci.* **19**, 4009 (2018).

74. Paravastu, A. K., Qahwash, I., Leapman, R. D., Meredith, S. C. & Tycko, R. Seeded growth of -amyloid fibrils from Alzheimer's brain-derived fibrils produces a distinct fibril structure. *Proc. Natl. Acad. Sci.* **106**, 7443–7448 (2009).

75. Kong, L.-X. & Zeng, C.-M. Effects of seeding on lysozyme amyloid fibrillation in the presence of epigallocatechin and polyethylene glycol. *Biochem.* **82**, 156–167 (2017).

76. Surmacz-Chwedoruk, W., Babenko, V., Dec, R., Szymczak, P. & Dzwolak, W. The emergence of superstructural order in insulin amyloid fibrils upon multiple rounds of self-seeding. *Sci. Rep.* **6**, 32022 (2016).

77. Khurana, R. *et al.* A General Model for Amyloid Fibril Assembly Based on Morphological Studies Using Atomic Force Microscopy. *Biophys. J.* **85**, 1135–1144 (2003).

78. Jimenez, J. L. *et al.* The protofilament structure of insulin amyloid fibrils. *Proc. Natl. Acad. Sci.* **99**, 9196–9201 (2002).

79. Kurouski, D., Dukor, R. K., Lu, X., Nafie, L. A. & Lednev, I. K. Normal and reversed supramolecular chirality of insulin fibrils probed by vibrational circular dichroism at the protofilament level of fibril structure. *Biophys. J.* **103**, 522–531 (2012).

80. Hong, D.-P., Ahmad, A. & Fink, A. L. Fibrillation of Human Insulin A and B Chains. *Biochemistry* **45**, 9342–9353 (2006).

81. Dolui, S., Roy, A., Pal, U., Saha, A. & Maiti, N. C. Structural Insight of Amyloidogenic Intermediates of Human Insulin. *ACS Omega* **3**, 2452–2462 (2018).

82. Choi, J. H., May, B. C. H., Wille, H. & Cohen, F. E. Molecular Modeling of the Misfolded Insulin Subunit and Amyloid Fibril. *Biophys. J.* **97**, 3187–3195 (2009).

83. Arora, A., Ha, C. & Park, C. B. Insulin amyloid fibrillation at above 100°C: New insights into protein folding under extreme temperatures. *Protein Sci.* **13**, 2429–2436 (2004).

84. Lee, C., Nayak, A., Sethuraman, A., Belfort, G. & Mcrae, G. J. A Three-Stage Kinetic Model of Amyloid Fibrillation.

Biophys. J. **92**, 3448–3458 (2007).

85. Jeppesen, M. D., Westh, P. & Otzen, D. E. The role of protonation in protein fibrillation. *FEBS Lett.* **584**, 780–784 (2010).

86. Vernaglia, B. A., Huang, J. & Clark, E. D. Guanidine hydrochloride can induce amyloid fibril formation from hen egg-white lysozyme. *Biomacromolecules* **5**, 1362–1370 (2004).

87. Iannuzzi, C., Borriello, M., Portaccio, M., Irace, G. & Sirangelo, I. Insights into Insulin Fibril Assembly at Physiological and Acidic pH and Related Amyloid Intrinsic Fluorescence. *Int. J. Mol. Sci.* **18**, 2551 (2017).

88. Brange, J., Andersen, L., Laursen, E. D., Meyn, G. & Rasmussen, E. Toward Understanding Insulin Fibrillation. *J. Pharm. Sci.* **86**, 517–525 (1997).

89. Editor. Diabetes Prevalence. (2019). Available at: https://www.diabetes.co.uk/diabetes-prevalence.html. (Accessed: 1st March 2020)

90. Ng, L. C. & Gupta, M. Transdermal drug delivery systems in diabetes management: A review. *Asian J. Pharm. Sci.* **15**, 13–25 (2020).

91. Cerf, M. E. Beta Cell Dysfunction and Insulin Resistance. *Front. Endocrinol. (Lausanne).* **4**, (2013).

92. Chausmer, A. B. Zinc, Insulin and Diabetes. *J. Am. Coll. Nutr.* **17**, 109–115 (1998).

93. Editor. Diabetes Treatments. (2020). Available at: https://www.diabetes.org.uk/diabetes-the-basics/diabetes-treatments. (Accessed: 2nd March 2020)

94. KNEGTEL, R. M. A., BOELENS, R., GANADU, M. L. & KAPTEIN, R. The solution structure of a monomeric insulin. A two-dimensional 1H-NMR study of des-(B26-B30)-insulin in combination with distance geometry and restrained molecular dynamics. *Eur. J. Biochem.* **202**, 447–458 (1991).

95. Engels, M., Jacoby, E., Krüger, P., Schlitter, J. & Wollmer, A. The t ⇋ r structural transition of insulin; pathways suggested by targeted energy minimization. *Protein Eng. Des. Sel.* **5**, 669–677 (1992).

96. Jorgensen, L. *et al.* Adsorption of insulin with varying self-association profiles to a solid Teflon surface—Influence on protein structure, fibrillation tendency and thermal stability. *Eur. J. Pharm. Sci.* **42**, 509–516 (2011).

97. Hua, Q. & Weiss, M. a. Mechanism of Insulin Fibrillation. *J. Biol. Chem.* **279**, 21449–21460 (2004).

98. Gast, K. *et al.* Rapid-Acting and Human Insulins: Hexamer Dissociation Kinetics upon Dilution of the Pharmaceutical Formulation. *Pharm. Res.* **34**, 2270–2286 (2017).

99. Hirsch, I. B. Insulin Analogues. *N. Engl. J. Med.* **352**, 174–183 (2005).

100. Evans, M., Schumm-Draeger, P. M., Vora, J. & King, A. B. A review of modern insulin analogue pharmacokinetic and pharmacodynamic profiles in type 2 diabetes: improvements and limitations. *Diabetes, Obes. Metab.* **13**, 677–684 (2011).

101. Nielsen, L., Frokjaer, S., Brange, J., Uversky, V. N. & Fink, A. L. Probing the mechanism of insulin fibril formation with insulin mutants. *Biochemistry* **40**, 8397–8409 (2001).

102. Ahmad, A., Uversky, V. N., Hong, D. & Fink, A. L. Early in the fibrillation of monomeric insulin. *J. Biol. Chem.* **280**, 42669–42675 (2005).

103. Vestergaard, B. *et al.* A Helical Structural Nucleus Is the Primary Elongating Unit of Insulin Amyloid Fibrils. *PLoS Biol.* **5**, e134 (2007).

104. Mauri, S., Volk, M., Byard, S., Berchtold, H. & Arnolds, H. Stabilization of Insulin by Adsorption on a Hydrophobic Silane Self-Assembled Monolayer. *Langmuir* **31**, 8892–8900 (2015).

105. Quianzon, C. C. L. & Cheikh, I. E. History of current non-insulin medications for diabetes mellitus. *J. Community Hosp. Intern. Med. Perspect.* **2**, 19081 (2012).

106. Grunberger, G. Insulin analogsdare they worth it. *Diabetes Care* **37**, 1767–1770 (2014).

107. American Diabetes Association. Insulin Basics. (2019). Available at: https://www.diabetes.org/diabetes/medication-management/insulin-other-injectables/insulin-basics. (Accessed: 20th September 2005)

108. Mohan, V. Which insulin to use? Human or animal? *Curr. Sci.* **83**, 1544–1547 (2002).

109. Berenson, D. F., Weiss, A. R., Wan, Z. & Weiss, M. A. Insulin analogs for the treatment of diabetes mellitus: therapeutic applications of protein engineering. *Ann. N. Y. Acad. Sci.* **1243**, E40–E54 (2011).

110. Buse, J. Insulin glargine (HOE901): first responsibilities: understanding the data and ensuring safety. *Diabetes Care* **23**, 576–578 (2000).

111. Yang, Y. *et al.* An Achilles' Heel in an Amyloidogenic Protein and Its Repair. *J. Biol. Chem.* **285**, 10806–10821 (2010).

112. Thirumalai, D., Reddy, G. & Straub, J. E. Role of Water in Protein Aggregation and Amyloid Polymorphism. *Acc. Chem. Res.* **45**, 83–92 (2012).

113. Kurouski, D. *et al.* Disulfide bridges remain intact while native insulin converts into amyloid fibrils. *PLoS One* **7**, 1–9 (2012).

114. Matthes, D., Gapsys, V. & De Groot, B. L. Driving forces and structural determinants of steric zipper peptide oligomer formation elucidated by atomistic simulations. *J. Mol. Biol.* **421**, 390–416 (2012).

115. General Aspects of Trace Analytical Methods—IV. Recommendations for Nomenclature, Standard Procedures and Reporting of Experimental Data for Surface Analysis Techniques. *Pure Appl. Chem.* **51**, 2243–2250 (1979).

116. Hudson, J. B. & Diehl, R. D. Surface Science: An Introduction. *Am. J. Phys.* **60**, 1155–1156 (1992).

117. Somorjai, G. A., Beaumont, S. K. & Alayoglu, S. Determination of Molecular Surface Structure, Composition, and Dynamics under Reaction Conditions at High Pressures and at the Solid-Liquid Interface. *Angew. Chemie Int. Ed.* **50**, 10116–10129 (2011).

118. Somorjai, G. A. & Li, Y. Impact of surface chemistry. *Proc. Natl. Acad. Sci.* **108**, 917–924 (2011).

119. Moores, B., Drolle, E., Attwood, S. J., Simons, J. & Leonenko, Z. Effect of Surfaces on Amyloid Fibril Formation. **6**, 1–8 (2011).

120. Norde, W. Driving forces for protein adsorption at solid surfaces. *Macromol. Symp.* **103**, 5–18 (1996).

121. Mauri, S. *Insulin unfolding and aggregation : a multi-disciplinary study (PhD thesis)*. (University of Liverpool, 2014).

122. Kastantin, M., Langdon, B. B. & Schwartz, D. K. A bottom-up approach to understanding protein layer formation at solid–liquid interfaces. *Adv. Colloid Interface Sci.* **207**, 240–252 (2014).

123. Rabe, M., Verdes, D. & Seeger, S. Understanding protein adsorption phenomena at solid surfaces. *Adv. Colloid Interface Sci.* **162**, 87–106 (2011).

124. Migliorini, E., Weidenhaupt, M. & Picart, C. Practical guide to characterize biomolecule adsorption on solid surfaces (Review). *Biointerphases* **13**, 06D303 (2018).

125. Arnebrant, T. & Nylander, T. Adsorption of insulin on metal surfaces in relation to association behavior. *J. Colloid Interface Sci.* **122**, 557–566 (1988).

126. Mollmann, S. H., Elofsson, U., Bukrinsky, J. T. & Frokjaer, S. Displacement of adsorbed insulin by tween 80 monitored using total internal reflection fluorescence and ellipsometry. *Pharm. Res.* **22**, 1931–1941 (2005).

127. Welinder, A. C., Zhang, J., Steensgaard, D. B. & Ulstrup, J. Adsorption of human insulin on single-crystal gold surfaces investigated by in situ scanning tunnelling microscopy and electrochemistry. *Phys. Chem. Chem. Phys.* **12**, 9999–10011 (2010).

128. Bürgi, T. Properties of the gold–sulphur interface: from self-assembled monolayers to clusters. *Nanoscale* **7**, 15553–15567 (2015).

129. Hammarström, P. *et al.* A catalytic surface for amyloid fibril formation. *J. Phys. Conf. Ser.* **100**, 052039 (2008).

130. Hammarström, P. *et al.* An Auto-Catalytic Surface for Conformational Replication of Amyloid Fibrils—Genesis of an Amyloid World? *Orig. Life Evol. Biosph.* **41**, 373–383 (2011).

131. Cheng, Y.-T. & Rodak, D. E. Is the lotus leaf superhydrophobic? *Appl. Phys. Lett.* **86**, 144101 (2005).

132. Majhy, B., Iqbal, R. & Sen, A. K. Facile fabrication and mechanistic understanding of a transparent reversible superhydrophobic – superhydrophilic surface. *Sci. Rep.* **8**, 18018 (2018).

133. Chandler, D. Interfaces and the driving force of hydrophobic assembly. *Nature* **437**, 640–647 (2005).

134. Henry, M. & Bertrand, P. Surface composition of insulin and albumin adsorbed on polymer substrates as revealed by multivariate analysis of ToF-SIMS data. *Surf. Interface Anal.* **41**, 105–113 (2009).

135. Nault, L. *et al.* Human insulin adsorption kinetics, conformational changes and amyloidal aggregate formation on hydrophobic surfaces. *Acta Biomater.* **9**, 5070–5079 (2013).

136. Nilsson, P., Nylander, T. & Havelund, S. Adsorption of insulin on solid surfaces in relation to the surface properties of the monomeric and oligomeric forms. *J. Colloid Interface Sci.* **144**, 145–152 (1991).

137. Nayak, A., Dutta, A. K. & Belfort, G. Surface-enhanced nucleation of insulin amyloid fibrillation. *Biochem. Biophys. Res. Commun.* **369**, 303–307 (2008).

138. Falde, E. J., Yohe, S. T., Colson, Y. L. & Grinstaff, M. W. Superhydrophobic materials for biomedical applications.

Biomaterials **104**, 87–103 (2016).

139. P., S. V. V. S. N. & P., S. V. V. S. A Review on Surface Modifications and Coatings on Implants to Prevent Biofilm. *Regen. Eng. Transl. Med.* **6**, 330–346 (2020).

140. Patra, J. K. *et al.* Nano based drug delivery systems: recent developments and future prospects. *J. Nanobiotechnology* **16**, 71 (2018).

141. Liechty, W. B., Kryscio, D. R., Slaughter, B. V. & Peppas, N. A. Polymers for Drug Delivery Systems. *Annu. Rev. Chem. Biomol. Eng.* **1**, 149–173 (2010).

142. Yohe, S. T., Colson, Y. L. & Grinstaff, M. W. Superhydrophobic Materials for Tunable Drug Release: Using Displacement of Air To Control Delivery Rates. *J. Am. Chem. Soc.* **134**, 2016–2019 (2012).

143. Chu, J. P., Yu, C.-C., Tanatsugu, Y., Yasuzawa, M. & Shen, Y.-L. Non-stick syringe needles: Beneficial effects of thin film metallic glass coating. *Sci. Rep.* **6**, 31847 (2016).

144. Jane, A., Dronov, R., Hodges, A. & Voelcker, N. H. Porous silicon biosensors on the advance. *Trends Biotechnol.* **27**, 230–239 (2009).

145. Vallet-Regí, M. & Balas, F. Silica Materials for Medical Applications. *Open Biomed. Eng. J.* **2**, 1–9 (2008).

146. Ma, Y., Huang, R., Qi, W., Su, R. & He, Z. Fluorescent silicon nanoparticles inhibit the amyloid fibrillation of insulin. *J. Mater. Chem. B* **7**, 1397–1403 (2019).

147. McCarthy, J. *et al.* Composition and stress analysis in Si structures using micro-raman spectroscopy. *Scanning* **26**, 235–239 (2006).

148. Ratner, B. D. & Hoffman, A. S. Physicochemical Surface Modification of Materials Used in Medicine. in *Biomaterials Science* 259–276 (Elsevier, 2013). doi:10.1016/B978-0-08-087780-8.00027-9

149. Christy, A. A. The Nature of Rest Silanol Groups on the Surfaces of Silica Based Solid Phase Extraction Materials. *Adv. Mater. Res.* **650**, 66–71 (2013).

150. Pricker, S. P. Medical uses of gold compounds: Past, present and future. *Gold Bull.* **29**, 53–60 (1996).

151. Bain, C. D., Biebuyck, H. A. & Whitesides, G. M. Comparison of self-assembled monolayers on gold: coadsorption of thiols and disulfides. *Langmuir* **5**, 723–727 (1989).

152. Lvov, Y. *Interfacing Molecular Assemblies and Immobilization Biotechnology*. (CRC Press, 2016).

153. Love, J. C., Estroff, L. A., Kriebel, J. K., Nuzzo, R. G. & Whitesides, G. M. Self-Assembled Monolayers of Thiolates on Metals as a Form of Nanotechnology. *Chem. Rev.* **105**, 1103–1170 (2005).

154. Vericat, C., Vela, M. E., Benitez, G., Carro, P. & Salvarezza, R. C. Self-assembled monolayers of thiols and dithiols on gold: New challenges for a well-known system. *Chem. Soc. Rev.* **39**, 1805–1834 (2010).

155. Dilimon, V. S., Rajalingam, S., Delhalle, J. & Mekhalif, Z. Self-assembly mechanism of thiol, dithiol, dithiocarboxylic acid, disulfide and diselenide on gold: An electrochemical impedance study. *Phys. Chem. Chem. Phys.* **15**, 16648–16656 (2013).

156. Nicosia, C. & Huskens, J. Reactive self-assembled monolayers: from surface functionalization to gradient formation. *Mater. Horiz.* **1**, 32–45 (2014).

157. Hsieh, S., Chang, C. wen & Chou, H. hung. Gold nanoparticles as amyloid-like fibrillogenesis inhibitors. *Colloids Surfaces B Biointerfaces* **112**, 525–529 (2013).

158. McMasters, M. J., Hammer, R. P. & McCarley, R. L. Surface-Induced Aggregation of Beta Amyloid Peptide by ω-Substituted Alkanethiol Monolayers Supported on Gold. *Langmuir* **21**, 4464–4470 (2005).

159. Knowles, T. P. J. *et al.* Kinetics and thermodynamics of amyloid formation from direct measurements of fluctuations in fibril mass. *Proc. Natl. Acad. Sci.* **104**, 10016–10021 (2007).

Chapter 2: Directed Human Insulin Fibrillation on Hydrophobic Silane Functionalised Silicon Surfaces

2.1. Introduction

This aim of this chapter is to investigate the amyloid-like fibrillation of two insulin variants, human insulin (HI) and insulin glargine, on a hydrophobically functionalised stepped silicon (Si) surface by reflection anisotropy spectroscopy (RAS). A stepped Si surface was used in this work to explore whether surface architecture induces the fibrillation pathway, which was measured using RAS to probe the electronic states of the aromatic amino acids within insulin to obtain orientation information associated with the fibrillation state at the interface. Chapter 1 introduced insulin glargine as a pharmaceutical analogue of HI with improved drug profiles (1.4.2. Mutations of insulin, page 48) therefore this chapter aims to examine whether there are any differences in the surface-catalysed fibrillation pathway attributed to the single-point mutations.

One method of surface-catalysed fibrillation is through the two-dimensional (2D) diffusion of surface-confined proteins at the surface interface, which has been shown to promote amyloid-like fibrillation for amyloid-β peptide (Aβ), α-synuclein (αS),[1] and insulin.[2] The 2D-diffusion process occurs when the monomeric species diffuses across the hydrophobic interface along with increased localised protein concentration at a confined region, which results in aggregation effects.[3] This diffusion process is affected by surface topography, where increased roughness has been reported to inhibit fibrillation events for Aβ[4] and insulin,[5] whilst surface chirality also induces insulin fibrillar changes.[6] It is already known that various surface properties affect self-assembly at the interface,[7] which is important as amyloid pathology has been reported to be intrinsically linked to fibril morphology, specifically toxicity and severity of the disease.[8,9] Additionally investigating whether surface architecture directs orientated amyloid-like fibrillation has a wide range of potential applications such as; catalysis[10] and biomaterials.[11]

Measuring the directed surface-confined fibrillation process at an interface is challenging, since non-destructive techniques such as vibrational spectroscopy only

probe the out-of-plane protein orientations, whereas for fibrillation the in-plane orientations are significant. The in-plane directionality of the protein, as resolved by its side chain or backbone components, is of interest for fibrillar pre-alignment investigations.[12] One analytical technique that can reveal in-plane orientation is atomic force microscopy (AFM), which has previously been used to show fibril alignment for collagen on mica[13] and for F-actin on silicon surfaces.[14] However AFM is time consuming and potentially destructive. An alternative approach is to use a non-destructive rapid surface-sensitive linear dichroism (LD) technique.

2.1.1. Obtaining orientation information of a molecule

Linear dichroism is a spectroscopic technique which measures the difference in light absorption (Abs) that has been linearly polarised parallel and perpendicular to the orientation axis, as shown in equation (2.1).[15]

$$LD = Abs_{parallel} - Abs_{perpendicular} \quad (2.1)$$

This technique can provide orientation information on the fibrillation pathway, as the fibrils provide an overall net electronic transition which is measurable. An issue with this methodology is that the sample must first be orientated along a principal axis to be measured, therefore in solution a Couette cell must be used. This technique is analogous to circular dichroism (CD) which measures the difference in light absorption between left and right circularly polarised light and is widely used to study the secondary structure of proteins.[16] In this research programme neither LD nor CD were applicable since neither technique will work on hydrophobic surfaces for amyloid-like fibrillation, where the substrate is not transparent to the light source. Modification of the optics used in LD provides a surface-sensitive technique, RAS, which was used to study the fibrillation pathway at the surface.

2.1.1.1. Reflection Anisotropy Spectroscopy (RAS)

Reflection anisotropy spectroscopy (RAS), is a technique which can probe in-plane order at the surface. RAS measures the difference in reflectivity of normal incidence plane-polarised light between two perpendicular directions on the surface which is normalised to the mean reflectance, as shown in equation (2.2):

$$\frac{\Delta_r}{r} = 2\frac{(r_x - r_y)}{r_x + r_y} \tag{2.2}$$

where r_x and r_y are the complex reflection coefficients in the *x* and *y* direction of the surface, with the sum of these quantities given by r. RAS is often used with a substrate in which the bulk is isotropic as the bulk response is cancelled due to the geometrical symmetry, thus rendering this a surface specific technique for measuring anisotropy.[17]

A schematic of the RAS instrument is illustrated in Figure 20. The sample is illuminated by linearly polarised light which is directed via: a photoelastic modulator (PEM), a second polariser (usually called an analyser) and a monochromator onto a detector. The PEM consists of two elements; a birefringent optical element (shown in light grey) and a piezo transducer element (shown in dark grey).

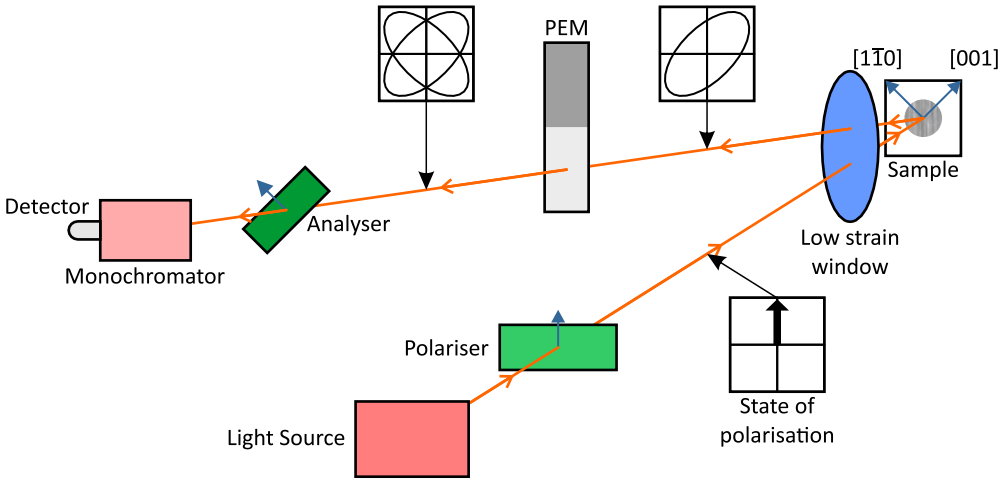

Figure 20: A schematic of the reflection anisotropy (RA) spectrometer, adapted from Weightman et al.[17]

The PEM is arranged so that when a voltage is applied to the piezo transducer, stress is induced in the optical element. When the optical element, which is a quartz crystal, is stressed it exhibits birefringence. The PEM is orientated so that the eigenvectors of the birefringence stress tensor act vertically and horizontally. These eigenvectors can also be referred to as the 'fast' and 'slow' axes. If the voltage applied to the piezo transducer alternates, then the changing stress in the optical element results in the 'fast' and 'slow' axes alternating between the horizontal and vertical

directions. Thus, light which has both vertical and horizontal components of polarisation will have that polarisation modulated by the PEM, as illustrated in Figure 20. Light which is entirely polarised in either the vertical or horizontal domain will not have its polarisation changed by the PEM. For example, an isotropic sample which reflects vertically polarised light will not be modulated by the PEM thus will remain vertically polarised and result in no RAS signal.

The reflected light for an anisotropic sample, which consists of both horizontal and vertically polarised components, will have its polarisation modulated by the PEM. This modulated polarised light will then enter the analyser and become polarised with amplitude modulation. At the detector the amplitude modulation gives rise to a varying alternating current ('AC') signal that will contain the $r_x - r_y$ information. The direct current ('DC') or average detector output will be proportional to the mean reflectance, r. The RAS signal thus becomes proportional to the ratio of these 'AC' and 'DC' signals.

In the special case, where an anisotropic sample is orientated such that the eigenvectors of its optical anisotropy act vertically and horizontally, then the vertically polarised light hitting the sample will also reflect from it with vertical polarisation. The reflected vertically polarised light will pass through the PEM without modulation and generate a zero RAS signal. This aspect of RAS can be exploited to find the optical eigenvectors of a sample, which for crystalline samples generally occurs along the crystal's principal axes, but which may be modified by absorbates. A detailed discussion of how RAS can be used to determine the absorbate orientation can be found in Paul Harrison's thesis.[18]

RAS was developed in the 1980's by Aspnes[19–21] to study semiconductor surfaces and an extensive literature review of the technique has been published.[17] The development of RAS from the ultra-high vacuum (UHV) environment studying semiconductors and molecular adsorption on metals in UHV through to studying the electrochemical interfaces is important as it is a non-destructive surface sensitive optical probe.

The Weightman group (collaborators on this work) have used RAS extensively to study various biological molecules at the solid / liquid interface including; nucleic acids,[22–27] deoxyribonucleic acid (DNA),[28–30] various amino acids,[31,32] peptides[33] and proteins,[34–36] on a gold (110) surface.[37] Other substrates have also been studied using RAS such as; DNA hybridisation on diamond,[30] DNA deposition onto a vicinal Si surface[38] and collagen secreted by fibroblast cells grown on polytetrafluoroethylene (PTFE) nanofibers.[39]

RAS studies have shown that orientational information can be obtained from the known orientations of the π-π* transitions in the nucleic acids with respect to the molecular structure[22] together with a three-phase model[40] that can be used to fit a RA spectrum. Another method that was developed to determine the orientation of the adsorbate was to rotate the sample.[41] Rotation of a perfect anisotropic face centred cubic (fcc) surface such as the Au (110) follows a $\sin(2\theta)$ rotation with maxima at 45° and a minimum at 135°, where the 0° and 90° correspond to the principal axes of the crystal. The adsorption of molecules onto the Au (110) surface have been found to align either perfectly or very slightly off the principal axis.[29] This trend has also been found for collagen secreted from fibroblast cells which aligned with the nanofibers.[39] Currently there are only a few known exceptions to this trend such as; the surface plasmon of Ag (110),[42] DNA on diamond,[43] stretching of polydimethylsiloxane (PDMS)[44], the (1×1) reconstruction of Au (110)[45] and in the study of thermotropic liquid crystals.[46,47]

2.1.1.2. Electronic transitions of the aromatic amino acids

The three aromatic amino acids (tryptophan, tyrosine and phenylalanine) are used in intrinsic fluorescence (IF, 7.1.1. Introduction to Fluorescence Spectroscopy, page 222) techniques to obtain information on the protein state. In this chapter it is the two electronic transitions, which are termed L_a and L_b, of the aromatic amino acid residues within the protein structure which are measured by RAS. The electronic transitions arise from the indole or benzene-type chromophore within the respective aromatic amino acid; tryptophan, tyrosine and phenylalanine,[48–51] which are shown in Figure 21.

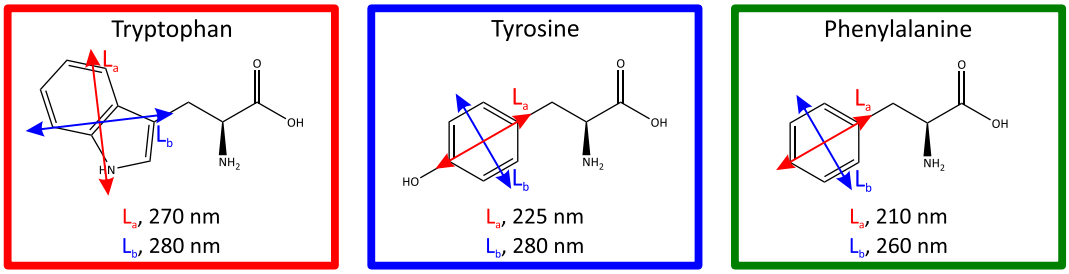

Figure 21: The electronic transitions of L_a and L_b for; (red) tryptophan, (blue) tyrosine and (green) phenylalanine. Electronic transition values shown were taken from Zimmerman et al[48] and Milan-Garces et al.[51]

The electronic transitions of L_a and L_b for the aromatic amino acids (Figure 21) vary in intensity. The strongest signals are observed from tryptophan because of stabilisation within the indole group and the intensity of the tyrosine signals are higher than those of phenylalanine. There are no tryptophan residues present in either insulin variant, therefore the RAS utilises the in-plane orientation with respect to the net tyrosine and phenylalanine transitions.

2.1.2. The adaptability of Silicon

Silicon, the chemical element with an atomic number of 14, is the second most abundant element on Earth[52] and is used in a wide variety of applications. In this thesis, Si is used because of its previous use in amyloid research,[53,54] and its spectroscopic potential, chemical functionalisation capability and commercial availability.

2.1.2.1. The application of reflection anisotropy on a silicon surface

A Si (110) substrate is used as a calibration standard for the RAS instrument because of the known positions of peaks in its RA spectrum and the ideal rotational behaviour of the surface crystallography as illustrated in Figure 22. Changes of 90° in the azimuth from 45° (red) to 90° (blue) to 135° (green) have a corresponding effect on the two anisotropic Si peaks (~290 and 356 nm), which have a maximum to minimum azimuthal dependence respectively.

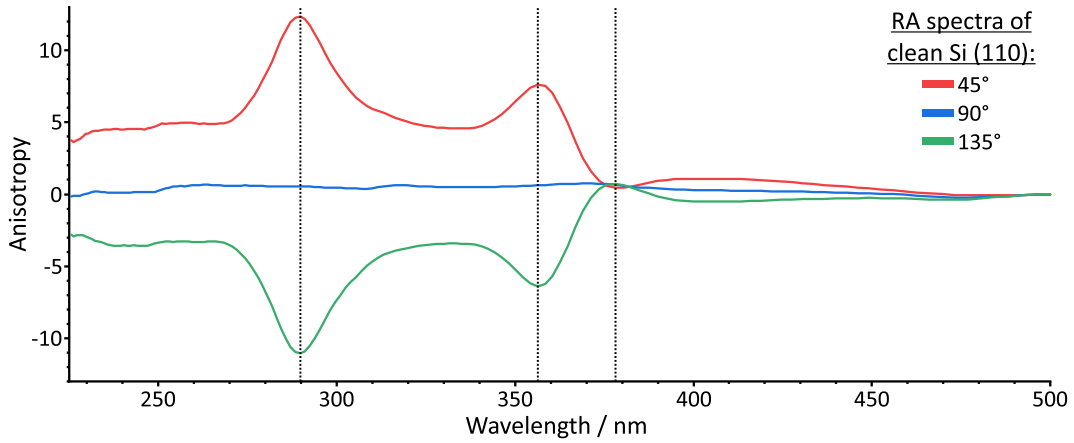

Figure 22: Reflection anisotropy (RA) spectra of a cleaned Si (110) surface at three different azimuths; (red) 45°, (blue) 90° and (green) 135°. The (dashed) lines show the approximate wavelengths for the peaks at; 290 nm, 356 nm and 371 nm.

The cleaned Si (110) surface (Figure 22) is shown to change from maximum to minimum anisotropy signal at the 45° and 135° azimuths, which corresponds to the Si surface structure. The characteristic Si peaks (~290 and 356 nm) arise from electronic transitions in the dielectric constant of the material.[55] A full 360° rotation of the sample, which is shown in Figure S1, demonstrates the ideal Si (110) surface architecture because of the symmetrical RA spectra and similarity at analogous azimuths.

The azimuthal dependence of the Si peaks (~290 and 356 nm) was tested by acquiring RA spectra for a full rotation (360°, 15° steps) of the sample. Figure 23 shows three wavelengths from the RA spectra (Figure S1), which correlate to the two characteristic Si peaks (~290 and 356 nm, red and blue respectively) that exhibit high anisotropy and a smaller anisotropic peak (~371 nm, green).

The azimuth dependence for the Si peaks of the cleaned Si (110) surface (Figure 23) shows that the intensity of the peaks follows a sin (2θ) wave description. The full 360° rotation of the surface shows where the maximum and minimum anisotropic signals are and when the signal is zero (at 0°, 90°, 180° and 270°) it is aligned to the crystal's principal axis. As the location of the surface's principal axes is known, then the adsorbed molecules orientation can be deduced in relation to the surface axes.

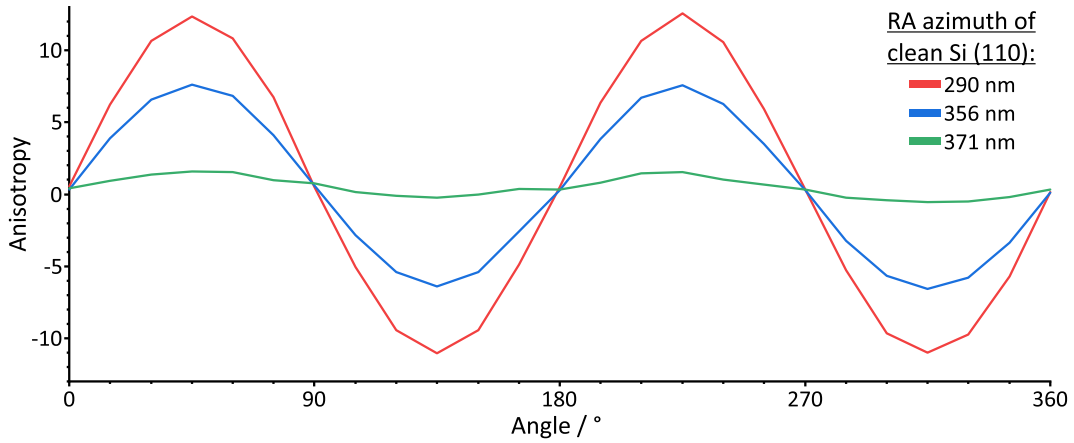

Figure 23: Azimuth dependence of the cleaned Si (110) surface for the three anisotropic peaks, at approximately; (red) 290 nm, (blue) 356 nm and (green) 371 nm.

2.1.2.2. The importance of surface crystallography

Pre-requisites for the research described in this chapter were highly reflective surfaces for RAS, with differing surface architectures of the same substrate crystallography to investigate whether architecture directs fibrillation events and surface functionalisation capability. Si (111) wafers are available commercially as substrates with either atomically flat or stepped surface crystallography, as is shown in Figure 24.

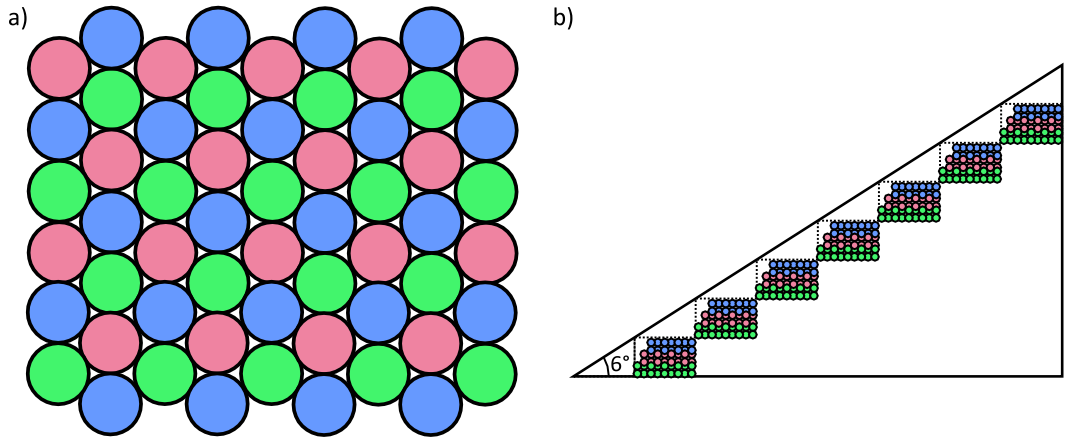

Figure 24: Schematic of the silicon (111) crystal structure for; (a) flat, (b) vicinal 6° offset in the [112] direction which results in the illustrated terraces. The colouration refers to the top three atomic layers at the surface; (blue) surface-, (pink) middle- and (green) lowest- atom. Adapted from Kim et al.[56]

A top-down overview of a Si (111) surface (Figure 24a) which is colour coded to highlight the hexagonal close-packed crystallography with the top three atomic layers; surface (blue), middle (pink) and lowest (green). The flat surface is a singularly

polished wafer of a Si (111) crystal, which is atomically flat with anticipated defects. Conversely a side-view schematic of the vicinal Si (111) surface (Figure 24b) shows that the 6° off-cut in the [112] direction results in 3 nm wide terraces with 0.3 nm steps.

2.1.2.2. Functionalisation of the interface using silane chemistry

Silane chemistry is a functionalisation methodology associated with organosilanes, which are silicon-based molecules consisting of at least one carbon-silicon bond.[57] In this chapter a hydrophobic organosilane, trimethoxypropylsilane (TMPS), as shown in Figure 25, was used to functionalise the Si (111) surface.

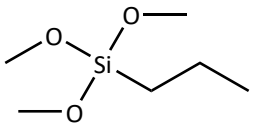

Figure 25: Chemical structure of trimethoxypropylsilane (TMPS).

TMPS, a trialkoxysilane with a propyl organofunctional group, has three hydrolysable methoxy groups which are hydrolysed at the surface to form alcohol groups thereby resulting in a propyl-terminated interface.[58] A generalised self-assembled monolayer (SAM) schematic for functionalising a Si surface has been shown previously (Figure 19,1.5.3. Changing surface properties by functionalisation techniques, page 58). TMPS was used since the termination of the Si surface with the propyl group provides a hydrophobic interface, with limited degrees of freedom to reduce the potential for associated anisotropy.

2.2. Materials and Methods

2.2.1. Sample Preparation

All sample preparations were performed in designated fume hoods and the reagents used were of analytical grade or higher. All samples were manipulated with the same tweezers and handled at similar regions located at the edges of the Si substrate, where possible, to limit cross-contamination and induced physical effects. The samples were stored singularly in petri-dishes, and where possible were analysed *in situ*, to reduce manipulation of the surfaces.

2.2.1.1. Surfaces

The silicon substrates, including all glassware and manual handling equipment, were cleaned with heated (~65°C) acidic Piranha solution (30% hydrogen peroxide and 70% sulfuric acid, 30 minutes). The cleaned items were rinsed at least three times with ultrapure (type I) water (Milli-Q, 18.2 MΩ cm^{-1}), with the equipment oven-dried and the cleaned silicon substrates submerged in water (18.2 MΩ cm^{-1}) prior to use.

The piranha cleaned Si substrates were dried under argon flow, then cleaned with UV-ozone (ProCleaner Plus, Bioforce Nanosciences) for 15 minutes on each side. A silane suspension, TMPS (0.5 mM) in toluene, was prepared and the ozone cleaned Si substrates were submerged in the sealed silane suspension, for 24 hours (~21°C).

After silanisation had been completed, a droplet of water onto the surface confirmed hydrophobicity as illustrated in Chapter 1 (1.5.2. Why is hydrophobicity key?, page 55). The surfaces were excessively rinsed with water (18.2 MΩ cm^{-1}) to remove any multilayers and then dried under argon flow.

2.2.1.2. Insulin suspensions

Human insulin (HI, 1 mg/mL, SAFC Biosciences) or insulin glargine (Lantus®, Sanofi, 1 mg/mL) were suspended in a pH 2.6 citrate-phosphate buffer (5.4 mL of 0.2 M dibasic sodium phosphate and 44.6 mL of 0.1 M citric acid).[59] Hydrophobically functionalised silicon substrates were immersed in a glass reaction vessel containing either HI or glargine for up to five days at ~75°C. Following the designated time period, the samples were briefly rinsed with water (18.2 MΩ cm^{-1}) to remove any excess multilayer formation and stored in petri-dishes for analysis.

2.2.2. Reflection Anisotropy Spectroscopy (RAS) experiments.

A Si substrate was mounted onto a rotational stage, with the region of interest situated directly in the centre of the stage.[18] The tilt of the stage was optimised to ensure maximum signal reaches the detector, it was important that the area to be probed was illuminated and situated directly in the centre of rotation to probe the same area throughout.[30] All the reflection anisotropy (RA) spectra were acquired between 1.5 and 5.5 eV (electron volt), converted into

wavelength (~827 – 225 nm) and then cropped (~225 – 500 nm) as the region above 500 nm had minimal RA signal from the Si substrate. Data from the instrument was acquired using LabView (National Instruments) and then plotted using Origin (OriginLabs).

2.3. Results and Discussion

2.3.1. The effect of surface architecture on reflection anisotropy

The RA principles of Si (110), (2.1.2.1. The application of reflection anisotropy on a silicon surface, page 73) which determine the principal axes of the surface, were applied to two Si (111) surfaces; atomically flat and vicinal with a 6° off-cut. The Si surfaces have differing oxide layers as the flat and vicinal Si (111) surfaces were both piranha and ozone cleaned prior to functionalisation, which results in a reduced and more consistent oxide layer,[17,60] whereas the Si (110) surface was utilised as a calibration standard and used 'as is'. In Figure 26, RA spectra of the three azimuths (45°, 90° and 135°) acquired are shown.

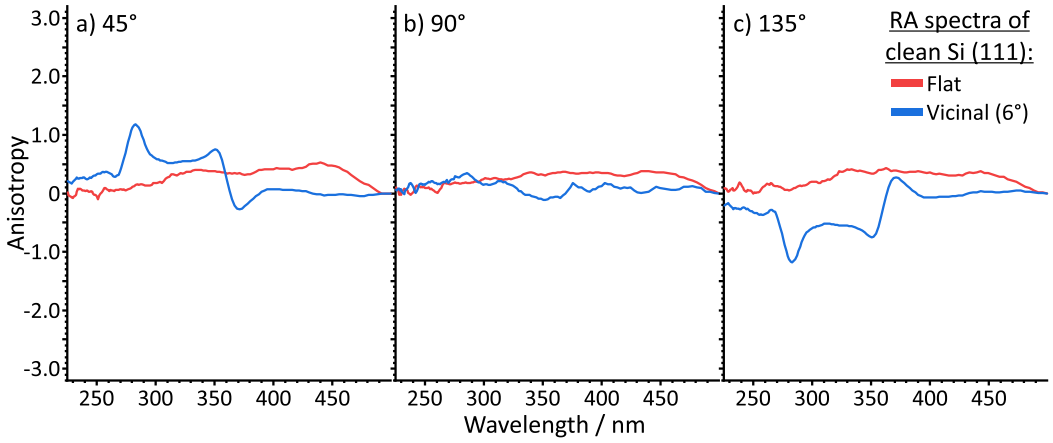

Figure 26: Reflection anisotropy (RA) spectra of a cleaned (red) flat or (blue) vicinal Si (111) surface at three different azimuths; (a) 45°, (b) 90° and (c) 135°.

The flat (red) and vicinal (blue) Si (111) RA spectra (Figure 26) for the three azimuths; (a) 45°, (b) 90° and (c) 135°, displayed significantly lower maximum anisotropic signals compared to the Si (110) surface. There are no characteristic Si peaks present in the flat RA spectra for all three azimuths, which is as expected since this is an isotropic surface with no difference in the *x* and *y* directions unlike in the crystallography of the Si (110) surface. In the vicinal spectra the characteristic Si

peaks, assigned to the Si (110) crystallography, are observed because the stepped surfaces give rise to a faceted Si (110) crystallography on the step edge.[61] The measured anisotropy signal for the vicinal Si (111) surfaces is lower than that of the Si (110), which correlates with the vicinal Si (111) peaks arising from the faceted steps, as there are limited regions of measurable Si (110) crystallographic regions at the stepped interface. There appears to be a slight blueshift of 6 nm for the Si peaks between the Si (110) and Si (111) surfaces, which may be attributed to the differences in crystallography or variations in the silicon oxide layer.[55]

A full 360° rotation of both flat and vicinal Si (111) surfaces was acquired, as shown in Figure S2 and Figure S3. The 360° rotation of the flat Si (111) surface (Figure S2) does not show the characteristic Si peaks at any of the azimuths, as it is isotropic, therefore it is not possible to determine the location of the principal axes. Most of the molecules studied by RAS have been shown to adsorb in line with the principal axes of a substrate,[23,24,29,35,36] therefore determining the location of the principal axes quickly is important to be able to determine adsorbed species orientation rapidly for both *in situ* studies and molecule screening purposes.

Similarly to the Si (110) surface, the azimuthal dependence of the Si peaks (~283 and 350 nm) for both vicinal and flat Si (111) surfaces was tested by acquiring RA spectra for a full rotation (360°, 15° steps) of the sample, which is shown in Figure 27. The three wavelengths studied correlate to the two Si peaks at their maxima (~283 and 350 nm, red and blue respectively) contrasted to the smaller anisotropic peak (~371 nm, green) measured previously for the Si (110) surface.

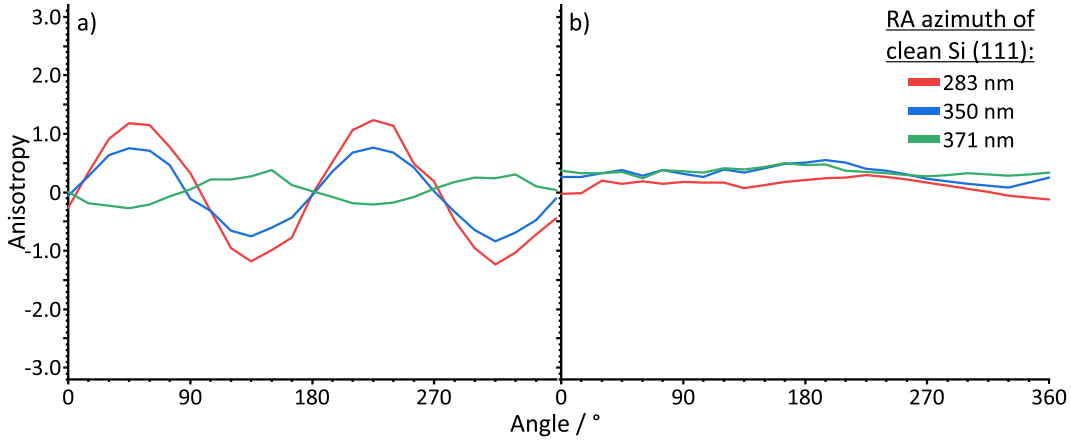

Figure 27: Azimuth dependence of the cleaned (a) vicinal and (b) flat Si (111) surfaces for the three anisotropic peaks, at approximately; (red) 283 nm, (blue) 350 nm and (green) 371 nm.

The azimuth dependence (Figure 27) shows that the vicinal surface (Figure 27a) follows the typical sin (2θ) variation in intensity arising from the anisotropy associated with the peaks in the Si RA spectrum. Conversely the flat surface (Figure 27b) exhibits no sin (2θ) dependence resulting in minimum signal across the azimuth.

It is possible to determine the location of the silicon substrate's principal axes by its cleaving pattern; Si (100) breaks as a square, Si (110) as a parallelogram, and Si (111) in a triangular pattern. Physically cracking the substrate however is a very destructive technique which may occasionally not result in a break along the principal axes and therefore not ideal for some studies. The principal axes of a Si (111) surface are 60° apart, observed in the triangular break angles, therefore the maximum-minimum anisotropy for the RA spectra are at; 60°, 120° and 180°. However, for the vicinal surface, the aligned anisotropy (45°, 90° and 135°) arises from the principal axes (45° parallelogram) of the faceted Si (110) at the steps. Vicinal Si (111) is preferred because of the terraced architecture which allows for rapid determination of the location of the principal axes, which means fewer RA spectra for determination of molecular orientation.

The presence of the terraces on the vicinal Si (111) surface was important for this research programme, to determine the surface orientation by RA (Figure 26 and Figure 27), however the size of these terraces (3 nm wide x 0.3 nm high)[62] was also

considered with regards to the HI monomer (2.5 x 2 x 3 nm).[63] As the monomer is smaller than the terraces, diffusion perpendicular or parallel to the terraces was possible. To determine the orientation of HI diffusion it was important that the hydrophobic functionalisation did not obscure the RA signal attributed to the terraces.

2.3.2. The effect of small molecule functionalisation on reflection anisotropy

The vicinal Si (111) surface was functionalised with TMPS and the RA spectra were collected at three azimuths (45°, 90° and 135°) as shown in Figure 28.

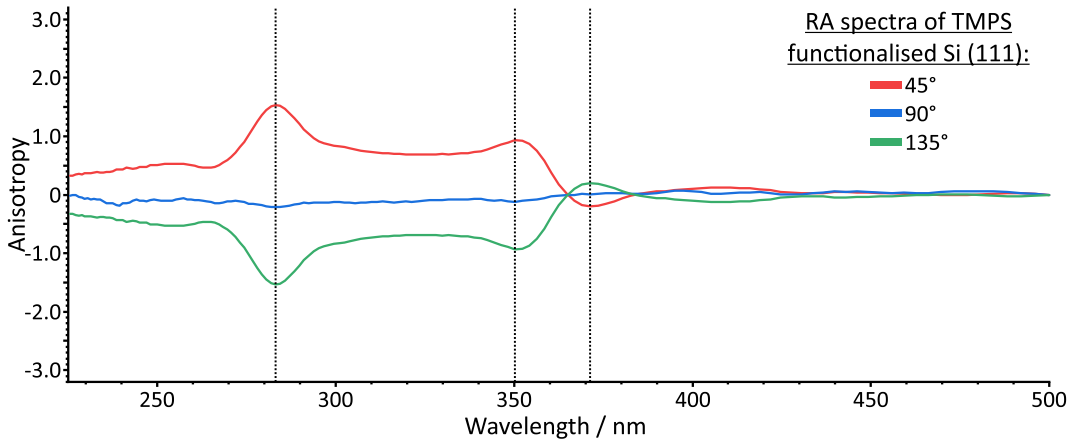

Figure 28: Reflection anisotropy (RA) spectra of a vicinal Si (111) surface functionalised with trimethoxypropylsilane (TMPS) at three different azimuths; (red) 45°, (blue) 90° and (green) 135°. The (dashed) lines show the approximate wavelengths for the peaks at; 290 nm, 356 nm and 371 nm.

The TMPS functionalised Si (111) surface RA spectra (Figure 28) are very similar to the RA spectra of the piranha cleaned vicinal Si (111) surface, which implies that the TMPS is aligned with the Si principal axes since no changes were observed in the full rotation spectra either (Figure S4). Another possibility for the lack of observed differences is the point group symmetry of TMPS, which as shown in Figure 25 is symmetrical, therefore generating no measured anisotropic signal. The azimuthal dependence associated with the Si peaks (~283 and 350 nm) is shown in Figure 29.

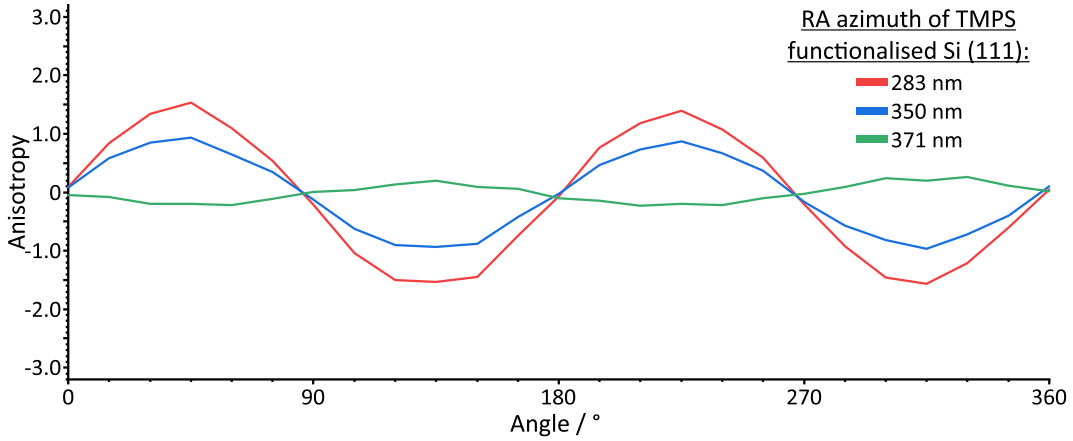

Figure 29: Azimuth dependence of a vicinal Si (111) surface terminated with trimethoxypropylsilane (TMPS) for the three anisotropic peaks, at approximately; (red) 283 nm, (blue) 350 nm and (green) 371 nm.

The azimuthal dependence of the RA spectra (Figure 29) shows that the TMPS functionalised vicinal Si (111) surface follows the typical sin (2θ) variation, which was previously observed for the piranha cleaned vicinal Si (111) surface (Figure 27a). There is also a small increase in the intensity of the signal, therefore the TMPS layer (~0.4 nm)[64] is aligned with the underlying crystallography. Increases in the intensity of the signal have also been observed for cytosine and adenine on Au (110), which are associated with interactions of the molecule with the electronic structure of the substrate.[22–26]

Similarly to the Si (110) surface, the orientation of the adsorbed molecules can be deduced in relation to the surface axes because the location of the surface's principal axes are known from the maximum and minimum anisotropic signal, therefore the TMPS terminated surface can be used for the HI fibrillation studies because the functionalisation does not impact the RAS.

2.3.3. Interfacial structural morphology inducing directed fibrillation

The TMPS-functionalised vicinal Si (111) surfaces were incubated in an acidic (pH 2.6, citrate-phosphate buffer) HI suspension (1 mg/mL) at elevated temperature (~75°C) over a one- or two- day period, with RA spectra acquired at the three azimuths (45°, 90° and 135°) as shown in Figure 30.

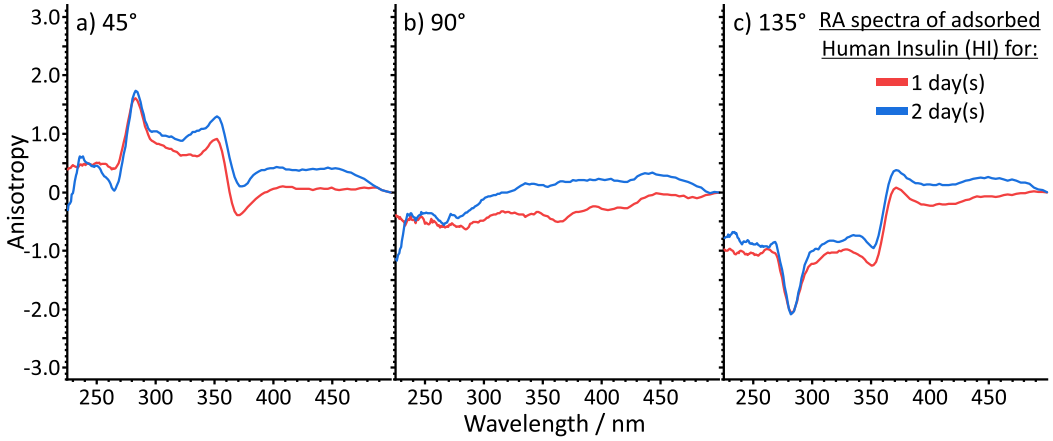

Figure 30: Reflection anisotropy (RA) spectra of a vicinal Si (111) surface functionalised with trimethoxypropylsilane (TMPS), incubated at ~75°C for (red) 1 day or (blue) 2 day, with human insulin (HI, 1 mg/mL) in citrate-phosphate buffer (pH 2.6) at the three different azimuths; (a) 45°, (b) 90° and (c) 135°.

Similarly as for the HI samples (Figure 30), RA spectra (45°, 90° and 135°) were acquired for the same incubation conditions (pH 2.6, citrate-phosphate buffer, 75°C for up to two days) of TMPS-functionalised vicinal Si (111) with insulin glargine (1 mg/mL), as shown in Figure 31.

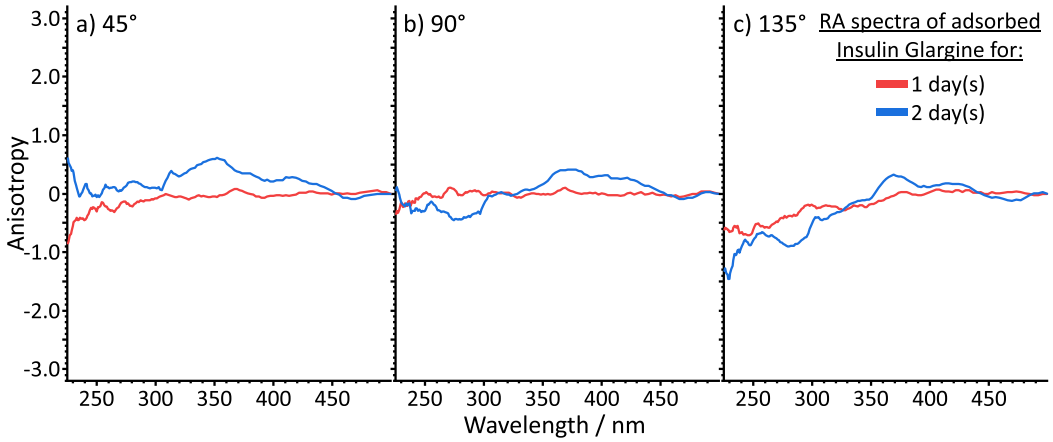

Figure 31: Reflection anisotropy (RA) spectra of a vicinal Si (111) surface functionalised with trimethoxypropylsilane (TMPS), incubated at ~75°C for (red) 1 day or (blue) 2 day, with insulin glargine (1 mg/mL) in citrate-phosphate buffer (pH 2.6) at the three different azimuths; (a) 45°, (b) 90° and (c) 135°.

The RA spectra (Figure 30) for the HI incubated TMPS-functionalised vicinal Si (111) surface shows similarity between the two incubation periods, specifically the observation of the characteristic Si peaks which indicates that the HI adsorption and

fibrillation events do not occur at the faceted Si (110) locations. In the case of cytosine adsorbed onto the Au (110) surface, the π-π* transition of the cytosine molecule was in the opposite direction to that of the signal arising from the Au (110) steps and resulted in the disappearance of the step signal.[22] If the HI was adsorbing onto the steps of the vicinal Si (111) surface, then any loss or reduction in anisotropy signal for the characteristic Si peaks as fibrillation proceeds would be indicative of HI adsorption or fibrillation at the faceted Si (110) locations.[65] There is however a small feature present at 225 nm for the two day incubated sample at 45° (Figure 30a), however the corresponding anisotropic peak is not observed for the 135° (Figure 30c), which implies that either the HI fibrillation is orientated off the principal axes or the fibrils are aligned perpendicular to the surface similar to that observed with DNA hybridisation on diamond.[43] This suggests that the HI is preferentially adsorbing onto the terraces of the vicinal Si (111) surface. At this point with this limited data set it is not possible to differentiate between adsorption on the terraces and the fibrils perpendicular to the surface, therefore a full 360˚ rotation of the sample was needed.

The RA spectra for insulin glargine (Figure 31) are overall distinctly different from that of the HI (Figure 30), with no Si peaks observed for either incubation period, which implies that the insulin glargine is adsorbing and fibrillating at the faceted locations as opposed to HI because of the suppressed characteristic Si peaks. A lower wavelength peak (~225 nm) is also observed, similar to the HI RA spectra (Figure 30), which had previously been observed.[64] It is possible that this peak is a marker for insulin fibrillation, associated with the net L_a electronic transition of the tyrosine residues (~225 nm).[66]

A full 360° rotation for both one- and two- day incubation periods of HI (Figure S5 and Figure S6) and insulin glargine (Figure S7 and Figure S8) are provided in the supplementary. For HI, the peak (~225 nm) is more pronounced for the longer incubation period (Figure S6), which implies association to the fibrillation state. A similar effect is observed for the insulin glargine, where the peak (~225 nm) for the two day incubation (Figure S8) results in increased anisotropy across a wider wavelength range. The 360° rotation shows that for HI the Si peaks are observed,

whereas there are no similar Si peaks shown in the incubated insulin glargine spectra. These results confirm that HI adsorbs on the terraces whilst glargine adsorbs at the step edges and in both cases, there is an increased concentration of fibrils as incubation time increases.

The results of the RAS for both HI and insulin glargine are overall encouraging as they show distinct differences for the variants; HI adsorbs along the terraces whereas insulin glargine on the step edges, as indicated by the differences in observed Si peaks. In both sample sets, the TMPS-functionalised vicinal Si surfaces were prepared similarly but with either HI or insulin glargine which gave rise to the distinctly different RA spectra.

The RA spectral differences arise from the orientation of the electronic transitions within the fibrillar insulin state. Discrimination of the electronic transitions to determine the specific fibrillar orientation is difficult as the tyrosine L_a (225 nm) is situated at the spectral edge with the respective phenylalanine L_a (210 nm) outside the scope of the measured region, and in both residues the L_b (280 and 260 nm respectively) transitions are located directly within the Si substrate feature. The β-sheets are orientated perpendicular to the fibril axis therefore the four tyrosine residues L_a and L_b electronic transitions are perpendicular and parallel to the fibril axis.[67] Assuming that the four residues are situated within the β-sheet component, then it is possible with detailed analysis to determine where these residues are in relation to the principal axis and hence their alignment on the surface. Before embarking on a detailed analysis of this data using the three-phase model[40] and the azimuthal dependence, to determine the orientation of the fibrils on the surface, it was necessary to show reproducibility of the obtained results as shown below (2.3.4. The impact of sample inhomogeneity, page 85).

2.3.4. The impact of sample inhomogeneity

The RA spectra of HI and insulin glargine were distinctly different, (2.3.3. Interfacial structural morphology inducing directed fibrillation, page 82), however this was only data from one batch, therefore more samples were necessary to correlate these findings directly to the insulin variants. As described previously, fresh

TMPS-functionalised vicinal Si (111) surfaces were incubated in an acidic (pH 2.6, citrate-phosphate buffer) HI suspension (1 mg/mL) at elevated temperature (~75°C) for a one day period, with RA spectra acquired at the three azimuths (45°, 90° and 135°) as shown in Figure 32. The RA spectra for HI incubated surfaces (Figure 32) were acquired for four sample batches (a – d), which were identically prepared.

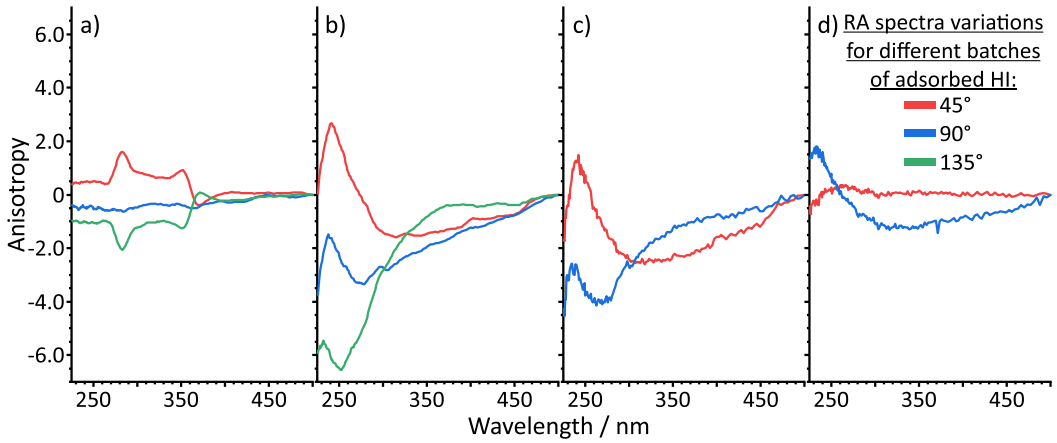

Figure 32: Reflection anisotropy (RA) spectra showing the differences between four sample sets (a – d) of a vicinal Si (111) surface functionalised with trimethoxypropylsilane (TMPS), incubated (~75°C, 1 day), with human insulin (HI, 1 mg/mL) in citrate-phosphate buffer (pH 2.6) at the three different azimuths; (red) 45°, (blue) 90° and (green) 135°.

The RA spectra from the four identically prepared samples (Figure 32) shows that there is significant variability in the RA spectra. The only similarity in the results being the anisotropic peak at lower wavelengths (~230 nm). In only one batch (Figure 32a) are the characteristic Si peaks observed, which indicates that the HI fibrillates as previously (Figure 30) on the terraces, whereas the other three batches fibrillate similarly to insulin glargine (Figure 31) on the steps.

Three TMPS-functionalised vicinal Si (111) surfaces (i – iii) were incubated in an acidic (pH 2.6, citrate-phosphate buffer) insulin glargine suspension (1 mg/mL) at elevated temperature (~75°C) for; (a) one-, (b) two- and (c) three- day period, with the 45° azimuth RA spectra shown in Figure 33.

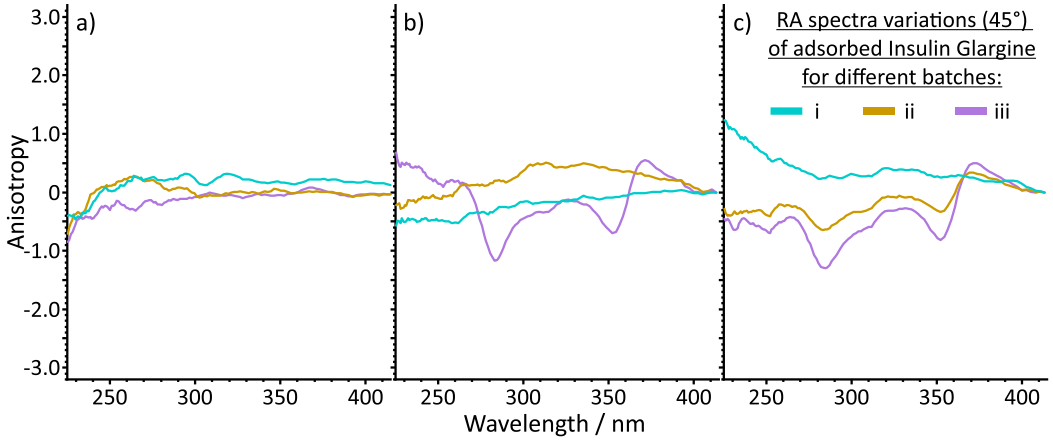

Figure 33: Reflection anisotropy (RA) spectra showing the spectral deviations at the same azimuth (45°) between three sample sets (teal, gold, and purple), which were labelled; i, ii, and iii. Each sample set is a vicinal Si (111) surface functionalised with trimethoxypropylsilane (TMPS), incubated (~75°C) with insulin glargine (1 mg/mL) in citrate-phosphate buffer (pH 2.6) for; (a) 1 day, (b) 2 day or (c) 3 day.

The three batches of insulin glargine incubated silicon surfaces (i – iii), show a similarity at one day incubation (Figure 33a) as previously observed for insulin glargine (Figure 31), with the presence of a lower wavelength anisotropic peak (~225 nm). This similarity across samples, is not present for either the two day (Figure 33b) or three day (Figure 33c) incubation periods, whereby the batches are spectrally dissimilar. At two day incubation (Figure 33b) neither i (teal) or ii (gold) batches display any anisotropic peaks, whereas the iii (purple) batch shows the characteristic Si peaks (~283 and 352 nm). The observed Si peaks for the iii (purple) batch continues into the third day incubation (Figure 33c), with the appearance of reduced anisotropy Si peaks for batch ii (gold), conversely for batch i (teal) the anisotropic peak (~230 nm) returns.

Overall the significant spectral dissimilarity between batches of identically prepared suspensions is concerning, which also correlated with the observation that surfaces were less optically reflective (by eye) with inconsistent coverage. The RAS technique is both reproducible and reliable, where the spectra of a stable sample over a period of time does not change, for example Si (110) provides a spectral fingerprint and is often used as a calibration standard for RAS instruments.[68] Surface

differences observed by eye and the irreproducible RA spectra, suggests that these issues may arise from the insulin suspension preparation.

To check the insulin purity, mass spectroscopy (MS) was used because the molecular weight was known; HI (5808 Da) and insulin glargine (6063 Da). The results showed that for HI (Figure S9 and Figure S10) the correct mass was measured (~5808 Da) with minimal fragmentation. Conversely for insulin glargine (Figure S11 and Figure S12) an additional molecular weight (~4849 Da) of approximately 30% concentration (Figure S12) with a large fragmentation pattern and a noisy baseline (Figure S11) was observed. As the insulin glargine spectra (Figure S11 and Figure S12) showed that there were other components present, it was deemed unsuitable for use post the work presented within this chapter, because of the uncertainty surrounding the other components measured and whether they were attributed to contamination or proprietary commercial stabilisers. Consequentially only HI was used for the remainder of this thesis' research programme, the challenges raised in this chapter surrounding the preparation of insulin suspensions for the synthesis of reproducible and reliable samples is further discussed in Chapter 3.

2.4. Conclusion

The work reported in this chapter has shown that RAS is a highly sensitive surface-specific spectroscopic technique and can measure the orientation of adsorbed insulin species at a hydrophobically functionalised surface. These results show that vicinal Si (111) surfaces are desired to increase the speed at which analysis can be undertaken, by rapidly determining the principal axes of the surface as a result of the faceted Si (110) crystallography at the steps. The functionalisation of the surfaces by TMPS was shown to be appropriate as the acquired RA spectra were not affected by this functionalisation.

The irreproducibility in the RA spectra of insulin glargine was primarily associated with the contamination found in the mass spectra and therefore work on this variant was abandoned. The HI preparation methodology was also a challenge as illustrated by the inconsistency in the RA spectra, since the variable thickness of

the HI adsorbate led to irreproducible surfaces, which reduced the intensity of the reflected light signal at the detector. Significant further work is necessary in order to synthesise reproducible and reliable surfaces for studying the fibrillation process further, where the appropriate preparation of HI samples is critical and will be discussed in Chapter 3.

2.5. Supplementary

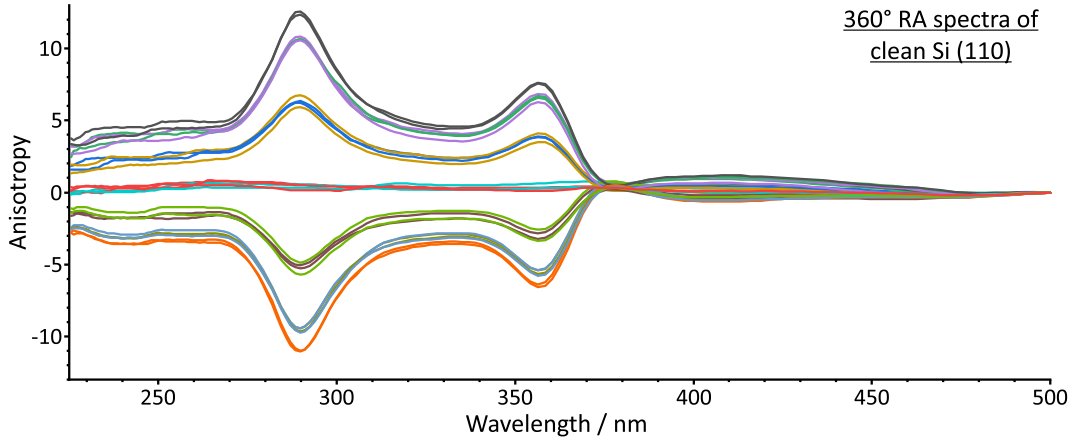

Figure S1: A full 360° reflection anisotropy (RA) spectra for the cleaned Si (110) surface.

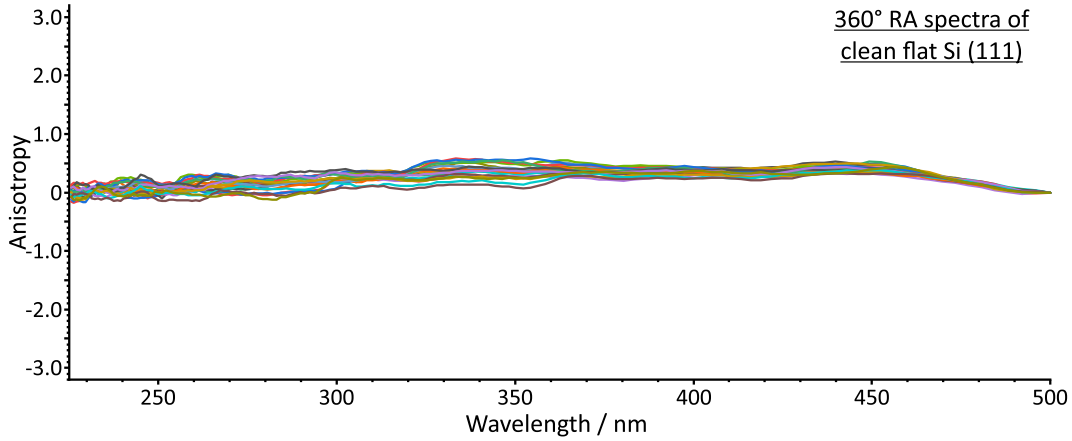

Figure S2: A full 360° reflection anisotropy (RA) spectra for the cleaned flat Si (111) surface.

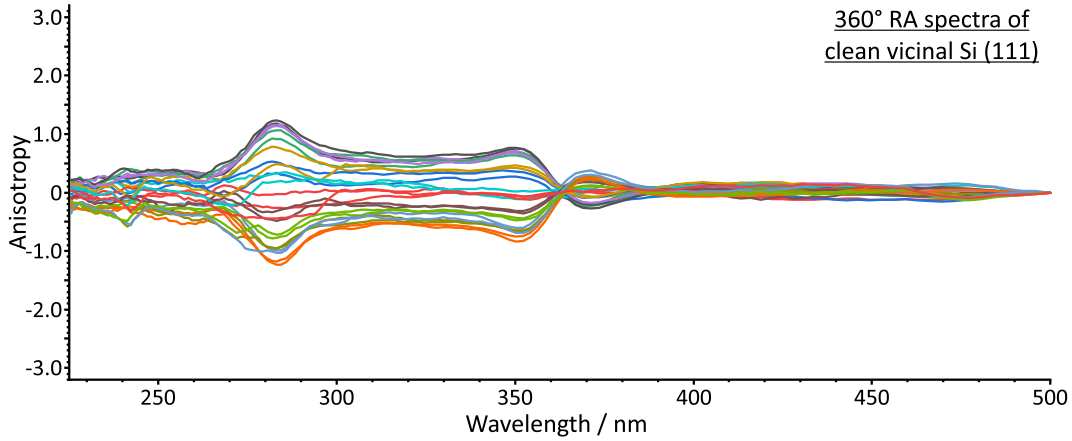

Figure S3: A full 360° reflection anisotropy (RA) spectra for the cleaned vicinal Si (111) surface.

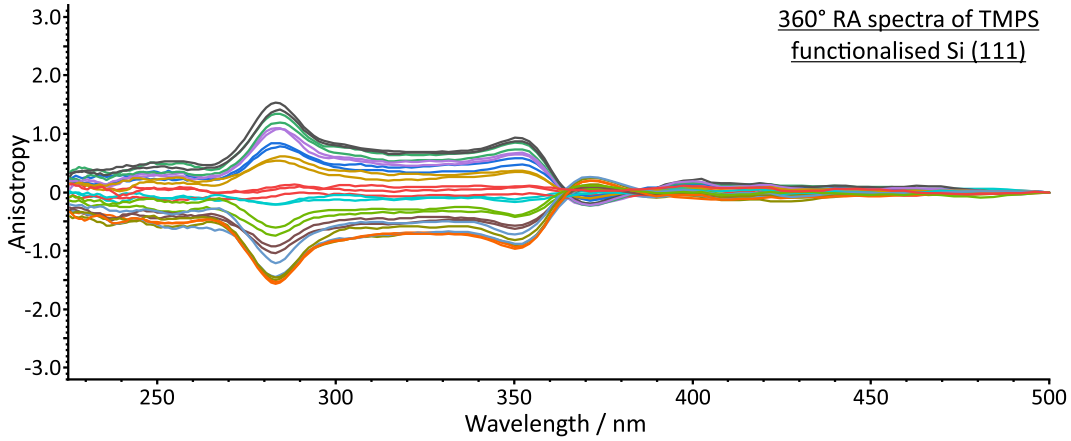

Figure S4: A full 360° reflection anisotropy (RA) spectra for the trimethoxypropylsilane (TMPS) functionalised vicinal Si (111) surface.

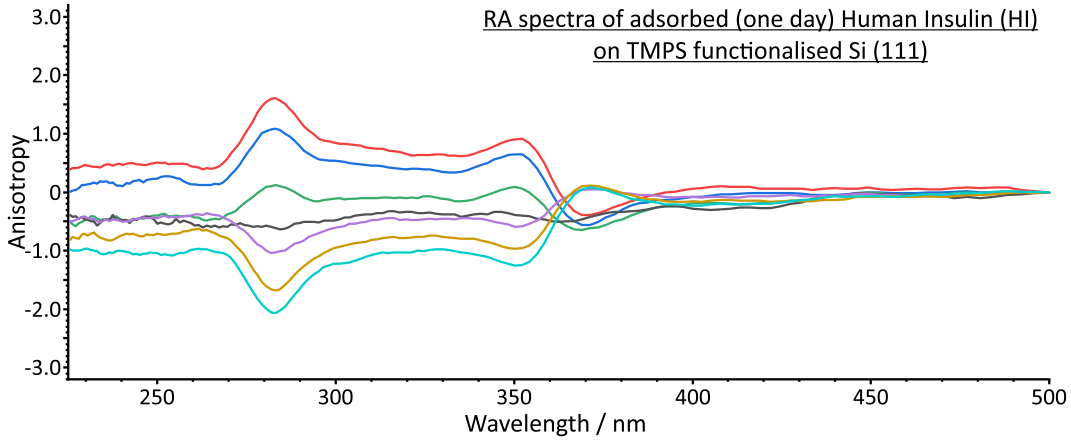

Figure S5: A 0 - 90° reflection anisotropy (RA) spectra of the trimethoxypropylsilane (TMPS) functionalised vicinal Si (111) surface after incubation (~75°C, 1 day) with human insulin (HI, 1 mg/mL) in citrate-phosphate buffer (pH 2.6).

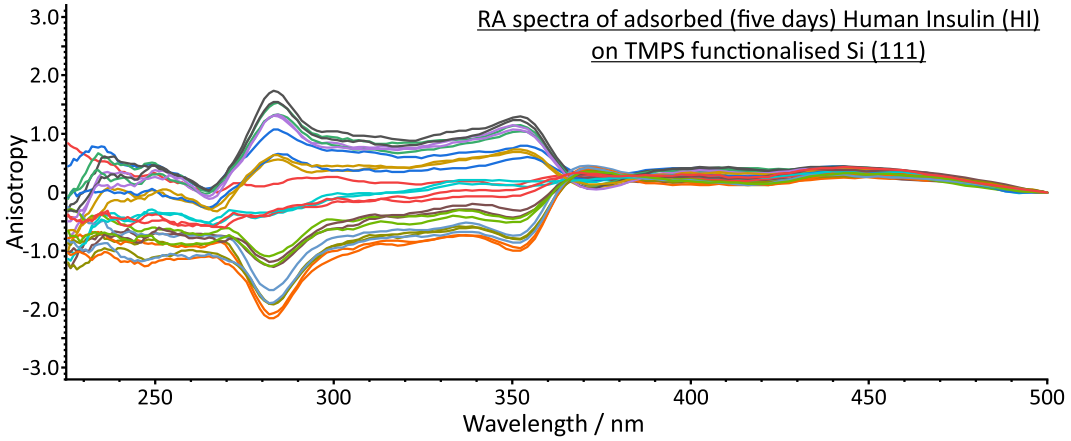

Figure S6: A full 360° reflection anisotropy (RA) spectra of the trimethoxypropylsilane (TMPS) functionalised vicinal Si (111) surface after incubation (~75°C, 5 day) with human insulin (HI, 1 mg/mL) in citrate-phosphate buffer (pH 2.6).

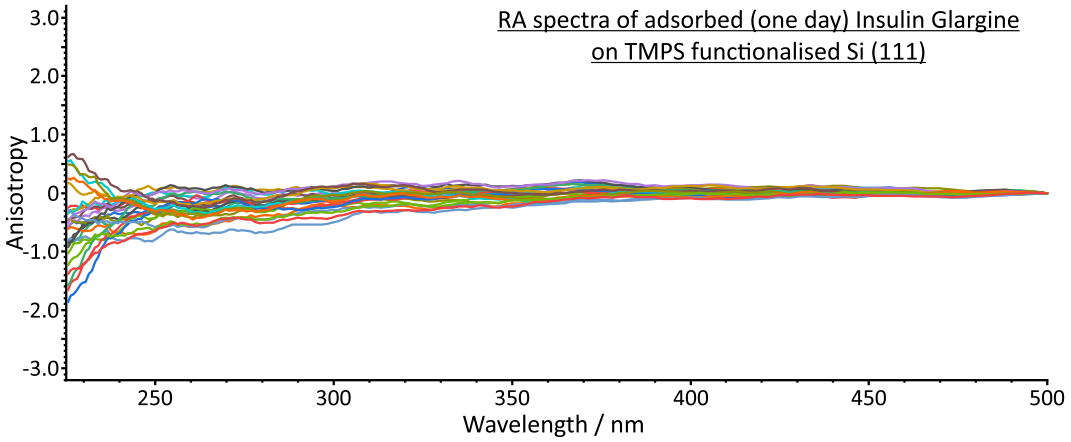

Figure S7: A full 360° reflection anisotropy (RA) spectra of the trimethoxypropylsilane (TMPS) functionalised vicinal Si (111) surface after incubation (~75°C, 1 day) with insulin glargine (1 mg/mL) in citrate-phosphate buffer (pH 2.6).

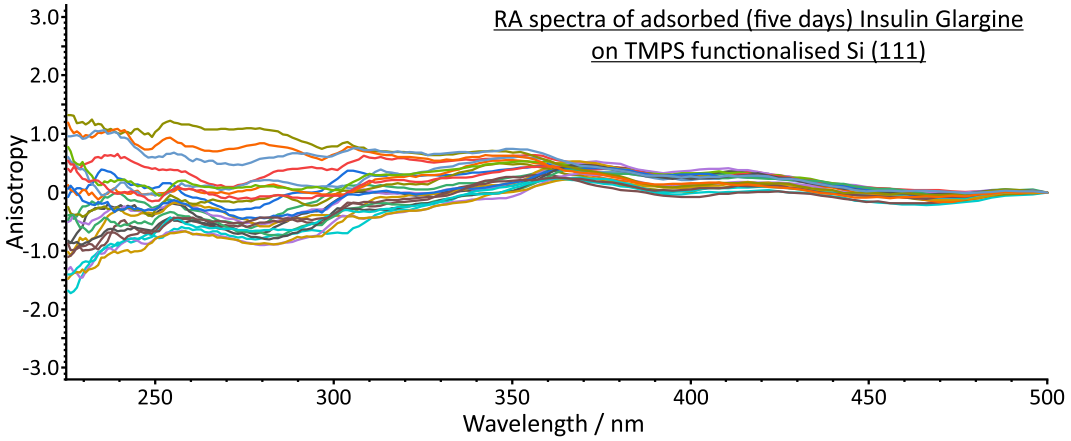

Figure S8: A full 360° reflection anisotropy (RA) spectra of the trimethoxypropylsilane (TMPS) functionalised vicinal Si (111) surface after incubation (~75°C, 5 day) with insulin glargine (1 mg/mL) in citrate-phosphate buffer (pH 2.6).

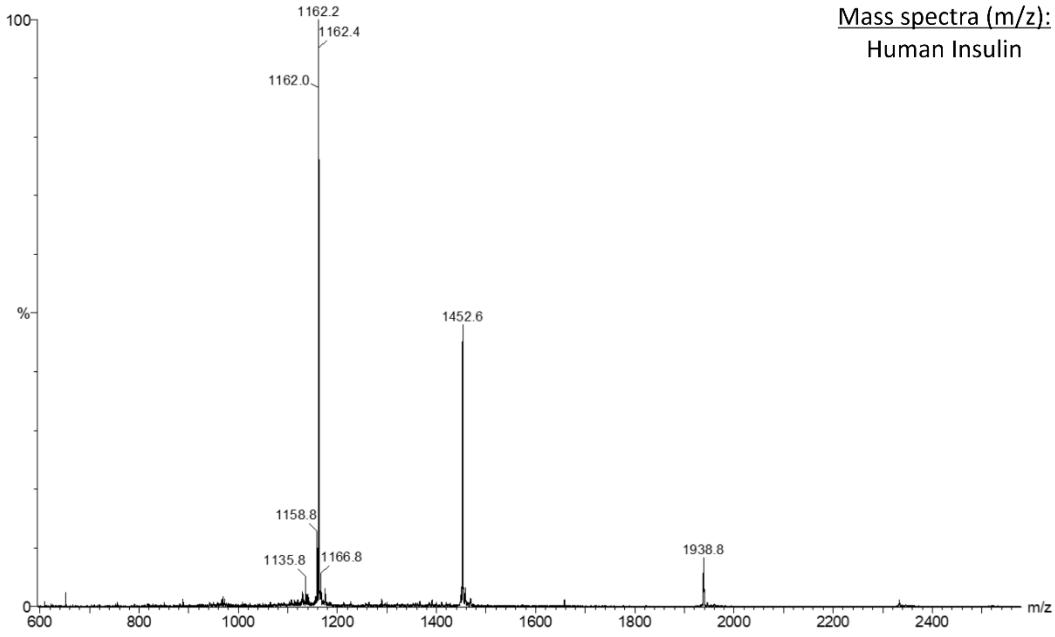

Figure S9: Mass spectra (m/z) of the human insulin (HI) used in this project, showing limited fragmentation pattern and minimal baseline noise level compared to the acquired spectra for insulin glargine.

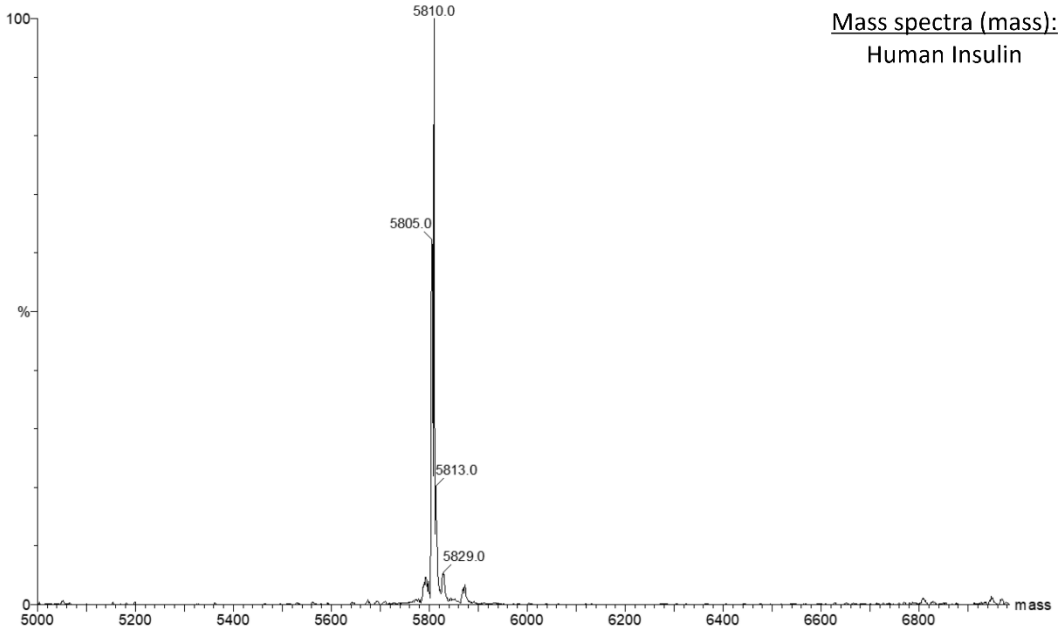

Figure S10: Mass spectra (mass) of the human insulin (HI) used in this project, showing the expected mass of HI at 5808 Da, with limited fragmentation pattern and minimal baseline noise level compared to the acquired spectra for glargine.

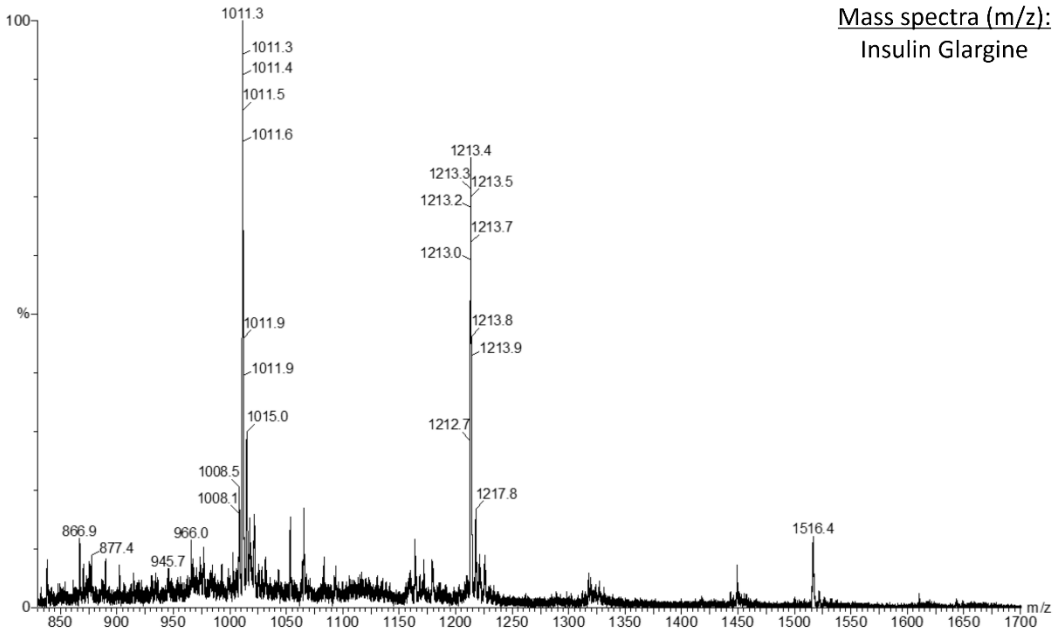

Figure S11: Mass spectra (m/z) of the insulin glargine used in this project, showing the prevalence of multiple species in the sample and an overall high baseline noise level.

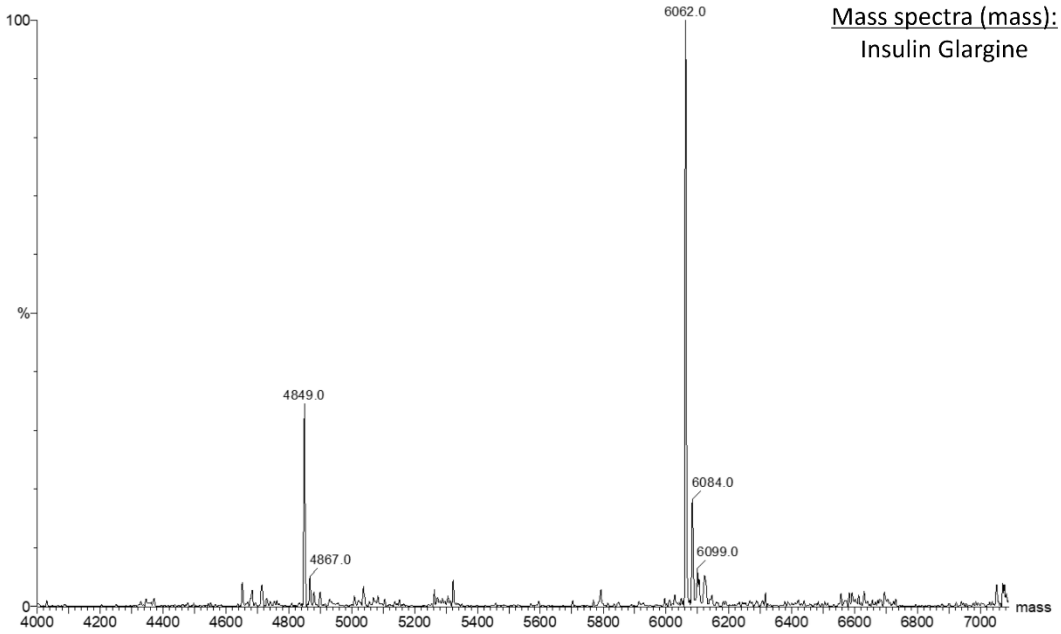

Figure S12: Mass spectra (mass) of the insulin glargine used in this project, showing two significant mass peaks; the expected 6063 Da at 6062 Da but an additional peak at 4849 Da.

Bibliography

1. Vácha, R., Linse, S. & Lund, M. Surface effects on aggregation kinetics of amyloidogenic peptides. *J. Am. Chem. Soc.* **136**, 11776–11782 (2014).

2. Zhou, X. *et al.* Hierarchical ordering of amyloid fibrils on the mica surface. *Nanoscale* **5**, 4816 (2013).

3. Shen, L., Adachi, T., Vanden Bout, D. & Zhu, X.-Y. A Mobile Precursor Determines Amyloid-β Peptide Fibril Formation at Interfaces. *J. Am. Chem. Soc.* **134**, 14172–14178 (2012).

4. Shezad, K. *et al.* Surface Roughness Modulates Diffusion and Fibrillation of Amyloid-β Peptide. *Langmuir* **32**, 8238–8244 (2016).

5. Nayak, A., Dutta, A. K. & Belfort, G. Surface-enhanced nucleation of insulin amyloid fibrillation. *Biochem. Biophys. Res. Commun.* **369**, 303–307 (2008).

6. Du, Z. *et al.* Cross-fibrillation of insulin and amyloid β on chiral surfaces: Chirality affects aggregation kinetics and cytotoxicity. *Nano Res.* **11**, 4102–4110 (2018).

7. Yang, B., Adams, D. J., Marlow, M. & Zelzer, M. Surface-Mediated Supramolecular Self-Assembly of Protein, Peptide, and Nucleoside Derivatives: From Surface Design to the Underlying Mechanism and Tailored Functions. *Langmuir* **34**, 15109–15125 (2018).

8. Petkova, A. T. Self-Propagating, Molecular-Level Polymorphism in Alzheimer's -Amyloid Fibrils. *Science* **307**, 262–265 (2005).

9. Verma, M., Vats, A. & Taneja, V. Toxic species in amyloid disorders: Oligomers or mature fibrils. *Ann. Indian Acad. Neurol.* **18**, 138–145 (2015).

10. Al-Garawi, Z. S. *et al.* The amyloid architecture provides a scaffold for enzyme-like catalysts. *Nanoscale* **9**, 10773–10783 (2017).

11. Peralta, M. D. R. *et al.* Engineering Amyloid Fibrils from β-Solenoid Proteins for Biomaterials Applications. *ACS Nano* **9**, 449–463 (2015).

12. Hoernke, M., Falenski, J. A., Schwieger, C., Koksch, B. & Brezesinski, G. Triggers for β-Sheet Formation at the Hydrophobic–Hydrophilic Interface: High Concentration, In-Plane Orientational Order, and Metal Ion Complexation. *Langmuir* **27**, 14218–14231 (2011).

13. Sun, M., Stetco, A. & Merschrod S., E. F. Surface-templated formation of protein microfibril arrays. *Langmuir* **24**, 5418–5421 (2008).

14. Naldi, M. *et al.* Self-assembly of biomolecules: AFM study of F-actin on unstructured and nanostructured surfaces. *Nanoscale Imaging, Sensing, Actuation Biomed. Appl. VI* **7188**, 71880Q (2009).

15. Rodger, A. & Nordén, B. *Circular dichroism and linear dichroism.* (Oxford University Press, 1997).

16. Greenfield, N. J. & Fasman, G. D. Computed circular dichroism spectra for the evaluation of protein conformation. *Biochemistry* **8**, 4108–4116 (1969).

17. Weightman, P., Martin, D. S., Cole, R. J. & Farrell, T. Reflection anisotropy spectroscopy. *Reports Prog. Phys.* **68**, 1251–1341 (2005).

18. Harrison, P. *The development of Reflection Anisotropy Spectroscopy instrumentation for the study of dynamic surface properties (PhD thesis)*. (University of Liverpool, 2018). doi:10.17638/03035932

19. Aspnes, D. E. Above-bandgap optical anisotropies in cubic semiconductors: A visible–near ultraviolet probe of surfaces. *J. Vac. Sci. Technol. B Microelectron. Nanom. Struct.* **3**, 1498 (1985).

20. Aspnes, D. E., Harbison, J. P., Studna, A. A. & Florez, L. T. Optical reflectance and electron diffraction studies of molecular-beam-epitaxy growth transients on GaAs(001). *Phys. Rev. Lett.* **59**, 1687–1690 (1987).

21. Aspnes, D. E., Harbison, J. P., Studna, A. A. & Florez, L. T. Application of reflectance difference spectroscopy to molecular-beam epitaxy growth of GaAs and AlAs. *J. Vac. Sci. Technol. A Vacuum, Surfaces, Film.* **6**, 1327–1332 (1988).

22. Weightman, P. *et al.* Orientation of Ordered Structures of Cytosine and Cytidine 5'-Monophosphate Adsorbed at Au(110)/Liquid Interfaces. *Phys. Rev. Lett.* **96**, 086102 (2006).

23. Smith, C. I. *et al.* Determination of the structure of adenine monolayers adsorbed at Au(110)/electrolyte interfaces using reflection anisotropy spectroscopy. *J. Chem. Phys.* **130**, 044702 (2009).

24. Bowfield, A. *et al.* The Structure of Adenine Adsorbed at Sub-Saturation Coverage at Au(110)/Electrolyte Interfaces. *e-Journal Surf. Sci. Nanotechnol.* **7**, 225–229 (2009).

25. Mansley, C. P. *et al.* Prevention of surface reconstruction at the Au(110)/electrolyte interface by the adsorption of cytosine. *J. Chem. Phys.* **132**, 214708 (2010).

26. Bowfield, A., Smith, C. I., Mansley, C. P. & Weightman, P. The influence of pH on the structure of adenine monolayers adsorbed at Au(110)/electrolyte interfaces. *Phys. status solidi* **247**, 1937–1940 (2010).

27. Molina Contreras, J. R., Smith, C. I., Bowfield, A., Tillner, F. & Weightman, P. The self assembly of thymine at Au(110)/liquid interfaces. *Phys. status solidi* **249**, 1206–1209 (2012).

28. Cuquerella, M. C., Smith, C. I., Fernig, D. G., Edwards, C. & Weightman, P. Adsorption of calf thymus DNA on Au(110) studied by reflection anisotropy spectroscopy. *Langmuir* **23**, 2078–2082 (2007).

29. Mansley, C. P. *et al.* Ordered structures of DNA on Au(110). *Phys. status solidi* **5**, 2582–2586 (2008).

30. Smith, C. I. *et al.* Detection of DNA hybridisation on a functionalised diamond surface using reflection anisotropy spectroscopy. *Europhys. Lett.* **85**, (2009).

31. Isted, G. E. *et al.* The adsorption of L-cysteine on Au(110) in ultra-high vacuum and electrochemical environments. *Phys. status solidi* **2**, 4012–4016 (2005).

32. LeParc, R. *et al.* Reflection Anisotropy Spectroscopy Study of the Adsorption of Sulfur-Containing Amino Acids at the Au(110)/Electrolyte Interface. *Langmuir* **22**, 3413–3420 (2006).

33. Morozzo Della Rocca, B., Smith, C. I., Tesauro, C., Desideri, A. & Weightman, P. Adsorption of the cysteine-tryptophan dipeptide at the Au(110)/liquid interface studied using reflection anisotropy spectroscopy. *Surf. Sci.* **604**, 2170–2176 (2010).

34. Messiha, H. L., Smith, C. I., Scrutton, N. S. & Weightman, P. Evidence for protein conformational change at a Au(110)/protein interface. *EPL (Europhysics Lett.* **83**, 18004 (2008).

35. Convery, J. H. *et al.* Controlling the formation of a monolayer of cytochrome P450 reductase onto Au surfaces. *Phys. Rev. E* **86**, 011903 (2012).

36. Smith, C. I., Convery, J. H., Khara, B., Scrutton, N. S. & Weightman, P. Ordered multilayers of cytochrome P450 reductase adsorbed at Au(110)/phosphate buffer interfaces. *Phys. status solidi* **252**, 181–186 (2015).

37. Smith, C. I., Convery, J. H., Khara, B., Scrutton, N. S. & Weightman, P. The influence of the structure of the Au(110) surface on the ordering of a monolayer of cytochrome P450 reductase at the Au(110)/phosphate buffer interface. *Phys. Status Solidi Basic Res.* **251**, 549–554 (2014).

38. Zahn, D. R. T., Silaghi, S. D., Cobet, C., Friedrich, M. & Esser, N. Spectroscopic ellipsometry and reflectance anisotropy spectroscopy of biomolecular layers on silicon surfaces. *Phys. Status Solidi Basic Res.* **242**, 2671–2680 (2005).

39. Schofield, A. L. *et al.* The use of reflection anisotropy spectroscopy to assess the alignment of collagen. *J. Phys. D. Appl. Phys.* **44**, 335302 (2011).

40. Cole, R. J., Frederick, B. G. & Weightman, P. Substrate dependence of adlayer optical response in reflectance anisotropy spectroscopy. *J. Vac. Sci. Technol. A Vacuum, Surfaces, Film.* **16**, 3088–3095 (1998).

41. Lane, P. D., Isted, G. E. & Cole, R. J. Molecular orientation studied by reflection anisotropy spectroscopy. *Phys. status solidi* **247**, 1969–1973 (2010).

42. Farrell, T., Harrison, P., Smith, C. I., Martin, D. S. & Weightman, P. Azimuthal dependent reflection anisotropy spectroscopy of Ag(110) near the plasmon resonance energy. *Appl. Phys. Lett.* **93**, 191102 (2008).

43. Smith, C. I. *et al.* Detection of DNA hybridisation on a functionalised diamond surface using reflection anisotropy spectroscopy. *EPL (Europhysics Lett.* **85**, 18006 (2009).

44. Smith, C. I. & Weightman, P. *unpublished work*.

45. Weightman, P., Harrison, P., Lucas, C. A., Grunder, Y. & Smith, C. I. The reflection anisotropy spectroscopy of the Au(1 1 0) surface structures in liquid environments. *J. Phys. Condens. Matter* **27**, 475005 (2015).

46. Macdonald, B. F., Law, J. S. & Cole, R. J. Azimuth-dependent reflection anisotropy spectroscopy. *J. Appl. Phys.* **93**, 3320–3327 (2003).

47. Timperley, C. A. *Reflectance anisotropy spectroscopy of thermotropic liquid crystals (PhD thesis)*. (University of Liverpool, 2005).

48. Zimmerman, S. S. Theoretical Methods in the Analysis of Peptide Conformation. in *Conformation in Biology and Drug Design* (ed. Hruby, V. J.) **7**, 165–212 (Elsevier, 1985).

49. Adachi, R. *et al.* Flow-induced alignment of amyloid protofilaments revealed by linear dichroism. *J. Biol. Chem.* **282**, 8978–8983 (2007).

50. Bulheller, B. M. *et al.* Flow Linear Dichroism of Some Prototypical Proteins. *J. Am. Chem. Soc.* **131**, 13305–13314 (2009).

51. Milán-Garcés, E. A., Kaptan, S. & Puranik, M. Mode-Specific Reorganization Energies and Ultrafast Solvation Dynamics of Tryptophan from Raman Line-Shape Analysis. *Biophys. J.* **105**, 211–221 (2013).

52. Kuhlmann, A. M. The Second Most Abundant Element in the Earth's Crust. *JOM* **15**, 502–505 (1963).

53. Hammarström, P. *et al.* A catalytic surface for amyloid fibril formation. *J. Phys. Conf. Ser.* **100**, 052039 (2008).

54. Gagni, P., Sola, L., Cretich, M. & Chiari, M. Development of a high-sensitivity immunoassay for amyloid-beta 1-42 using a silicon microarray platform. *Biosens. Bioelectron.* **47**, 490–495 (2013).

55. Seidel, F., Ding, L., Gordan, O. D. & Zahn, D. R. T. Multi-phase model for reflection anisotropy spectra of copper phthalocyanine films on anisotropic silicon substrates. *J. Vac. Sci. Technol. B, Nanotechnol. Microelectron. Mater. Process. Meas. Phenom.* **30**, 012401 (2012).

56. Kim, H. J. *et al.* Photonic crystal alloys: a new twist in controlling photonic band structure properties. *Opt. Express* **16**, 6579 (2008).

57. Thames, S. F. & Panjnani, K. G. Organosilane polymer chemistry: A review. *J. Inorg. Organomet. Polym.* **6**, 59–94 (1996).

58. Ratner, B. D. & Hoffman, A. S. Physicochemical Surface Modification of Materials Used in Medicine. in *Biomaterials Science* 259–276 (Elsevier, 2013). doi:10.1016/B978-0-08-087780-8.00027-9

59. Mohan, C. A guide for the preparation and use of buffers in biological systems. *Calbiochem* 32 (2003).

60. Fleischer, K., Chandola, S., Esser, N., Richter, W. & Mcgilp, J. F. Reflectance anisotropy spectroscopy of Si(111)-(4 × 1)-In. *Phys. Status Solidi Appl. Res.* **188**, 1411–1416 (2001).

61. Stateikina, I., Landsberger, L. M., Kahrizi, M., Hoque, N. & Rossokhaty, V. Silicon wet etch anisotropy: Analysis of the impact of {111}-, {110}-, {100}-terrace widths. *Sensors Mater.* **17**, 199–210 (2005).

62. O'Mahony, J. D., McGilp, J. F., Leibsle, F. M., Weightman, P. & Flipse, C. F. J. Control of terrace width and atomic step distribution on vicinal Si(111) surfaces by thermal processing. *Semicond. Sci. Technol.* **8**, 495–501 (1993).

63. Pohl, R. *et al.* Ultra-rapid absorption of recombinant human insulin induced by zinc chelation and surface charge masking. *J. Diabetes Sci. Technol.* **6**, 755–763 (2012).

64. Mauri, S. *Insulin unfolding and aggregation : a multi-disciplinary study (PhD thesis)*. (University of Liverpool, 2014).

65. Weightman, P. *private communication*.

66. Fornander, L. H., Feng, B., Beke-Somfai, T. & Nordén, B. UV Transition Moments of Tyrosine. *J. Phys. Chem. B* **118**, 9247–9257 (2014).

67. Jimenez, J. L. *et al.* The protofilament structure of insulin amyloid fibrils. *Proc. Natl. Acad. Sci.* **99**, 9196–9201 (2002).

68. Hahn, P. H., Schmidt, W. G. & Bechstedt, F. Bulk Excitonic Effects in Surface Optical Spectra. *Phys. Rev. Lett.* **88**, 016402 (2001).

Chapter 3: The Importance of Protein Pre-Treatment

3.1. Introduction

Chapter 2 showed that human insulin (HI) adsorption on the hydrophobic functionalised silicon (Si) surfaces, was inconsistent and irreproducible both within and across batches. This inconsistency manifested as a variable blue colouration on the surface as shown in Figure 34.

Figure 34: Image of a trimethoxypropylsilane (TMPS) functionalised silicon wafer adsorbed with human insulin (HI) and mounted in an optical rotation stage. The reflective silicon surface shows inhomogeneous insulin adsorption with blue colouration on differing aspects of the surface.

The blue coloured regions were of reduced reflectivity and with clearly defined transition between blue and non-coloured areas. This blue colouration was observed on multiple Si surfaces in various sample batches incubated with HI but was not consistent across the Si surface. The irreproducibility of the samples was therefore assumed to be linked with poor preparation of HI suspensions. This chapter aims to provide a standard methodology for handling HI to formulate reproducible and reliable HI adsorbed surfaces for investigating amyloid-like fibrillation.

Overall, the scope of this thesis is to investigate the physical and chemical origins of amyloid at interfaces, with the hydrophobic interface modifications as the primary variable. The effect of surface functionalisation, specifically hydrophobicity, on the HI fibrillation has shown that differing surfaces affect the fibrillation pathway.[1] It is of paramount importance that the surfaces studied were controlled, specifically

reproducible, across batches for the same conditions studied. The introduction of additional inconsistency and irreproducibility associated with the surfaces, leads to difficulty in ascertaining the effects that hydrophobicity has on the interface. Furthermore, as this objective is to investigate the effect of oligomeric species on the HI fibrillation pathway at acidic and neutral pH, it is important that these HI suspensions are consistently reliable.

3.2. Materials and Methods

In this chapter, HI protein solutions (10 mg/mL) are prepared at pH 2, but the same preparation methodology was later applied to the pH 7 series. All experimental preparation was undertaken within designated fume hoods.

3.2.1. Sample Preparation

Investigating proteins requires lab workstations and glassware to be as clean as possible, to limit the potential for both biological and chemical contamination to occur. It should be noted that, where possible, lab stations were cleaned down with ethanol and multi-purpose cleaner daily and prior to sample preparation or analysis.

3.2.1.1. Equipment Preparation

All glassware was cleaned, at least overnight, in a Decon 90 bath and oven dried to remove any source of potential debris. Prior to usage, glassware, sample vials and any other glass / metal / plastic equipment was acidic Piranha cleaned (70% sulphuric acid: 30% hydrogen peroxide, ~65^{o}C). Hydrogen peroxide (30 mL, 30%) was added slowly to the sulphuric acid (70 mL). The piranha synthesis is a self-heating process, however, to ensure complete efficiency, the solution was left until effervescence had subsided before being added to the required glassware and further heated (~65^{o}C, 30 minutes). After heating, the piranha solution was removed, carefully neutralised with sodium hydroxide and diluted before disposal, whilst the glassware was rinsed at least three times with ultrapure (type I) water (18.2 MΩ cm^{-1}) before being oven-dried ready for use.

3.2.1.2. Buffers

The buffer solutions were prepared fresh, with enough volume; to suspend the protein at the required concentration, to use as a spectrometric blank, and

should any dilution be required. For the pH 2 buffer, sodium chloride (137.9 mM) and water (80 mL, 18.2 MΩ cm^{-1}) were added to a conical flask (250 mL), with acetic acid (20 mL). For the pH 7 buffer, a phosphate-buffered saline (PBS) tablet (1 tablet) was dissolved in water (100 mL, 18.2 MΩ cm^{-1}). Both solutions were sonicated (30 minutes) to ensure complete dissolution.

The pH of the buffers was first checked by universal indicator paper, which was validated by pH meter (SevenEasy, Mettler Toledo). The buffer solutions were then syringe filtered (0.22 µm, polyethersulfone (PES) membrane, Merck) into laboratory bottles (Duran) using a large volume syringe (60 mL). Aliquots of the buffers were taken for; protein suspension, buffer blanks and dilution solutions.

3.2.1.3. Suspension of human insulin

To allow comparability regarding the efficiency of the pre-treatment, the HI (10 mg/mL) was suspended in a pH 2 buffer (20% acetic acid and 139.7 mM sodium chloride) and then stored in a lo-bind Eppendorf tube (2 mL) prior to use.

Untreated methodology

The HI (10 mg/mL) was suspended in the prepared pH 2 buffer (20% acetic acid and 139.7 mM sodium chloride) directly into a lo-bind Eppendorf tube, which was briefly vortexed (Vortex Mixer) to ensure complete dissolution.

Treatment by hexafluoroisopropanol

The HI (10 mg/mL) was dissolved in hexafluoroisopropanol (HFIP, 20 mL), which was vortexed (Vortex Mixer) until complete dissolution. The HFIP was evaporated under nitrogen flow overnight. Buffer (pH 2, 20% acetic acid and 139.7 mM sodium chloride) was added, and the suspended HI (10 mg/mL) was briefly vortexed before the solution was transferred into a lo-bind Eppendorf tube.

Treatment by syringe filtration

The HI (10 mg/mL) was suspended in the prepared pH 2 buffer (20% acetic acid and 139.7 mM sodium chloride) directly into a lo-bind Eppendorf tube, which was briefly vortexed, and then immediately syringe-filtered (0.22 µm, PES).

3.2.2. Methods

To reduce any potential sample variability resulting from sample handling, manual handling was limited.

3.2.2.1. Dynamic Light Scattering (DLS)

To investigate the size distribution of the protein constituents, dynamic light scattering (DLS) was employed using a Zetasizer Nano ZSP (Malvern Panalytical Ltd, UK), which has a stated size range of 0.3 nm to 10 µm. Quartz cells (700 µL, fluorescence cells) with a parallel path length (1 cm) were used throughout. HI was suspended in an acidic buffer (pH 2, 20% acetic acid buffer), with instrumental parameters set; dispersant (water, 1.330 refractive index, 0.8872 mPa s^{-1} viscosity), temperature (25°C, 60 s equilibration time) and operating in back scatter (173°, 10 scans, 50 s acquisition time).

3.2.2.2. Infrared (IR) spectroscopy and microscopy

Infrared (IR) spectroscopy was performed on a Fourier transform infrared (FTIR) microscope (LUMOS, Bruker) in reflection mode. The instrumental parameters set were; spectral range (4000 cm^{-1} to 400 cm^{-1}), resolution (2 cm^{-1}), multiple scans to increase signal (100 scans for both background and sample), and atmospheric compensation. Although this investigation only utilised the Amide I (1700 - 1600 cm^{-1}) and Amide II (1580 - 1510 cm^{-1}) regions, the entire spectral range was acquired.

3.2.2.3. Atomic Force Microscopy (AFM)

Atomic force microscopy (AFM) images were kindly provided by Dr Alan Massey, Surface Science Research Centre (University of Liverpool), using an Agilent 5500 atomic force microscope.[2] All measurements were carried out in air at room temperature.

3.3. Results and Discussion

3.3.1. Investigation of the blue coloured adsorbate

The blue coloured adsorbate, which varied in size and shape, randomly appeared on different samples despite maintaining the same experimental parameters was investigated, to determine the composition. This area was initially

analysed by IR microscopy, as shown in Figure 35, to probe the Amide I (1700 – 1600 cm^{-1}) and Amide II (1580 – 1510 cm^{-1}) regions.

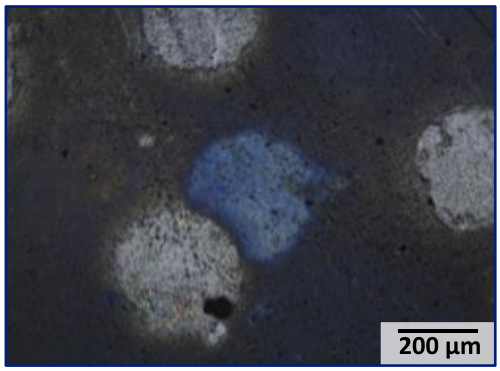

Figure 35: A bright-field optical microscope image (acquired at x5 visible zoom), attained on the LUMOS FTIR microscope, of the blue coloured adsorbed species on the trimethoxypropylsilane-functionalised vicinal Si (111) surface. The image shows inhomogeneous distribution of the blue adsorbed species, surrounded by regions of grey. The FTIR spectra was acquired at the centre of the image with a 50 µm diameter spot.

The bright-field optical microscopy image (Figure 35) shows the inhomogeneity of the blue adsorbed species, which is located at the centre of the image, as it is surrounded by grey regions of Si. There is a clear phase separation between the blue and light grey area, as observed at the lower left corner of the central blue region, where the curved boundary changes in colour from blue through dark grey to the light grey region. In both the upper and lower right quadrants of the image a diffuse blue colouring can be observed, which implies that the blue colouration is a component of the fibrillation process as opposed to a contaminant, since it is not an isolated event located in one region. The centre of the image (50 µm), which contained the blue adsorbed species only, was measured by IR with the resulting Amide I (1700 – 1600 cm^{-1}) and Amide II (1580 – 1510 cm^{-1}) regions shown in Figure 36.

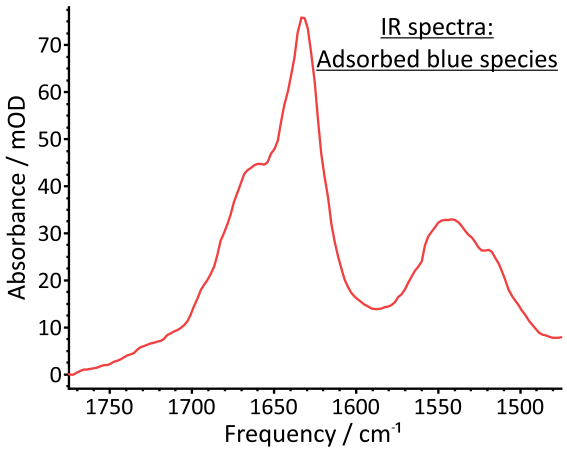

Figure 36: A FTIR spectrum of the blue coloured adsorbed species region on the trimethoxypropylsilane (TMPS) functionalised vicinal Si (111) surface, acquired on the LUMOS FTIR microscope with a 50 µm diameter spot.

The FTIR spectrum obtained from the blue adsorbed species (Figure 36) shows the secondary structural features of a protein; a sharp β-sheet peak and a α-helix shoulder, located at ~1630 cm^{-1} and ~1660 cm^{-1} respectively.[3] This data correlates with an investigation by Amenabar *et al*[4] using infrared nanospectroscopy to probe insulin fibrils, which reported that the fibrils contain a β-sheet core surrounded by secondary structures of random orientation including α-helices. The Amide I and II bands observed in the measured IR spectra implies that the blue adsorbate consists of protein with the distinctly β-sheet and α-helical features therefore confirming that the blue regions are areas of adsorbed insulin. The higher proportion of β-sheet characteristic compared to α-helices, suggests that the adsorbed species is largely fibrillar.[5]

FTIR spectra and optical images were acquired of four other samples, which also exhibited regions of blue colouration but varied in size and colour intensity. The four samples were labelled A – D, of decreasing blue colouration with A (blue) highest and D (gold) the least, as shown in Figure 37.

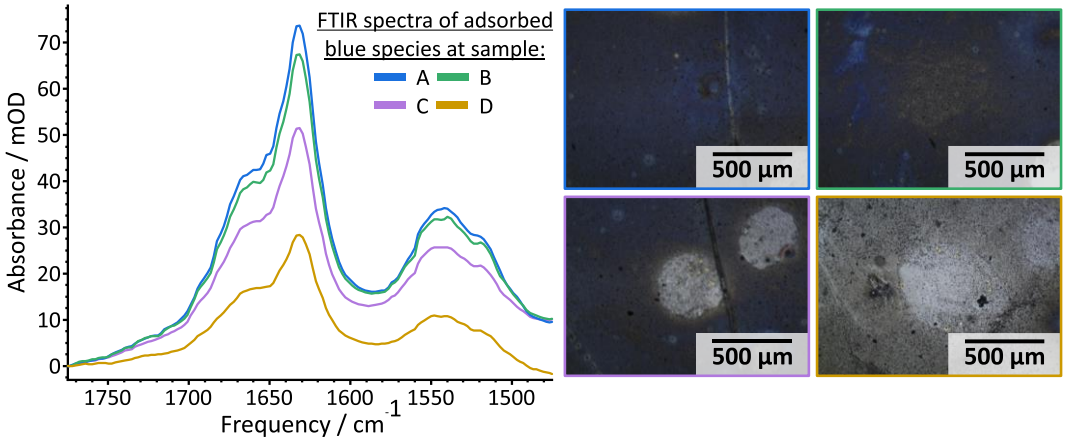

Figure 37: FTIR spectra and optical microscopy images for four samples (A – D) of blue coloured adsorbed species on the trimethoxypropylsilane-functionalised vicinal Si (111) surface. The spectra for each sample; (blue) A, (green) B, (purple) C and (gold) D, are colour coded to the corresponding FTIR microscope image (acquired at x5 visible zoom). The FTIR spectra and optical images were recorded simultaneously with the spectra attained from the centre of each image with a 50 µm diameter spot.

The IR spectra of the four samples of various blue colouration (Figure 37), shows that all four samples contain a sharp β-sheet peak (~1630 cm^{-1}) and a α-helix shoulder (~1660 cm^{-1}). There is a perceived visual difference between the four samples in the amount of blue colouration present, this is correlated to the IR spectra which shows a higher absorbance for the blue sample A (blue) which decreases in relation to observed blue colouration until the light grey sample D (gold). This correlation between blue colouration and IR absorbance, implies that the blue colour is indicative of high insulin content. It is not clear by IR spectroscopy whether this content is due to fibrillar species or higher levels of HI adsorption, therefore AFM microscopy was used to investigate whether there is any structure at the surface and the resultant topography, as shown in Figure 38.

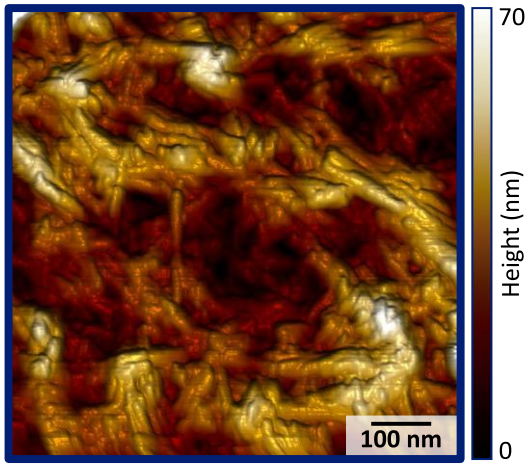

Figure 38: Atomic force microscopy (AFM) image of the blue coloured adsorbed species on the trimethoxypropylsilane-functionalised vicinal Si (111) surface, showing inhomogeneous distribution with coverages up to ~68 nm thick.

The AFM image of the blue adsorbed species (Figure 38), shows that there is an overall inhomogeneous distribution of fibrillar structures, with very thick layers of HI present at various locations. The layer thickness is ~68 nm, however it is possible that the minimum regions which are situated inside the 'valleys' are of monolayer or multilayer HI coverage and not the Si substrate, therefore the HI thickness is at a minimum of ~68 nm. Assuming that the fibrils are lying flat on the surface, as observed in the AFM image, this would imply a seven-layer HI fibrillar coverage using the fibrillar size as 10 nm.[6]

The AFM results correlate with the IR spectra suggesting that the regions of blue colouration are areas of concentrated HI fibrils. It is therefore not surprising that the reflection anisotropy spectroscopy (RAS) was struggling to measure these regions because of the thickness of the adsorbed layer and consequent reduction in reflectivity. Inhomogeneous coverage is likely due to the auto-catalytic effect, as previously described by Hammarstrom,[7,8] and for surface-sensitive techniques like RAS homogeneous and reflective surfaces are optimal, therefore a reproducible and reliable surface methodology is required. It is unknown as to why the high concentrations of fibrillar HI structures result in a visibly blue colouration, however there have been reports of a blue coloured fluorescence effect, which is further discussed and investigated in Chapter 7.

3.3.2. The impact of headspace

The blue colouration, which was determined to be insulin fibrils, appeared different for samples within the same batch, however the surfaces prior to incubation did not visually or spectrally vary. The potential root cause of the irreproducibility was due to the sample vessels, which were piranha cleaned glass jars, since it was not possible to control the size of the Si samples when cracking the wafers these jars were of varying sizes with differing headspace. The varying air:water interfaces for each jar, results in independent fibrillation kinetics despite similar treatment and incubation within the same environment.[9,10] The differing fibrillation kinetics were experimentally observed as the incubated HI suspensions varied in appearance ranging from; clear and colourless, to cloudy with varying concentrations of white precipitate. The presence of the white precipitate was indicative of mature fibrils, which are insoluble and fall out of solution.[11–13]

Firstly, the incubation vessels were changed rather than individual glass jars the surfaces were placed together into a large glass crystallising dish which contained an entire sample set treated under the same conditions. The purpose for incubating all the samples together was to ensure the same air:water interface, thereby eliminating any deviations attributed to the incubation vessel. This did not solve the issue as despite being in the same incubation vessel some samples still displayed the same blue colouration, therefore the cause of irreproducibility was more complicated than the incubation vessel or the air:water interface.

Secondly the piranha-cleaned glass surfaces were also of concern as subtle differences in surface chemistry may arise due to variations in the piranha-cleaning process as a result of its synthesis, which may affect the availability of insulin to adsorb to the substrate and thus vary HI concentration in suspension. The Eppendorf lo-bind tubes (2 mL) were utilised for future work, as these satisfied the requirements; commercially available, chemically and temperature compatible, limited protein adsorption and all the same size. However, the low volumes meant that incubation with large substrates like silicon could no longer be incubated *in situ*.

3.3.3. Fibrillation conditions

The insulin preparations in Chapter 2, were designed in order that fibrillar structures were present on the functionalised silicon surface and therefore an extreme fibrillation methodology was utilised to ensure the sigmoidal curve attained saturation phase. To promote protein fibrillation a common methodology is to denature the protein, which is when proteins lose their secondary, tertiary and quaternary structure, through disruption of the intramolecular forces.[14,15] Denaturation has previously been exploited in amyloid research, as partial unfolding accelerates the amyloid-like fibrillation process, resulting in more favourable experimental conditions for which to measure fibrillation.[16–20] As previously stated in Chapter 1 (1.3.1. What is protein fibrillation?, page 40), several experimental conditions have been used to denature proteins, such as; temperature,[17] agitation,[21,22] pH,[23,24] concentrations,[25] and denaturation additives.[18,26–28]

The main issues associated with denaturation is that the extreme conditions no longer correlate to physiological and these variables are often difficult to control leading to increased deviations in fibrillation propensity. As this work investigates insulin adsorption and fibrillation at interfaces using an ensemble of spectroscopic techniques, it was therefore imperative that the process occurred on a convenient timeframe. A convenient timeframe is defined as one in which; samples remained stable between measurements, incubation time was minimised to allow for regular repeat batches, and any *in situ* analysis had to be captured within the convenient timeframe. A standardised protocol is needed for reproducible and reliable samples of HI, to control fibrillation so that the same conditions could be analysed in each spectroscopic technique. Consideration was given to minimise the impact associated with any time sensitive components, therefore; time, temperature, pH, protein concentration and preparation methodology is discussed here. Agitation of the HI suspensions was deemed unsuitable since it has been reported that the air-water interface can induce nucleation,[29] through the incorporation of air bubbles into the suspension therefore leading to irreproducibility across samples.[30,31]

Temperature was interlinked with time, as a variable which affected the fibrillation kinetics, for example; increasing temperature resulted in a shortened

timeframe for fibrillation. The work in Chapter 2 used an elevated temperature (~75°C), which were far from physiological, to accelerate the surface kinetics; adsorption, diffusion and fibrillation.[32] High temperatures have been shown to increase fibrillation through denaturation of the protein[17,33], however it has been reported that temperatures above 50°C for HI results in irreversible denaturation attributed to the destruction of disulfide bridges.[34–36] A minimum temperature to reduce any impact from seasonal fluctuations within the laboratory resulted in an effective room temperature (~21°C). This work designated two temperatures to be used to investigate the fibrillation pathway; effective room temperature (~21°C) and physiological (~37°C) which increases the fibrillation timescales however avoids the issues associated with temperature induced denaturation.[22]

The initial premise for this investigation was to investigate two pH conditions; physiological similar and one which promoted the HI fibrillation process. Neutral buffer conditions were made by dissolution of a PBS tablet, resulting in buffer similarities across batches. The acidic conditions, which promote fibrillation, were initially generated with citrate-phosphate buffer at pH 2 to inhibit the hexameric oligomerisation.[37] The issue with this buffer is the potential variability in monomeric / dimeric distribution, other studies have shown that HI suspended in a 20% acetic acid buffer generates a monomeric insulin preference.[38–40] In all future work, HI was suspended in acidic (pH 2) buffer (20% acetic acid and 137.9 mM sodium chloride) as these conditions were shown to promote the HI monomeric state.[41]

In addition to the pH buffer conditions, Jorgensen *et al*[42] showed that HI concentration was of importance as this was correlated with oligomeric state thus fibrillation kinetics. Low concentrations within 20% acetic acid buffer result in the preferred monomeric state but with reduced fibrillation kinetics, whereas too high concentrations increase fibrillation kinetics through the promotion of higher order species.[43] This work utilised a concentration of ~10 mg/mL, as this typically achieved fibrillation within the measurable timeframe requirements and within the detection limits for the various spectroscopic instrumentation.

The experimental variables; time, pH, temperature and HI concentration were all controlled in addition to the incubation vessels, to reduce the variability observed in Chapter 2. These controls were all designed to ensure that the HI achieves one oligomeric state so that the fibrillation process was reliable and reproducible, however this assumes that the HI is monomerised when suspended.

3.3.4. Pre-treatment of proteins for an aggregate-free suspension

The HI fibrillation pathway (Figure 8) consists of nucleation events, termed primary or secondary as illustrated in Chapter 1 (1.3.1. What is protein fibrillation?, page 40), which are important for the fibrillation kinetics. Any aggregate in an insulin suspension has the potential to act as a secondary nucleation site, thereby affecting the fibrillation pathway through a seeded-growth mechanism.[44–47] Sample irreproducibility arises from the variability in HI fibrillation pathway associated with the seeded-growth mechanisms,[48–50] therefore an aggregate-free suspension is necessary to reduce fibrillation deviations across samples. The effects of variable fibrillation were evidenced in the RAS as shown in Chapter 2 and this correlated with the observation that vials of equally prepared but independently incubated HI suspensions, exhibited varying degrees of fibrillation associated with a lack of insulin pre-treatment. Proteins and peptides such as insulin[51] and amyloid-β peptide (Aβ) readily aggregate,[52] it is therefore important that a pre-treatment methodology is used so that the measured fibrillation pathways are not affected by aggregate attributed seeded-growth mechanisms. Pre-treatment of insulin by physical and chemical processes, such as; syringe-filtration have been reported to remove insulin's seeding capability[53] and reaction with HFIP has been shown to disaggregate Aβ.[54]

One method for removing aggregates present within insulin suspensions is by syringe-filtration, which physically removes aggregates larger than the pore size of the filter membrane. It was also important that the integrity of the suspensions was not affected, therefore a sterile system was utilised to avoid any possible introduction of unforeseen contaminants. The conditions studied in this work dictated the specific filter membrane necessary, as it had to be operable in both

acidic and neutral pH conditions.[55] The best membrane available was polyethersulfone (PES) and the structure is shown in Figure 39.

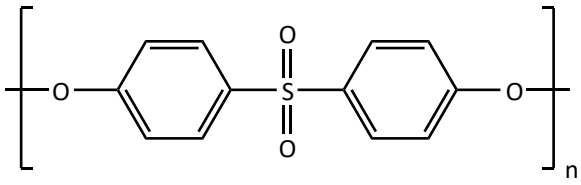

Figure 39: Chemical structure of polyethersulfone (PES).

Treatment of protein suspensions by syringe-filtration technique is a common practice in biochemistry and has been used previously in a variety of insulin studies.[56,57] The disadvantage of this technique is the limited volumes that the system can process at any one time, therefore a disaggregation process for larger volumes at the same time is desirable.

Chemical treatment for the disaggregation of proteins can be performed in bulk using volatile chemicals such as HFIP and trifluoroacetic acid (TFA),[58,59] where HFIP was used here with its structure shown in Figure 40.

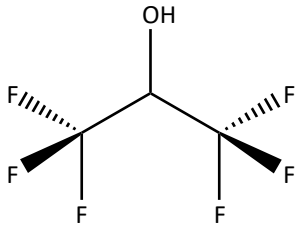

Figure 40: Chemical structure for hexafluoroisopropanol (HFIP).

HFIP was chosen for this work as it is a widely used biochemical technique to standardise solutions[60] specifically in the treatment of α-synuclein (αS).[61,62] These chemicals are used to monomerise the protein through removal of any aggregate states present[63] with the mechanism believed to be that HFIP displaces the water molecules surrounding the protein, which reduces the preferential aggregation because of the diminished hydrophobic effect.[64] This technique works in native proteins with predominantly α-helical secondary structures[65] and has been shown to maintain stability when stored in dilute HFIP for long durations,[66] however there have

been reports that the protofibrillar structure differs from native fibrillation pathways.[67]

3.3.4.1. Protein pre-treatment for reduction of suspension aggregates

Particle size analysis as measured by DLS was used to investigate the effectiveness of HI pre-treatment for an aggregate-free suspension, with untreated or treated HI using physical or chemical techniques. HI was suspended in the pH 2 buffer (20% acetic acid and 139.7 mM sodium chloride) as shown in Figure 41, where the untreated HI suspension (red) and treated HI using syringe-filtration (blue) or HFIP (green).

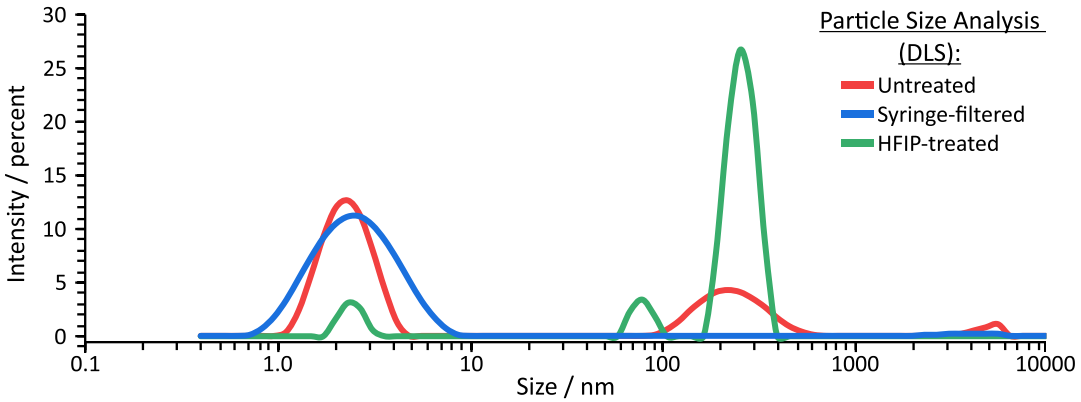

Figure 41: Dynamic Light Scattering (DLS) traces for human insulin (HI, 10 mg/mL) suspended in a pH 2 buffer (20% acetic acid and 139.7 mM sodium chloride) showing the effectiveness of pre-treatment in reducing protein aggregates; (red) untreated, (blue) syringe-filtered and (green) HFIP-treated.

The DLS results for the HI suspensions (Figure 41) show a distinct difference between the three treatment methods, with results ranging across four size distributions; ~0.7 – 10 nm, ~60 – 100 nm, ~100 – 700 nm and ~3000 – 6000 nm. There are three discrete size regions for the untreated HI suspension (red); ~0.8 – 5 nm, ~75 – 700 nm and ~2500 – 6500 nm, which demonstrates that suspending HI without pre-treatment induces aggregation components. Treatment of the HI suspensions has varying results, with the syringe-filtered HI suspension (blue) reducing the measured size regions to one polydisperse peak, ~0.6 – 10 nm centred at ~2.5 nm, whereas HFIP (green) resulted in three distinct size regions with a higher distribution towards the larger species; ~1.5 – 4 nm, ~50 – 110 nm, and ~150 – 400 nm.

In all three treatment methods the DLS shows a signal intensity between 1 and 10 nm, which is consistent with an amalgamation of HI oligomeric states. The oligomeric states of HI range in size, from the small monomeric (2.5 x 2 x 3 nm)[68] to the larger hexameric (3.5 x 5 nm).[37] The untreated and syringe-filtered results have peak maxima at ~2.3 and ~2.5 nm respectively, which implies a majority of monomeric states whereas the HFIP-treated peak is skewed towards a higher size distribution. The polydispersity of the peaks is associated with the DLS methodology, which interpolates particle size through the assumption that particles are spherical[69] therefore a HI monomer species can range in size from 2 to 3 nm depending on its orientation in the media at the point of measurement.

Overall, the DLS results demonstrate that the HI suspensions must first be pre-treated to remove any aggregates, which have the potential to provide a seeding-like fibrillation process thus affecting reproducibility between HI samples. The significant size distributions between the untreated and HFIP-treated are of concern because the large size populations will increase the likelihood of differing aggregates, thus reducing the reproducibility of the insulin suspensions due to aggregate induced nucleation. The DLS results (Figure 41) show that for HFIP treatment there is a population of large species, which although HFIP is a standard technique monomerising Aβ peptides[66] it does not work for HI. As shown by the DLS results (Figure 41) syringe filtration treatment was the most effective in providing an aggregate-free suspension, reducing the potential for cross-seeding events.[70] As a consequence of the effectiveness of syringe filtration, all the buffers were also syringe-filtered to remove any potential aggregates or physical contaminants associated with the buffer components during preparation.

3.3.5. Optimised human insulin protein suspension protocol

The results obtained within this chapter show the importance of handling HI suspensions correctly to avoid any sample irreproducibility issues. These issues were attributed to aggregate formation and general protein denaturation, therefore pre-treatment and reduced denaturation conditions were critical.

3.3.5.1. Preparation standards

Throughout this work, all reagents were of analytical grade or higher, and all preparation was carried out in a designated fume hood which was cleaned with ethanol and anti-bacterial cleaner daily and prior to sample preparation or analysis. The reusable equipment and glassware to be used were first cleaned in either an acidic Piranha solution (30% hydrogen peroxide and 70% sulfuric acid, 30 minutes) to remove any hard deposits or in a basic 10% Decon 90 (overnight), rinsed with water (18.2 MΩ cm^{-1}) and then dried in an oven. Any single-use equipment, such as; syringes, pipette tips or Eppendorf tubes, were first rinsed with the relevant buffer or reagent immediately prior to contact with the HI. All single-use equipment, where possible, was graded lo-bind to enable maximum recovery of HI. In general, there was an overall motivation to limit manual handing of HI for reduction of any potential influences upon the protein.

3.3.5.2. Buffer preparation

The buffers for this work were optimised for the acidic and neutral pH conditions investigated, as previously discussed (3.3.3. Fibrillation conditions, page 108). All buffers were prepared fresh on the same day as the associated HI suspensions, where any excess volume was frozen for use as; spectroscopic blanks or for rinsing at a later date.

The acidic (pH 2) buffer, 20% acetic acid and sodium chloride (137.9 mM), was prepared by dissolution of the sodium chloride in acetic acid and sonicated for 30 minutes. For the neutral (pH 7) buffer, a phosphate-buffer saline (PBS, 0.01 M) tablet was dissolved in water (100 mL, 18.2 MΩ cm^{-1}) and sonicated for 30 minutes.

After sonication, the solutions were briefly vortexed to ensure complete suspension and homogeneity with the pH of each buffer checked. The buffers were then syringe filtered (0.22 µm, PES) into piranha cleaned Duran vessels, and aliquots taken for the; insulin suspensions, spectroscopic blanks and rinsing volumes.

3.3.5.3. Human insulin suspensions

Following the confirmation by DLS (3.3.4.1. Protein pre-treatment for reduction of suspension aggregates, page 112), that pre-treatment of HI by syringe

filtration was essential to ensure an aggregate-free suspension. Prior to filtration of the HI suspensions, the clean syringe filters (0.22 µm, PES) were first wetted by rinsing with the relevant filtered pH solution. For pH 2 a small aliquot of buffer (20% acetic acid and sodium chloride 137.9 mM), whereas for pH 7 an aliquot of hydrochloric acid (0.1 M) was used.

For the acidic insulin suspension, HI (10 mg/mL) was suspended in the filtered pH 2 buffer (20% acetic acid and 137.9 mM sodium chloride) in a lo-bind Eppendorf tube (2 mL) which was briefly vortexed to ensure complete dissolution and then immediately syringe-filtered through the pre-wetted filter (0.22 µm PES). To maximise insulin recovery, the used filter was then flushed with the minimum volume of buffer, back into HI suspension. Conversely for the neutral insulin suspension, HI (10 mg/mL) was suspended in the minimum volume of hydrochloric acid (0.1 M), which was briefly vortexed, and immediately syringe-filtered through the pre-wetted filter (0.22 µm PES). Similarly, to the acidic suspension methodology, the filter was flushed through with dilute hydrochloric acid to ensure maximum insulin recovery. The suspension was back titrated to pH 7 by addition of filtered sodium hydroxide (0.1 M), then filtered pH 7 buffer (0.01 M PBS) added to attain the appropriate HI concentration (10 mg/mL). Aliquots of both suspensions were acquired, with the concentration checked by ultraviolet-visible (UV-Vis) spectroscopy at 280 nm.

3.3.5.4. Incubation of the human insulin samples

The various samples of HI suspensions in lo-bind Eppendorf tubes (2 mL) were loaded into a tube rack and incubated in a designated incubator at either room (~21°C) or elevated (~37°C) temperature. This incubator only held the HI samples, therefore reducing any uncontrolled variability in temperature from the opening and closing of the doors.

3.3.5.5. Generalised sampling methodology

Aliquots of the HI samples were acquired at specific time points as a function of incubation duration, the entire tube rack was removed from the incubator and each tube briefly vortexed to ensure homogeneity. A fresh lo-bind pipette tip (epT.I.P.S., Eppendorf) was used per sample with aliquots taken from the centre

of the incubated microcentrifuge tube into a new tube, then the fibrillation tubes were rapidly returned to the incubator. The aliquoted samples were flash frozen (using liquid nitrogen) prior to storage in a -77°C freezer, for later analysis. This was to ensure the integrity of the samples were not subjected to multiple freeze-thaw cycles which are known to affect fibrillation events.[71–75]

3.4. Conclusion

This work has shown that a standardised protocol for preparing HI suspensions is critical for reproducible and reliable samples. The distinct blue coloured regions that correlated with sample variability, contained high coverages of fibrillar HI as the AFM topography showed thick layers (~68 nm) of fibrillar structures with defined β-sheet and α-helical features in the Amide I (1700 – 1600 cm^{-1}) region as ascertained by IR microscopy.

Pre-treatment of the HI suspensions was necessary, as the DLS results showed aggregates present within the untreated suspensions. The best pre-treatment method was syringe-filtration, as DLS showed no higher order species, therefore providing an aggregate-free suspension. The presence of aggregates increases the sample irreproducibility due to seeded-growth mechanisms.

The optimised procedure for handling HI fibrillation was designed to reduce sample variability, previously attributed to denaturation processes such as high temperature incubation. This optimised methodology is therefore utilised in all subsequent chapters.

Bibliography

1. Mauri, S., Volk, M., Byard, S., Berchtold, H. & Arnolds, H. Stabilization of Insulin by Adsorption on a Hydrophobic Silane Self-Assembled Monolayer. *Langmuir* **31**, 8892–8900 (2015).

2. Susarrey-Arce, A. *et al.* Pattern Formation by Staphylococcus epidermidis via Droplet Evaporation on Micropillars Arrays at a Surface. *Langmuir* **32**, 7159–7169 (2016).

3. Barth, A. Infrared spectroscopy of proteins. *Biochim. Biophys. Acta - Bioenerg.* **1767**, 1073–1101 (2007).

4. Amenabar, I. *et al.* Structural analysis and mapping of individual protein complexes by infrared nanospectroscopy. *Nat. Commun.* **4**, 2890 (2013).

5. Waeytens, J. *et al.* Probing amyloid fibril secondary structures by infrared nanospectroscopy: experimental and theoretical considerations. *Analyst* **146**, 132–145 (2021).

6. Jimenez, J. L. *et al.* The protofilament structure of insulin amyloid fibrils. *Proc. Natl. Acad. Sci.* **99**, 9196–9201 (2002).

7. Hammarström, P. *et al.* A catalytic surface for amyloid fibril formation. *J. Phys. Conf. Ser.* **100**, 052039 (2008).

8. Hammarström, P. *et al.* An Auto-Catalytic Surface for Conformational Replication of Amyloid Fibrils—Genesis of an Amyloid World? *Orig. Life Evol. Biosph.* **41**, 373–383 (2011).

9. Mauri, S., Weidner, T. & Arnolds, H. The structure of insulin at the air/water interface: monomers or dimers? *Phys. Chem. Chem. Phys.* **16**, 26722–26724 (2014).

10. Jayamani, J. & Shanmugam, G. Diameter of the vial plays a crucial role in the amyloid fibril formation: Role of interface area between hydrophilic-hydrophobic surfaces. *Int. J. Biol. Macromol.* **101**, 290–298 (2017).

11. Rambaran, R. N. & Serpell, L. C. Amyloid fibrils. *Prion* **2**, 112–117 (2008).

12. L. Lyubchenko, Y. Amyloid misfolding, aggregation, and the early onset of protein deposition diseases: insights from AFM experiments and computational analyses. *AIMS Mol. Sci.* **2**, 190–210 (2015).

13. Chuang, E., Hori, A. M., Hesketh, C. D. & Shorter, J. Amyloid assembly and disassembly. *J. Cell Sci.* **131**, jcs189928 (2018).

14. Neurath, H., Greenstein, J. P., Putnam, F. W. & Erickson, J. A. The Chemistry of Protein Denaturation. *Chem. Rev.* **34**, 157–265 (1944).

15. Buxbaum, E. *Fundamentals of Protein Structure and Function*. *Fundamentals of Protein Structure and Function, Second Edition* (Springer International Publishing, 2015). doi:10.1007/978-3-319-19920-7

16. Sharp, J. S., Forrest, J. a. & Jones, R. a L. Surface denaturation and amyloid fibril formation of insulin at model lipid-water interfaces. *Biochemistry* **41**, 15810–15819 (2002).

17. Arora, A., Ha, C. & Park, C. B. Insulin amyloid fibrillation at above 100°C: New insights into protein folding under extreme temperatures. *Protein Sci.* **13**, 2429–2436 (2004).

18. Vernaglia, B. A., Huang, J. & Clark, E. D. Guanidine hydrochloride can induce amyloid fibril formation from hen egg-white lysozyme. *Biomacromolecules* **5**, 1362–1370 (2004).

19. Muzaffar, M. & Ahmad, A. The mechanism of enhanced insulin amyloid fibril formation by NaCl is better explained by a conformational change model. *PLoS One* **6**, (2011).

20. Goto, Y., Adachi, M., Muta, H. & So, M. Salt-induced formations of partially folded intermediates and amyloid fibrils suggests a common underlying mechanism. *Biophys. Rev.* **10**, 493–502 (2018).

21. DHANAPATI, N., ISHIOROSHI, M., YOSHIDA, I. & SAMEJIMA, K. Effects of Mechanical Agitation, Heating and pH on the Structure of Bovine Alpha Lactalbumin. *Nihon Chikusan Gakkaiho* **68**, 545–554 (1997).

22. Lee, C., Nayak, A., Sethuraman, A., Belfort, G. & McRae, G. J. A Three-Stage Kinetic Model of Amyloid Fibrillation. *Biophys. J.* **92**, 3448–3458 (2007).

23. Jeppesen, M. D., Westh, P. & Otzen, D. E. The role of protonation in protein fibrillation. *FEBS Lett.* **584**, 780–784 (2010).

24. Bernson, D. *et al.* Amyloid formation of bovine insulin is retarded in moderately acidic pH and by addition of short-chain alcohols. *Eur. Biophys. J.* **49**, 145–153 (2020).

25. Librizzi, F. & Rischel, C. The kinetic behavior of insulin fibrillation is determined by heterogeneous nucleation pathways. *Protein Sci.* (2005). doi:10.1110/ps.051692305

26. Nielsen, L. *et al.* Effect of Environmental Factors on the Kinetics of Insulin Fibril Formation: Elucidation of the

Molecular Mechanism †. *Biochemistry* **40**, 6036–6046 (2001).

27. Ahmad, A., Millett, I. S., Doniach, S., Uversky, V. N. & Fink, A. L. Stimulation of Insulin Fibrillation by Urea-induced Intermediates. *J. Biol. Chem.* **279**, 14999–15013 (2004).

28. Kishore, D., Kundu, S. & Kayastha, A. M. Thermal, Chemical and pH Induced Denaturation of a Multimeric β-Galactosidase Reveals Multiple Unfolding Pathways. *PLoS One* **7**, (2012).

29. Sluzky, V., Tamada, J. A., Klibanov, A. M. & Langer, R. Kinetics of insulin aggregation in aqueous solutions upon agitation in the presence of hydrophobic surfaces. *Proc. Natl. Acad. Sci. U. S. A.* **88**, 9377–9381 (1991).

30. Nakajima, K. *et al.* Nucleus factory on cavitation bubble for amyloid β fibril. *Sci. Rep.* **6**, 22015 (2016).

31. Nakajima, K. *et al.* Drastic acceleration of fibrillation of insulin by transient cavitation bubble. *Ultrason. Sonochem.* **36**, 206–211 (2017).

32. Hedegaard, S. F., Cárdenas, M., Barker, R., Jorgensen, L. & Van De Weert, M. Lipidation Effect on Surface Adsorption and Associated Fibrillation of the Model Protein Insulin. *Langmuir* **32**, 7241–7249 (2016).

33. Borzova, V. A. *et al.* Kinetics of Thermal Denaturation and Aggregation of Bovine Serum Albumin. *PLoS One* **11**, e0153495 (2016).

34. Volkin, D. B. & Klibanov, A. M. Thermal destruction processes in proteins involving cystine residues. *J. Biol. Chem.* **262**, 2945–2950 (1987).

35. Huus, K., Havelund, S., Olsen, H. B., van de Weert, M. & Frokjaer, S. Thermal Dissociation and Unfolding of Insulin. *Biochemistry* **44**, 11171–11177 (2005).

36. Jiang, C. & Chang, J.-Y. Unfolding and breakdown of insulin in the presence of endogenous thiols. *FEBS Lett.* **579**, 3927–3931 (2005).

37. Pohl, R. *et al.* Ultra-rapid absorption of recombinant human insulin induced by zinc chelation and surface charge masking. *J. Diabetes Sci. Technol.* **6**, 755–763 (2012).

38. Nielsen, L., Frokjaer, S., Brange, J., Uversky, V. N. & Fink, A. L. Probing the mechanism of insulin fibril formation with insulin mutants. *Biochemistry* **40**, 8397–8409 (2001).

39. Uversky, V. N. *et al.* Prediction of the association state of insulin using spectral parameters. *J. Pharm. Sci.* **92**, 847–858 (2003).

40. Ahmad, A., Uversky, V. N., Hong, D. & Fink, A. L. Early Events in the Fibrillation of Monomeric Insulin. *J. Biol. Chem.* **280**, 42669–42675 (2005).

41. Whittingham, J. L. *et al.* Insulin at pH 2: Structural Analysis of the Conditions Promoting Insulin Fibre Formation. *J. Mol. Biol.* **318**, 479–490 (2002).

42. Jorgensen, L. *et al.* Adsorption of insulin with varying self-association profiles to a solid Teflon surface—Influence on protein structure, fibrillation tendency and thermal stability. *Eur. J. Pharm. Sci.* **42**, 509–516 (2011).

43. Ahmad, A., Uversky, V. N., Hong, D. & Fink, A. L. Early Events in the Fibrillation of Monomeric Insulin. *J. Biol. Chem.* **280**, 42669–42675 (2005).

44. Kumar, S. *et al.* Extracellular phosphorylation of the amyloid β-peptide promotes formation of toxic aggregates during the pathogenesis of Alzheimer's disease. *EMBO J.* **30**, 2255–2265 (2011).

45. Surmacz-Chwedoruk, W., Nieznańska, H., Wójcik, S. & Dzwolak, W. Cross-Seeding of Fibrils from Two Types of Insulin Induces New Amyloid Strains. *Biochemistry* **51**, 9460–9469 (2012).

46. Morales, R., Moreno-Gonzalez, I. & Soto, C. Cross-Seeding of Misfolded Proteins: Implications for Etiology and Pathogenesis of Protein Misfolding Diseases. *PLoS Pathog.* **9**, e1003537 (2013).

47. Sulatskaya, A. I. *et al.* Investigation of the kinetics of insulin amyloid fibrils formation. *Cell tissue biol.* **8**, 186–191 (2014).

48. Petkova, A. T. Self-Propagating, Molecular-Level Polymorphism in Alzheimer's -Amyloid Fibrils. *Science* **307**, 262–265 (2005).

49. Andersen, C. B. *et al.* Branching in amyloid fibril growth. *Biophys. J.* **96**, 1529–1536 (2009).

50. Paravastu, A. K., Qahwash, I., Leapman, R. D., Meredith, S. C. & Tycko, R. Seeded growth of -amyloid fibrils from Alzheimer's brain-derived fibrils produces a distinct fibril structure. *Proc. Natl. Acad. Sci.* **106**, 7443–7448 (2009).

51. Li, S. & Leblanc, R. M. Aggregation of Insulin at the Interface. *J. Phys. Chem. B* **118**, 1181–1188 (2014).

52. Salomon, A. R., Marcinowski, K. J., Friedland, R. P. & Zagorski, M. G. Nicotine Inhibits Amyloid Formation by the β-Peptide. *Biochemistry* **35**, 13568–13578 (1996).

53. Heldt, C. L. *et al.* Isolating Toxic Insulin Amyloid Reactive Species that Lack β-Sheets and Have Wide pH Stability. *Biophys. J.* **100**, 2792–2800 (2011).

54. Zagorski, M. G. *et al.* [13] Methodological and chemical factors affecting amyloid β peptide amyloidogenicity. in *Methods in Enzymology* 189–204 (1999). doi:10.1016/S0076-6879(99)09015-1

55. Millipore. Chemical Compatibility of Filter Components Compatibility of materials used in the construction of EMD Millipore products. *Manual* **26**, 1791–1796 (2015).

56. Sneideris, T. *et al.* pH-Driven Polymorphism of Insulin Amyloid-Like Fibrils. *PLoS One* **10**, e0136602 (2015).

57. Frankær, C. G. *et al.* Insulin fibrillation: The influence and coordination of Zn 2+. *J. Struct. Biol.* **199**, 27–38 (2017).

58. Chen, S. Solubilization and disaggregation of polyglutamine peptides. *Protein Sci.* **10**, 887–891 (2001).

59. Burra, G. & Thakur, A. K. Anhydrous trifluoroacetic acid pretreatment converts insoluble polyglutamine peptides to soluble monomers. *Data Br.* **5**, 1066–1071 (2015).

60. Broersen, K. *et al.* A standardized and biocompatible preparation of aggregate-free amyloid beta peptide for biophysical and biological studies of Alzheimers disease. *Protein Eng. Des. Sel.* **24**, 743–750 (2011).

61. Sung, Y.-H. & Eliezer, D. Structure and dynamics of the extended-helix state of alpha-synuclein: Intrinsic lability of the linker region. *Protein Sci.* **27**, 1314–1324 (2018).

62. Paul, A. *et al.* Novel Mannitol-Based Small Molecules for Inhibiting Aggregation of α-Synuclein Amyloids in Parkinson's Disease. *Front. Mol. Biosci.* **6**, (2019).

63. Hirota, N., Goto, Y. & Mizuno, K. Cooperative α-helix formation of β-lactoglobulin and melittin induced by hexafluoroisopropanol. *Protein Sci.* **6**, 416–421 (1997).

64. Roccatano, D., Fioroni, M., Zacharias, M. & Colombo, G. Effect of hexafluoroisopropanol alcohol on the structure of melittin: A molecular dynamics simulation study. *Protein Sci.* **14**, 2582–2589 (2005).

65. Barrow, C. J., Yasuda, A., Kenny, P. T. M. & Zagorski, M. Solution conformations and aggregational properties of synthetic amyloid b-peptides of Alzheimer's disease. *J. Mol. Biol.* **225**, 1075–1093 (1992).

66. Zhang-Haagen, B. *et al.* Monomeric Amyloid Beta Peptide in Hexafluoroisopropanol Detected by Small Angle Neutron Scattering. *PLoS One* **11**, e0150267 (2016).

67. Nichols, M. R. *et al.* Amyloid-β Protofibrils Differ from Amyloid-β Aggregates Induced in Dilute Hexafluoroisopropanol in Stability and Morphology. *J. Biol. Chem.* **280**, 2471–2480 (2005).

68. Brange, J., Owens, D. R., Kang, S. & Volund, A. Monomeric Insulins and Their Experimental and Clinical Implications. *Diabetes Care* **13**, 923–954 (1990).

69. Berne, B. J. & Pecora, R. *Dynamic light scattering : with applications to chemistry, biology, and physics.* (Dover Publications, 2000).

70. Ren, B. *et al.* Fundamentals of cross-seeding of amyloid proteins: an introduction. *J. Mater. Chem. B* **7**, 7267–7282 (2019).

71. Schoonenboom, N. S. M. *et al.* Effects of Processing and Storage Conditions on Amyloid β (1–42) and Tau Concentrations in Cerebrospinal Fluid: Implications for Use in Clinical Practice. *Clin. Chem.* **51**, 189–195 (2005).

72. Sigurdsson, E. M., Calero, M. & Gasset, M. *Amyloid proteins. methods and protocols.* (Humana Press, 2012).

73. Domigan, L. J., Healy, J. P., Meade, S. J., Blaikie, R. J. & Gerrard, J. A. Controlling the dimensions of amyloid fibrils: Toward homogenous components for bionanotechnology. *Biopolymers* **97**, 123–133 (2012).

74. Castillo-León, J. & Svendsen, W. E. *Micro and Nanofabrication Using Self-Assembled Biological Nanostructures.* (William Andrew Publishing, 2015).

75. Liu, H.-C., Chiu, M.-J., Lin, C.-H. & Yang, S.-Y. Stability of Plasma Amyloid-β 1–40, Amyloid-β 1–42, and Total Tau Protein over Repeated Freeze/Thaw Cycles. *Dement. Geriatr. Cogn. Dis. Extra* **10**, 46–55 (2020).

Chapter 4: The Co-incubation Effect of Functionalised Mesoporous Silica Microparticles with Human Insulin, on Amyloid-like Fibrillation

4.1. Introduction

This aim of this chapter is to investigate fibrillation events *in situ* with modified (functionalised) hydrophobic silica microparticles, utilising conventional bulk solution spectroscopic techniques. The effect of varying hydrophobic functionalisation on the silica surfaces will be studied to observe if there are any kinetic or structural differences on the typical human insulin (HI) amyloid-like fibrillation pathway.

Hydrophobic surfaces are considered to be 'bad' for a protein interface since they are known to cause the protein of interest to adsorb and aggregate on the surface, thus leading to fibrillation events.[1,2] There has been limited research on how the extent of hydrophobicity affects and induces amyloid fibrillation, therefore a large variety of hydrophobic surfaces should ideally be studied to investigate the interactions between the protein and the surface type. There have already been studies of protein fibrillation at the solid-liquid interface, such as the work by Sluzky *et al*[3]which showed insulin aggregation in the presence of a hydrophobic surface, however the interfaces within these studies are often stationary with the surface inserted into the suspension or just the walls of the vessel itself. Characterisation of the hydrophobic interface effect is usually separated into the solution and surface studies, such as with Nayak *et al*[2] who showed that HI fibrillation increases in the presence of hydrophobic surfaces by thioflavin-T (ThT) assay of aliquots from the incubated HI solution with the surfaces later analysed by atomic force microscopy (AFM). Conversely Ballet *et al*[4] showed HI nucleation and fibrillation at pH 7 occurred on the hydrophobic surface by incubating within the 96-well microplate, which was then measured by ThT assay. Whereas Moores *et al*[5] showed hydrophobic surfaces promoted the formation of spherical amorphous clusters of amyloid-β (Aβ) by AFM. These studies recognise the importance of surfaces, which can promote fibrillation through the autocatalytic effect into bulk suspension,[6,7] however do not investigate the species simultaneously. The effect of

mobile hydrophobic surfaces in the solution on the HI fibrillation pathway will be investigated and provide information on HI adsorption and fibrillation.

Chapter 2 showed that HI fibrillation occurred on a hydrophobically functionalised silicon surface using Reflection Anisotropy Spectroscopy (RAS), which is a surface sensitive spectroscopic technique. The disadvantage of RAS and other surface sensitive spectroscopies is that they only probe the immediate surface. Protein adsorption and fibrillation can occur on the surface, however when an active fibril leaves the surface and goes into bulk solution then further nucleation or fibrillation can occur through seeded-growth mechanisms within the suspension, which these surface sensitive spectroscopies cannot probe. These surface techniques cannot quantify the changes occurring within the bulk suspension as a result of the functionalised surface interface, therefore a different methodology which utilises bulk suspension and functionalised surfaces is necessary. Silica microparticles which have a high surface area and the ability to be functionalised, can be suspended in the solution, enabling investigation of the bulk amyloid-like fibrillation pathway by solution-based spectroscopic techniques.

To investigate the effect of hydrophobic microscopic particles on fibrillation, this chapter uses four types of mesoporous silica microparticles, which have various hydrophobic modifications ranging from bare silica through to large alkyl-chain functionalised surfaces. These functionalised interfaces are designed to disturb HI amyloid-like fibrillation by means of hydrophobic interactions, whilst the mesoporous nature of the particles is to allow for increased protein adsorption events. This chapter will study the effect of the hydrophobic functionalised microparticles on the HI amyloid-like fibrillation pathway by measuring and observing any differences in the fibrillation kinetics and the resultant fibrillar structures.

4.1.1. What are silica microparticles?

The silica microparticles studied here (~5 µm diameter), have been kindly provided by Professor P. Myers, Department of Chemistry (University of Liverpool), and are typically used in High Performance Liquid Chromatography (HPLC) systems,

which separates compounds within an analyte by polarity. The nature of these microparticles are beneficial due to their increased surface area (220 m^2/g, Spherisorb),[8] which is ideal for protein adsorption,[9] whilst the mesoporous design allows for small particles to pass through their "honeycomb-like" architecture.[10] The mesoporous silica microparticles provided have a pore size of 8 nm, which is a similar size to that of a HI monomer (2.5 x 2 x 3 nm) and hexamer (3.5 x 5 nm),[11–13] therefore there is a likelihood that the HI can fit within the pore. Silica nanoparticles have previous been reported to efficiently adsorb protein,[14–16] and functionalisation of such particles have been shown to inhibit α-synuclein fibrillation.[17,18] Protein adsorption to mesoporous silicates have also been reported by Deere *et al*.[19]

The particles studied were functionalised with increasing hydrophobic alkyl chain length from bare silicon (Si), to six carbon (hexyl-functionalised, C_6), through to eighteen (octadecyl functionalised, ODS1 and ODS2), as shown in Figure 42. The ODS2 particles were also end-capped with a trimethyl group, to render the surface non-acidic and non-polar, in addition to preventing degradation of the silicon surface.[20] All four particles have the same 5 µm diameter and silica bulk substrate,[8] which allows for comparison of the effect of only varying the functionalised interface (as shown in Figure S13).

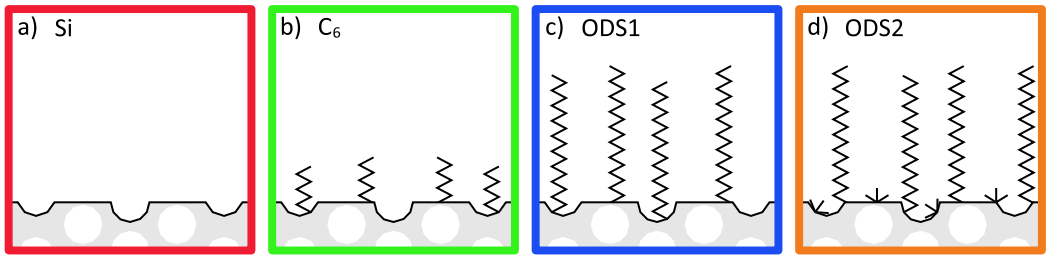

Figure 42: Schematic showing the functionalised mesoporous silica microparticle; (a) non-bonded silica (Si, red), (b) hexyl-functionalised (C_6, green), (c) octadecyl-functionalised (ODS1, blue) and (d) end-capped octadecyl-functionalised (ODS2, orange). The (grey) mesoporous silica substrate is shown with the (black) outermost interface.

As shown in Figure 42, the particles have the same core mesoporous silica substrate architecture which is an important factor for this work as these particles were considered analogous to the functionalised silicon substrate in Chapter 2. The objective for using particles was to be able to spectroscopically characterise the

effect of hydrophobic functionalised interfaces using solution-based methodologies, with the ability to separate the particles from the fibrillar species. It was the concept of particle separation that dictated the particle size; large particles such as polytetrafluoroethylene (PTFE) leads to sedimentation effects[21] whereas small particles like nanoparticles can be incorporated into fibrillation inducing inhibition[22,23] or acceleration.[24] The purpose for the particles in this work are for only the hydrophobic functionalisation to give rise to HI amyloid-like fibrillation effects and not to be directly involved in the fibrillation process. Microparticles were therefore chosen for this work to avoid the fibrillation and instrumentation issues associated with nanoparticles,[25] with systems in place to reduce the effect of sedimentation.[26,27]

4.1.2. Probing the effect of functionalised microparticles on the amyloid-like fibrillation pathway

To investigate how the microparticles influence the amyloid-like fibrillation pathway, requires; the amount of protein adsorbed to the particle, the particles effect on the kinetics and the resultant fibril morphology to be evaluated. Each of these factors are important to consider, in determining whether the fibrillation pathway has been altered.

4.1.2.1. Determination of the amount of human insulin adsorbed to the particle

To evaluate whether hydrophobicity induces HI fibrillation, this chapter will test both the amount of HI adsorbed to the particle and the corresponding secondary structure. Specifically, is the amount of HI adsorbed correlated to the various hydrophobic interfaces and therefore a factor in the propensity for HI adsorption. Determination of the amount of protein adsorbed to the various hydrophobic interfaces, will be both quantitatively and qualitatively assessed.

CHN Elemental Microanalysis

Elemental Microanalysis (CHN) is a highly sensitive but destructive analytical technique that precisely quantifies the relative percentage of Carbon, Hydrogen and Nitrogen within a sample. The purpose for the CHN technique in this investigation is to be able to quantify the amount of protein which can adsorb to the hydrophobically

functionalised mesoporous silica microparticles. Elemental analysis has previously been used in determination of elemental content for nanoparticles,[28] mesoporous silica[29] and protein adsorption studies.[30–32] The disadvantages of this technique is that the sample is entirely combusted, therefore preventing the same sample being utilised for further analysis and any moisture content will lead to miscalculations.

Infrared spectroscopy

This chapter utilises infrared spectroscopy (IR), specifically the mid-IR range (4000 - 400 cm^{-1}) to study protein adsorption to the particle, by probing the Amide I region (1700 - 1600 cm^{-1}). IR is a vibrational spectroscopic technique which probes molecular vibrations, by the analyte absorbing an IR photon, however only certain vibrational modes are IR active. A vibration is IR active when it results in a dipole moment change, such as an asymmetric carbonyl. Furthermore, the greater the polarity, the larger the IR absorption.

IR is advantageous as it is non-destructive, can acquire functional group information rapidly, is able to probe both solids and liquids, and requires low sample quantities. For protein research it also allows marker-free analysis of the system and can resolve secondary structure by analysis of the Amide I (1700 - 1600 cm^{-1}) region.[33] IR does have disadvantages such as; lack of specificity attributed to overlapping absorption peaks, and atmospheric issues since both water and carbon dioxide molecules absorb IR strongly.[34,35] Analysis of the adsorbed protein content by integration of the Amide I band in IR spectroscopy reduces the impact of non-protein contamination, therefore providing complementary information to the CHN analysis.

4.1.2.2. Amyloid-like fibrillation kinetics

The kinetics of the fibrillation pathway can be manipulated using parameters such as; pH, protein concentration, addition of a denaturant, agitation and temperature (1.3.1. What is protein fibrillation?, page 40). Ideally the fibrillation kinetics for the HI suspensions will be similar across both pH conditions so that a complete sigmoidal curve is acquired. A sigmoidal curve is important for studying the fibrillation kinetics as it is used as a reference point for the fibrillation progression. This work studies the effect of pH on the fibrillation kinetics of HI suspensions,

therefore neither pH nor HI concentration can be varied whilst the addition of a denaturant or varying agitation will increase irreproducibility across batches. Temperature is the only variable which can be controlled and be consistent between the two pH conditions studied.

Producing a suitable sigmoidal curve (1.3.1. What is protein fibrillation?, page 40) is difficult as an appropriate number of data points are needed and is complicated as mature fibrils, which form as the fibrillation proceeds, are insoluble and fall out of solution.[36,37] For example fluorescence assays are one method of studying fibrillation kinetics, where the measured fluorescence intensity increases as fibrillation proceeds. Prolonged measurement time after the saturation phase has been achieved can lead to a fluctuation in fluorescence intensity which is associated to the mature fibrils falling out of solution therefore skewing the fluorescence data.[38] Experimentally the issue is to ensure sufficient data points are obtained, so that fibrillation occurs in both pH conditions but that the experimental duration does not exceed the saturation phase for the fastest condition. This investigation uses an elevated temperature of 50°C in order to study both pH 2 and 7 in the same timeframe.

Measuring fibrillation kinetics

A standard methodology used in biochemistry to monitor the formation of amyloid-like fibrils as a function of time, is fluorescence spectroscopy which is further discussed in Chapter 7. Typically, *in vitro* studies utilise a chemical probe, which for amyloid research is an amyloid-specific dye molecule such as; Congo-Red (CR) or Thioflavin-T (ThT), to measure the amount of fibrils present within the sample.

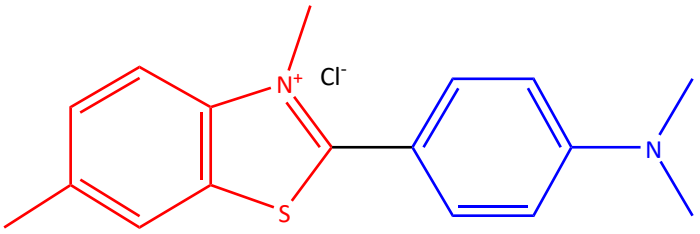

Figure 43: The chemical structure of thioflavin-T (ThT); (red) benzothiazole ring, (black) central carbon bond and (blue) benzamine ring.

The amyloid-specific dye molecule, ThT (Figure 43), is widely utilised to investigate fibrillation kinetics due to its fluorescent profile; upon binding to the amyloid fibril's cross-β structure, a characteristic blue-shift of emission maxima (510 to 480 nm)[38] and a corresponding intensity increase is observed. The observed fluorescence is believed to originate from the ThT binding into the cross-β morphology, specifically the grooves and ridges, which when bound restricts rotamer movement of the benzothiazole (red) and benzamine (blue) rings around the central carbon bond.[39] Fluorescence intensity is considered an indication of fibril content due to the correlation between increasing intensity as fibrillation proceeds, resulting from additional fibrils or increasing fibrillar length.[40] Quantification of the ThT kinetics results in a sigmoidal curve, as previously discussed in Chapter 1.[41]

Fluorescence spectroscopy is highly advantageous because using a well-plate reader allows rapid acquisition of the fibrillation kinetics, therefore enabling studies of the pathway *in situ*. A 96-well plate allows for improved reproducibility, since triplicate wells can be run in parallel simultaneously with as many samples as logistically possible, albeit in smaller volumes. There are two methodologies which could be utilised to investigate the kinetics; continuous and end-point. In the continuous methodology, a plate is incubated within the reader, with the fluorescence of each well measured consecutively as fibrillation proceeds. In contrast the end-point methodology measures the fluorescence from sample aliquots which were taken at specific time intervals during the fibrillation process. Both methodologies are valid systems to monitor fibrillation events but due to the microparticles, which needed to be agitated to ensure dispersal, the end-point methodology was utilised in this investigation.

4.1.2.3. Structural morphology of the amyloid-like fibril

This research programme proposes the use of hydrophobically functionalised mesoporous silica microparticles, as an analogous substrate to silicon wafers, for investigating the effect of surface hydrophobicity on the HI amyloid-like fibrillation pathway. In addition to the examination of the HI adsorption onto the particles and fibrillation kinetics, characterisation of the resultant fibrillar morphology is important. It is known that amyloid fibril morphology is critical because polymorphism potentially affects disease pathology.[42] Amyloid fibrils are hallmarks of amyloidosis and although compositions vary between pathology; the critical cross-β structure, which has discrete β-sheet strands perpendicular to the fibrils long-axis, are always present.[43,44]

The fibrillar morphology is obtained from images acquired by transmission electron microscopy (TEM), which can resolve nanometre structures (>0.2 nm), because it has a higher resolution than light microscopy due to the diffraction limit of the electrons.[45] There are limitations to this technique; microscopic images may not be representative of the entire sample,[46] and the prerequisite for analysis under vacuum thereby unable to image under 'native' solution conditions. TEM has previously been used to characterise HI fibrils in acidic and neutral pH conditions[47,48] and microparticles have also been studied,[49] although neither have been investigated concurrently.

4.2. Materials and Methods

4.2.1. Sample Preparation

All the equipment and HI suspensions were prepared as described earlier, Chapter 3 (3.3.5. Optimised human insulin protein suspension protocol, page 113), but an abridged version is reproduced here. To reduce variability between studies, all the sample solutions were produced in bulk and used fresh or frozen (-77°C) for later use, a maximum of one thaw cycle was performed to reduce any potential freezing influences.[50–54] Additionally, all reagents used throughout this thesis were of analytical grade or higher.

4.2.1.1. Buffers

The buffer solutions (pH 2 and pH 7) were prepared fresh, with enough volume; to suspend the protein at the required concentration, to use as a spectrometric blank and for any required dilution. For the pH 2 buffer (20% acetic acid and 137.9 mM NaCl), sodium chloride (137.9 mM) and water (80 mL, 18.2 MΩ cm^{-1}) were added to a conical flask (250 mL), with acetic acid (20 mL). For the pH 7 buffer, a phosphate-buffered saline (PBS) tablet (1 tablet, 0.01 M) was dissolved in water (100 mL, 18.2 MΩ cm^{-1}). Both solutions were sonicated for 30 minutes and vortexed to ensure both had been suitably mixed.

The pH of the buffers was first checked by universal indicator paper, which was validated by pH meter. Following acquisition of the correct pH, the buffer solutions were then polyethersulfone (PES) membrane syringe filtered (0.22 µm) into Durans' using a large volume syringe (60 mL). Aliquots of the buffers were taken for; protein suspension, buffer blanks and dilution solutions.

4.2.1.2. Human insulin suspensions

The HI (10 mg/mL) was suspended in a pH 2 buffer (20% acetic acid and 139.7 mM sodium chloride) in a lo-bind Eppendorf tube (2 mL), briefly vortexed to ensure complete dissolution and then immediately syringe-filtered (0.22 µm PES). Preparation of HI in pH 7 buffer involved firstly suspending HI in the minimum volume of hydrochloric acid (0.1 M), briefly vortexed and then immediately syringe-filtered. The solution was titrated back to pH 7 by addition of sodium hydroxide (0.1 M) and PBS buffer added to dilute the suspension to the required concentration.

4.2.1.3. Functionalised mesoporous silica microparticle suspension preparation

The hydrophobic functionalised mesoporous silica microparticles (Si, C_6, ODS1 and ODS2, Spherisorb) are very light and dusty, thus when dry must be handled within a fume cupboard. To suspend these particles into solution, their hydrophobic nature has to be overcome firstly by creating a solvation shell, otherwise they remain at the air:water interface.

A suspension of acetonitrile (80%, HPLC grade) in ultrapure (type I) water (20%, 18.2 MΩ cm^{-1}) was vortexed, before an aliquot was taken and added to

a glass sample vial (14 mL) containing the silica microparticles. The particles were wetted when they were no longer observed at the air:water interface. The buffers were titrated into the suspension, until the volume of acetonitrile mixture was displaced. Aliquots of the silica microparticles were then added into HI suspensions, which were prepared in lo-bind microcentrifuge tubes (2 mL), until the effective concentrations of HI (10 mg/mL) and silica particles (20 mg/mL) were attained.

4.2.1.4. Incubation of the suspensions

The various microcentrifuge tubes, which contained the suspensions of both the controls (HI-only and silica microparticles-only) and the samples (HI and silica microparticles), were briefly vortexed to ensure homogeneity before incubation at room temperature (~21°C) or elevated temperature (~37°C). Aliquots of the suspensions were acquired at specific time points as a function of incubation duration. The final aliquots taken for the fibrillar state were visibly cloudy. At each time point, the tubes were briefly vortexed and then aliquoted into a new microcentrifuge tube, with the fibrillation tubes returned rapidly to the incubator and the aliquoted samples flash frozen for later analysis. The samples were stored frozen (-20°C short or -77°C for longer durations) until needed, then thawed back to laboratory temperature before being analysed.

4.2.2. Characterisation of the particle's influence upon amyloid-like fibrillation

4.2.2.1. CHN Elemental Microanalysis

The CHN analysis was performed in-house, within the Department of Chemistry's analytical services (University of Liverpool), with a minimum of eight results (n=8) acquired for each sample. The HI and microparticle suspensions (4.2.1.3. Functionalised mesoporous silica microparticle suspension preparation, Page 128) were studied by CHN to determine the amount of HI adsorbed for the initial adsorption before fibrillation occurs. The suspensions were briefly vortexed (30 seconds), allowed to rest (60 minutes), after which they were vortexed again (30 seconds) to ensure homogeneity.

An aliquot of this suspension was taken and set aside, labelled *'adsorbed'*, whilst the remaining suspension was rinsed three times with the specific buffer and

after rinsing, an aliquot was removed and labelled *'adsorbed fraction after rinsing'*. Both aliquots were dried under air-flow, with samples taken for IR analysis. The remaining material was dried in an incubator (~100°C) overnight to remove any residual moisture content.

To calculate the coverage of insulin on the particles, the following equation was used:

$$coverage\ (\mu \cdot mol \cdot m^{-2}) = \frac{10^6 * P_c}{S * [(1200 * N_c) - P_c(MW - 1)]} \quad (4.3)$$

where P_c = % carbon, N_c = number of carbons in HI, MW = molecular weight of HI, and S = silica particle surface area.[55]

4.2.2.2. Infrared spectroscopy

The airdried aliquots were analysed by IR spectroscopy to determine the amount of HI present through quantification of the Amide I band (1600 – 1700 cm^{-1}). IR spectroscopy was performed using a diamond mounted attenuated total reflection (ATR) IR instrument (Alpha, Bruker). The diamond window, stage and clamp were cleaned extensively with isopropanol prior to use and between samples. The instrumental parameters were; spectral range (4000 – 400 cm^{-1}), resolution (2 cm^{-1}), multiple scans to increase signal-to-noise (100 scans for both background and sample) and atmospheric compensation. The insulin coverage was calculated by integration of the Amide I band as described by Mauri *et al*.[56]

4.2.2.3. End-point fluorescence kinetics

The aliquots acquired during the fibrillation incubation were first thawed (~21°C, 1 hour) in their microcentrifuge tubes (2 mL, lo-bind, Eppendorf). A non-treated optical bottom black well-plate (96-well, Nunc, ThermoFisher) was prepared with ThT (1 µL, 2 mM). The sample tubes were briefly vortexed (10 seconds) to ensure solution homogeneity and pipetted into the wells (100 µL) in triplicate, resulting in a final dye concentration of 20 µM. The plate reader (FlexStation III, Molecular Devices) was pre-heated (~25°C) and parameters set for a top-read emission scan (λ_{Ex} 440 – 475 nm, λ_{Em} 480-600 nm, 10 nm intervals, low detector sensitivity and shake once prior to acquisition) of each well. The fibril

kinetic data (λ_{Em} 490 nm) was analysed using Origin Pro (2016 64-bit) and for the incubated silica microparticles fluorescence reads the controls (i.e. particle only) were subtracted from the data shown. The statistical analysis, by ANOVA one-way, for the kinetics resulted in the reported significant values of $p \leq 0.05$.

4.2.2.4. Transmission Electron Microscopy

The prepared carbon electron microscopy (EM) grids and uranyl acetate (4%) were supplied by the Physiology department at the University of Liverpool. An aliquot of the end-point sample solution (10 µL) and uranyl acetate (10 µL) were pipetted onto opposite sides of a Parafilm section. A pair of tweezers were utilised to manipulate the EM grids, with the dull side applied onto the sample droplet for 30 seconds, excess solution was removed by blotting onto filter paper. The EM grid was then added same side down onto the uranyl acetate droplet for 30 seconds, again excess solution was removed by blotting onto filter paper, and the EM grid left to air dry overnight (~16 hours) before analysis. Samples were imaged using an electron microscope, Tecnai G2 Spirit BioTwin (FEI) at 120 kV.

4.2.2.5. Dynamic Light Scattering and Zeta Potential

To investigate the size distribution and zeta potential of the functionalised silica microparticles, dynamic light scattering (DLS) was employed using a Zetasizer Nano ZSP (Malvern Panalytical Ltd, UK), which has a stated size range of 0.3 nm to 10 µm ($1.0x10^{04}$ nm). Quartz cells (700 µL, fluorescence cells) with a parallel path length (1 cm) were used. HI was suspended in an acidic buffer (pH 2, 20% acetic acid buffer), with instrumental parameters set to; dispersant (water, 1.330 refractive index, 0.8872 mPa s^{-1} viscosity), temperature (25°C, 60 s equilibration time), and operating in back scatter (173°, 10 scans, 50 s acquisition time). The zeta potentials were acquired (10 scans per sample) using folded capillary cells (Malvern Panalytical Ltd, UK).

4.3. Results and Discussion

4.3.1. Characterisation of mesoporous silica particles

The hydrophobically functionalised mesoporous silica microparticles were first characterised by DLS and zeta potential. The particle size, distribution and zeta potential results for all particle types within both pH conditions are shown in Table 2.

Table 2: Characterisation of the functionalised mesoporous silica microparticles within pH 2 and pH 7 conditions by dynamic light scattering (DLS) and zeta potential (ZP), resulting in particle size, polydispersity index (PDI) and zeta potential measurements. The standard deviation (SD) was attained from 10 consecutive analysis.

Microparticle type	pH	Particle size / µm ± SD	Polydispersity index	Zeta potential / mV ± SD
Si	2	5.61 ± 0.3	1.00	-5.74 ± 0.4
Si	7	5.27 ± 0.3	1.00	-20.04 ± 1.4
C_6	2	5.86 ± 2.1	0.75	-4.83 ± 0.3
C_6	7	1.77 ± 0.0	0.90	-1.22 ± 0.2
ODS1	2	3.09 ± 0.8	0.70	-7.59 ± 0.7
ODS1	7	3.94 ± 3.2	0.71	-15.16 ± 0.9
ODS2	2	8.52 ± 0.1	1.00	-12.37 ± 1.8
ODS2	7	8.64 ± 0.0	1.00	-22.70 ± 1.3

The characterisation of the microparticles by DLS and zeta potential (Table 2) show that there is a large variation between the various particle types, particularly for the larger functionalised particles. Each particle type was commercially defined as having a mean particle size of 5 µm (± 2 µm), which all particles with respect to their standard deviation fulfil except for the ODS2 functionalised. The ODS2 functionalisation resulted in a higher calculated size than expected, which is possibly attributed to its inherent fluorescence (4.3.3. Measuring the amyloid-like fibrillation kinetics, page 144) therefore affecting size acquisition by DLS. There does not appear to be any trend correlated with hydrophobic functionalisation or pH conditions, however there is variation between the particle types. The bare silica particle, Si, resulted in similar particle size for both pH conditions and correlated with the assumed 5 µm size. Conversely C_6 for pH 2 conditions resulted in a similar 5 µm size

however this value was with a ± 2.1 µm SD, whereas at pH 7 the resultant size was far smaller at 1.77 µm. The ODS1 particles resulted in a smaller than anticipated size of 3.09 and 3.94 µm for pH 2 and 7 respectively, where the neutral pH result included ± 3.2 µm SD, therefore not correlating with the effect of pH on C_6.

The polydispersity index (PDI) is a statistic of how heterogeneous a sample is, which ranges from a value of 0 for a uniform (monodisperse) sample to 1 for a non-uniform (polydisperse sample) with varying particle size populations.[57] In this project all particle types in both conditions studied resulted in a very broad size distribution, therefore are highly disperse as the values acquired ranged from 0.7 to 1 PDI. The high PDI values for the samples mean that they are unsuitable for particle size characterisation by DLS since the instrumental algorithms are optimised for lower PDI samples. An advantage for with this instrument was the ability to acquire zeta potentials simultaneously.

Zeta potentials are a useful factor to investigate colloidal stability of a sample, which is ascertained from the particle's surface charge, where high positive or negative values are indicative of high stability because of electrostatic repulsion.[58] Conversely low values are correlated to low stability as the particles can overcome the electrostatic interactions therefore leading to the particles aggregating.[58] It is important to note that zeta potentials are only one factor used to predict colloidal stability, since other factors notably suspension chemistry and use of surfactants affect the physical stability.[59] In all the particle types, except for C_6, the change in pH from pH 2 to 7 results in a decrease in zeta potential therefore suggesting increased stability. In all samples the zeta potential values are not associated to the high values stated by others, less than -25 mV and higher than +25 mV,[60] therefore the particles are likely to aggregate. The OSD2 particles in both pH conditions are shown to be more stable than the ODS1 particles as indicated by the increased negative values. The C_6 particles show an inverse trend, where pH 7 increases in zeta potential which also correlates with the particle size that resulted in a decreased mean size.

The trend for hydrophobic functionalisation shows increasing functionalisation at pH 2 results in an increased assumed stability, whereas no trend is observed for pH 7. While these zeta potential values imply instability due to the

low values, others have reported that colloidal silica shows exceptional stability at low zeta potentials,[61] furthermore these results were obtained on poly disperse samples, which are not considered ideal for zeta potential measurements.[62]

Overall, the microparticles are shown to be highly polydisperse, which correlates with the fluctuating particle size values attained demonstrating that the particles consist of a range of size distributions. This is an important factor to consider when calculating the amount of HI adsorbed to each particle as a result of variable surface areas.

4.3.2. Determining amount of insulin adsorbed to the particle surface

The adsorption of HI to the functionalised mesoporous silica microparticles, which was quantified by CHN microanalysis and IR spectroscopy, was first considered. The amount of HI adsorbed in pH 2 conditions to the functionalised particles, which were; Si (red), C_6 (green), ODS1 (blue) and ODS2 (orange), was quantified by CHN for the adsorbed (filled circles) and rinsed (open circles) as shown in Figure 44. The net carbon and nitrogen percentage results are plotted on the *x*- and *y*- axis respectively, where HI content is correlated to increases in both axes (Figure 44).

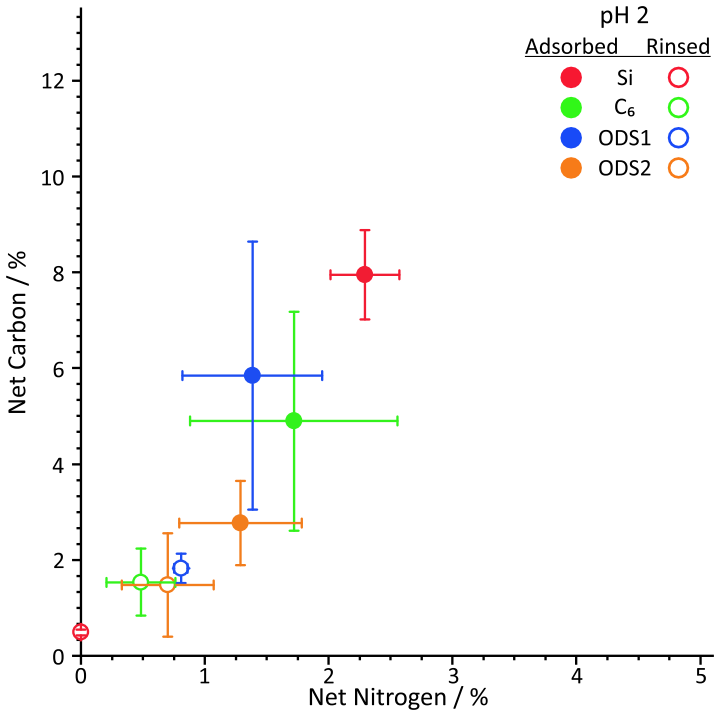

Figure 44: The net (control-subtracted) amount of carbon and nitrogen, at pH 2 (20% acetic acid and 137.9 mM NaCl), for the microparticles (filled circles) adsorbed with human insulin (HI) after 60 minutes and (open circles) rinsed with buffer solution. These are the mean values with error bars showing the standard deviation for all samples of the microparticles; (red) Si, (green) C_6, (blue) ODS1 and (orange) ODS2.

At pH 2, all adsorbed states are shown to have higher net carbon and nitrogen percentages compared to the rinsed states, therefore higher HI content for the adsorbed samples. The CHN results showed the largest difference in adsorbed and rinsed states for the bare silica particles, Si, with overall both the highest and lowest HI content for the adsorbed and rinsed states respectively. The smallest difference between adsorbed and rinsed states was shown for the ODS2 particles, whilst a high variation attributed to large error bars was observed for the C_6 and ODS1 adsorbed and rinsed states. There is an overall reduction in the attributed error for the rinsed states as opposed to the adsorbed states, corresponding to loss of less tightly bound HI (physisorbed) layers.

The CHN analysis for the HI adsorbed and rinsed states of the silica particles in pH 2 (Figure 44), shows lower net carbon and nitrogen percentages for the rinsed compared to adsorbed states implying loss of HI from the particles, because the rinsing process removes excess (non-adsorbed) HI from the samples. If all the HI was

removed from the particles, then the rinsed states would result in zero for the net carbon and nitrogen as the data has been control (particle) subtracted, however Figure 44 shows this is not the case, therefore there is residual HI adsorbed to the particles. The CHN for the rinsed state of Si resulted in no net nitrogen but minimal carbon, which implies that HI has been entirely removed as there is no nitrogen content, therefore the residual carbon load is potentially due to instrumental error, organic contamination, or as a result of a drying artefact.

Functionalisation of the particles appear to reduce the overall capability for HI adsorption in acidic conditions, with Si the least hydrophobically functionalised adsorbing the most HI, and ODS2 the most functionalised adsorbing the least HI. A potential reason for the adsorption difference is due to the steric properties of the functionalised groups, which may block access into the particle's pores, therefore reducing the accessible surface area for HI adsorption. ODS2 is both C_{18} functionalised and endcapped, which further reduces the accessible HI adsorption area. The reduction of both carbon and nitrogen net percentages between the adsorbed and rinsed states is lowest for the functionalised particles (C_6, ODS1, and ODS2) compared to Si, which implies that the adsorbed HI is strongly bound to the Si surface.

The work in this section aims to investigate whether there are any differences in HI adsorption which are specifically attributed to the microparticle's hydrophobic functionalisation. It is known that surface adsorption is important to the amyloid-like fibrillation pathway, as described in Chapter 1. Importantly is the presence of the particles inducive to fibrillation or the hydrophobic functionalisation. Statistical significance was determined by ANOVA with Tukey post-hoc analysis ($p < 0.05$), which resulted in only eighteen sets of significantly difference for the net carbon and one for the net nitrogen. The net carbon showed; adsorption and rinsed states of the Si, C_6 and ODS1, adsorbed Si to the adsorbed and rinsed states of C_6, ODS1 and ODS2, rinsed Si to the adsorbed states of C_6, ODS1 and ODS2, adsorbed C_6 to rinsed ODS1, adsorbed C_6 to both adsorbed and rinsed ODS2, rinsed C_6 to adsorbed ODS1, and the adsorbed ODS1 to the adsorbed and rinsed states of ODS2. The net nitrogen showed significant difference between the adsorbed and rinsed state of Si.

The amount of HI adsorbed in pH 7 conditions to the functionalised particles, which were; Si (red), C_6 (green), ODS1 (blue) and ODS2 (orange), was quantified by CHN for the adsorbed (filled circles) and rinsed (open circles) states as shown in Figure 45. The overall adsorbed state HI content is similar to the pH 2 CHN results (Figure 44), however the pH 7 results (Figure 45) show considerable variability with regards to the rinsed states providing no clear trend. The Si and ODS1 particles show reduction in the HI content for the rinsed state, however only Si exhibits difference between the two with ODS1 having overlapping error bars (Figure 45). The C_6 particles, for both adsorbed and rinsed states, have very similar mean results but with substantial overlapping error bars. The ODS2 results exhibit a contrasting trend, with increased HI content for the rinsed state as opposed to adsorbed, which is compounded by a significant difference with no error bar overlap.

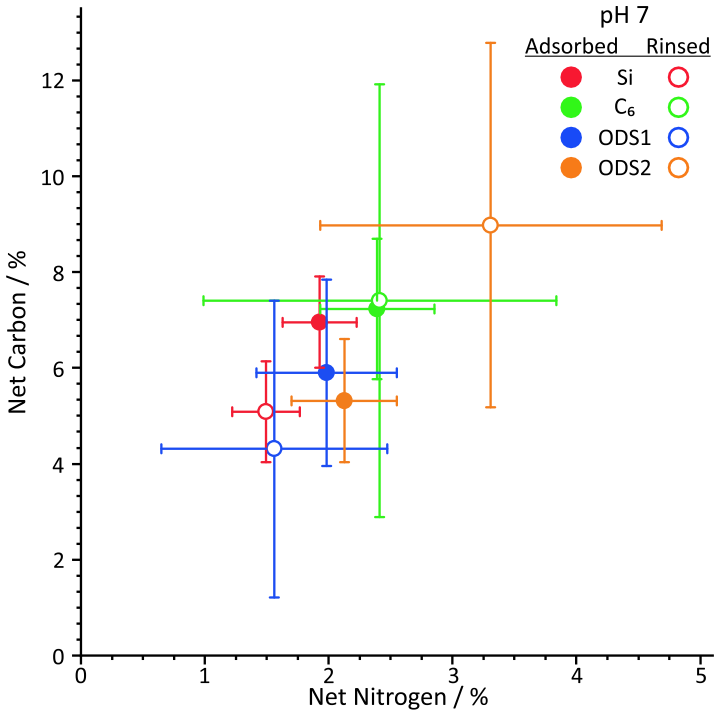

Figure 45: The net (control-subtracted) amount of carbon and nitrogen, at pH 7 (0.01 M PBS), for the net (control-subtracted) amount of carbon and nitrogen, at pH 2 (20% acetic acid and 137.9 mM NaCl), for the microparticles (filled circles) adsorbed with human insulin (HI) after 60 minutes and (open circles) rinsed with buffer solution. These are the mean values with error bars showing the standard deviation for all samples of the microparticles; (red) Si, (green) C_6, (blue) ODS1 and (orange) ODS2.

The CHN analysis for the HI adsorbed and rinsed states of the silica particles in pH 7 (Figure 45) conditions shows a high variability between the net carbon and nitrogen percentages and thus the HI content. Each mean point consists of large error bars, which makes it difficult to ascertain whether the rinsed state HI content is less than the adsorbed state, with the exception to Si as this shows a clear reduction. This high variability was not observed to the same extent at pH 2, implying that the issue is attributed to the pH conditions as opposed to the analytical technique. It is known that at pH 7, the HI equilibrium is shifted towards higher order oligomeric species such as dimer or hexamer as opposed to the pH 2's monomeric preference. The rinsing of the particles may lead to surface adsorbate reorganisation or additional oligomeric species adsorption resulting in oligomerisation, therefore increasing the variability across the samples.

The Si and ODS1 particles exhibit similar reduction in both net carbon and nitrogen percentages, with higher errors attributed to ODS1, which implies that the functionality plays a smaller role for neutral pH compared to acidic, however this trend is not observed for C_6 and ODS2. The C_6 particles result in very similar mean carbon and nitrogen percentages for both adsorbed and rinsed, with the latter having an increased mean, which implies higher HI content for the rinsed as opposed to the adsorbed state. Conflicting trends are observed for the ODS2 particles, where the net carbon and nitrogen percentages increase from the adsorbed to rinsed states, which implies that there is additional HI content for the rinsed state but these have very large error bars. Statistical significance was determined by ANOVA with Tukey post-hoc analysis ($p < 0.05$), which resulted in only three sets of significantly difference for the net carbon; rinsed state of Si and ODS2, rinsed state of ODS1 and ODS2, and adsorbed and rinsed state of ODS2.

Overall, the rinsed state percentages for the C_6, ODS1, and ODS2 functionalised particles have very high error bars, therefore caution is necessary regarding any perceived trends. Conversely the adsorbed state percentages for all the particles, are both similar to those obtained at pH 2 conditions suggesting the maximum HI adsorption obtainable. To investigate the maximum HI coverage for the particles in both pH conditions, a non-invasive spectroscopic technique and

comparison with literature is necessary. Additional sample aliquots, which had not been oven dried, were examined by IR spectroscopy to ascertain the HI content through integration of the Amide I region (1600 – 1700 cm^{-1}), which was compared to the HI coverage as determined by CHN analysis.

The calculated HI coverage on the particles is shown in Figure 46, for pH 2 (Figure 46a – c) and pH 7 (Figure 46d – f) conditions as determined by; CHN carbon (Figure 46a, d), CHN nitrogen (Figure 46b, e) and integration of the IR Amide I region (Figure 46c, f). The pink shaded region is indicative of the theoretical HI adsorbed monolayer coverage, which others have determined to range between 1.1 – 1.7 mg/m^2 for the adsorption of insulin on solid surfaces.[63–65]

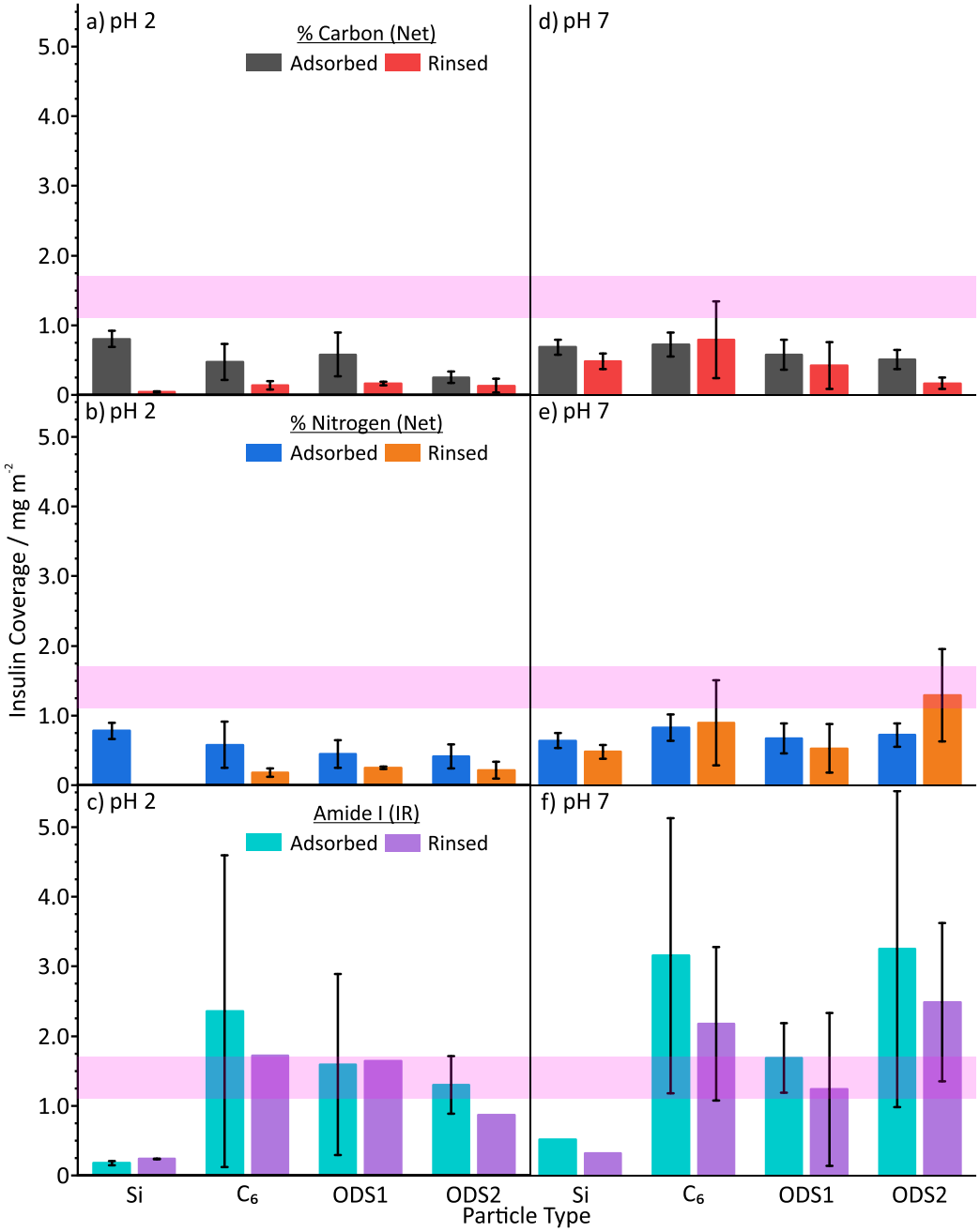

Figure 46: The human insulin (HI) coverage on each particle, after 60 minutes adsorption, for (a – c) pH 2 (20% acetic acid and 137.9 mM NaCl) and (d – f) pH 7 (0.01 M PBS) as determined by CHN elemental analysis; (a, d) net carbon, (b, e) net nitrogen and by (c, f) integration of the IR Amide I region. (shaded pink region) The theoretical monolayer coverage of HI, as determined by Arnebrant et al[63] and Mollman et al.[65] These are the mean values with error bars showing the standard deviation.

The HI coverage calculated from the CHN and IR results is shown in Figure 46, with the theoretical monolayer coverage shown as a purple bar, where no immediate trends related to functionalisation are observed. The CHN

results (Figure 46a, b, d and e) generally highlights that the monolayer coverage was not attained for any of the samples studied, with exception to the rinsed pH 7 C_6 (% carbon and nitrogen) and pH 7 ODS2 (% nitrogen) samples which were within the error bars. Conversely the IR results (Figure 46c and f) show that for all functionalised microparticles the HI monolayer coverage was attained or exceeded. The CHN and IR results obtained do not appear to correlate, as CHN shows reduced HI coverage compared to IR. It is likely that this lack of correlation is attributed to the instrumental setups, as both sample sets were acquired from the same experiment with the observed deviation occurring from the CHN samples having been dried overnight to remove any residual moisture content.

The undercalculated HI monolayer coverage for the CHN samples is likely attributed to the drying process, where the samples were heated overnight in an incubator (~100°C). The high temperature will denature the HI but as CHN is an elemental analysis technique which probes the carbon and nitrogen content, the denaturation effect is of no concern since the probed elemental species will remain similar. However, a consequence of this denaturation is sample instability, which results in a lack of consistency within the sample therefore when aliquoting the very small amounts of sample for CHN analysis leads to large error bars, as shown.

Conversely it is possible that the IR analysis overcalculates the monolayer coverage because although the samples were not heated (no heat induced degradation),[66] however there is potential for oversampling. This oversampling is observed for the adsorbed likely due to multilayer coverage, whereas this is removed for the rinsed state. Furthermore, the IR samples were air-dried when analysed therefore potential for non-adsorbed HI species to be included in the measurements. Additionally, there are instrumental considerations specifically the packing of the sample and lack of sensitivity of the ATR. Experimentally the IR is sampling from below and has a penetration depth of ~2 μm,[67] which leads to a varying assessment of the HI species on the small portion of the microparticles surface studied giving rise to the variation in results.

A decreasing trend for the adsorbed HI content as microparticle functionalisation increases is generally observed for the CHN

results (Figure 46a, b, d and e), however this is largely dependent on the pH conditions. The pH 2 conditions clearly exhibit this decreasing trend in both adsorbed and rinsed sample sets, whereas this trend is inconclusive for pH 7 conditions because of the large variation in error bars. The HI content is higher for the pH 7 adsorbed states compared to the pH 2, which is likely attributed to the HI oligomeric state within the two pH conditions. At pH 2, the HI species is likely monomeric therefore strongly bound to the hydrophobic microparticle because of the hydrophobic effect. A HI monomer preferentially adsorbs to a hydrophobic surface, which is entropically driven by the loss of water,[68] to limit exposure of its hydrophobic domain. This drive to limit exposure is entropically driven therefore is a strong interaction to the hydrophobic functionalised interface. At the same time the higher order oligomeric species present in neutral pH conditions does not have the same hydrophobic effect to drive adsorption, since the hydrophobic domain is buried within the dimer structure. However, a HI oligomer species can adsorb to the particle by physisorption processes, with the same adsorption sites possible as for the monomer. Assuming a close-packed monolayer coverage,[69] for every adsorption site a monomer (5.8 kDa), dimer (11.6 kDa) or hexamer (34.8 kDa) HI species can adsorb. The higher HI content observed for the neutral pH conditions is a result of higher order oligomeric HI species adsorbed to the available sites.

The HI oligomeric state does not account for the differences in rinsed states between the pH conditions, where pH 2 resulted in reduction of HI content and pH 7 maintained similar content. Rinsing the particles after a short adsorption time removes the excess HI from the particle, which corresponds with the pH 2 results however is not observed for pH 7. The pH 7 rinsed states for the particles, except Si, result in a largely similar HI content. The HI content for the rinsed compared to adsorbed states, is possibly due to the particles undergoing hydrophobic collapse,[70] where the particles aggregate to reduce exposure to the rinse buffer thus trapping the HI oligomers. The acquired data for the rinsed particles have large error values, therefore it is difficult to ascertain the contribution from hydrophobic collapse.

The IR results (Figure 46c and f) show a higher error variability than the CHN data however there are possible trends to be considered here. Firstly, in both pH

conditions, the non-functionalised Si particle exhibits the lowest HI content which is below the monolayer coverage. Conversely for all the functionalised particles, the monolayer coverage was attained, and the HI content decreased with a trend from C_6 to OSD2 with the exception for pH 7 ODS2 which increased. Similarly, to the CHN results, the pH 7 samples by IR analysis shows a higher HI content compared to the pH 2 conditions. Conversely, the rinsed states for the IR samples are on average lower than the associated adsorbed states which does not correlate to the CHN results. However as initially stated the high error variability for the neutral pH conditions means that these results are difficult to distinguish.

A theoretical monolayer coverage of HI on the microparticles was calculated by first using the surface area of the silica microparticles (220 m^2/g)[8] as described by the manufacturer. In all samples, 20 mg/mL microparticles were suspended in 2 mL resulting in 40 mg of microparticles within the vial therefore providing a total silica microparticle surface area (8.8 m^2). The amount of HI monolayer coverage varies depending on the packing of the system, however using the minimum (1.1 mg/m^2)[63] and maximum (1.7 mg/m^2)[65] packing density results in 10 – 15 mg HI required for monolayer coverage, which is appropriate for this work. A possibility as to why variation in the HI monolayer coverage was observed is in relation to the stated surface area, which does not account for the accessible surface area. The surface area was commercially obtained[8] using Brunauer Emmett Teller (BET) methods, which determine surface area based on gas adsorption to a surface.[71] The BET theory presents an issue with this surface area determination, where the HI species are far larger than gas molecules so are likely unable to access the same surface area sites within the mesoporous architecture, which reduces the microparticles available surface area for adsorption.

Overall the work to quantify the amount of HI adsorbed to the silicon particles has shown that; there is a greater amount of HI adsorbed at pH 7 conditions compared to pH 2, the functionalised particles results in increased HI adsorbed compared to bare Si particles however this trend reduces as alkyl length increases. The obtained CHN and IR results implies that the C_6 alkyl hydrophobicity is the optimum functionalisation, within the samples studied, for HI adsorption in both

pH 2 and 7 conditions which implies that the increasing chain length affects adsorption sites. A general trend is observed between the adsorbed and rinsed particle states, where the rinsed state results in a reduction of the amount of HI adsorbed however a few exceptions to this trend are within the observed error margins. The initial aim for this section of work was to determine whether the amount of HI adsorbed provides information on the expected HI fibrillation pathway, by ascertaining multilayer growth which may implicate structural rearrangement events. This aim was not achieved since quantification of adsorbed HI on mesoporous Si microparticles by elemental microanalysis or IR spectroscopy was not ideal, as shown by the variation in results between samples and the lack of correlation between CHN and IR. In future other techniques, which address these shortcomings, should be utilised to give rise to a better methodology.

4.3.3. Measuring the amyloid-like fibrillation kinetics

The results presented within this section utilise ThT kinetic assays to determine the effect of incubating HI with the functionalised mesoporous silica microparticles on the HI amyloid-like fibrillation pathway. The ODS2 particles are not presented here, as particle-only control experiments (see Figure S14) resulted in ODS2 exhibiting an inherent intrinsic fluorescence profile as incubation time proceeded, therefore could not be used in this experiment. In the next section where TEM was used to observe fibril structural morphology, images were obtained for all samples thus the effect of ODS2 functionalisation will be continued later (4.3.4. Observing structural morphology changes, page 149).

4.3.3.1. The effect of pH on human insulin amyloid-like fibrillation kinetics

The effect of pH on the fibrillation of the control, HI-only, over a four-day incubation (37°C) period is shown in Figure 47. At pH 2 a sigmoidal curve is observed, which is indicative of complete fibrillation, however at day 4 a reduced fluorescence intensity was observed, which implies that the insoluble mature fibrils have fallen out of solution.[36,37] Conversely in pH 7 conditions, only a partial sigmoidal curve is observed which does not attain the same fluorescence intensity as for pH 2 conditions.

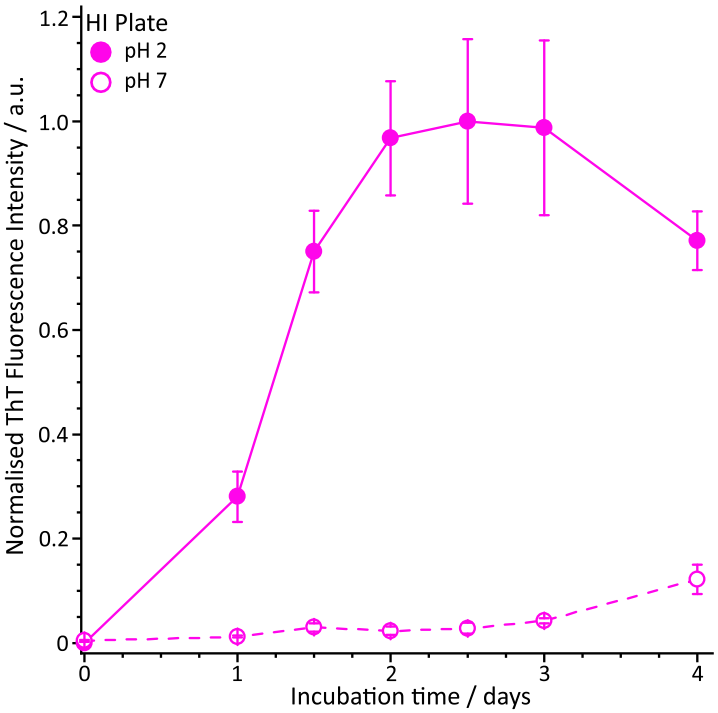

Figure 47: Thioflavin-T (ThT) end-point assay (n=3) showing human insulin (HI) amyloid-like fibrillation at 37°C incubation for (solid) pH 2 (20% acetic acid and 137.9 mM NaCl) and (dashed) pH 7 (0.01 M PBS) conditions. The ThT fluorescence is normalised to the pH 2 mean maxima, with error bars showing the standard deviation.

Figure 47 shows that the parameters used were suitable as both pHs exhibited fibrillation within a reasonable timeframe with enough datapoints to determine any influence of the silica microparticles on the HI fibrillation pathway. These results provide a good baseline for which the effect of silica microparticles can be observed.

4.3.3.2. Presence of functionalised mesoporous silica microparticles upon the amyloid-like fibrillation kinetics of human insulin

The incubation of HI with the functionalised particles, which were; Si (red), C_6 (green) and ODS1 (blue), in pH 2 conditions compared to the HI-only control (pink) is shown in Figure 48. A complete sigmoidal curve, achieving saturation phase, followed by a decreased fluorescence intensity at the day four incubation is observed for all samples. An overall reduction in the normalised fluorescence intensity for the incubated silica particles is observed, with a further reduced intensity shown for day 2 compared to the HI-only control. The fluorescence intensity for the particles is shown to be highest for Si, and lowest for ODS1.

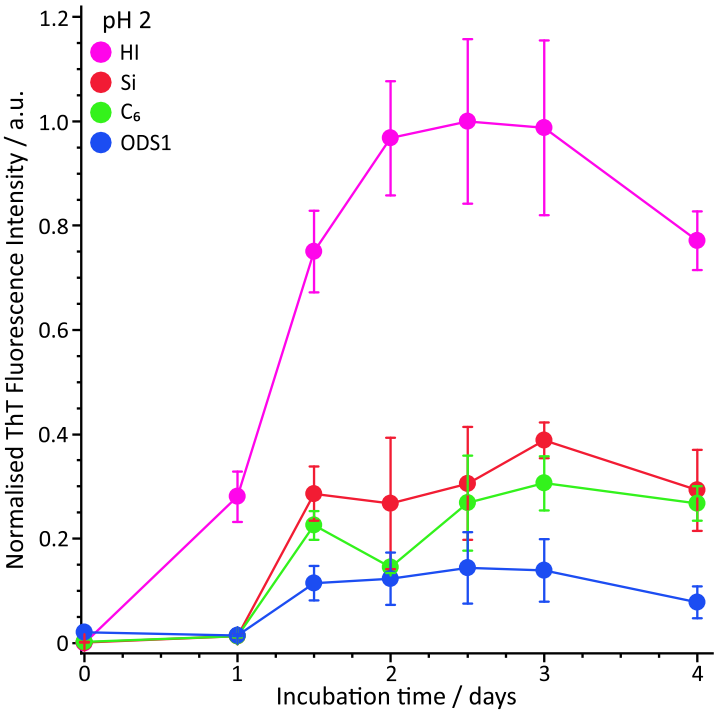

Figure 48: Thioflavin-T (ThT) end-point assay (n=3) showing human insulin (HI) amyloid-like fibrillation at 37°C incubation for pH 2 (20% acetic acid and 137.9 mM NaCl) for the (pink) HI-only control compared to incubation with functionalised mesoporous silica microparticles; (red) Si, (green) C_6 and (blue) ODS1. The ThT fluorescence shown has been control subtracted and normalised to the mean fluorescence maxima, day 2.5 HI-only control, with error bars showing the standard deviation. The (pink) HI-only control is the same data as shown in Figure 47.

The ThT end-point assay for pH 2 conditions, shows that the fibrillation pathway for all samples has completed since a saturation phase was observed (Figure 48). This is further reinforced by a decreased fluorescence observed at the day four incubation compared to the day three, which implies that the insoluble mature fibrils in all the samples are falling out of solution.[36,37] The fibrillation kinetics data for pH 2 clearly shows that the presence of the functionalised silica microparticles, inhibits the typical HI amyloid-like fibrillation pathway. The different fibrillation kinetics observed for the various microparticles, with the highest intensity for Si and the lowest for ODS1 implies the possibility of divergent fibrillation pathways. An observed reduction in mean fluorescence intensity at day two is observed for C_6, and possibly Si given the large error bars, implying that there are two differing fibrillation pathways as the same trend is not observed for ODS1. Statistical significance was determined by ANOVA with Tukey post-hoc

analysis ($p < 0.05$), which resulted in significant fluorescence data for all HI results compared to the particles; Si, C_6 and ODS1, except for day 0.

The incubation of HI with the functionalised particles for pH 7 conditions compared to the HI-only control is shown in Figure 49. A partial sigmoidal curve is observed in all samples, with an overall increased fluorescence intensity for the incubated silica particles.

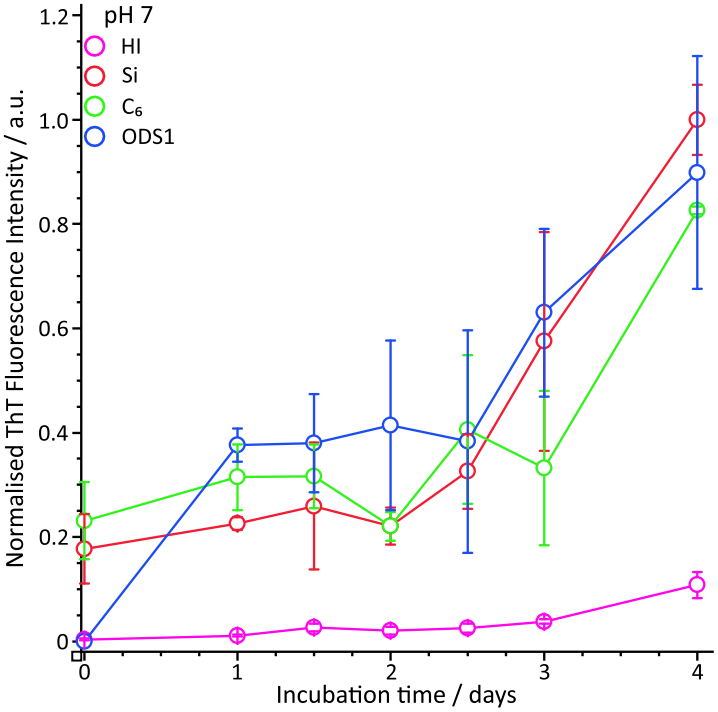

Figure 49: Thioflavin-T (ThT) end-point assay (n=3) showing human insulin (HI) amyloid-like fibrillation at 37°C incubation for pH 7 (0.01 M PBS) for the (pink) HI-only control compared to incubation with functionalised mesoporous silica microparticles; (red) Si, (green) C_6 and (blue) ODS1. The ThT fluorescence shown has been control subtracted and normalised to the mean fluorescence maxima, day 4 Si incubated with HI, with error bars showing the standard deviation. The (pink) HI-only control is the same data as shown in Figure 47.

The ThT end-point assay for pH 7 conditions shows that within the same parameters as for pH 2, only a partial fibrillation pathway for all samples has occurred, which is indicated by the observed elongation phase since the fluorescence intensity does not plateau by the day four incubation. A plateau region is observed for the functionalised particles between days one and two, followed by an exponential intensity rise which suggests that the particles provide distinctly different fibrillation pathways, since this trend is not observed in the control trace.

The diverging pathways of the functionalised particles, as previously shown in pH 2, are observed here where ODS1 has an overall typically higher fluorescence intensity at incubation days zero and four. The presence of particles in pH 7 conditions clearly shows an enhancement in the fibrillation kinetics of the HI amyloid-like pathway. Statistical significance was determined by ANOVA with Tukey post-hoc analysis ($p < 0.05$), which resulted in significant fluorescence data for day 4 incubated HI fluorescence compared to; Si, C_6 and ODS1.

There appears to be a fluorescence signal at pH 7 for both Si and C_6 particles at day zero, which would imply that ThT has bound to cross-β structure present here. A potential source and most likely factor for this fluorescence stems from sample preparation, the fluorescence data is acquired from end-point reads, whereby aliquots of the same solutions were taken, flash frozen and stored in a freezer (-77°C) until required. The first data point was taken about an hour after protein addition to ensure protein adsorption to the particles, therefore it is possible that a ThT-active species has been generated between first synthesis and freezing, or alternatively between thawing and analysis.[50,52]

Overall, the incubation of HI with functionalised mesoporous silica microparticles are clearly shown to inhibit for pH 2 and enhance for pH 7 the HI amyloid-like fibrillation kinetics. The general kinetics trends are correlated to the overall fluorescence intensity for the particles compared to controls, where reduced intensity is inhibition and increased is enhancement. In addition to the overall intensity changes, the particles exhibit specific fluorescence variations such as; reduction at day two for pH 2, and for pH 7 a plateau followed by exponential region is observed, which implies a fibrillation pathway change for the particles.

To investigate the mechanistic effect of particles on the HI fibrillation pathways further techniques such as fluorescence microscopy are necessary, because of the complications arising from the ThT measurements. The ThT molecules, which bind to the cross-β structure,[72] are assumed to attach at active sites of the fibril however the complication arises from the various fibrillar locations. HI fibrillation can occur in solution through nucleation mechanisms, see Chapter 1 (1.3.1. What is protein fibrillation?, page 40), however the addition of particles

provides an alternative pathway through protein adsorption events[73] or an autocatalytic approach resulting in fibrillation by seeded growth.[6,7] The overall ThT complexity makes fibrillation pathway determination using this technique difficult, however the results clearly show that the particles affect the HI amyloid-like fibrillation through inhibition or enhancement processes.

4.3.4. Observing structural morphology changes

The TEM images shown in this section were acquired from the same samples previously studied in the kinetics measurements (4.3.3. Measuring the amyloid-like fibrillation kinetics, page 144), but from different aliquots.

4.3.4.1. The effect of pH on human insulin amyloid-like fibril morphology

Variations of pH have previously been reported to affect the morphology of insulin fibrils,[48,74–77] however there is no other study which have utilised the same experimental conditions as this investigation. The effect of pH on the HI-only control, post-incubation (37°C, four days) is shown in Figure 50, which shows fibrillar structures in the acidic conditions (Figure 50a and c), and only smaller pre-fibrillar aggregates for the neutral conditions (Figure 50b and d).

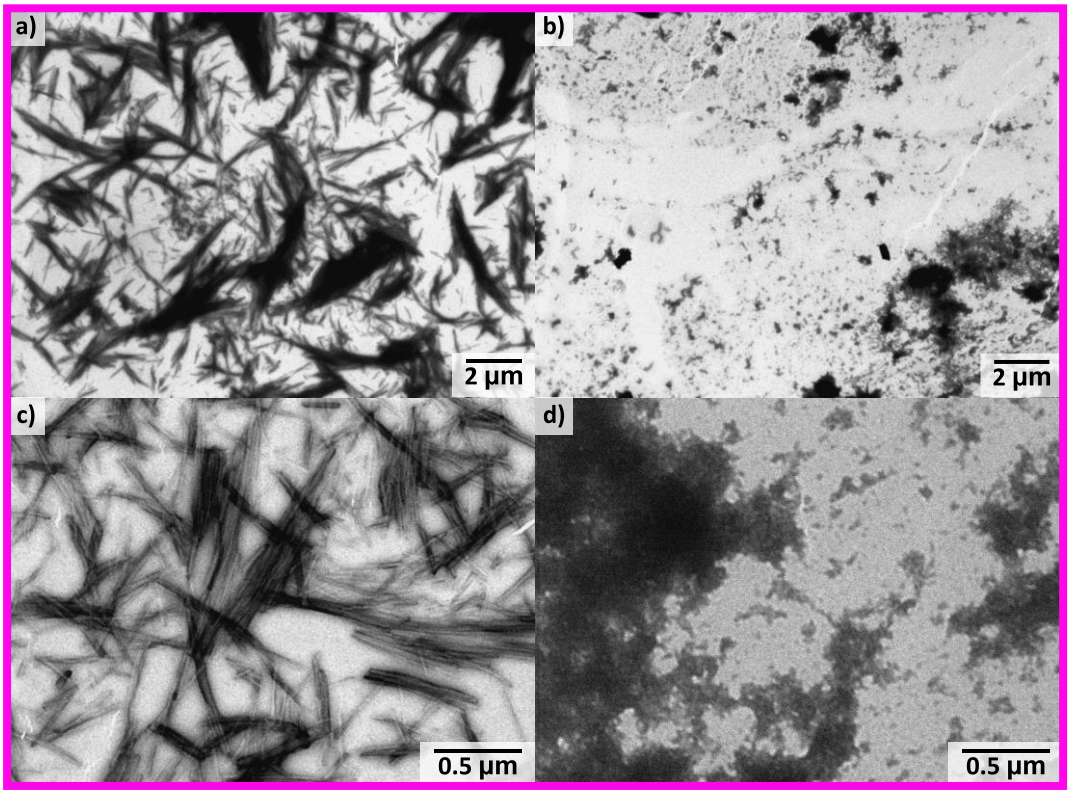

Figure 50: Transmission electron microscopy (TEM) images of the human insulin (HI) control in both (a, c) pH 2 (20% acetic acid and 137.9 mM NaCl) and (b, d) pH 7 (0.01 M PBS) fibrillation conditions.

The TEM images for the HI-only control (Figure 50) confirm the trends observed in the measured kinetics (Figure 47), because fibrillar and pre-fibrillar aggregates were observed by TEM for pH 2 and pH 7 respectively. The obtained end-state species are similar to those reported in literature where acidic pH produces long fibrils, whereas neutral pH has much smaller structures.[48] The presence of fibrillar (Figure 50a and c) and pre-fibrillar species (Figure 50b and d) in the TEM images for the HI end-state species, confirms that the sigmoidal saturation and elongation phases were attained, respectively. An attempt was made using ImageSXM[79] to quantify the fibrillar structures present, however due to the background noise levels, the analysis assumes an increased distribution for smaller objects.[80] In addition to the overlapping fibrils this made quantification using image analysis difficult. The overall higher population distribution of pre-fibrillar species (0 – 50 nm) in the pH 7 conditions, contrasts with the small population of larger assemblies observed in the pH 2 conditions. The pH 2 fibrils, which were acquired from the non-aggregated species, were on average longer (0.407 – 1.54 µm)

compared to the pH 7 pre-fibrillar species (0.02 – 0.33 µm). Morphologically for the pH 2 fibrillar species a feathering effect was observed, which is attributed to surface catalysed fibrillation events or fibrillar aggregation, whilst the pH 7 pre-fibrillar species were difficult to distinguish from the grid.

4.3.4.2. Presence of functionalised mesoporous silica microparticles on amyloid-like fibril morphology

The morphology of the fibrillar HI-only control has been observed to be affected by acidic and neutral pH conditions, and also the presence of the mesoporous silica microparticles were shown to affect the HI amyloid-like fibrillation kinetics (4.3.3.2. Presence of functionalised mesoporous silica microparticles upon the amyloid-like fibrillation kinetics of human insulin, page 145) therefore TEM will be used to investigate the effect of particles on the HI fibrillar morphology. The purpose for the TEM imaging in this study is to investigate whether there is a difference in the resultant fibrillar species upon incubation with the particles which is associated to a variation in the fibrillation pathway.

The TEM images for the HI amyloid-like fibrillation in pH 2 conditions, are shown in Figure 51, for the incubation with the hydrophobically functionalised mesoporous silica microparticles; Si (Figure 51a), C_6 (Figure 51b), ODS1 (Figure 51c) and ODS2 (Figure 51d), compared to the HI-only control (Figure 51e). All TEM images show fibrillar structures for the pH 2 conditions, therefore supporting the kinetic data that the saturation phase of the sigmoidal curve was attained because of the presence of mature fibrils. The functionalised particles give rise to fibrils which are thinner and less straight ('wispy') in morphology compared to the HI-only control. The Si incubated fibrils are morphologically similar to HI but on average shorter (~0.5 µm) and thinner compared to the HI (~1 µm), whereas the C_6, ODS1, and ODS2 incubated fibrils are much longer and exhibit twisted morphology.

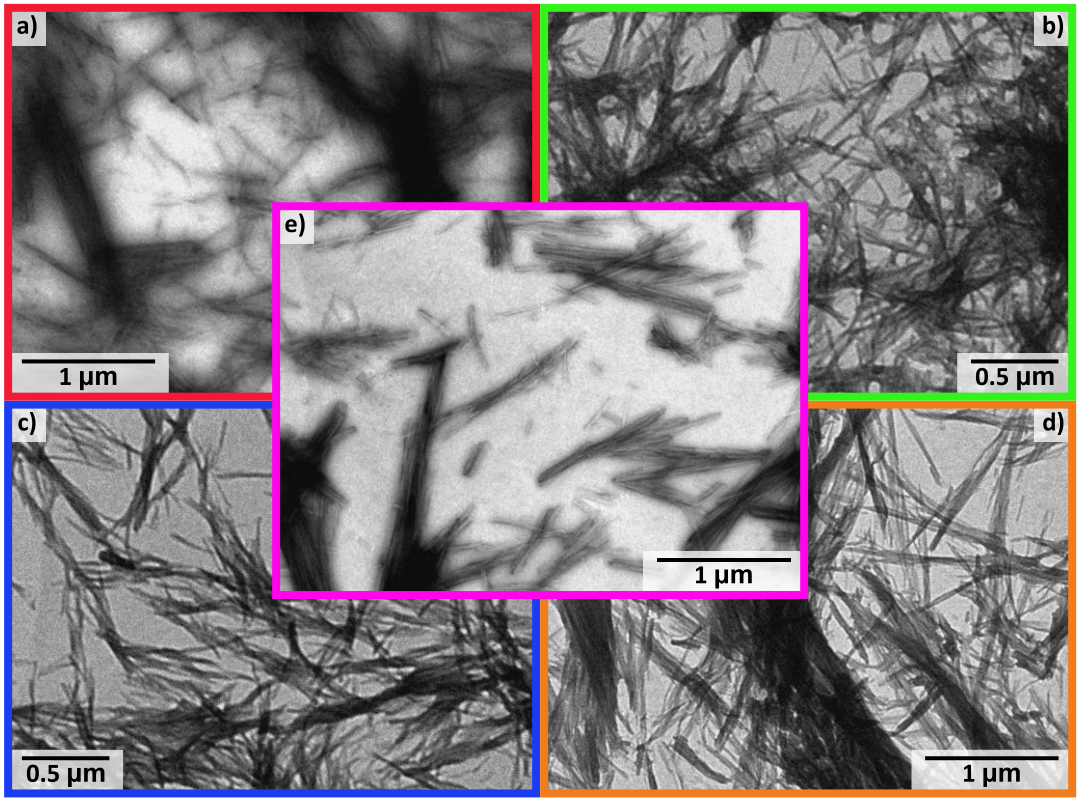

Figure 51: Transmission electron microscopy (TEM) images showing the human insulin (HI) fibril morphology at pH 2 (20% acetic acid and 137.9 mM NaCl) conditions, (e) for HI-only and in the presence of mesoporous silica microparticles; (a) Si, (b) C_6, (c) ODS1 and (d) ODS2.

The TEM images for the HI amyloid-like fibrillation at pH 2 conditions (20% acetic acid and 137.9 mM NaCl) shows that presence of the microparticles have greatly affected the observed fibrillar structures (Figure 51), with the fibrils aggregated into large clusters. In TEM images for the incubation with C_6, ODS1, and ODS2 particles (Figure 51b – d) the fibrils are longer than the HI-only control, which implies an increased elongation phase with limited fragmentation events. All the incubated particles exhibited an overall reduced fluorescence intensity kinetics (Figure 48), implying a reduced saturation phase corresponding to the maximum number of ThT-binding sites, however there appears to be more fibrils produced. The formation of fibrils with less available ThT-binding sites implies morphologically dissimilar fibrils from the control, which is shown in Figure 51.

The TEM images for the HI amyloid-like fibrillation in pH 7 conditions, are shown in Figure 52, for the incubation with the hydrophobically functionalised

mesoporous silica microparticles; Si (Figure 52a), C_6 (Figure 52b), ODS1 (Figure 52c) and ODS2 (Figure 52d), compared to the HI-only control (Figure 52e). The TEM images show a variation of pre-fibrillar structures, which is consistent with the kinetic data that the sigmoidal curve was not completed, as the saturation phase was not attained, therefore pre-fibrillar aggregates of various dimensions are observed. The incubated particle images exhibit fibrillar structures, with variable morphology, however only aggregates are observed in the HI-only control (Figure 52e). The TEM images for the incubated particles (Figure 52a – d) showed; small (~0.5 µm) fibrillar species with one large aggregate for Si, long (~0.5 – 1.0 µm) wispy fibrils for C_6, short (~0.25 – 0.75 µm) pre-fibrillar structured aggregates for ODS1, and pre-fibrillar aggregates for ODS2 with very similar morphology to the HI-control.

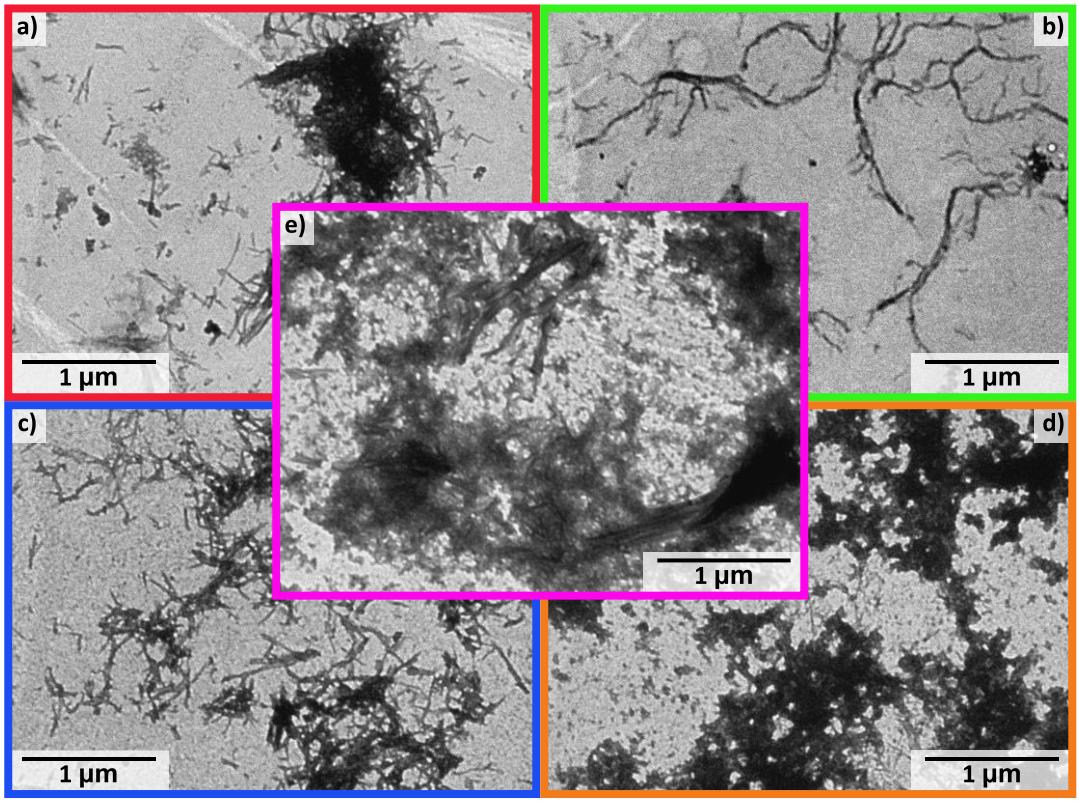

Figure 52: Transmission electron microscopy (TEM) images showing the human insulin (HI) fibril morphology at pH 7 (0.01 M PBS) conditions, (e) HI-only and in the presence of mesoporous silica microparticles; (a) Si, (b) C_6, (c) ODS1 and (d) ODS2.

The TEM images for the HI amyloid-like fibrillation at pH 7 conditions (0.01 M PBS) supports the ThT kinetics data (Figure 49) which showed that the particles enhance fibrillation, since more fibril-like aggregates are observed

by TEM (Figure 52). There are distinct morphology differences for the aggregate species in the presence of particles; smaller fibrillar structures for Si and C_6 (Figure 52a and b), for ODS1 (Figure 52c) pre-fibrillar aggregates, whilst ODS2 (Figure 52d) appears very similar to the HI-only control with limited pre-fibrillar aggregates observed. These images correspond to the ThT data, where incubation with the particles enhances fibrillation for the three particle types measured; Si, C_6 and ODS1.

The TEM images for the HI amyloid-like fibrillation in pH 2 (Figure 51) and pH 7 (Figure 52) conditions were acquired in regions free from particles, in an attempt to alleviate fibril masking.[81] The effect of HI amyloid-like fibrillation in the vicinity of the hydrophobic functionalised silica microparticles for both pH conditions are shown in Figure 53 (a – h), to observe the association of particles and fibrils. At pH 2 (Figure 53a – d) the fibrils and particles are dispersed within the imaged area, whereas in neutral pH conditions (Figure 53e – h) particles aggregate together and the fibrils aggregate.

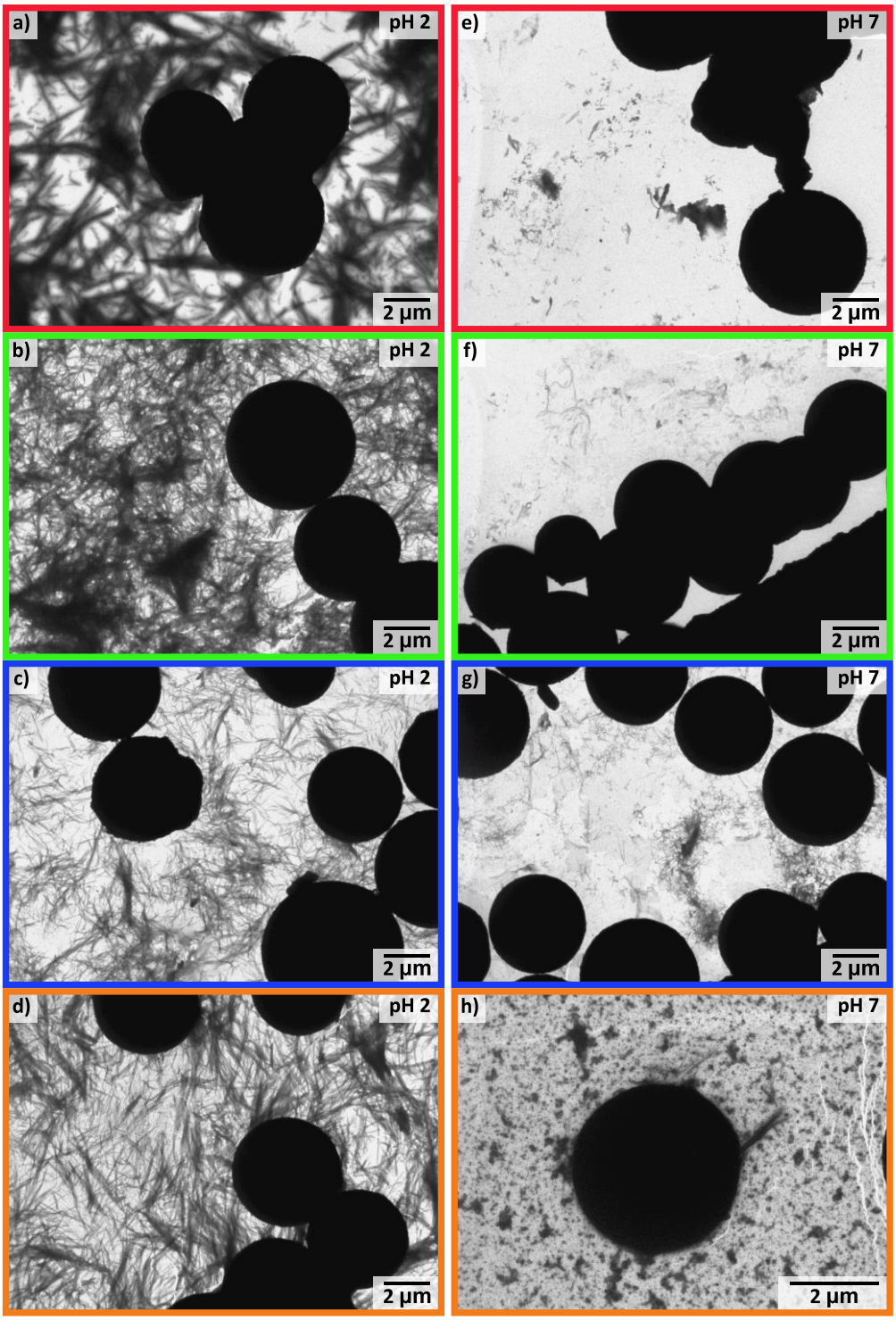

Figure 53: Transmission electron microscopy (TEM) images showing the human insulin (HI) fibril morphology for both (a-d) pH 2 (20% acetic acid and 137.9 mM NaCl), and (e-h) pH 7 (0.01 M PBS) conditions in the presence of mesoporous silica microparticles; (a, e) Si, (b, f) C_6, (c, g) ODS1 and (d, h) ODS2.

The TEM images for HI amyloid-like fibrillation at both pH conditions in the vicinity of the microparticles (Figure 53) shows that there are fewer fibrillar

structures at pH 7 (Figure 53e – h) compared to pH 2 conditions. At pH 7 there appears to be high aggregate density in the vicinity of the particles, in addition to an overall clustering of particles (specifically the particles along the grid lines) implying a hydrophobic aggregation effect. This clustering effect is not observed in pH 2, as the particles appear dispersed within the imaged area (Figure 53a – d). These TEM images show that the commercially available hydrophobically functionalised mesoporous silica microparticles, which are listed as 5 µm diameter with a polydispersity of 40%, are variable in both morphology and size[8] correlating to the DLS results (Table 2). The observed geometric distortions can occur from unstable particles, defined in the images by large protrusions, or adsorbed protein layers which are shown by a fuzzy appearance around the particle edge. These variations do not affect this investigation since the aim of this work was to investigate whether the hydrophobic functionalised particles affect the HI amyloid-like fibrillation in both pH 2 and 7 conditions.

The kinetics investigation using ThT has shown the particles affect the HI amyloid-like fibrillation pathway at both pH 2 and pH 7 conditions, through observed inhibition (Figure 48) and enhancement (Figure 49) respectively. In the presence of particles, a modified sigmoidal curve is measured implying altered fibrillation pathways, which is apparent at neutral pH with a plateau region followed by an exponential fluorescence increase. These results were supported by the TEM imaging which showed that the structural morphology of the HI amyloid-like fibrils differed in the presence of hydrophobically functionalised mesoporous silica microparticles, from the controls, in both pH conditions. The TEM images for the inhibited fibrillation kinetics at pH 2 (Figure 51 and Figure 53a – d), showed elongated and twisted fibrillar morphology for the resultant fibrils incubated with particles (C_6, OSD1 and ODS2), but shorter and thinner fibrils in the presence of Si particles. Conversely the TEM images for the enhanced fibrillation kinetics at pH 7 (Figure 52 and Figure 53e – h), showed a higher variation with the incubated particles; small fibrillar species with wispy morphology for the Si and C_6 particles, pre-fibrillar aggregates for ODS1 and ODS2. The variable structural morphology for the TEM imaged fibrils confirms that the particles induce a modified fibrillation pathway for HI.

4.3.5. The effect of mesoporous silica microparticles on the human insulin amyloid-like fibrillation pathway

The mesoporous silica microparticles were chosen to be studied because they were comprised of identical core substrate architecture but with differing hydrophobically functionalised surfaces, which enabled a controlled study for the effect of variable hydrophobic interfaces. These particles have a large surface area and exhibit dynamic behaviour within solution when suspended, therefore leading to increased interactions between the HI and particles.

Each functionalised particle varied in the degree of hydrophobicity by modification of the surface alkyl chain. Importantly the hydrophobicity arises from the alkyl chain length as opposed to other functionalisation groups. The functionalisation is comparable to studying other substrates through chemical methodologies like; silane, thiol or disulphide-based chemistry. Notably the constituent functional groups are commercially widely available, which allowed for further work by modification of other surfaces.

A hydrophobic surface is known to accelerate amyloid-like fibrillation events for hydrophobic proteins,[1,73,82,83] because the protein is more likely to adsorb therefore inducing misfolding events. Hydrophobicity is a key driving force because the exposed hydrophobic domain of the HI monomer preferentially adsorbs to the hydrophobic surface to reduce interaction with water molecules, which is entropically favourable with the release of bound water molecules. Furthermore, strong adsorption to the surface can provide a misfolding potential for HI, which unfolds to minimise exposure to water, therefore providing fibrillation through propagation of the misfolded adsorbed species.

The work in this chapter shows no clear correlation between increasing the functionalised particles' alkyl chain length and HI adsorption or amyloid-like fibrillation. Adsorption results characterised by microanalysis and IR, were inconclusive with large standard deviations suppressing any potential trends. Kinetics analysis shows that the amyloid-like fibrillation in the presence of particles does deviate from the HI-only controls, however there is no definitive trend with regards

to functionalisation. The inability to assess the kinetics of ODS2, due to its inherent fluorescence, further complicated the kinetics analysis. Fibrillar morphology also failed to provide any trend consistent with the functionalisation, however the acquired images appear to show an increased quantity of fibrils for the fibrillation with particles compared to the controls.

In addition to the influence of the particles' hydrophobicity, the HI state was also considered within this work. At acidic conditions, particularly with the buffer used in this investigation, HI existed in a predominantly monomeric state whereas at neutral pH an amalgamation of oligomeric states was possible. These states were predominantly dimer and higher order oligomeric states, hexameric species were also likely since this work used HI suspensions containing zinc.[84] The HI oligomeric state is critical for particle adsorption and amyloid-like fibrillation, the hydrophobic effect drives HI monomers to adsorb to the hydrophobic interface, however at neutral pH this exposed hydrophobic domain is inaccessible. Higher order oligomeric states, such as dimers and hexamer species, are complexes whereby the hydrophobic domain is buried between the dimeric interfaces, therefore negating the hydrophobic attraction and by extension the entropic gain is no longer a driving factor for adsorption.

This chapter has shown that the pH conditions do affect the amount of HI adsorbed to the particles by microanalysis and IR techniques. At pH 2 there is a substantial difference between the adsorbed and desorbed HI content, whereas at pH 7 there is minimal observed difference due to the significant errors attained. This difference in adsorbed HI implies that for acidic conditions the HI is strongly bound to the particles surface potentially through chemisorption. Conversely for neutral conditions the amount of HI adsorbed fluctuates, which implies that physisorption occurs corresponding to variations of bound oligomeric state HI. It is already known that pH affects the amyloid-like fibrillation kinetics and fibrillar morphology,[48,85] therefore it is not surprising that differences in ThT assays and TEM images were observed. In both conditions, the particles appear to accelerate fibrillation. In the presence of particles the lag time decreases, however in acidic pH the fluorescence intensity associated with the saturation phase reduced compared to the control,

whereas for neutral pH the intensity is greater but saturation phase has not been attained. Fibrillar morphology in the presence of the particles is also affected, where a trend is difficult to determine for pH 2, whilst at pH 7 the particles clearly favour pre-fibrillar aggregates.

The results of this work also show that the presence of the particles likely induces amyloid-like fibrillation through a different pathway as opposed to the controls. This is particularly evident in the pH 7 kinetics data where the particles appear to reach a plateau between days 1 and 2.5, which implies that the ThT dye has bound to cross-β structure with a secondary stage fibrillation occurring after 2.5 days. A plateau was not observed for the pH 2 however the decreased lag phase and saturation phase suggests that a different fibrillation pathway than the control was used. These results are supported by the differences observed in the TEM images with respect to amyloid-like fibrillation in the presence of particles. Further work is necessary in order to characterise the fibrillation pathways in the presence of hydrophobic particles; however the results clearly show differences between the HI-only controls and the incubation with particles supporting the implication that the particles affect the fibrillation pathway. It is likely that acidic conditions, which promote HI monomer adsorption, leads to an increased amyloid-like fibrillation through surface-catalysed interactions such as; seeded-growth mechanisms. Conversely for neutral pH conditions, where HI exists as a multi-oligomeric species with physisorption adsorption events, results in chaperone-type fibrillation processes by bringing the HI species together.

4.4. Conclusion

This investigation has shown that the presence of hydrophobically functionalised mesoporous silica microparticles affect the HI amyloid-like fibrillation pathway in both acidic and neutral pH conditions. The fibrillation kinetics, as measured by ThT assay, demonstrate that the particles affect the distinctive sigmoidal curve through inhibition at pH 2 and enhancement at pH 7. The associated differences between the two pH conditions implies a divergence of the amyloid-like fibrillation pathway. Enhancement at neutral pH is likely attributed to a different fibrillation pathway undertaken, since a plateau phase was observed. Conversely at

acidic pH the lag phase kinetics were decreased but demonstrated a reduced fluorescence intensity for the saturation phase. This variation was statistically significant between the control HI samples and the particles in both pH conditions, in contrast the variation between the functionalised particles themselves was insignificant, which corresponds to the effect of particles as opposed to the change in pH conditions. These results were correlated by TEM microscopy with the resultant fibrillar morphology, which showed marked differences between pH and the functionalisation types, whereby the morphological dissimilarities imply the hydrophobic functionalisation acts a scaffold resulting in various fibrillation pathways.

All hydrophobic surfaces are not equivalent, as shown by the fibril morphology for the four hydrophobically functionalised mesoporous silica microparticles. Importantly the pronounced difference in morphology suggests that a structural rearrangement is induced by the interface. The limited differences in protein adsorption and fibrillation kinetics, would imply a templated-type process occurs during prolonged adsorption which induces structural rearrangement, whilst maintaining a cross-β structure.

The results generated within this work were far from ideal because of challenges surrounding the; constituent components and analytical techniques. Firstly, although the microparticles used were commercially available, there were large variations of size and shape that were not initially accounted for. Secondly the ODS2 particles were inherently fluorescent, which resulted in failure to analyse the amyloid-like fibrillation kinetics along with the other particles studied. Thirdly the analytical techniques used for studying the adsorbed HI content on the particles, which were by microanalysis and IR techniques, were greatly affected by variations in sample preparation therefore leading to significant error values.

4.5. Supplementary

Product Code	Material	Bonded Type	Particle Size / µm (1)	Particle size dist. / µm (2)	Surface Area / m^2g^{-1} (3)	Pore diameter (range, 4) / nm	% Carbon Load
S5	Silica	-	5	± 2	220	8 (5.4 – 11.0)	-
S5 C6	Silica	Hexyl	5	± 2	220	8 (5.4 – 11.0)	4.7
S5 ODS1	Silica	Octadecyl	5	± 2	220	8 (5.4 – 11.0)	6.2
S5 ODS2	Silica	Octadecyl	5	± 2	220	8 (5.4 – 11.0)	11.5

(1) Mean particle size, µm

(2) 90% of distribution, µm.

(3) Specific surface area m^2g^{-1}, Brunauer-Emmett-Teller (BET) adsorption isotherm.

(4) 5-95% of total (nm). Measured by nitrogen adsorption.

Figure S13: Data Table specifications of the mesoporous silica microparticles utilised in this chapter; Si, C_6, ODS1 and ODS2, reproduced from Spherisorb.[8]

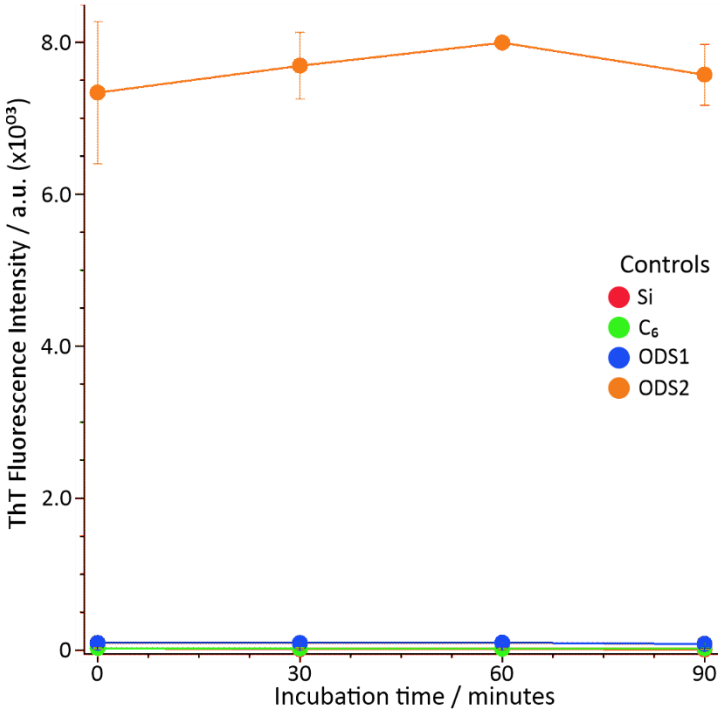

Figure S14: Thioflavin-T (ThT) end-point assay (n=3) showing the fluorescence exhibited by ThT binding onto the functionalised silica microparticles; (red) Si, (green) C_6, (blue) ODS1 and (orange) ODS2, over 90 minutes in pH 7. Note the detector saturates at 8000 a.u. therefore rendering ODS2 unfeasible in the kinetics investigation. The error bars show the standard deviation.

Bibliography

1. Sluzky, V., Tamada, J. A., Klibanov, A. M. & Langer, R. Kinetics of insulin aggregation in aqueous solutions upon agitation in the presence of hydrophobic surfaces. *Proc. Natl. Acad. Sci. U. S. A.* **88**, 9377–9381 (1991).

2. Nayak, A., Dutta, A. K. & Belfort, G. Surface-enhanced nucleation of insulin amyloid fibrillation. *Biochem. Biophys. Res. Commun.* **369**, 303–307 (2008).

3. Sluzky, V., Klibanov, A. M. & Langer, R. Mechanism of insulin aggregation and stabilization in agitated aqueous solutions. *Biotechnol. Bioeng.* **40**, 895–903 (1992).

4. Ballet, T. *et al.* DnaK Prevents Human Insulin Amyloid Fiber Formation on Hydrophobic Surfaces. *Biochemistry* **51**, 2172–2180 (2012).

5. Moores, B., Drolle, E., Attwood, S. J., Simons, J. & Leonenko, Z. Effect of Surfaces on Amyloid Fibril Formation. *PLoS One* **6**, e25954 (2011).

6. Hammarström, P. *et al.* A catalytic surface for amyloid fibril formation. *J. Phys. Conf. Ser.* **100**, 052039 (2008).

7. Hammarström, P. *et al.* An Auto-Catalytic Surface for Conformational Replication of Amyloid Fibrils—Genesis of an Amyloid World? *Orig. Life Evol. Biosph.* **41**, 373–383 (2011).

8. PhaseSeparations. Spherisorb Packing Materials and Columns for HPLCS. 16 (1985).

9. Shezad, K. *et al.* Surface Roughness Modulates Diffusion and Fibrillation of Amyloid-β Peptide. *Langmuir* **32**, 8238–8244 (2016).

10. Engelhardt, H. & Müller, H. Chromatographic characterization of silica surfaces. *J. Chromatogr. A* **218**, 395–407 (1981).

11. Gualandi-Signorini, A. M. & Giorgi, G. Insulin formulations--a review. *Eur. Rev. Med. Pharmacol. Sci.* **5**, 73–83 (2001).

12. Hua, Q. & Weiss, M. A. Mechanism of Insulin Fibrillation. *J. Biol. Chem.* **279**, 21449–21460 (2004).

13. Pohl, R. *et al.* Ultra-rapid absorption of recombinant human insulin induced by zinc chelation and surface charge masking. *J. Diabetes Sci. Technol.* **6**, 755–763 (2012).

14. Lundqvist, M., Sethson, I. & Jonsson, B. H. Protein adsorption onto silica nanoparticles: Conformational changes depend on the particles' curvature and the protein stability. *Langmuir* **20**, 10639–10647 (2004).

15. He, Q. *et al.* The effect of PEGylation of mesoporous silica nanoparticles on nonspecific binding of serum proteins and cellular responses. *Biomaterials* **31**, 1085–1092 (2010).

16. Chen, L. *et al.* Novel mesoporous silica spheres with ultra-large pore sizes and their application in protein separation. *J. Mater. Chem.* **19**, 2013–2017 (2009).

17. Taebnia, N. *et al.* The effect of mesoporous silica nanoparticle surface chemistry and concentration on the α-synuclein fibrillation. *RSC Adv.* **5**, 60966–60974 (2015).

18. Taebnia, N. *et al.* Curcumin-Loaded Amine-Functionalized Mesoporous Silica Nanoparticles Inhibit α-Synuclein Fibrillation and Reduce Its Cytotoxicity-Associated Effects. *Langmuir* **32**, 13394–13402 (2016).

19. Deere, J., Magner, E., Wall, J. G. & Hodnett, B. K. Mechanistic and structural features of protein adsorption onto mesoporous silicates. *J. Phys. Chem. B* **106**, 7340–7347 (2002).

20. SiliCycle. What is endcapping? (2018).

21. Shah, V., Bharatiya, B., Shah, D. O. & Mukherjee, T. Correlation of Dynamic Surface Tension with Sedimentation of PTFE Particles and Water Penetration in Powders. *Langmuir* **31**, 13725–13733 (2015).

22. Hsieh, S., Chang, C. & Chou, H. Gold nanoparticles as amyloid-like fibrillogenesis inhibitors. *Colloids Surfaces B Biointerfaces* **112**, 525–529 (2013).

23. Sukhanova, A. *et al.* Nanoparticles With a Specific Size and Surface Charge Promote Disruption of the Secondary Structure and Amyloid-Like Fibrillation of Human Insulin Under Physiological Conditions. *Front. Chem.* **7**, (2019).

24. Colvin, V. L. & Kulinowski, K. M. Nanoparticles as catalysts for protein fibrillation. *Proc. Natl. Acad. Sci.* **104**, 8679–8680 (2007).

25. Maiti, N., Chadha, R., Das, A. & Kapoor, S. Adsorption and sub-nanomolar sensing of thioflavin T on colloidal gold nanoparticles, silver nanoparticles and silver-coated films studied using surface-enhanced Raman scattering. *Spectrochim. Acta Part A Mol. Biomol. Spectrosc.* **149**, 949–956 (2015).

26. Ganguly, S. & Chakraborty, S. Sedimentation of nanoparticles in nanoscale colloidal suspensions. *Phys. Lett. A* **375**, 2394–2399 (2011).

27. Yazdimamaghani, M., Barber, Z. B., Hadipour Moghaddam, S. P. & Ghandehari, H. Influence of Silica Nanoparticle Density and Flow Conditions on Sedimentation, Cell Uptake, and Cytotoxicity. *Mol. Pharm.* **15**, 2372–2383 (2018).

28. Akgöl, S., Öztürk, N. & Denizli, A. New generation polymeric nanospheres for catalase immobilization. *J. Appl. Polym. Sci.* **114**, 962–970 (2009).

29. Li, Z. *et al.* Mesoporous nitrogen-rich carbons derived from protein for ultra-high capacity battery anodes and supercapacitors. *Energy Environ. Sci.* **6**, 871–878 (2013).

30. Liu, X. *et al.* Monodispersed MCM-41 large particles by modified pseudomorphic transformation: Direct diamine functionalization and application in protein bioseparation. *Microporous Mesoporous Mater.* **122**, 114–120 (2009).

31. Nagase, K. *et al.* Thermoresponsive anionic copolymer brushes containing strong acid moieties for effective separation of basic biomolecules and proteins. *Biomacromolecules* **15**, 3846–3858 (2014).

32. Niu, Y. *et al.* Formation of cyclodextrin monolayer through a host–guest interaction with tailor-made phenyltriethoxysilane self-assembled monolayer. *Colloids Surfaces A Physicochem. Eng. Asp.* **470**, 224–229 (2015).

33. Schultz, K. C. *et al.* A Genetically Encoded Infrared Probe. *J. Am. Chem. Soc.* **128**, 13984–13985 (2006).

34. Barth, A. Infrared spectroscopy of proteins. *Biochim. Biophys. Acta - Bioenerg.* **1767**, 1073–1101 (2007).

35. Haris, P. I. Can infrared spectroscopy provide information on protein-protein interactions? *Biochem. Soc. Trans.* **38**, 940–946 (2010).

36. L. Lyubchenko, Y. Amyloid misfolding, aggregation, and the early onset of protein deposition diseases: insights from AFM experiments and computational analyses. *AIMS Mol. Sci.* **2**, 190–210 (2015).

37. Chuang, E., Hori, A. M., Hesketh, C. D. & Shorter, J. Amyloid assembly and disassembly. *J. Cell Sci.* **131**, jcs189928 (2018).

38. Gade Malmos, K. *et al.* ThT 101: a primer on the use of thioflavin T to investigate amyloid formation. *Amyloid* **24**, 1–16 (2017).

39. Groenning, M. Binding mode of Thioflavin T and other molecular probes in the context of amyloid fibrils-current status. *J. Chem. Biol.* **3**, 1–18 (2010).

40. Manno, M., Craparo, E. F., Martorana, V., Bulone, D. & San Biagio, P. L. Kinetics of Insulin Aggregation: Disentanglement of Amyloid Fibrillation from Large-Size Cluster Formation. *Biophys. J.* **90**, 4585–4591 (2006).

41. Kuznetsova, I. M., Sulatskaya, A. I., Uversky, V. N. & Turoverov, K. K. Analyzing Thioflavin T Binding to Amyloid Fibrils by an Equilibrium Microdialysis-Based Technique. *PLoS One* **7**, e30724 (2012).

42. Tycko, R. Amyloid Polymorphism: Structural Basis and Neurobiological Relevance. *Neuron* **86**, 632–645 (2015).

43. Nelson, R. *et al.* Structure of the cross-β spine of amyloid-like fibrils. *Nature* **435**, 773–778 (2005).

44. Jahn, T. R. *et al.* The Common Architecture of Cross-β Amyloid. *J. Mol. Biol.* (2010). doi:10.1016/j.jmb.2009.09.039

45. Rosenauer, A., Krause, F. F., Müller, K., Schowalter, M. & Mehrtens, T. Conventional Transmission Electron Microscopy Imaging beyond the Diffraction and Information Limits. *Phys. Rev. Lett.* **113**, 096101 (2014).

46. Morris, R. E. The use of nonparametric statistics in quantitative electron microscopy. *J. Electron Microsc. (Tokyo).* **49**, 545–549 (2000).

47. Ivanova, M. I., Sievers, S. A., Sawaya, M. R., Wall, J. S. & Eisenberg, D. Molecular basis for insulin fibril assembly. *Proc. Natl. Acad. Sci.* **106**, 18990–18995 (2009).

48. Iannuzzi, C., Borriello, M., Portaccio, M., Irace, G. & Sirangelo, I. Insights into Insulin Fibril Assembly at Physiological and Acidic pH and Related Amyloid Intrinsic Fluorescence. *Int. J. Mol. Sci.* **18**, 2551 (2017).

49. Maciel, V., Yoshida, C., Pereira, S., Goycoolea, F. & Franco, T. Electrostatic Self-Assembled Chitosan-Pectin Nano- and Microparticles for Insulin Delivery. *Molecules* **22**, 1707 (2017).

50. Schoonenboom, N. S. M. *et al.* Effects of Processing and Storage Conditions on Amyloid β (1–42) and Tau Concentrations in Cerebrospinal Fluid: Implications for Use in Clinical Practice. *Clin. Chem.* **51**, 189–195 (2005).

51. Sigurdsson, E. M., Calero, M. & Gasset, M. *Amyloid proteins. methods and protocols.* (Humana Press, 2012).

52. Domigan, L. J., Healy, J. P., Meade, S. J., Blaikie, R. J. & Gerrard, J. A. Controlling the dimensions of amyloid fibrils: Toward homogenous components for bionanotechnology. *Biopolymers* **97**, 123–133 (2012).

53. Castillo-León, J. & Svendsen, W. E. *Micro and Nanofabrication Using Self-Assembled Biological Nanostructures.* (William Andrew Publishing, 2015).

54. Liu, H.-C., Chiu, M.-J., Lin, C.-H. & Yang, S.-Y. Stability of Plasma Amyloid-β 1–40, Amyloid-β 1–42, and Total Tau Protein

over Repeated Freeze/Thaw Cycles. *Dement. Geriatr. Cogn. Dis. Extra* **10**, 46–55 (2020).

55. Myers, P. *private communication*.

56. Mauri, S., Volk, M., Byard, S., Berchtold, H. & Arnolds, H. Stabilization of Insulin by Adsorption on a Hydrophobic Silane Self-Assembled Monolayer. *Langmuir* **31**, 8892–8900 (2015).

57. Danaei, M. *et al.* Impact of Particle Size and Polydispersity Index on the Clinical Applications of Lipidic Nanocarrier Systems. *Pharmaceutics* **10**, 57 (2018).

58. Gaikwad, V. L., Choudhari, P. B., Bhatia, N. M. & Bhatia, M. S. Characterization of pharmaceutical nanocarriers: in vitro and in vivo studies. in *Nanomaterials for Drug Delivery and Therapy* (ed. Grumezescu, A. M. B. T.-N. for D. D. and T.) 33–58 (Elsevier, 2019). doi:10.1016/B978-0-12-816505-8.00016-3

59. Chi, E. Y., Krishnan, S., Randolph, T. W. & Carpenter, J. F. Physical stability of proteins in aqueous solution: mechanism and driving forces in nonnative protein aggregation. *Pharm. Res.* **20**, 1325–36 (2003).

60. Shnoudeh, A. J. *et al.* Synthesis, Characterization, and Applications of Metal Nanoparticles. in *Biomaterials and Bionanotechnology* (ed. Tekade, R. K. B. T.-B. and B.) 527–612 (Elsevier, 2019). doi:10.1016/B978-0-12-814427-5.00015-9

61. Bhattacharjee, S. DLS and zeta potential – What they are and what they are not? *J. Control. Release* **235**, 337–351 (2016).

62. Roebben, G. *et al.* Interlaboratory comparison of size and surface charge measurements on nanoparticles prior to biological impact assessment. *J. Nanoparticle Res.* **13**, 2675–2687 (2011).

63. Arnebrant, T. & Nylander, T. Adsorption of insulin on metal surfaces in relation to association behavior. *J. Colloid Interface Sci.* **122**, 557–566 (1988).

64. Mollmann, S. H., Bukrinsky, J. T., Frokjaer, S. & Elofsson, U. Adsorption of human insulin and AspB28 insulin on a PTFE-like surface. *J. Colloid Interface Sci.* **286**, 28–35 (2005).

65. Mollmann, S. H. *et al.* Interfacial adsorption of insulin: Conformational changes and reversibility of adsorption. *Eur. J. Pharm. Sci.* **27**, 194–204 (2006).

66. Phillips, N. B., Whittaker, J., Ismail-Beigi, F. & Weiss, M. A. Insulin Fibrillation and Protein Design: Topological Resistance of Single-Chain Analogs to Thermal Degradation with Application to a Pump Reservoir. *J. Diabetes Sci. Technol.* **6**, 277–288 (2012).

67. Bruker. *Application Note AN 74, Attenuated Total Reflection (ATR) – a versatile tool for FT-IR spectroscopy*. (2011).

68. Nilsson, P., Nylander, T. & Havelund, S. Adsorption of insulin on solid surfaces in relation to the surface properties of the monomeric and oligomeric forms. *J. Colloid Interface Sci.* **144**, 145–152 (1991).

69. Mollmann, S. H. *et al.* Interfacial adsorption of insulin: Conformational changes and reversibility of adsorption. *Eur. J. Pharm. Sci.* **27**, 194–204 (2006).

70. Przybyciel, M. & Majors, R. E. Phase Collapse in Reversed-Phase LC. *LC GC Eur.* (2002).

71. Liu, P. S. & Chen, G. F. *Characterization Methods*. *Porous Materials* (Elsevier, 2014). doi:10.1016/B978-0-12-407788-1.00009-5

72. Biancalana, M. & Koide, S. Molecular mechanism of Thioflavin-T binding to amyloid fibrils. *Biochim. Biophys. Acta - Proteins Proteomics* **1804**, 1405–1412 (2010).

73. Jorgensen, L. *et al.* Adsorption of insulin with varying self-association profiles to a solid Teflon surface—Influence on protein structure, fibrillation tendency and thermal stability. *Eur. J. Pharm. Sci.* **42**, 509–516 (2011).

74. Shammas, S. L. *et al.* Perturbation of the stability of amyloid fibrils through alteration of electrostatic interactions. *Biophys. J.* **100**, 2783–2791 (2011).

75. Khurana, R. *et al.* A General Model for Amyloid Fibril Assembly Based on Morphological Studies Using Atomic Force Microscopy. *Biophys. J.* **85**, 1135–1144 (2003).

76. Kurouski, D., Dukor, R. K., Lu, X., Nafie, L. A. & Lednev, I. K. Normal and reversed supramolecular chirality of insulin fibrils probed by vibrational circular dichroism at the protofilament level of fibril structure. *Biophys. J.* **103**, 522–531 (2012).

77. Kurouski, D. *et al.* Disulfide bridges remain intact while native insulin converts into amyloid fibrils. *PLoS One* **7**, 1–9 (2012).

78. Rueden, C. T. *et al.* ImageJ2: ImageJ for the next generation of scientific image data. *BMC Bioinformatics* **18**, 529 (2017).

79. Barrett, S. ImageSXM. (2015). Available at: http://www.imagesxm.org.uk.

80. Barrett, S. *private communication*.

81. Williams, D. B. & Carter, C. B. *Transmission Electron Microscopy*. *Transmission Electron Microscopy: A Textbook for Materials Science* (Springer US, 2009). doi:10.1007/978-0-387-76501-3

82. Sharp, J. S., Forrest, J. a. & Jones, R. a L. Surface denaturation and amyloid fibril formation of insulin at model lipid-water interfaces. *Biochemistry* **41**, 15810–15819 (2002).

83. Giacomelli, C. E. & Norde, W. Influence of hydrophobic teflon particles on the structure of amyloid β-peptide. *Biomacromolecules* **4**, 1719–1726 (2003).

84. Nettleton, E. J. *et al.* Characterization of the Oligomeric States of Insulin in Self-Assembly and Amyloid Fibril Formation by Mass Spectrometry. *Biophys. J.* **79**, 1053–1065 (2000).

85. Sneideris, T. *et al.* pH-Driven Polymorphism of Insulin Amyloid-Like Fibrils. *PLoS One* **10**, e0136602 (2015).

Chapter 5: Hydrophobic Functionalisation of Gold Surfaces on Human Insulin Fibrillation

5.1. Introduction

This chapter will investigate how hydrophobic functionalisation affects the human insulin (HI) amyloid-like fibrillation pathway, by means of mass and structural changes on a hydrophobic functionalised gold substrate. Chapter 4 showed how the presence of hydrophobic functionalised mesoporous silica microparticles affected the amount of HI adsorbed and the fibrillation kinetics, which resulted in modification of the HI pathway as shown in the different fibril morphologies. The implication of the results from Chapter 4, suggested that it was the hydrophobic functionalisation which affected the typical amyloid-like fibrillation pathway, therefore this chapter will investigate the effect of surface hydrophobic variability, specifically the adsorption and structural features of the adsorbed HI monolayer.

The hydrophobicity of the silica microparticles were shown to result in different fibril morphologies, indicating that key fibrillation pathway differences are a consequence of HI restructuring at the interface, most likely due to the autocatalytic mechanism (1.5.1. Protein interaction at the liquid-solid interface, page 52).[1,2] The objective of this chapter is to investigate the effect that hydrophobic variability has on HI adsorption in both acidic and neutral pH as a function of time, in order to probe if the divergence of the fibrillation pathway can be observed by associated changes in mass and structural character. To investigate the difference in mass and structural features at an interface *in situ*, requires a new set of analytical techniques to be utilised; Quartz-Crystal Microbalance with Dissipation (QCM-D) and Raman spectroscopy. QCM-D is necessary to measure the mass changes associated with HI adsorbing in a flow system over time, and Raman spectroscopy to probe the structural features of the adsorbed HI to determine whether structural rearrangement has occurred. The typical operating mode of the QCM-D is with gold sensors and so in this chapter an analogous silane functionalisation is adopted for these gold sensors.

5.1.1. Hydrophobic functionalisation of gold surfaces

A bare gold substrate is spectroscopically advantageous as it is reflective and thus can be utilised in surface-sensitive techniques, and typically functionalised using self-assembled monolayers (SAMs) such as thiol and disulfide chemistry.[3–6] The conventional SAM scheme, Figure 54, for these methods is a four step approach; physisorption, surface rearrangement, chemisorption through nucleation at the sulfur head group, and reorganisation into a perpendicular orientation.[5] The ability to functionalise the gold surface is important for investigating the effect of various hydrophobic interfaces on the HI amyloid-like fibrillation pathway.

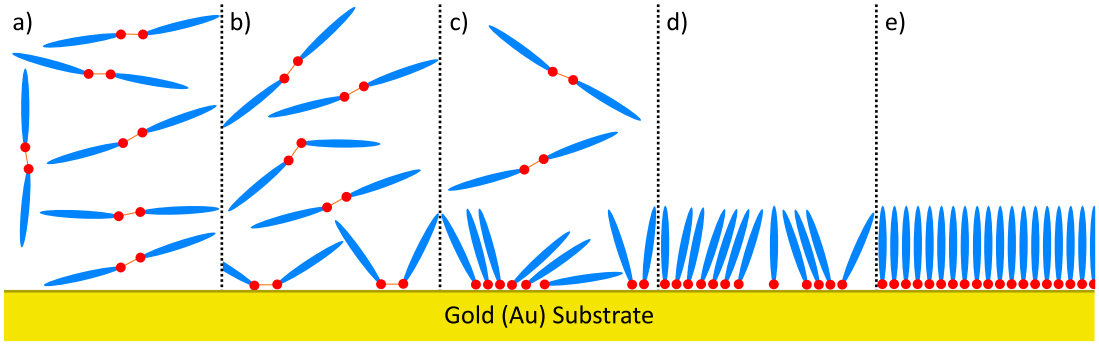

Figure 54: Schematic for the (red) disulfide functionalisation of (yellow) gold, showing; (a) free disulfide in solution, (b) physisorption, (c) surface rearrangement, (d) chemisorption and (e) perpendicular reorganisation processes. Adapted from Vericat et al.[5]

This chapter utilises disulfide chemistry in order to functionalise the surface, because of the safety concerns associated with thiols, however both result in the desired functionality.[4] For this chapter to provide complementary data to Chapter 4, similar hydrophobic interfaces were needed, which required analogous disulfide components. Firstly, the non-bonded silica surface (Si) could not be replicated, as the analogous substrate is bare gold which is hydroxylated and hydrophilic after cleaning, thereby will not provide similar fibrillation routes with possible insulin distortion.[7] Secondly the octadecyl endcapped (ODS2) surface was composed of octadecyl alkyl groups and end-capped with trimethoxysilane, which could not be replicated with disulfide chemistry on a gold substrate. The remaining functionalisation modifications hexyl (C_6) and octadecyl (ODS1, C_{18}) were both available commercially in disulfide form. The functionalisation of gold with dihexyl disulfide or

dioctadecyl disulfide, results in a hydrophobic variation associated with increasing alkyl chain length.[8]

5.1.2. Obtaining layer thickness of an adsorbate

Quartz-crystal microbalance with dissipation (QCM-D) is a sensitive technique to calculate the amount of substance adsorbed to a sensor, which is determined from the measured differences in frequency and dissipation of the oscillating quartz crystal after excitation.[9] A QCM-D instrument utilises a piezoelectric sensor to determine mass changes, this works by measuring the change in frequency of the sensor's oscillation, and the dampening of the dissipation, which refers to the wave decay time after power to the sensor is removed. Generally adsorbed species on the sensor result in a decrease in the measured frequency and a corresponding increase in the decay time. QCM-D with or without dissipation has previously been used to investigate; blood coagulation on spin-coated titanium sputtered gold sensors,[10] fibrillation of human islet amyloid polypeptide (hIAPP),[11] and the adsorption of; thiols,[12] cell tissue,[13] mucin[14] and fibronectin on the gold sensors.[15] The ability to measure both frequency and dissipation simultaneously can provide information on the species mass and the rigidity of the adsorbed layer, for example a globular protein like bovine serum albumin (BSA) results in moderate frequency reduction and a low dissipation value,[16] a typical QCM-D trace is shown in Figure 55.

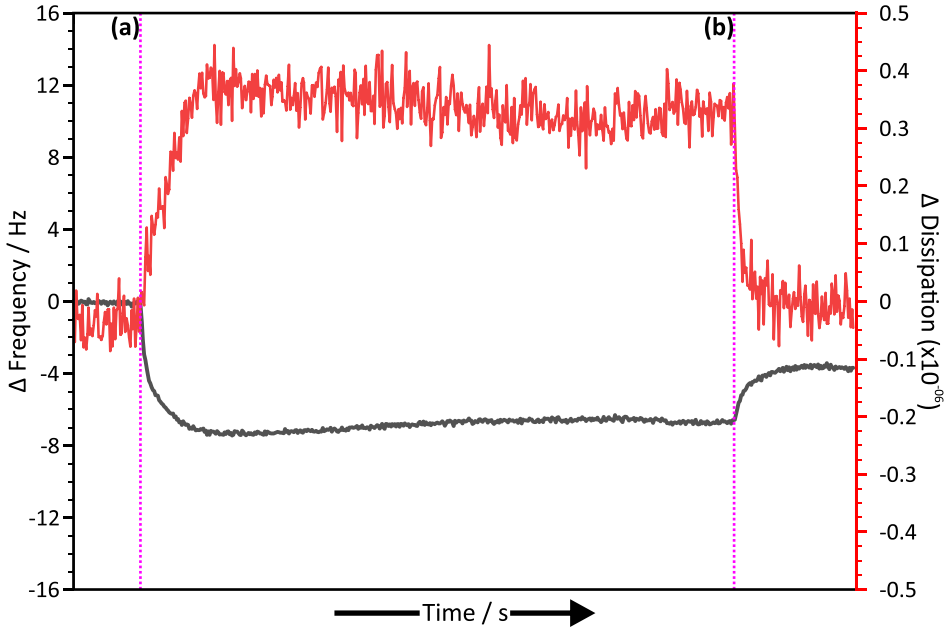

Figure 55: A typical representative quartz-crystal microbalance with dissipation (QCM-D) trace, with (black) change in frequency on the primary and (red) change in dissipation on the secondary y-axis and increasing time on the x-axis, for (a) human insulin (HI) adsorption and (b) desorption from the sensor as (magenta dashed lines) solution is changed.

The typical QCM-D trace (Figure 55) shows change in frequency (Hz, black) on the primary and change in dissipation (red) on the secondary *y*-axis, with respect to increasing time on the *x*-axis. In Figure 55, the addition of HI is shown at the first dashed line (a) and a buffer rinse is shown at the second dashed line (b). The addition of HI causes a change in the frequency and dissipation traces, with frequency decreasing and the dissipation increasing, which is associated to an increased mass and a change in the adsorbed layer viscosity.[9] The buffer rinse removes the excess HI, as shown by the increase in the frequency and decrease in the dissipation. In this QCM-D trace example (Figure 55), the frequency and dissipation do not return to the baseline prior to protein adsorption therefore this implies that not all the HI has been desorbed from the surface. This representative trace is only one of the harmonics acquired from the sensor, each sensor is capable of acquiring multiple harmonics which will be discussed further (5.1.2.1. Which harmonic?, page 169).

5.1.2.1. Which harmonic?

The QCM-D used in this research programme is a multi-harmonic instrument, where it can excite the gold sensor at different frequencies. Each gold sensor can

resonate at different harmonics (n≥1), where the first frequency (5 MHz) is termed the fundamental (n=1) with the following termed overtones (n>1). The overtones provide differing gold sensor frequencies, for example the next overtone (n=3) corresponds to a frequency of 25 MHz. In each harmonic, the frequency and corresponding dissipation are acquired simultaneously therefore allowing for information on the adsorbed layer mass and viscosity, the principals of which are shown in Figure 56.

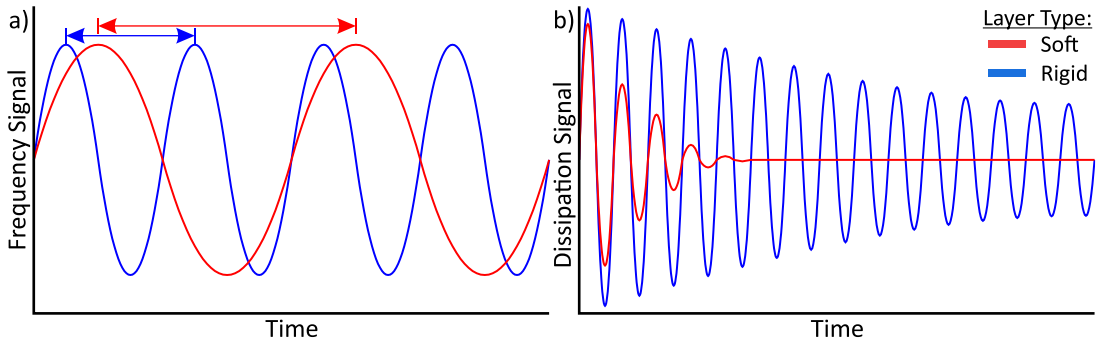

Figure 56: Typical differences observed in the measured (a) frequency and (b) dissipation profiles for (red) soft and (blue) rigid layers adsorbed to a quartz crystal microbalance with dissipation (QCM-D) sensor. The decreasing rigidity of an adsorbed layer leading to a soft or viscoelastic type results in a wave frequency reduction and rapid loss of dissipation intensity. Adapted from Biolin Scientific.[9]

As described earlier, a QCM-D sensor measures the change in frequency of the sensor's oscillation (Figure 56). Adsorption of a species to the sensor results in a change in the frequency (Figure 56a), which can be used to determine the adsorbed mass (5.1.2.2. Quantifying adsorbed layer thickness, page 171). However, acquiring the dissipation value provides further information on the adsorbed species, particularly if the adsorbed species is soft or viscoelastic therefore is not a rigid, evenly distributed thin film. The viscoelasticity of the adsorbed layer is considered by dissipation measurement (Figure 56b), which refers to the wave decay time and whether the sensor is dampened by a rigid of soft adsorbed layer.[9] Acquiring both the frequency and dissipation, allows for quantification of the adsorbed layer by a modelling system (5.1.2.2. Quantifying adsorbed layer thickness, page 171) such as; the Sauerbrey equation or Voigt model to calculate the adsorbed layer thickness.

5.1.2.2. Quantifying adsorbed layer thickness

Quantification of the adsorbed protein layer thickness is calculated by using one of two models; Sauerbrey or Voigt. The Sauerbrey equation relates frequency with mass,[17] as shown in equation (5.4):

$$\Delta m = -C \cdot \frac{\Delta f}{n} \tag{5.4}$$

where m is mass, C is a constant for quartz, Δf is change in frequency and n is the harmonic used in the analysis. The Sauerbrey equation only uses the acquired frequency to determine the adsorbed layer mass, as it assumes the layer is rigid and thin, and has previously been used in amyloid-like fibrillation studies of insulin.[18] Conversely Voigt is a viscoelastic model**,** which considers dissipation and uses all the acquired sensor harmonics,[12,19] as shown in equation (5.5):

$$G^* = G' + iG'' = \mu_1 + i2\pi f n_1 \tag{5.5}$$

where G* is the complex shear modulus, G´ is the storage modulus, G´´ is the loss modulus, μ is the elasticity coefficient, f is the frequency coefficient and n is the shear viscosity coefficient.[12] The Voigt model has previously been used to investigate amyloid-like fibrillation of glucagon resulting in multi-layer growth.[20]

Generally, both models provide adsorbed layer thickness information, however the Sauerbrey model characterises a rigid species and only utilises the frequency harmonic, whereas the Voigt viscoelasticity model can determine softer species as a result of considering the dissipation. In this research programme, QCM-D is used to quantify the amount of HI adsorbed to the functionalised gold sensor, with respect to the pH conditions and the hydrophobic functionalisation of the surface. The data will be modelled using both models to determine which model is more suitable for insulin adsorption.

5.1.3. Obtaining structural information of the adsorbed insulin

Investigation of the adsorbed HI layer requires a non-destructive surface-sensitive technique, which can provide structural information of the adsorbed layer. Raman spectroscopy (Raman) is a vibrational spectroscopic technique similar to infrared (IR) spectroscopy, in that it interrogates the vibrational

modes of a molecule however the approach is different; IR absorbs a photon to excite the molecule to a higher vibration level whereas Raman probes the scattering effect. There are three possible scattering effects; Rayleigh, Stokes, and Anti-Stokes, which are either inelastic or elastic, and are shown in Figure 57. Rayleigh is elastic as there is no change in energy, whereas both Stokes and Anti-Stokes are inelastic with an energy change. This can be expressed as the laser energy (E_0) can be scattered by a species (E_s) resulting in; Rayleigh ($E_s = E_0$), Anti-Stokes ($E_s < E_0$), and Stokes ($E_s > E_0$). The selectivity rules for Raman are different from IR. IR activity requires a change in dipole, however for Raman a change in polarizability is necessary.

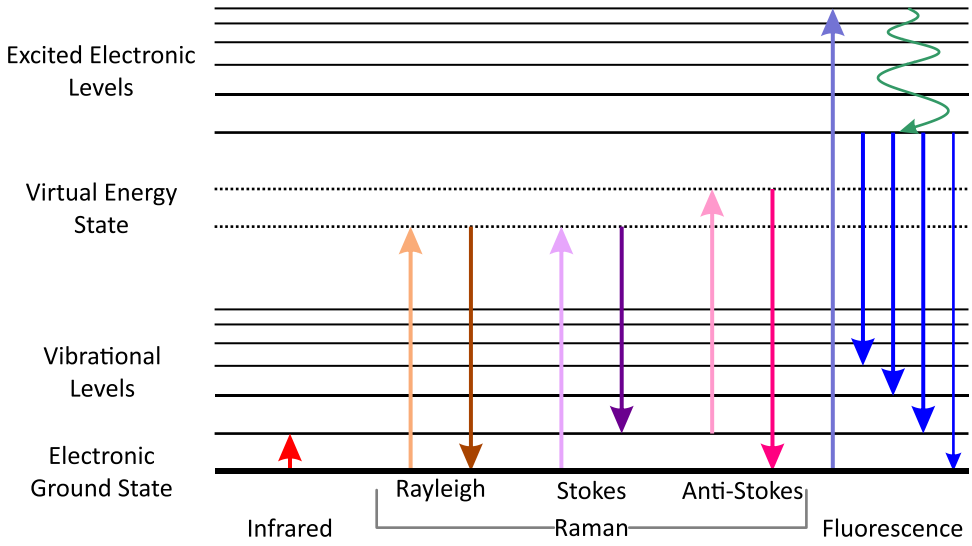

Figure 57: Energy level diagram comparing the probed energetic states of a sample by spectroscopy with the three scattering effects of (orange, purple and pink) Raman (Rayleigh, Stokes and Anti-Stokes) compared to (red) infrared and (blue) fluorescence spectroscopy. The (green) energetic relaxation is also shown for fluorescence spectroscopy. Adapted from Marcelli et al.[21]

A major benefit for the use of Raman spectroscopy within this work is that it is not affected by either water or carbon dioxide, unlike IR, therefore the presence of any encapsulated water within the adsorbed HI layer will not be of concern. Assuming an appropriate instrumental setup is already established, there are very few disadvantages to Raman spectroscopy. The inherent weakness of Raman is that scattering results in an extremely low signal, which is often overcome instrumentally by increasing the signal integration time or the laser power. The issue with this solution is that the effect of increasing the beam time or laser power, may result in

sample degradation, due to localised sample heating. A further disadvantage, albeit sample-specific, is undesired fluorescence overwhelming the Raman signal and thus the spectra, which occurs when the laser excitation wavelength is near to the electronic transition energy state of the sample.

Resolving the undesired fluorescence effects is relatively simple, assuming accessibility to other lasers, the excitation wavelength can be switched to a different wavelength further away from the transition energy state. Addressing the low Raman signal issue is more complicated, however recent spectroscopic developments have resulted in two innovative spectroscopic techniques which improve the signal by chemical and electromagnetic enhancement effects. Manipulation of metallic properties is key for both techniques, which are termed Surface Enhanced Raman Scattering (SERS) and Tip Enhanced Raman Scattering (TERS).

5.1.3.1. Surface Enhanced Raman Spectroscopy (SERS)

SERS improves the Raman spectroscopy signal by the presence of either a roughened surface or by the addition of metallic nanoparticles, because of two signal enhancement mechanisms; electromagnetic (EM) or chemical enhancement (CE). The EM is a plasmonic enhancement, which arises from the nano-systems free electrons oscillating in respect to the electromagnetic field.[22–24]. The CE, also termed Charge-Transfer, arises by the promotion of an electron from the highest occupied molecular orbital (HOMO) to the lowest unoccupied molecular orbital (LUMO) of the adsorbed species as a result of the metallic nanoparticles electronic fermi level.[25,26]

Importantly, gold nanoparticle addition can enhance the Raman signal through SERS, which is desirable however it has been reported the presence of particles can affect fibrillation.[27] The aim of this chapter is to probe the effect that hydrophobic interfaces have on the human insulin amyloid-like fibrillation pathway, it is therefore crucial no other variables are introduced.

5.2. Materials and Methods

5.2.1. Sample preparation

All the equipment and HI suspensions were prepared as described earlier, Chapter 3, and all reagents used throughout this thesis were of analytical grade or higher.

5.2.1.1. Cleaning Gold Surfaces

The gold sensors (QSX 301, Biolin Scientific) and tweezers (Erem by Weller, RS) were cleaned following the manufacturer's instructions. This involved two UV-ozone cleans (10 minutes, Bioforce Nanosciences) on either side followed by immersion in an alkaline piranha solution (ultrapure (type I) water (18.2 MΩ cm^{-1}), 30% hydrogen peroxide, 25% ammonia) and heated to ~75°C for 15 minutes, which were then rinsed excessively and dried under argon flow. A final UV-ozone clean (10 minutes) was performed on either side to oxidise the surface. The sensors were briefly stored on lint-free medical wipes in petri-dishes until surface functionalisation could occur.

Disulfide functionalisation

In two glass vials (14 mL), dihexyl disulfide (0.1 M) and dioctadecyl disulfide (0.1 M) solutions were suspended in toluene (14 mL). The freshly cleaned, dried, gold sensors were submerged within the solutions (60 minutes), removed, dried under argon flow and mounted into the QCM-D modules. The sensors were always handled carefully using the same tweezers to prevent any potential cross-contamination. Successful hydrophobic functionalisation with limited exposed hydroxylated gold, was determined by contact angle measurements using ImageJ.[28]

5.2.1.2. Synthesis of Gold Nanoparticles (50 nm core)

The synthesis of spherical gold nanoparticles was adapted from Huhn *et al,*[29] with author Mahmoud Soliman kindly providing assistance.[30] The procedure itself was a modification on Bastus *et al*[31] using a step-wise approach to form the larger cores. Firstly, all glassware utilised was thoroughly cleaned to remove any potential contaminants, which would disrupt the synthesis, and rinsed multiple times with water (18.2 MΩ cm^{-1}). A three-necked round-bottom flask was fitted with a stirrer

bar (10 mm, PTFE), a large Liebig condenser on the central neck and septa inserted into the other two necks to permit injections into the reaction vessel. This setup was installed onto a hotplate (IKA RCT Basic), equipped with a temperature-controlled probe (IKA ETS-D5) and a heating block (Radley).

Firstly, small gold nanoparticle seeds (18 nm diameter) were synthesised by heating (~75°C) the sodium citrate solution (150 mL, 1.32 mM) on a vigorous boil (~100°C) for ~10 minutes. Tetrachloroauric acid (1.5 mL, 25 mM) was injected into the solution, which resulted in a colour change after 5 minutes from straw-yellow to blue and finally a crimson red coloured solution. This solution was maintained at a vigorous boil (~100°C) for ~10 minutes, before the temperature was reduced (~90°C) and an aliquot taken (labelled g_0).

An additional volume of tetrachloroauric acid (1 mL, 25 mM) was injected into this seeded suspension at a reduced temperature (~90°C) with vigorous stirring for ~30 minutes, before two further doses (1 mL, 25 mM) were injected, each with a rest period in between (~30 minutes). The solution was then diluted, 90 minutes after first gold injection, by removal of nanoparticle suspension (55 mL, labelled g_1), with water (53 mL, 18.2 MΩ cm^{-1}, Milli-Q) and sodium citrate (2 mL, 60 mM) added into the heated solution (~30 minutes).

This process of three tetrachloroauric additions (1 mL, 25 mM) followed by dilution, occurred four more times which resulted in six aliquots (labelled g_1 to g_6). At each aliquot, the resultant nanoparticle suspension was analysed by Ultraviolet-visible (UV-Vis) spectroscopy to determine the gold nanoparticle size by their surface plasmon resonance (SPR),[32] as shown in Figure S16. After synthesis, all particle solutions were refrigerated (~4°C) until use.

5.2.2. Analytical Methodologies

5.2.2.1. QCM-D

The QCM-D instrument (E4 Q-Sense, Biolin Scientific) utilised throughout this chapter was a four-channel setup enabling simultaneous data acquisition across all four sensors. Prior to running experiments and before removing crystals, the system was cleaned as per the protocols provided by Biolin Scientific.

Cleaning

A two-step cleaning approach was consistently applied to the QCM-D instrument, a daily clean was carried out both before and after experiments, whilst a thorough clean was performed when necessary. A daily clean involved installing a 'cleaning crystal', a previously used sensor crystal now deemed unfit for purpose, into the flow module. The system was heated to ~35°C, then firstly water (18.2 MΩ cm^{-1}) was flowed through at 50 µL min^{-1} for 60 minutes, followed by a 2% sodium dodecyl sulfate (SDS) solution at 50 µL min^{-1} for 60 minutes, and then finally a final water rinse at 100 µL min^{-1} for 120 minutes. The system was left to air dry, before the sample crystals could be installed. A thorough instrument clean involved opening the flow modules to clean the seals of the flow modules. The parts were submerged in ethanol and sonicated for 5 minutes, dried under argon flow and reinstalled into the instrument. This process was performed when necessary, monthly or if there were any deviations in performance observed.

Data acquisition

The experimental procedure first required the clean sample crystals to be installed into the flow modules, the system was heated to ~21°C and water flowed at 50 µL min^{-1} for 120 minutes to equilibrate the system. Equilibrium was achieved when a flat baseline was attained across all the relevant sensor harmonics (5s averaging) using the acquisition program (QSoft 401, Biolin Scientific). The typical experiment used the flow rate of 50 µL min^{-1} with the following arrangement; water flow (18.2 MΩ cm^{-1}, 20 minutes), buffer rinse (60 minutes), HI (60 minutes), buffer rinse (20 minutes), water flow (18.2 MΩ cm^{-1}, 20 minutes), and finally the daily cleaning process.

The data was processed using QTools (Biolin Scientific), firstly the data was cropped to remove the water and cleaning cycles, which were not necessary for modelling parameters. Cropped data was then offset to the origin and fitted using Sauerbrey and Voigt models.

5.2.2.2. Raman Spectroscopy

Raman analysis of the protein adsorbed sensors was carried out using a portable probe-based instrument (MiniRam, BWTek), equipped with a red

laser (785 nm), all experiments were performed using reduced laser power (75%). The sample region was aligned below the laser (785 nm), which was optimised (1 s integration time, 1 scan) using the software (BWRam 10). Once the conditions and beam position were optimised, ten spectra were co-added at the same location, each spectrum consisted of an average of three spectra acquired at 60 s integration time, this process was repeated at several locations across the surface. The acquired spectral data were then processed using Origin (2016). Baseline correction was achieved by fitting a 3rd degree polynomial.

Surface Enhanced Raman Spectroscopy (SERS)

The HI adsorbed QCM-D sensors were dried under argon flow, and then 100 µL concentrated centrifuged gold nanoparticle solution was pipetted onto the surface and left for 60 minutes with the excess nanoparticle solution removed by filter paper blotting. The sample region was aligned below the laser (785 nm), which was optimised (1 s integration time, 1 scan) using the software (BWRam 10). Once the conditions and beam position were optimised, ten spectra were co-added at the same location, each spectrum consisted of an average of three spectra acquired at 60s integration time, this process was repeated at several locations across the surface. The acquired spectral data was exported (csv) to Origin and processed.

5.2.2.3. Contact Angle Measurements

A droplet (50 µL) of water (18.2 MΩ cm^{-1}) was added to the surface, which was then captured using a webcam. The images were then processed by ImageJ,[28] with the contact angle calculated. Representative images of the contact angle measurement are shown in Figure S15, which resulted in contact angles of; 47° for the piranha cleaned gold, 105° for the C_6 functionalised and 109° for the C_{18} functionalised surfaces. The results showed that the piranha cleaned gold was hydrophilic with contact angle less than 90°, whilst both functionalised surfaces were hydrophobic with contact angles greater than 90°.

5.3. Results and Discussion

5.3.1. The effect of pH and surface hydrophobicity on human insulin adsorption

The adsorption of HI at both pH 2 and pH 7 conditions on C_6 and C_{18} functionalised gold surfaces was monitored by QCM-D, with representative traces (where N>8) as shown in Figure 58.

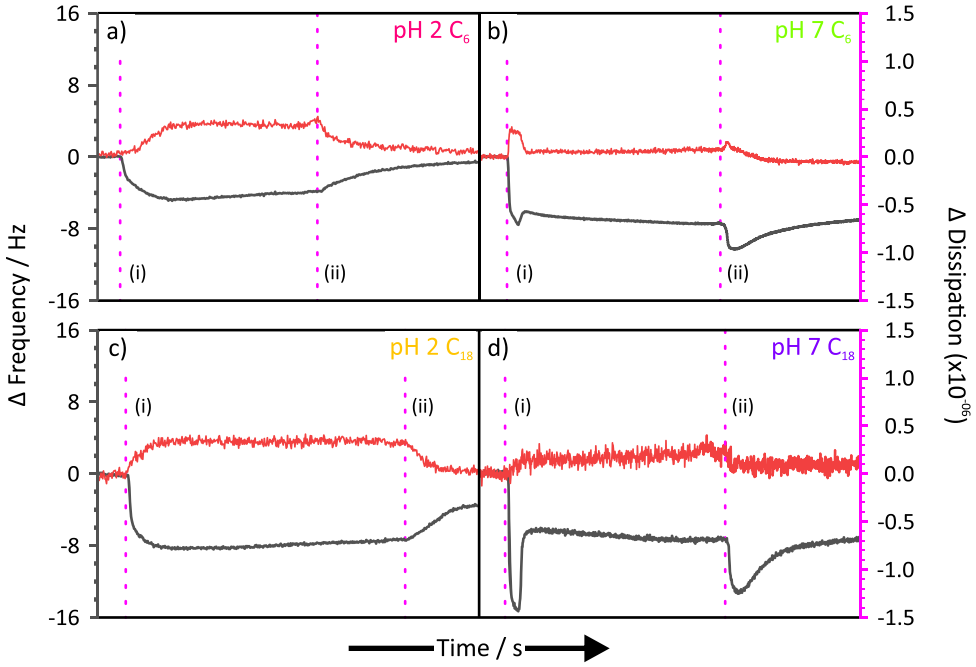

Figure 58: Representative (N>8) quartz crystal microbalance with dissipation (QCM-D) for human insulin (HI) adsorption on (a and b) hexyl (C_6) and (c and d) dioctadecyl (C_{18}) functionalised gold surfaces at (a and c) pH 2 (20% acetic acid and 137.9 mM NaCl) and (b and d) pH 7 (0.01 M PBS) conditions. Solution changes are indicated with (magenta) dashed lines for (i) buffer to HI and (ii) HI to buffer.

There are significant variations in the QCM-D traces (Figure 58) for the pH conditions and the functionalised surfaces studied, with observed differences in both adsorbed mass (black) and viscosity (red) traces.

The HI adsorbed C_6 functionalised surface at pH 2 (Figure 58a) is similar to a typical QCM-D trace where upon injection of HI into the system, frequency decreases with a corresponding dissipation increase, which is indicative of an adsorbed layer. This also correlates with a desorption event attributed to a buffer rinse, as the

frequency increases and dissipation decreases. The HI adsorbed C_6 functionalised surface at pH 7 (Figure 58b) is similar to pH 2 (Figure 58a), with respect to adsorption and desorption events but with a larger decrease in frequency which implies a larger adsorbed mass, however there are peaks present at the point of solution change.

The HI adsorbed C_{18} functionalised surface at pH 2 (Figure 58c) also shows similarity to C_6 at pH 2 and a typical QCM-D trace, however there is a larger C_{18} frequency decrease which suggests a thicker adsorbed layer. At pH 7 (Figure 58d), the frequency decreases further, suggesting an increased adsorbed layer thickness than at pH 2. Similarly, to C_6 pH 7 (Figure 58b), the peaks located at the solution change locations are also present for C_{18} pH 7 (Figure 58d), which supports the assumption that the peaks are associated to the pH 7 conditions as opposed to the functionalised surface. As the peaks were present across all the data acquired for pH 7, but not for pH 2, the implication is these peaks arise from the HI oligomeric state. In both traces (Figure 58b and d), the peaks are observed in both frequency and dissipation which is indicative of increased protein mass and viscosity change, implying that it is attributed to the HI oligomeric association and dissociation. The first peak which is the introduction of HI into the system is likely attributed to HI adsorption, dissociation and diffusion on the surface, whilst the second peak correlates with the buffer rinse implying reassociation of the HI.

Overall, there are no observed changes between the “adsorption” and “desorption” events in any of the representative traces (Figure 58), as both frequency and dissipation remain stable, which implies that no structural rearrangement occurs to the adsorbed layer or multi-layer formation. The adsorption of HI to the hydrophobically functionalised gold sensor occurs over a very short timeframe, therefore unlikely to undergo any extensive structural reorganisation without any thermal activation.[33] Furthermore, the frequency does not return to baseline in any trace, which implies a very rigid HI monolayer adsorbed or residual trace amount. The frequency variations across all four traces suggests that both pH and surface functionalisation affect the layer thickness, however quantification is necessary to ascertain thickness information (5.3.1.1. Quantification of the adsorbed human insulin layer thickness, page 180).

5.3.1.1. Quantification of the adsorbed human insulin layer thickness

The thickness of the adsorbed HI layer on the C_6 and C_{18} functionalised gold surfaces was quantified by using both the Sauerbrey and Voigt models, the results of which are shown in Figure 59.

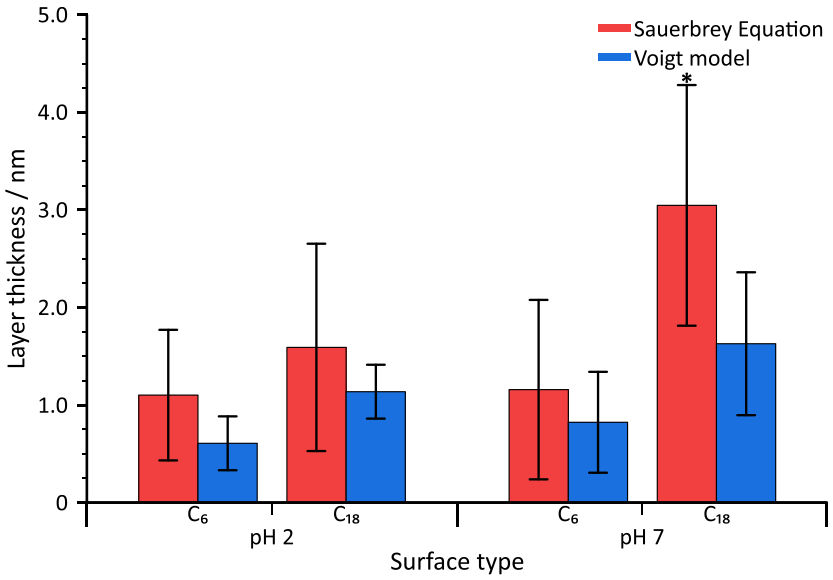

Figure 59: Quantification of the adsorbed human insulin (HI) layer thickness on the hexyl (C_6) or octadecyl (C_{18}) functionalised gold substrate at pH 2 (20% acetic acid and 137.9 mM NaCl) and pH 7 (0.01 M PBS) as determined by the (red) Sauerbrey equation or (blue) Voigt model. All data shown consisted of N>8, (*) statistical significance was determined by ANOVA with Tukey post-hoc analysis at $p < 0.05$.

The adsorbed HI layer thickness as quantified by the Sauerbrey and Voigt models (Figure 59) show that the layer thickness differs with respect to; pH condition, surface functionalisation and the model used. The mean results show that there is a thicker adsorbed HI layer at pH 7 compared to pH 2, across both functionalised surface types determined by either Sauerbrey (red) or Voigt (blue) models. This increased layer thickness for pH 7 implies that it is the HI oligomeric species which adsorbs to the interface, whereas for pH 2 the reduced thickness corresponds to monolayer adsorption. The effect of pH on the C_{18} functionalisation highlights that the oligomers provide an increased layer thickness compared to the monomers, however this is not observed for the C_6 functionalisation.

The C_6 functionalisation results in a thinner adsorbed HI layer compared to the C_{18} surface and only a minor increase for pH 7 is observed, which implies that there are other factors affecting the HI adsorption other than pH. It is possible that the C_6 functionalised surface was inhomogeneous or unstable resulting in areas of exposed gold, which can destabilise the HI particularly the monomer through unfolding as previously reported by Welinder *et al*.[7] Unfolding of the HI monomer, will reduce the adsorbed HI layer thickness in both pH conditions. Conversely, the C_{18} functionalisation shows a thicker adsorbed HI layer for pH 2, which increases for the pH 7 conditions implying that either the C_{18} functionalisation is more stable or homogeneous than C_6, or that the increasing alkyl chain length leads to greater hydrophobicity thus adsorption.[8] Another possible explanation is a result of the functionalisation, where the silica microparticles in Chapter 4 were endcapped to reduce the potential for hydrophobic collapse,[34] which results in the functionalised groups falling onto the surface therefore increasing layer thickness.

The quantification of adsorbed layer thickness (Figure 59) highlights that the Sauerbrey (red) and Voigt (blue) models provide differing layer thickness, although the general trends of increased layer thickness for pH 7 and the C_{18} functionalised surface compared to C_6 remain true. Layer thickness as determined by Sauerbrey is shown to have higher mean values than the Voigt model, which is confirmation that the models do not produce comparable results. The Sauerbrey model calculates layer thickness using the acquired frequency only, which assumes that the adsorbed layer is rigid and a thin film,[9] therefore this model is likely overestimating the adsorbed HI layer thickness since HI is a soft protein.[35] Conversely the Voigt model considers the dissipation and is better suited for soft proteins, which implies the ideal modelling system for HI. However, as observed with the C_6 functionalised surface at pH 2 if HI monomers are adsorbing directly to the exposed gold surface then unfolding may occur,[7] therefore resulting in a rigid thin film that is better suited for the Sauerbrey model.

Overall, the QCM-D results have shown that HI suspended in pH 7 conditions results in the largest amount of adsorbed species as shown by the increased layer thickness compared to pH 2, as this is likely due to the oligomeric state. An increased

thickness for C_{18} compared to C_6, which suggests that either the C_6 functionalisation is unstable or that the hydrophobicity attributed to alkyl length promotes HI adsorption. If the C_6 surface is unstable resulting in degradation of the functionalised interface thus exposure of the gold surface, then HI distortion is likely to occur as evidenced by Welinder *et al*.[7] This can be investigated by using Raman spectroscopy to probe whether the disulfide bonding is intact.

5.3.2. Investigating adsorbed protein structural rearrangement by Raman spectroscopy

The QCM-D results have shown on average an increased layer thickness for the pH 7 samples compared to the pH 2, which likely arises from the HI oligomeric state, whilst the C_{18} functionalised gold surfaces are generally thicker than the C_6 at both pH conditions. A possible explanation for the difference in layer thickness for the functionalised surfaces, with an observed thickness reduction for the C_6 surfaces, arises from stability of the interface specifically whether the functionalisation was inhomogeneous or removed from the surface therefore rending an exposed gold surface. Adsorption of HI onto an exposed gold surface, may induce protein unfolding because of the gold – sulfur interactions (1.5.1. Protein interaction at the liquid-solid interface, page 52), therefore Raman spectroscopy is used here to investigate the HI structural features.

5.3.2.1. The effect of hydrophobic functionalisation on Raman spectroscopy

Raman spectra of the three control surfaces; gold, C_6 and C_{18} functionalised, with no HI adsorbed are shown in Figure 60.

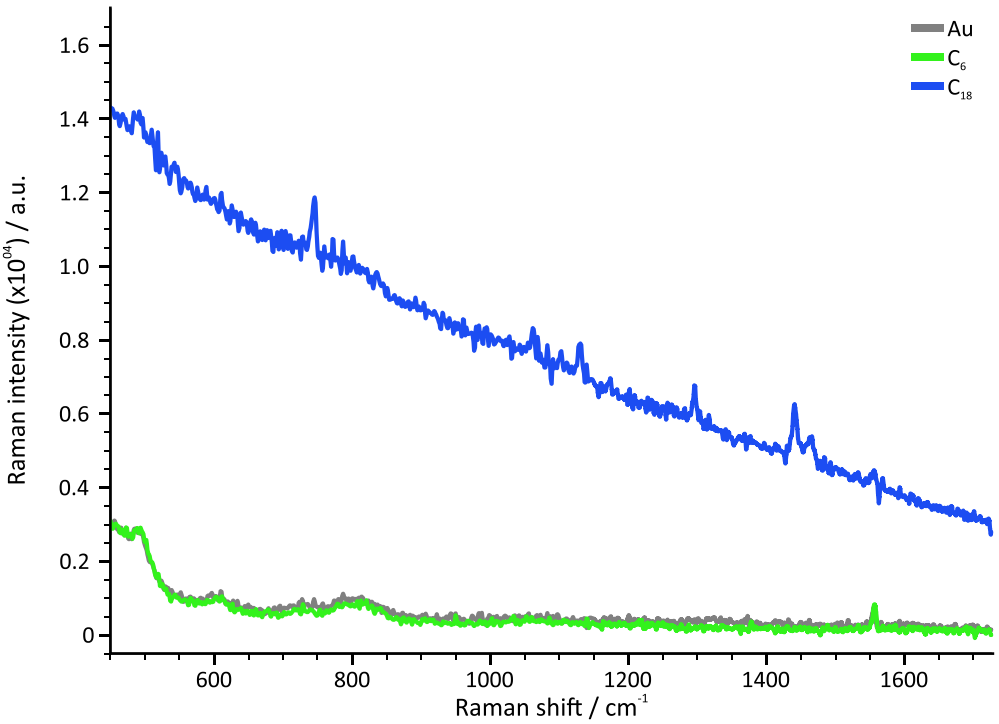

Figure 60: Raman spectra for the control surfaces; (grey) bare gold, and disulfide functionalised (green) hexyl (C_6) and (blue) octadecyl (C_{18}).

The Raman spectra for the gold (grey) and C_6 functionalised (green) control surfaces (Figure 60) show a flat baseline with limited Raman intensity, whereas the C_{18} functionalised (blue) surface has an overall higher Raman intensity with a sloping background. The sloping background for the C_{18} interface (blue) is indicative of fluorescence,[36] which implies that the long chain alkyl group contributes to this effect. Ideally the observed fluorescence would be resolved by changing the excitation wavelength of the laser used,[37] however as only a 785 nm probe was available this was not possible. Baseline correction of the spectra is therefore necessary (5.2.2.2. Raman Spectroscopy, page 176), which results in the normalised Raman spectra as shown in Figure 61.

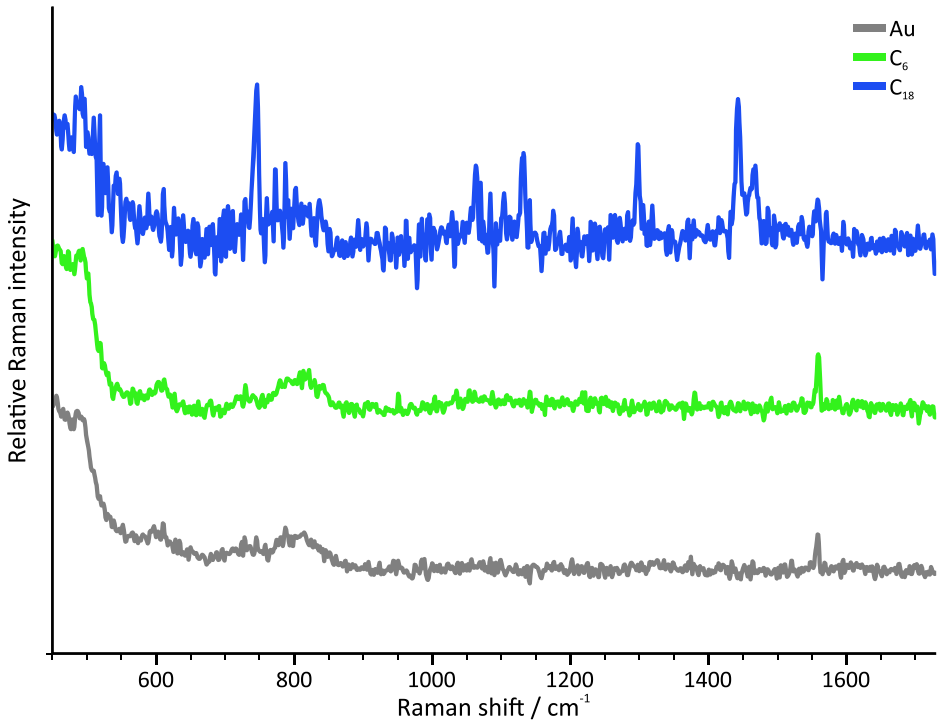

Figure 61: Baseline corrected and spectra normalised (490 cm^{-1}) for the control surfaces; (grey) bare gold, and disulfide functionalised (green) hexyl (C_6) and (blue) octadecyl (C_{18}).

Removal of the fluorescence background and normalisation of the control surface spectra to the similar 490 cm^{-1} peak, results in the similar spectra shown in Figure 61. Overall there is a lack of signal clarity across the three surfaces, particularly the C_{18} functionalised, which is very noisy and difficult to study. The sharp feature present at 1556 cm^{-1} corresponds to the atmospheric oxygen Raman peak.[38] The appearance of the atmospheric oxygen and nitrogen Raman peaks are evidence that there is a significant lack of Raman signal present on these surfaces, which is expected since metals are Raman in-active.

5.2.2.2. The effect of pH on human insulin adsorption at the functionalised interface

Raman spectra for the adsorption of HI at both pH 2 and 7 conditions on the C_6 functionalised surface is shown in Figure 62.

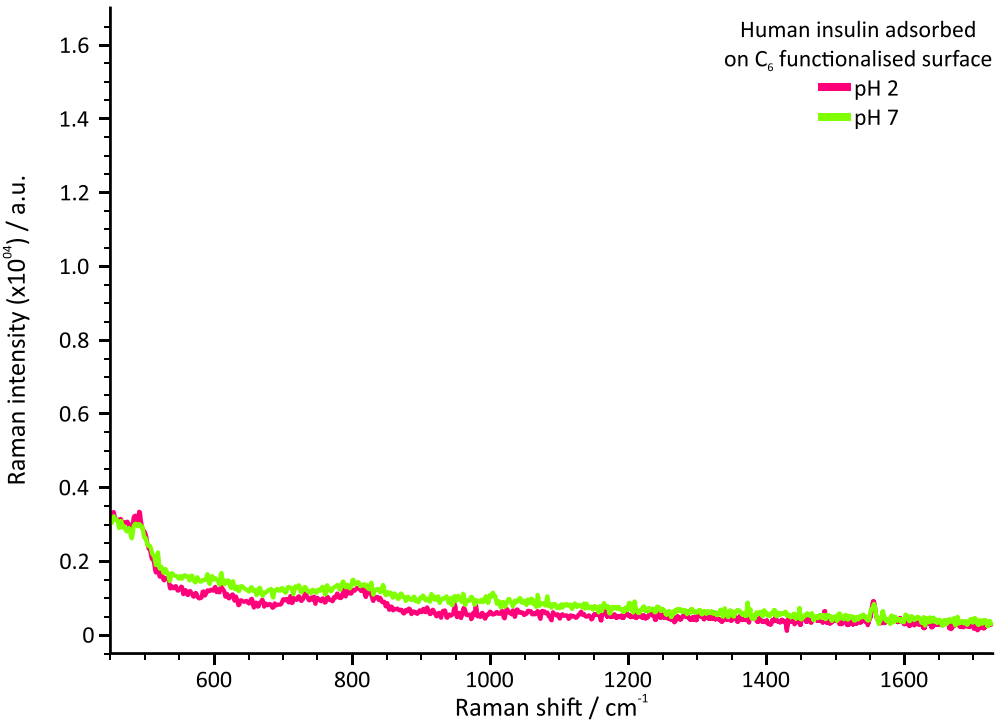

Figure 62: Raman spectra for the adsorbed human insulin (HI) on the hexyl (C_6) functionalised gold surface at (pink) pH 2 (20% acetic acid and 137.9 mM NaCl) and (green) pH 7 (0.01 M PBS).

Raman spectra of the HI adsorbed onto C_6 functionalised gold surface at pH 2 (pink) and pH 7 (green) shows a strong similarity to the control C_6 surface (Figure 60). Similarly to the control spectra, there is limited Raman intensity for adsorbed HI at either pH 2 or pH 7, as the atmospheric peaks are also observed. The corresponding Raman spectra for the adsorption of HI at both pH 2 and 7 conditions on the C_{18} functionalised surface is shown in Figure 63.

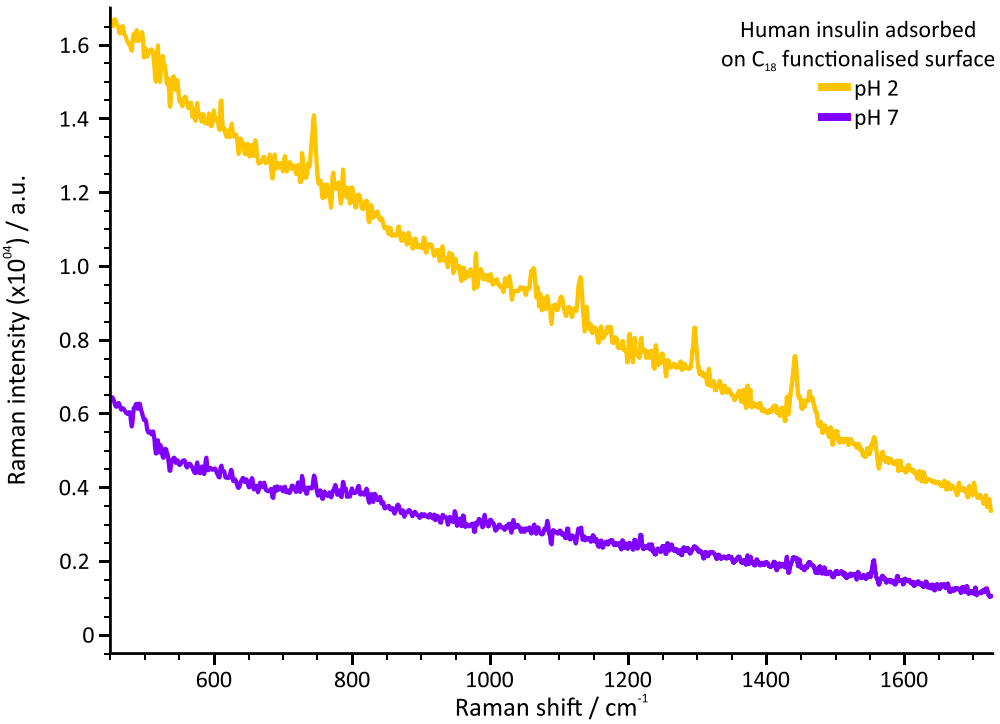

Figure 63: Raman spectra for the adsorbed human insulin (HI) on the octadecyl (C_{18}) functionalised gold surface at (orange) pH 2 (20% acetic acid and 137.9 mM NaCl) and (purple) pH 7 (0.01 M PBS).

Equally the Raman spectra of HI adsorbed onto the C_{18} functionalised gold surface (Figure 63) at pH 2 (blue) and pH 7 (red), also resembles the corresponding C_{18} functionalised control surface (Figure 60). The characteristic fluorescence background is present in both pH 2 and 7 spectra, with an increased intensity for pH 7, which further implies that the fluorescence is a result of C_{18} functionalisation.

The Raman spectra for HI adsorbed to both C_6 and C_{18} functionalised gold surfaces regardless of pH conditions is very similar to the control spectra, implying that there is trace amount of adsorbed HI, which is confirmed in QCM-D (Figure 59). A challenge due to the limited Raman-active species present, is the lack of signal intensity or low signal-to-noise, which increases the difficulty in discerning the Raman signal thus enhancement is necessary. One method for signal enhancement is through surface roughening, however this will damage the sensor therefore preventing normal QCM-D operation and influence functionalisation and HI adsorption mechanisms at the interface. A better solution is to utilise metallic particles onto the surface, in order to exploit the surface enhanced Raman effects such as EM or CE. In this research programme, gold nanoparticles with a citrate shell

are preferable since the core correlates to the gold substrate thus reducing any potential variability arising from different substrate properties.

5.3.2.3. The need for surface enhanced Raman scattering (SERS)

In this work, gold nanoparticles with a citrate shell were used to enhance the Raman intensity by SERS which resulted in a ten-fold increase in Raman intensity. The SERS spectra for the HI at pH 2 or pH 7 conditions adsorbed to C_6 or C_{18} functionalised surfaces, is shown in Figure 64 and the non-baseline corrected or normalised in Figure S17.

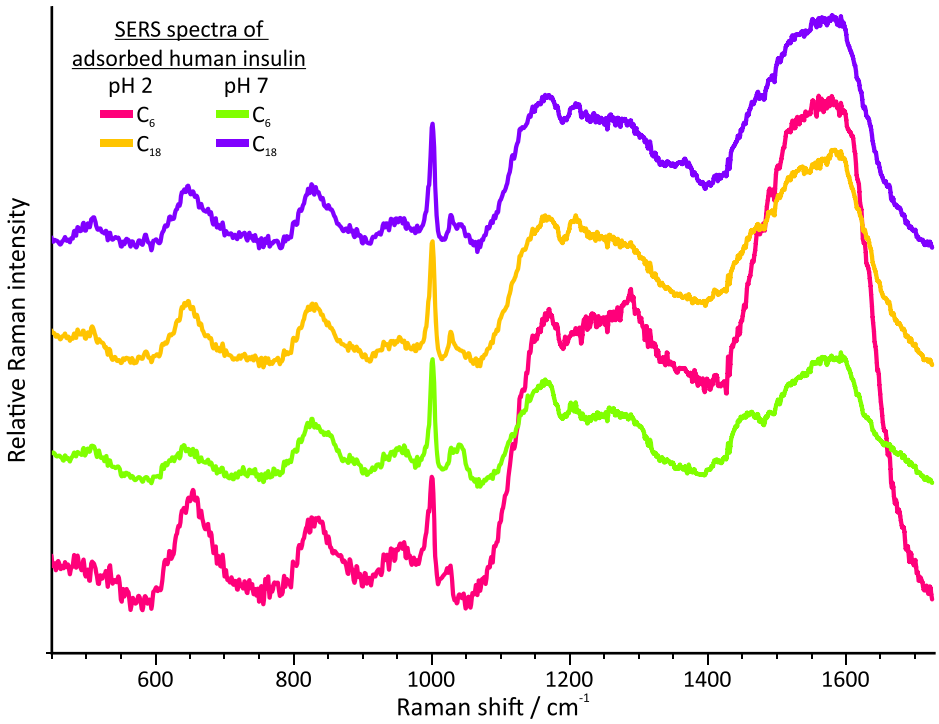

Figure 64: Surface enhanced Raman spectra (SERS), which have been baseline corrected and normalised (1000 cm^{-1}) for the adsorbed human insulin (HI) on the hexyl (C_6) or octadecyl (C_{18}) functionalised gold surface at either pH 2 (20% acetic acid and 137.9 mM NaCl) or pH 7 (0.01 M PBS) conditions. (pink) C_6 pH 2, (green) C_{18} pH 2, (orange) C_6 pH 7 and (purple) C_{18} pH 7.

The use of gold nanoparticles to generate SERS spectra, has a clear enhancement on the Raman spectra (Figure 64) with elucidation of structural features for the adsorbed HI samples on the; C_6 pH 2 (pink), C_{18} pH 2 (green), C_6 pH 7 (orange) and C_{18} pH 7 (purple) surfaces. The SERS spectra (Figure 64) have been baseline corrected and normalised to the phenylalanine peak (1000 cm^{-1}) to correlate the wavelength shifts and intensity changes for the adsorbed HI samples. It

is apparent from the normalisation that the Amide I band (1650 cm^{-1}) varies in intensity across all four samples, however discrimination of the various modes contributing to this peak is not suitable due to the lack of signal and resolution. The key characteristic peaks of the SERS spectra are correlated with literature as detailed in Table 3, with additional assignments provided in Figure S18.

Table 3: The key vibrational assignments for the SERS Raman spectra that differentiate between the four samples; adsorbed human insulin (HI) on the hexyl (C_6) or octadecyl (C_{18}) functionalised gold surface at either pH 2 (20% acetic acid and 137.9 mM NaCl) or pH 7 (0.01 M PBS).

Wavenumber /cm^{-1}	**Assignment**	**pH 2**		**pH 7**	
		C_6	**C_{18}**	**C_6**	**C_{18}**
500 – 530	S – S stretch[39]	-	510	510	510
640	Tyrosine (Tyr)[39]	645	645	645	645
830 – 853.	Tyr stretch and ring breathing[39,40]	825, 855	825, 855	825, 855	825, 855
938 – 940	C – C skeletal α-helical stretch[39,40]	950	950	950	950
1007	Phe stretch and ring breathing[39,40]	1003	1003,	1003	1003
1028	Phe stretch and ring breathing[39,40]	1023	1027	1027	1027
1050	β-sheet stretch (Amide III)[40]	-	-	1040	1040
1066 – 1162	C – N stretch[39,40]	1161	1161	1161	1161
1209	Tyr	-	1208	1208	1208
1276 - 1277	Tyr/Phe, Amide III α or random coil, CH deformation[39,40]	1285			

The key Raman vibrational modes of the adsorbed HI samples (Table 3), highlight the structural differences between the samples with respect to the pH and functionalised surface. The vibrational modes associated to HI are present in the spectra therefore it is evident that the Raman spectroscopy is probing the HI adsorbed layer and any wavelength shifts are associated to differences in the HI structure.[41,42] There is a noticeable spectral deviation between the surface functionalisation as shown within the disulfide region (~510 cm^{-1}), specifically its absence within the HI adsorbed to the C_6 surface at pH 2. The disulfide region is significant because the HI monomer consists of three disulfide bonds connecting the cysteine residues, which are retained during fibrillation[43,44], but have been shown to fragment upon adsorption to bare gold.[7] The absence of the disulfide Raman signal

for the C_6 surface at pH 2 indicates that the HI monomer has adsorbed to the gold surface, which correlates with the QCM-D data (Figure 59) showing that the C_6 functionalised surface at pH 2 resulted in the thinnest adsorbed HI layer. The presence of the disulfide region in the C_{18} surface at pH 2, supports the implication that the C_6 functionalisation is unstable or inhomogeneous thus exposing the bare gold substrate allowing HI monomer adsorption. Further evidence that the HI adsorbed on the C_6 surface at pH 2 is structurally different to the other samples is the absence of the tyrosine peak (1209 cm^{-1}) which implies the tyrosine residue is located in a different environment to that other the other HI adsorbed to C_6 at pH 7 or C_{18} surfaces.

Differences in the secondary structure of HI adsorbed to the C_6 functionalised surface at pH 2 are also observed in the Amide III region (1220 – 1300 cm^{-1}), which is studied in lieu of the Amide II region (1520 – 1570 cm^{-1}) because this is not observed due to the weak signal from near-IR excitation (785 nm),[44,45] and the Amide I region (1640 – 1678 cm^{-1}) is suppressed as an effect of SERS.[46] There is a sharp α-helical peak (1276 – 1277 cm^{-1}) for the C_6 functionalised surface at pH 2 that is not observed for the other surfaces, which implies α-helical structural rearrangement or alignment on the surface as the surfaces have not been thermally activated.[33] These results overall show that the adsorbed HI on the C_6 functionalisation at pH 2, is structurally different to the other three conditions studied, which supports the QCM-D data that the C_6 functionalisation layer is unstable as shown by HI monomers adsorbing to the exposed gold surface and unravelling.[7]

The other three surfaces are not spectrally identical, with deviations associated to the pH conditions specifically the presence of a β-sheet stretch peak (1050 cm^{-1}) for the C_6 and C_{18} functionalisation at pH 7. The shape of the C-N peak (1066 – 1162 cm^{-1}) also varies with pH for both C_6 and C_{18} functionalisation, with a singlet shape for pH 2 and doublet for pH 7. These spectral differences indicate that the adsorbed HI is of different oligomeric states for pH 2 and pH 7, which is consistent with the results obtained by QCM-D.

In summary, these results show that although Raman spectroscopy is suitable to probe the adsorbed HI layer on hydrophobically functionalised gold surfaces, SERS

is necessary in order to characterise the surface. The SERS spectra have shown that there are subtle differences across all four sample sets, which indicate that the hydrophobic functionalisation (specifically alkyl chain length) and pH affect the adsorbed HI structural arrangement. The C_6 functionalised surface, specifically at pH 2, appears to be unstable or inhomogeneous as shown by the absent disulfide bonding region and a defined α-helical peak (1276 – 1277 cm^{-1}) which correlates with the QCM-D data implying a proportion of the adsorbed HI is to an exposed gold surface. It is likely that the spectroscopic profile is an amalgamation of structural features consistent with HI adsorbed to the hydrophobic C_6 functionalisation and hydrophilic bare gold, with the latter affecting HI stability. Conversely the C_6 functionalised surface at pH 7, does not exhibit the same characteristics as pH 2 but similar to the C_{18} functionalised surface, this is likely due to the oligomeric state of the HI adsorbed as the hydrophobic domain is buried within the oligomer thus protected from fragmentation. The C_{18} surface functionalisation spectra are similar, with differences arising from the pH conditions.

Differences in the pH conditions are observed in the SERS spectra (Figure 64), where both pH 7 show a Raman feature (1050 cm^{-1}) that is not within the pH 2 spectra. This feature corresponds to the β-sheet stretch,[40] which implies that the pH 7 adsorbed HI layer consists of oligomeric species. This confirms that the HI is of a different oligomeric state at pH 2 and pH 7 conditions, which correlates with the QCM-D that implicated the thicker HI adsorbed layers for pH 7 were attributed to oligomeric adsorption.

Overall, the Raman spectra are still noisy and present limited opportunities to study the surfaces due to the acquisition parameters, as any increase in acquisition times or laser power led to degradation of the sample through localised heating.[47] The excitation wavelength used (785 nm) also limited the investigation as the samples exhibited a fluorescence background, thus baseline correction was necessary to reduce this effect from overwhelming the spectra. Ideally other techniques, such as change in wavelength, would be used to avoid or reduce this effect in future.

5.4. Conclusion

The work in this chapter has shown that the hydrophobically functionalised (C_6 or C_{18}) gold surfaces differ in the adsorption of HI with respect to pH 2 and pH 7 conditions. Observation of the HI adsorption layer to the surface by QCM-D showed greater HI adsorption for C_{18} than for C_6 functionalised surfaces at both pHs, which implied that the increased alkyl length promoted adsorption. A similar trend was also observed with the pH conditions, where pH 7 had an increased adsorbed HI layer thickness as opposed to C_6, which was associated to the oligomeric state. Conversely, the C_6 functionalised surface at pH 2 conditions resulted in thin layers, which the modelling showed were a rigid layer because of HI unfolding.

Raman spectroscopy was used to investigate structural changes of the adsorbed HI, however the results showed minimal Raman intensity therefore SERS was necessary. The Raman spectra corresponded with the QCM-D data, with the adsorbed C_6 surface at pH 2 conditions having lost the disulfide bonding region which confirmed that the HI had unfolded on adsorption to the surface. Conversely the thicker adsorbed layer associated to pH 7 adsorption, exhibited a β-sheet feature which was not present for pH 2, therefore implying oligomeric adsorption. The oligomeric adsorption is correlated with the two strong peaks in the frequency and dissipation shown in QCM-D at pH 7, and attributed to the structural reorganisation of the oligomeric species on adsorption.

5.5. Supplementary

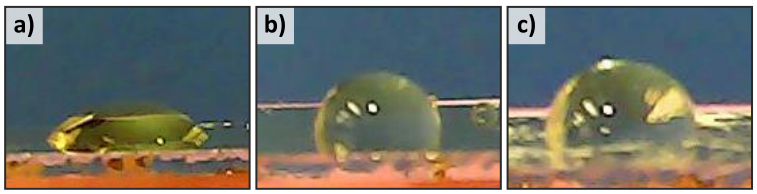

Figure S15: Representative images of the samples used for contact angle measurement, (a) piranha cleaned gold, (b) C_6 functionalised and (c) C_{18} functionalised.

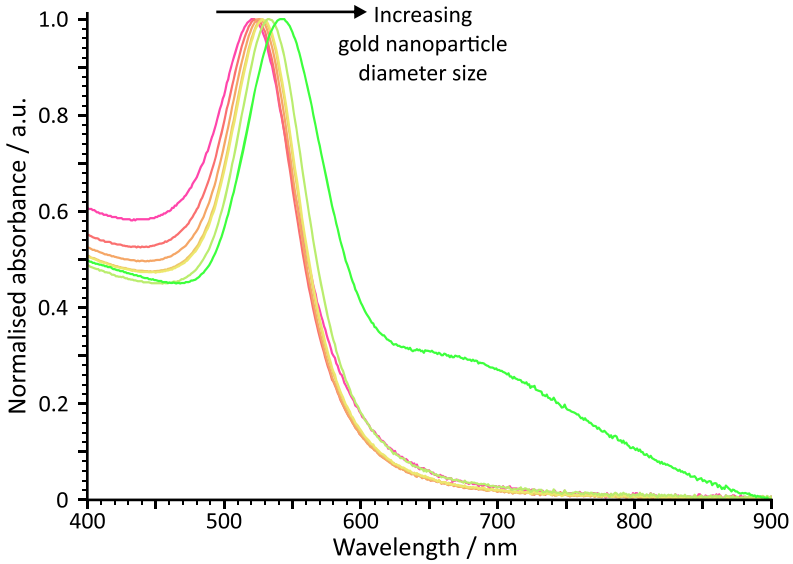

Figure S16: The Ultraviolet-Visible (UV-Vis) spectra of the aliquots (g_0 – g_6, pink – green) from the gold nanoparticle (50 nm) synthesis, showing the increasing gold nanoparticle diameter size with respect to increasing surface plasmon resonance (SPR) wavelength. The synthesis was terminated at 532 nm corresponding with 50 nm diameter particles.

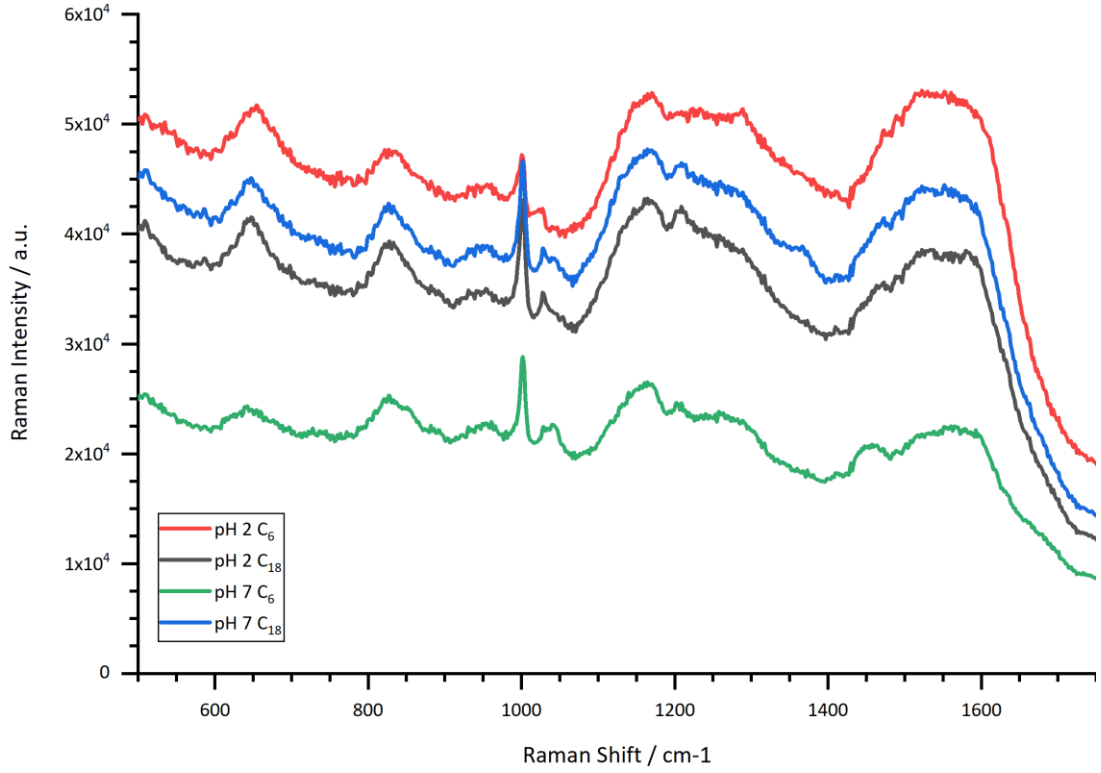

Figure S17: Non-baseline corrected or normalised SERS spectra for the four representative samples; (red) C_6 and (black) C_{18} at pH 2 (20% acetic acid and 137.9 mM NaCl), with (green) C_6 and (blue) C_{18} at pH 7 (0.01 M PBS).

Wavenumber (cm^{-1})	Assignment	pH 2		pH 7	
		C_6	C_{18}	C_6	C_{18}
500 – 530	S – S stretch[39]	-	Present		
600 – 620	Phe or COO^- wag[39,40]	Present			
640	Tyr[39]	Present			
662 – 687, 705 – 765,	C-S stretch[39,40]	Not present			
830 – 853. 863	Tyr stretch and ring breathing[39,40]	Low	Present		
938 – 940	C – C skeletal α-helical stretch[39,40]	Present			
959 – 963	C – C skeletal β-sheet stretch[39,40]	Present			
1007, 1028	Phe stretch and ring breathing[39,40]	Low	Present		
1050	β-sheet stretch (Amide III)[40]	-	Present	-	Present
1066 – 1162	C – N stretch[39,40]	-	Present	-	Present
1121	NH_3^+ deformation[40]	Possibly			
1130	CH_2 stretch	Possibly			
1150	Phe	Present			
1151	NH_3^+ deformation[40]	Possibly			
1209	Tyr	Low	Present	Low	Present
1220 – 1300	Amide III	α		β	
1236	Tyr/Phe, Amide III β or random coil, CH deformation[39]	-	Present		
1276 - 1277	Tyr/Phe, Amide III α or random coil, CH deformation[39,40]	Present	Possibly		
1311	CH_2 wag[40]	Possibly			
1316, 1343	CH deformation[39]	-			
1396	COO^- sym stretch[39]	-		Present	
1400 – 1480	CH_2 stretch, scissoring or bending[39,40]	Shoulder	Present	shoulder	
1494	Tyr[39]	Present			
1560	COO^- asym stretch[39]	Possibly			
1584 - 1585	Phe[39]	Possibly			
1590	Tyr[39]	Possibly			
1594	COO^- asym stretch[40]	Possibly			
1630 – 1700	Amide I[39]	-			
1750	Carbonyl[48]	-	Present		

Figure S18: Comparison of typical protein adsorbed SERS assignments available in literature with the experimentally acquired data for both functionalised interfaces hexyl (C_6), octadecyl (C_{18}), with adsorbed human insulin from acidic (pH 2) and neutral (pH 7) conditions.

Bibliography

1. Hammarström, P. *et al.* A catalytic surface for amyloid fibril formation. *J. Phys. Conf. Ser.* **100**, 052039 (2008).

2. Hammarström, P. *et al.* An Auto-Catalytic Surface for Conformational Replication of Amyloid Fibrils—Genesis of an Amyloid World? *Orig. Life Evol. Biosph.* **41**, 373–383 (2011).

3. Bain, C. D., Biebuyck, H. A. & Whitesides, G. M. Comparison of self-assembled monolayers on gold: coadsorption of thiols and disulfides. *Langmuir* **5**, 723–727 (1989).

4. Love, J. C., Estroff, L. A., Kriebel, J. K., Nuzzo, R. G. & Whitesides, G. M. Self-Assembled Monolayers of Thiolates on Metals as a Form of Nanotechnology. *Chem. Rev.* **105**, 1103–1170 (2005).

5. Vericat, C., Vela, M. E., Benitez, G., Carro, P. & Salvarezza, R. C. Self-assembled monolayers of thiols and dithiols on gold: New challenges for a well-known system. *Chem. Soc. Rev.* **39**, 1805–1834 (2010).

6. Dilimon, V. S., Rajalingam, S., Delhalle, J. & Mekhalif, Z. Self-assembly mechanism of thiol, dithiol, dithiocarboxylic acid, disulfide and diselenide on gold: An electrochemical impedance study. *Phys. Chem. Chem. Phys.* **15**, 16648–16656 (2013).

7. Welinder, A. C., Zhang, J., Steensgaard, D. B. & Ulstrup, J. Adsorption of human insulin on single-crystal gold surfaces investigated by in situ scanning tunnelling microscopy and electrochemistry. *Phys. Chem. Chem. Phys.* **12**, 9999–10011 (2010).

8. Gao, Y. *et al.* The effect of hydrophobic alkyl chain length on the mechanical properties of latex particle hydrogels. *RSC Adv.* **7**, 44673–44679 (2017).

9. Biolin-Scientific. QCM-D Measurement. (2020). Available at: https://www.biolinscientific.com/measurements/qcm-d.

10. Andersson, M. *et al.* Quartz crystal microbalance-with dissipation monitoring (QCM-D) for real time measurements of blood coagulation density and immune complement activation on artificial surfaces. *Biosens. Bioelectron.* **21**, 79–86 (2005).

11. Hajiraissi, R. *et al.* Adsorption and Fibrillization of Islet Amyloid Polypeptide at Self-Assembled Monolayers Studied by QCM-D, AFM, and PM-IRRAS. *Langmuir* **34**, 3517–3524 (2018).

12. Slavin, S. *et al.* Adsorption behaviour of sulfur containing polymers to gold surfaces using QCM-D. *Soft Matter* **8**, 118–128 (2012).

13. Garcia, M. P., Shahid, A., Chen, J. Y. & Xi, J. Effects of the expression level of epidermal growth factor receptor on the ligand-induced restructuring of focal adhesions: a QCM-D study. *Anal. Bioanal. Chem.* **405**, 1153–1158 (2013).

14. Oh, S., Wilcox, M., Pearson, J. P. & Borrós, S. Optimal design for studying mucoadhesive polymers interaction with gastric mucin using a quartz crystal microbalance with dissipation (QCM-D): Comparison of two different mucin origins. *Eur. J. Pharm. Biopharm.* **96**, 477–483 (2015).

15. Hemmersam, A. G., Rechendorff, K., Foss, M., Sutherland, D. S. & Besenbacher, F. Fibronectin adsorption on gold, Ti-, and Ta-oxide investigated by QCM-D and RSA modelling. *J. Colloid Interface Sci.* **320**, 110–116 (2008).

16. Molino, P. J., Higgins, M. J., Innis, P. C., Kapsa, R. M. I. & Wallace, G. G. Fibronectin and Bovine Serum Albumin Adsorption and Conformational Dynamics on Inherently Conducting Polymers: A QCM-D Study. *Langmuir* **28**, 8433–8445 (2012).

17. Sauerbrey, G. The use of quartz oscillators for weighing thin layers and for microweighing. *Zeitschrift fur Phys.* **155**, 206–222 (1959).

18. Knowles, T. P. J. *et al.* Kinetics and thermodynamics of amyloid formation from direct measurements of fluctuations in fibril mass. *Proc. Natl. Acad. Sci.* **104**, 10016–10021 (2007).

19. Liu, S. X. & Kim, J.-T. Application of Kevin—Voigt Model in Quantifying Whey Protein Adsorption on Polyethersulfone Using QCM-D. *JALA J. Assoc. Lab. Autom.* **14**, 213–220 (2009).

20. Hovgaard, M. B., Dong, M., Otzen, D. E. & Besenbacher, F. Quartz Crystal Microbalance Studies of Multilayer Glucagon Fibrillation at the Solid-Liquid Interface. *Biophys. J.* **93**, 2162–2169 (2007).

21. Marcelli, A., Cricenti, A., Kwiatek, W. M. & Petibois, C. Biological applications of synchrotron radiation infrared spectromicroscopy. *Biotechnol. Adv.* **30**, 1390–1404 (2012).

22. Tame, M. S. *et al.* Quantum Plasmonics. *Nat. Phys.* **9**, 329–340 (2013).

23. Moskovits, M. Persistent misconceptions regarding SERS. *Phys. Chem. Chem. Phys.* **15**, 5301–5311 (2013).

24. Mueller, N. S. *et al.* Plasmonic enhancement of SERS measured on molecules in carbon nanotubes. *Faraday Discuss.*

205, 85–103 (2017).

25. Jensen, L., Aikens, C. M. & Schatz, G. C. Electronic structure methods for studying surface-enhanced Raman scattering. *Chem. Soc. Rev.* **37**, 1061–1073 (2008).

26. Darby, B. L., Auguié, B., Meyer, M., Pantoja, A. E. & Le Ru, E. C. Modified optical absorption of molecules on metallic nanoparticles at sub-monolayer coverage. *Nat. Photonics* **10**, 40–45 (2016).

27. Zhang, D. *et al.* Gold nanoparticles can induce the formation of protein-based aggregates at physiological pH. *Nano Lett.* **9**, 666–671 (2009).

28. Rueden, C. T. *et al.* ImageJ2: ImageJ for the next generation of scientific image data. *BMC Bioinformatics* **18**, 529 (2017).

29. Hühn, J. *et al.* Selected standard protocols for the synthesis, phase transfer, and characterization of inorganic colloidal nanoparticles. *Chem. Mater.* **29**, 399–461 (2017).

30. Soliman, M. G. *private communication*.

31. Bastús, N. G., Comenge, J. & Puntes, V. Kinetically controlled seeded growth synthesis of citrate-stabilized gold nanoparticles of up to 200 nm: Size focusing versus ostwald ripening. *Langmuir* **27**, 11098–11105 (2011).

32. Haiss, W., Thanh, N. T. K., Aveyard, J. & Fernig, D. G. Determination of Size and Concentration of Gold Nanoparticles from UV−Vis Spectra. *Anal. Chem.* **79**, 4215–4221 (2007).

33. Phillips, N. B., Whittaker, J., Ismail-Beigi, F. & Weiss, M. A. Insulin Fibrillation and Protein Design: Topological Resistance of Single-Chain Analogs to Thermal Degradation with Application to a Pump Reservoir. *J. Diabetes Sci. Technol.* **6**, 277–288 (2012).

34. Przybyciel, M. & Majors, R. E. Phase Collapse in Reversed-Phase LC. *LC GC Eur.* (2002).

35. Mauri, S. *Insulin unfolding and aggregation : a multi-disciplinary study (PhD thesis)*. (University of Liverpool, 2014).

36. Tuschel, D. Selecting an excitation wavelength for raman spectroscopy. *Spectrosc. (Santa Monica)* **31**, 14–23 (2016).

37. Asher, S. & Johnson, C. Raman spectroscopy of a coal liquid shows that fluorescence interference is minimized with ultraviolet excitation. *Science* **225**, 311–313 (1984).

38. Misra, A. K., Sharma, S. K., Chio, C. H., Lucey, P. G. & Lienert, B. Pulsed remote Raman system for daytime measurements of mineral spectra. in *Spectrochimica Acta - Part A: Molecular and Biomolecular Spectroscopy* (2005). doi:10.1016/j.saa.2005.02.027

39. Grass, S. & Treuel, L. Mechanistic aspects of protein corona formation: Insulin adsorption onto gold nanoparticle surfaces. *J. Nanoparticle Res.* **16**, (2014).

40. Wang, M., Benford, M., Jing, N., Coté, G. & Kameoka, J. Optofluidic device for ultra-sensitive detection of proteins using surface-enhanced Raman spectroscopy. *Microfluid. Nanofluidics* **6**, 411–417 (2009).

41. Drachev, V. P., Thoreson, M. D., Khaliullin, E. N., Davisson, V. J. & Shalaev, V. M. Surface-enhanced raman difference between human insulin and insulin lispro detected with adaptive nanostructures. *J. Phys. Chem. B* **108**, 18046–18052 (2004).

42. Dolui, S., Roy, A., Pal, U., Saha, A. & Maiti, N. C. Structural Insight of Amyloidogenic Intermediates of Human Insulin. *ACS Omega* **3**, 2452–2462 (2018).

43. Jimenez, J. L. *et al.* The protofilament structure of insulin amyloid fibrils. *Proc. Natl. Acad. Sci.* **99**, 9196–9201 (2002).

44. Kurouski, D. *et al.* Disulfide bridges remain intact while native insulin converts into amyloid fibrils. *PLoS One* **7**, 1–9 (2012).

45. Ortiz, C., Zhang, D., Ribbe, A. E., Xie, Y. & Ben-Amotz, D. Analysis of insulin amyloid fibrils by Raman spectroscopy. *Biophys. Chem.* **128**, 150–155 (2007).

46. Kurouski, D., Postiglione, T., Deckert-Gaudig, T., Deckert, V. & Lednev, I. K. Amide i vibrational mode suppression in surface (SERS) and tip (TERS) enhanced Raman spectra of protein specimens. *Analyst* **138**, 1665–1673 (2013).

47. Johansson, J., Pettersson, S. & Taylor, L. S. Infrared imaging of laser-induced heating during Raman spectroscopy of pharmaceutical solids. *J. Pharm. Biomed. Anal.* **30**, 1223–1231 (2002).

48. Bouchard, M. & Auger, M. Solvent history dependence of gramicidin-lipid interactions: a Raman and infrared spectroscopic study. *Biophys. J.* **65**, 2484–2492 (1993).

Chapter 6: Interrogating Human Insulin Adsorption on Hydrophobically Functionalised Gold Interfaces with Infrared Scanning Near-field Optical Microscopy (IR-SNOM)

6.1. Introduction

For the work in this chapter to be possible, a collaboration with Mr Conor Whitley (CW), Physics Ph.D Student, Department of Physics, University of Liverpool, was established. I (Nathan Cumberbatch, NC) formulated the project outline, prepared specimens and evaluated the data, whilst Mr Whitley performed the infrared-scanning near-field optical microscopy (IR-SNOM) measurements.

The objective of this chapter is to study analogous samples representative of those used in Chapter 5 and probe the secondary structure further using microscopic techniques. Importantly the results obtained will be the first study of adsorbed human insulin (HI) on functionalised gold substrates to be resolved using IR-SNOM instrumentation in reflection with a quantum cascade laser (QCL). This technique will be used to characterise the adsorbed HI layer across the surface to determine whether the surface architecture is homogeneous, any preferential adsorption sites exist across the hydrophobic interface and any influence attributed to the oligomeric state.

The previous chapters have shown that all hydrophobic interfaces are not equal, Chapter 4 investigated the effects of functionalised mesoporous silica microparticles on the HI amyloid-like fibrillation pathway, whilst adsorption was similar the fibrillation kinetics and resultant fibril morphology were disrupted. In Chapter 5 the HI adsorption state at a functionalised gold surface was studied, and while protein changes were observed between the functionalised interfaces there was no definitive evidence that the critical nucleation phase was induced by the hydrophobic adsorption. This previous work did not definitively conclude how homogeneous the adsorbed HI layer was and thus no evidence for divergent fibrillation routes was determined. This chapter aims to combine spectroscopic and microscopic methods to assess the secondary structural features present relative to

surface position, thus determining whether preferential structural rearrangement is derived from hydrophobic sites.

6.1.1. What is infrared scanning near-field optical microscopy?

Optical microscopy is an essential tool within many fields of science, because it is non-destructive, fast and able to resolve objects which cannot be viewed with the naked eye. There have been extensive uses for optical microscopy some of which are; semiconductor, education, food industry, pharmaceuticals, forensics, biochemistry, medical and pathology.[1] Another term for optical microscopy is a light microscope, because visible light is utilised to illuminate the specimens, however this poses an issue. The resolution of optical microscopy is physically limited not only by the quality of the optics but also by the diffraction limit, defined in 1873 'as the smallest resolvable distance between two points may never be smaller than half the wavelength of the imaging light'.[2] For visible light this results in an obtainable resolution of ~200 nm,[3] this is on a similar scale to cell nuclei and any smaller structures are difficult to resolve.

The challenge to break this diffraction limit, led to the development of near-field imaging which demonstrated spatial resolution of λ/60. Scanning near-field optical microscopy (SNOM) was established as a means of imaging a surface through use of an optical fibre with a small aperture ($a < \lambda$), which when brought close enough to the sample acquired images by illumination or light collection from the surface.[4,5]

Recent SNOM instrumentation developments are apertureless SNOM; where a metal cantilever tip in the near-field is used to influence the far field, and scattering SNOM which scatters the near-field component of a sample illuminated and imaged within the far field. Amenabar *et al*[6] have previously reported use of a scattering SNOM to probe two-year-old insulin, on a gold film adhered to silicon substrate. The collaborators for this project have invested in an aperture SNOM as it more closely aligned to their purpose of studying soft biological samples.[7] SNOM has been previously used with visible light, however the adaptability of visible to IR light is most significant for biological samples of interest, the IR wavelengths involved are on the

order of the wavelength of visible light. By circumventing the diffraction limit, sub wavelength imaging can give a greater insight into the sample. Aperture IR-SNOM has previously been applied to organic thin films[8] and keratinocyte cells[9–11] from human skin exhibiting successful imaging at length scales much less than the wavelength of IR light.

The prerequisites to obtain these IR images are an intense, tuneable IR source which previously required a free electron laser (FEL) whereby synchrotron radiation was emitted from an oscillated electron beam in a laser cavity as the lasing mechanism, with the capability of very high powers over a range of wavelengths.[12–14] This IR-SNOM had been previously been used for the imaging of oesophageal tissue biopsy samples[13,15,16] and cell lines.[7] Ingham *et al*[7] showed a direct comparison between images of the same cancer cell in both the SNOM and an imaging Fourier-transform IR (FTIR) microscope. This showed the strength and weakness of the two techniques but how they complement each other can yield information relating to the chemical structure of biological systems.

Quantum cascade lasers (QCL) are commercially available highly tuneable lasers with high optical power output and viable for room temperature operation, which have previously been used in a variety of applications.[17,18] Discrete frequency infrared (DF-IR) methods have initially evaluated to determine the capability of wavelengths as analytical tools.[19–21] Recent developments have coupled the QCL with IR imaging to study tissue samples for high throughout as a means for clinical use[22,23] and has been recently reviewed.[24,25]

The collaborators for this project, Smith *et al*[15], have previously established a proof-of-principal concept that the QCL is a suitable alternative light source to the IR FEL by demonstrating images acquisition at four wavelengths within the Amide I of the protein using the SNOM in transmission mode. This thesis chapter's main objective is to provide evidence that the same IR-SNOM apparatus can also be utilised in reflection mode and thus these are the first ever images obtained by this method.

The Amide I region (1700 – 1600 cm^{-1}), represented in Figure 65 is derived from the results of Susi and Byler,[26,27] signifies the contribution of four Gaussian peaks associated to; (left to right) anti-parallel β-sheets (red), random coils (green), α-helices (blue) and parallel β-sheets (red). The QCL is able to obtain a narrow bandwidth (1 cm^{-1}) as opposed to the larger IR-FEL bandwidth (20 cm^{-1}), therefore allowed the acquisition of the three discrete wavenumbers (Figure 65, magenta dashed lines).

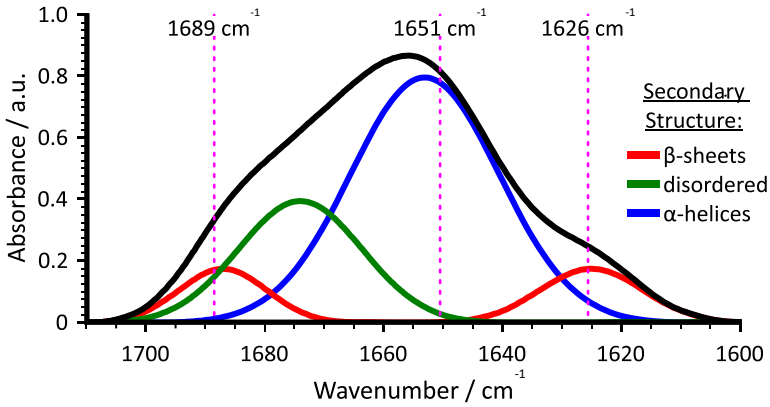

Figure 65: The (black) Amide I (1700 – 1600 cm^{-1}) region demonstrating the individual secondary structural contributions of; (red) anti- / parallel ß-sheets, (green) disordered structures and (blue) α-helices. The (magenta) four wavenumbers shown are attributed to the collaborators previous work for SNOM in transmission mode. Adapted from Jabs et al.[28]

The purpose of this chapter is to acquire spectral information of the adsorbed HI layer, therefore only three of the wavelengths were utilised here; anti-parallel β-sheets (1689 cm^{-1}), α-helices (1651 cm^{-1}) and parallel β-sheets (1626 cm^{-1}),[29] as shown in Table 4.

Table 4: Amide I wavenumbers probed by the infrared-scanning near-field optical microscopy (IR-SNOM) and the corresponding secondary structure feature.

Wavenumber / cm^{-1}	Secondary structure features
1689	Anti-parallel β-sheet
1651	α-helix
1626	Parallel β-sheet

6.2. Materials and Methods

This chapter probes the HI adsorbed layer, which was prepared similarly to Chapter 5, therefore a brief outline of the sample preparation is written here.

6.2.1. Sample Preparation

Pre-treated HI (10 mg/mL) suspended in either pH 2 (20% acetic acid and 137.9 mM sodium chloride) or pH 7 (PBS) conditions, were adsorbed to hydrophobic functionalised gold substrates (dihexyl and dioctadecyl disulfide). The controls (gold and functionalised interfaces) and samples (adsorbed surfaces) were air-dried, mounted onto a glass slide and analysed using microscopic methods; IR-SNOM and optical microscopy.

6.2.2. Infrared scanning near-field optical microscopy (IR-SNOM)

The IR-SNOM instrument utilised throughout this chapter is represented in a schematic in Figure 66.

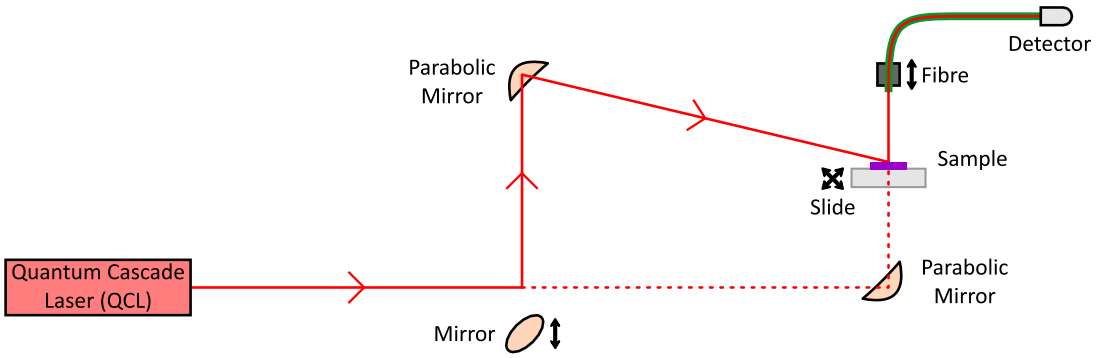

Figure 66: Schematic of the infrared-scanning near-field optical microscopy (IR-SNOM) operating in (solid line) reflection mode for the (red) IR beam from the Quantum Cascade Laser (QCL) onto the (purple) sample which is placed on a (grey) slide then mounted on a bidirectional x-y stage. The reflected light is collected into the (green) fibre and detected by the nitrogen cooled mercury cadmium telluride detector. Figure adapted from Smith et al.[15]

As illustrated in Figure 66, the IR SNOM measurements could be acquired in either reflection or transmission modes, dependent upon the initial mirror position. The IR-SNOM is mounted onto an inverted optical microscope (IX73, Olympus) however due to the restrictions of the gold substrate, which was highly reflective but non-transparent, this could neither be used to locate sample positions or for the

current transmission mode. The sample locations were obtained using a portable microscope (USB 400x microscope, Maplin) and the reflection mode used to collect IR light.

The mounted samples, described previously, were installed onto a bidirectional (*x*-*y* plane) piezo scanning stage. A cleaved (6 µm) IR transmitting fibre was inserted into a corresponding unidirectional *z*-piezo stage, situated directly above the centre of the sample piezo stage. The sample was then rastered with respect to the fibre tip (Figure 67), whereby shear-force feedback maintained a constant tip-to-sample distance, at a rate of 20 pixels per second.

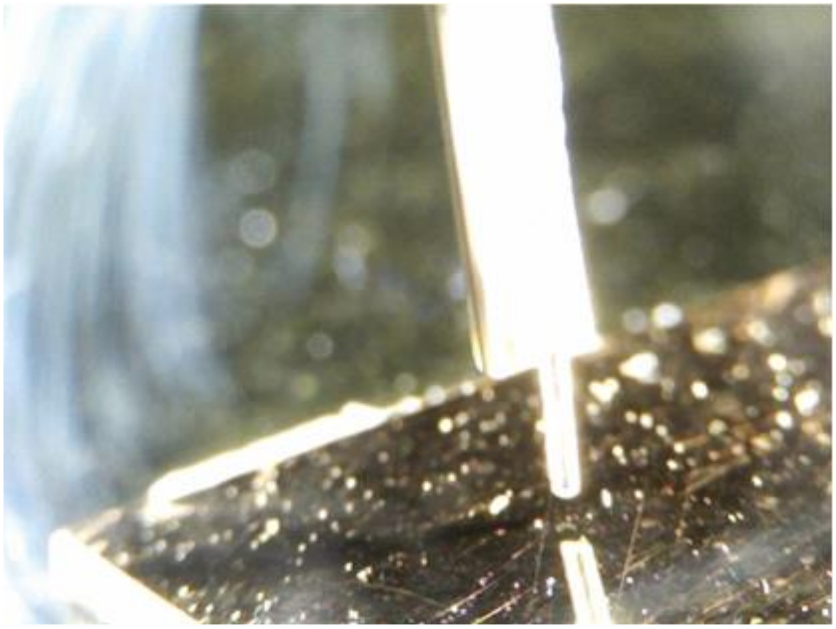

Figure 67: A cleaved tip, for the IR-SNOM, approaching the surface of a cleaned gold substrate.

A quantum cascade laser (QCL, MirCat, DRS Daylight Solutions, San Diego USA) in pulse mode (80 – 120 kHz repetition rate) was utilised as the mid-IR light source (~1965 to 1145 cm^{-1}). The laser intensity was altered using the pulse duration, which was set at 500 – 800 ns for the data presented in this research programme. The QCL was calibrated by using a polystyrene calibration specimen (National Institute of Standards and Technology), scanning the QCL wavelength while recording the IR through the fibre in transmission mode.

The reflected signal from the sample was transmitted through the aperture fibre and a liquid cooled mercury-cadmium-telluride (MCT) detector collected the

transmitted IR-light at each pixel. The shear-force topographical data, was simultaneously acquired as the fibre moves along the surface (feedback loop set to 90% of the applied voltage) whereby the piezoelectric component resisted the change as the tip desired to approach the surface thus producing the topographic images. As the topography data was collected simultaneously *in situ* to the spectral, this allowed any structural information to be concordant with the sample height presented within the topological data. The piezo stage moves in such a way that the SNOM collects a forward and backward scan over the same area such that a duplicate image is obtained on each experiment.

6.2.2.1 Reproducibility of IR-SNOM Images

A potential concern for the IR-SNOM was the reproducibility of the system over time, particularly with respect to localised heating of the sample and the surrounding environment. To eliminate these concerns, the IR-SNOM was operated on the exact same area which resulted in four scans as shown in Figure 68.

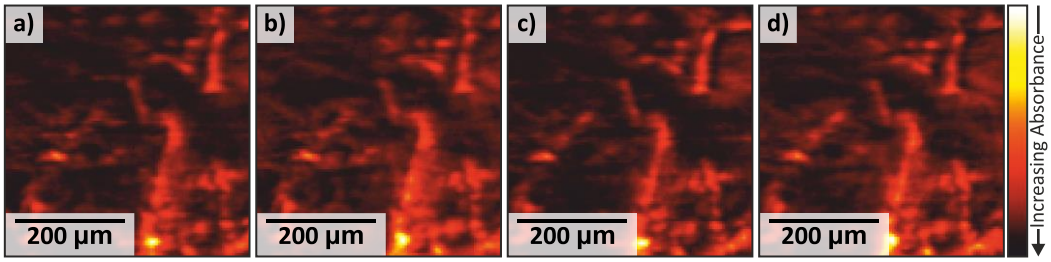

Figure 68: IR-SNOM images for the same location, (a – d) imaged sequentially.

The four scans of the same area (Figure 68) shows that there are no discernible differences between the four panels therefore no observed changes as a function of time. It was therefore determined that the system is a reliable instrument due to the acquisition of four very similar images of the same area with no observed differences associated to sample damage. In this research programme a minimum of N=8 images were taken for each substrate.

6.2.2.2. Data Processing

The topography and IR-SNOM images have been creep corrected to correct for the known non-linearity in the *x*-*y* piezo stage[30] then normalised to compensate

for the different laser power and lock-in settings. Images were prepared using Matlab.

6.2.2.3. Histogram Processing

To attempt to quantify the images from the IR-SNOM, each image was converted into a histogram using MatLab. The in-built `histogram` function was used with an automatic number of bins and plotted using the same x and y scale to make it easier to compare values and are shown in Figure 77. The histograms without plotting on the same scale are shown in Figure S20.

6.2.3. Optical Microscopy

The mounted samples, for the IR-SNOM, were installed onto the optical microscope (BX51, Olympus) stage, and imaged at all four objectives (x4, x10, x20 and x40). Polarisation was also shifted, for certain samples at objective magnification (x40).

6.2.4. Contact Angle Measurements

A droplet (50 µL) of water (18.2 MΩ cm^{-1}) was added to the surface, which was then captured using a webcam. The images were then processed by ImageJ,[31] with the contact angle calculated. Representative images of the contact angle measurement are shown in Figure S19, which resulted in contact angles of; 58° for the piranha cleaned gold, 108° for the C_6 functionalised and 107° for the C_{18} functionalised surfaces. The results showed that the piranha cleaned gold was hydrophilic with contact angle less than 90°, whilst both functionalised surfaces were hydrophobic with contact angles greater than 90°.

6.3. Results and Discussion

The main objective for this chapter was for the collaboration to provide evidence that IR-SNOM has sub-micron imaging potential for biochemical applications. For the physics perspective (CW) was it possible to couple the QCL with the correct optics to enable the light-path in reflection mode and attain suitable images. For the chemistry perspective (NC) to probe the biochemistry of HI adsorbed on functionalised gold surfaces to assess the secondary structural features present

relative to surface position, thus determining whether preferential structural rearrangement is derived from hydrophobic sites.

6.3.1. Changing the optics of the IR-SNOM

Since the IR-SNOM used in this research programme was developed for use on the FEL on the Accelerators and Lasers in Combined Experiments (ALICE) beamline at Daresbury as its Mid-IR light source it had a complicated optical beam path.[32] The initial experiments to test whether a QCL could replace the FEL as the light source utilised the same beam path and optics.[15] When the Weightman group purchased the MirCat QCL and brought the IR-SNOM to Liverpool then the optics were simplified by removing the polarisers and replacing the ZnSe lenses with an off-axis parabolic gold coated mirror, which focuses the IR beam without making the focal length of the laser spot wavelength dependant. This was done successfully and used for the IR-SNOM in transmission mode, however in reflection mode it was not as simple.

To develop an optical beam path for the IR light in reflection two major considerations have to be taken into account, (i) the focal length such that the beam is tightly focused onto the sample below the fibre and (ii) the angle at which light hits the sample. The success of the parabolic mirror in transmission mode led to the design of a custom-made off-axis parabolic mirror which not only should focus the IR light at the fibre tip but hit the sample at the Brewster angle (15˚ of horizontal) for maximum collection of light at the tip. This mirror was installed, and IR light was successfully collected at the MCT enabling the second part of the collaboration to proceed with imaging of the HI on functionalised gold substrates.

6.3.2. Imaging the control surfaces with reflection IR-SNOM

It was first necessary to determine whether the controls (gold substrate only and alkyl functionalised surfaces only) affect the resulting SNOM images, this section therefore is provided to support any conclusions that the results obtained are directly attributed to the adsorbed insulin layer as opposed to the substrate or functionalisation thereof.

The images from the specimens, both substrates and adsorbates, are presented in four-panel figures which are acquired from the same region;

(a) shear-force topography and (b, c, d) three IR images. The three IR images are acquired at the three wavenumbers which correspond to secondary structural features; (b) anti-parallel β-sheets at 1689 cm^{-1}, (c) α-helices at 1651 cm^{-1} and (d) parallel β-sheets at 1626 cm^{-1}. A non-hydrophobically functionalised or HI adsorbed gold substrate, which had been piranha cleaned, was first analysed by IR-SNOM as shown in Figure 69.

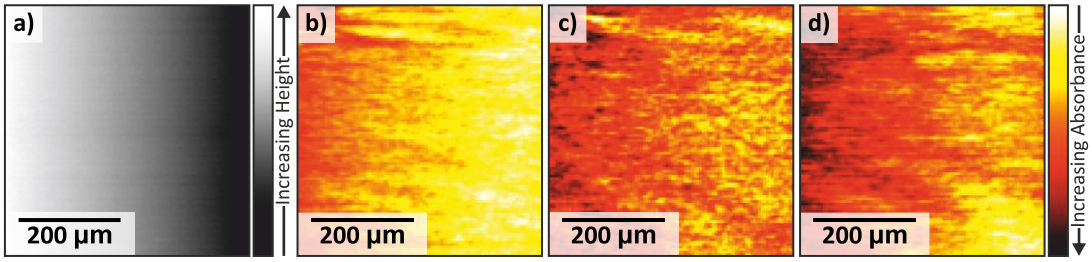

Figure 69: IR-SNOM images of a 500 µm ✕ 500 µm area of the gold substrate only; (a) shear-force topography, (b) 1689 cm^{-1}, (c) 1651 cm^{-1} and (d) 1626 cm^{-1}.

In Figure 69, a sloped gradient (from left to right) of decreasing shear-force topography and IR image maps for three wavenumbers is observed for the gold-only control over a large area (2.5 x 10^{05} μm^2). The colour scaling used provides a strong contrast across all four images (Figure 69a – d), which implies content, however the images are consistent with no profound features therefore suggesting a control surface. The observed tilt in the images is often seen in scanning probe microscopy, but here the images have not been processed to correct for this.[33] The clear surface shown in the images with no adsorbed species present or IR-activity is consistent with the expectation that a piranha cleaned gold substrate has no adsorbed species. This consistent imagery shows promise that the IR-SNOM in reflection mode can be used to image the samples. Imaging the functionalised-only control samples are the next priority, to investigate whether the functionalisation provides a response in the IR-SNOM. The hexyl-functionalised (C_6) gold substrate was also imaged by IR-SNOM, as shown in Figure 70.

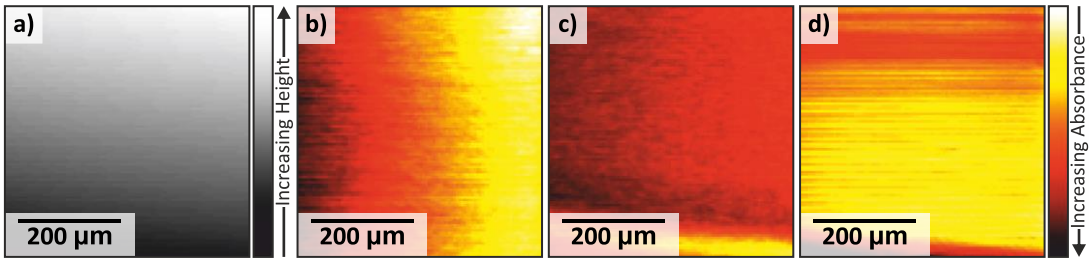

Figure 70: IR-SNOM images of a 500 µm ✕ 500 µm area of the hexyl-functionalised (C_6) gold substrate only; (a) shear-force topography, (b) 1689 cm^{-1}, (c) 1651 cm^{-1} and (d) 1626 cm^{-1}.

Similarly to the gold-only control IR-SNOM images (Figure 69), the C_6 functionalised-only control (Figure 70) also displayed a consistent and clear surface, which implied that there no adsorbed species or IR-activity present on the surface. There are image banding present in the IR-SNOM images, particularly observed for the 1626 cm^{-1} (Figure 70d) wavelength, which is likely attributed to the challenges faced with imaging using a coherent laser source as it provides a diffraction pattern (coherence fringes).[34] However, the C_6 functionalised-only control also shows that the functionalisation can be used as a substrate for IR-SNOM in reflection mode. The octadecyl-functionalised (C_{18}) gold substrate was also imaged by IR-SNOM, as shown in Figure 71.

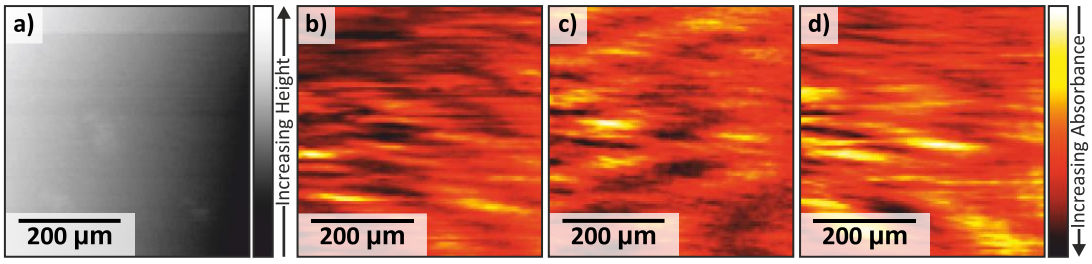

Figure 71: IR-SNOM images of a 500 µm ✕ 500 µm area of the octadecyl-functionalised (C_{18}) gold substrate only; (a) shear-force topography, (b) 1689 cm^{-1}, (c) 1651 cm^{-1} and (d) 1626 cm^{-1}.

The C_{18} functionalised-only control exhibits consistent and clear surface topography (Figure 71a) as previously observed for the gold-only (Figure 69a) and C_6-only (Figure 70a) controls. There is a variable colour contrast across the three IR-SNOM images (Figure 71b – d), which implies content on the surface, however similarly to the gold-only images this is due to the scaling used. The consistent IR-SNOM images obtained for the C_{18} functionalised-only control surface, shows that this functionalisation is also suitable as a substrate for IR-SNOM in reflection mode.

Overall, the control surfaces are shown to be suitable for use as substrates in IR-SNOM, as they exhibit clear and consistent surface topography and IR-SNOM imagery, with no adsorbed species or IR-activity. The colour scaling used within the spectral images, can portray differences however these differences are attributed to colour scaling as they are scaled from the individual minimum to maximum absorbance values.

6.3.2.1. Optical microscopy of the control surfaces

In addition to the IR-SNOM, optical microscopy images of the surface were acquired (Figure 72) although these regions do not correspond to the regions studied above however, they are representative of the surface.

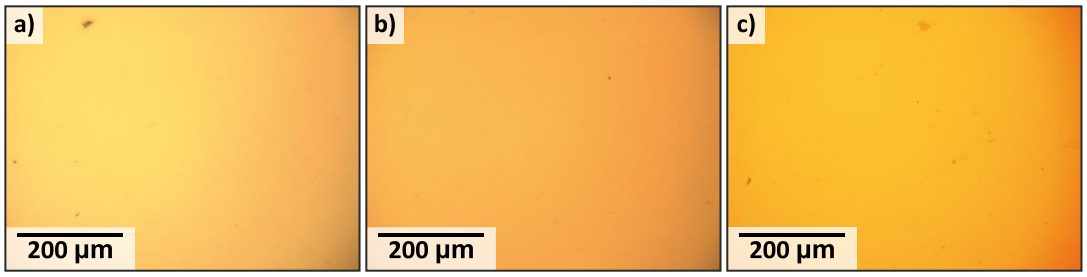

Figure 72: Optical microscopy images acquired at x20 magnification of the controls; (a) gold, (b) C_6 and (c) C_{18} functionalised surfaces. No adsorbed species are observed in any of the optical images.

The optical images acquired (Figure 72) correlate with the IR-SNOM images acquired previously (Figure 69, Figure 70 and Figure 71) whereby there are no observed adsorbed species present at the surfaces, which was to be expected. Optical microscopy however does appear to show a dull orange colour for the larger functionalisation (C_{18} surface, Figure 72c) as opposed to the other surfaces microscopically attained, which exhibited a bright orange colour. There were no apparent differences observed visually, therefore these colour changes are more likely to be an effect of the microscopic illumination and thus contrast balance.

6.3.3. Imaging the human insulin adsorbed surfaces with reflection IR-SNOM

The previous section demonstrated that disulfide functionalisation does not affect the IR-SNOM images, therefore enabling the objective to be pursued; acquisition of the first reflection IR-SNOM images of HI at a hydrophobic

functionalised gold surface. The data presented in this thesis has been subsequently confirmed with additional images and these did not change the interpretation.

6.3.3.1. The hexyl-functionalised (C_6) surface

Adsorbed with human insulin at pH 2

Following confirmation that the hydrophobically functionalised surfaces and gold substrate were suitable for IR-SNOM in reflection mode, the first sample studied was HI adsorbed on C_6 functionalised surface at pH 2, as shown in Figure 73.

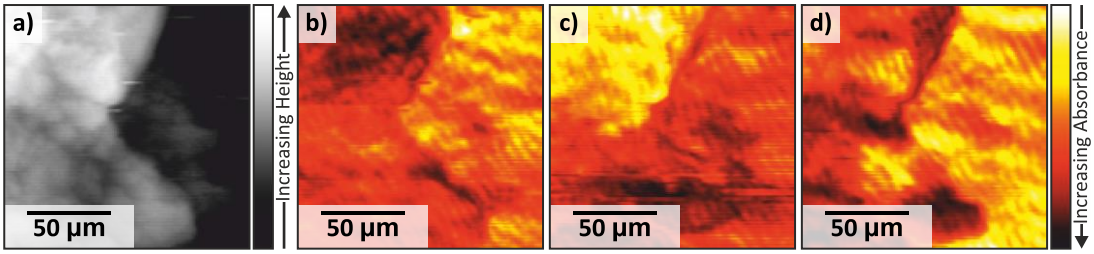

Figure 73: IR-SNOM images of a 150 µm ✕ 150 µm area of the hexyl-functionalised (C_6) gold substrate with human insulin (10 mg/mL, HI) adsorbed at acidic conditions (pH 2); (a) shear-force topography, (b) 1689 cm^{-1}, (c) 1651 cm^{-1} and (d) 1626 cm^{-1}.

The IR-SNOM images of the C_6 functionalised surface at pH 2 (Figure 73) appears to show that this sample was inhomogeneous. The topography (Figure 73a) shows this inhomogeneity with a sharp transition between white and black, which is correlated with a boundary in the IR-SNOM images (Figure 73b – d). The IR-SNOM images for the 1689 cm^{-1} and 1626 cm^{-1} (Figure 73b and d) show regions of β-sheet structure on the left side of the image with decreased absorbance shown on the right of the image. This is contrasted with 1651 cm^{-1} (Figure 73c) which shows the opposite trend, regions of α-helical structure where there is reduced absorbance for the β-sheet structures. These observations imply that there are two distinct regions of differing structural features of HI on this surface.

Chapter 5 showed using QCM-D and Raman that the C_6 functionalisation at pH 2 was unstable, as evidenced through a reduced adsorbed HI layer thickness compared to the other surfaces and the loss of the disulfide bonding region in Raman. It is possible that the IR-SNOM images presented (Figure 73) demonstrate that the functionalisation has been removed on the left section, exposing the gold surface,

which results in a reduced absorbance associated with α-helical structure due to insulin distortion.[35]

Adsorbed with human insulin at pH 7

The next sample to be studied was the C_6 functionalised surface at pH 7, as shown in Figure 74.

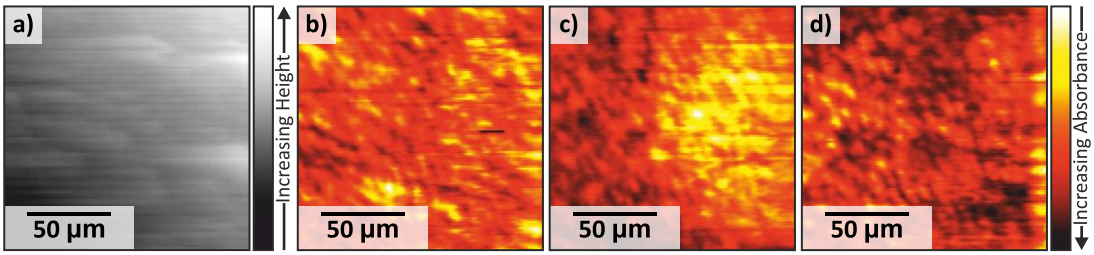

Figure 74: IR-SNOM images of a 150 µm ✕ 150 µm area of the hexyl-functionalised (C_6) gold substrate with human insulin (10 mg/mL, HI) adsorbed at neutral conditions (pH 7); (a) shear-force topography, (b) 1689 cm^{-1}, (c) 1651 cm^{-1} and (d) 1626 cm^{-1}.

The IR-SNOM images of the C_6 functionalised surface at pH 7 (Figure 74) contrasts with the pH 2 images (Figure 73), as the pH 7 topography (Figure 74a) shows a relatively even topography which implies a consistent adsorbed HI coverage across the surface. The IR-SNOM images (Figure 74b – d) are comparable, with contrasting 1651 cm^{-1} and 1626 cm^{-1} (Figure 74c and d) areas, which implies regions of α-helices with reduced absorbance whilst the same regions show increased absorbance for parallel β-sheets. There is an overall reduced absorbance for the 1689 cm^{-1} (Figure 74b) as shown with limited dark areas, which implies reduced anti-parallel β-sheet structure present on the surface.

The presence of the α-helical content, contrasts with the pH 2, implying that the surface is not degraded in this sample and the adsorbed HI is not degraded by the surface functionalisation. As discussed in Chapter 5, the QCM-D measured thicker HI adsorbed layers for the pH 7 conditions which were attributed to the HI adsorption in the oligomeric state, therefore the adsorbed HI layer likely consists of both structural features as shown.

6.3.3.2. Octadecyl functionalised (C_{18}) surface

Adsorbed with human insulin at pH 2

Figure 75 shows the IR-SNOM images of HI adsorbed on the C_{18} functionalised surface at pH 2.

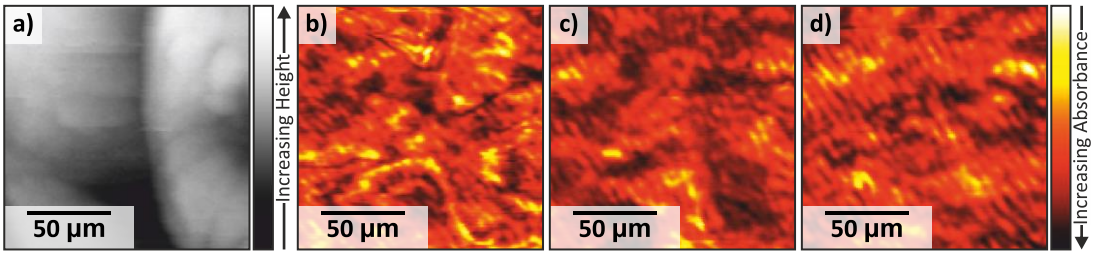

Figure 75: IR-SNOM images of a 150 µm ✕ 150 µm area of the octadecyl-functionalised (C_{18}) gold substrate with human insulin (10 mg/mL, HI) adsorbed at acidic conditions (pH 2); (a) shear-force topography, (b) 1689 cm^{-1}, (c) 1651 cm^{-1} and (d) 1626 cm^{-1}.

The IR-SNOM images of the C_{18} functionalised surface at pH 2 (Figure 75) show a similar topography (Figure 75a) to that of the C_6 functionalised surface at pH 2 (Figure 73a). This topography shows contrast, which would imply regions of variation in the thickness of adsorbate, however the topography areas do not have corresponding regions in the IR-SNOM images (Figure 75b – d). The IR-SNOM images for the 1689 cm^{-1}, 1651 cm^{-1} and 1626 cm^{-1} (Figure 75b, c, d) show similar variation, with the same trend of regions of α-helical absorbance contrasting with regions of β-sheet absorbance. This contrast suggests a consistent adsorbed HI coverage across the surface with pockets of α-helical and β-sheet character attributed to the HI. There are also no distinct regions of structural change observed which correlate with the topography, therefore this suggests that the surface functionalisation is stable and does not degrade due to pH 2, as was shown for the C_6 functionalised surface at pH 2.

Adsorbed with human insulin at pH 7

Figure 76 shows the IR-SNOM images of HI adsorbed onto the C_{18} functionalised surface at pH 7.

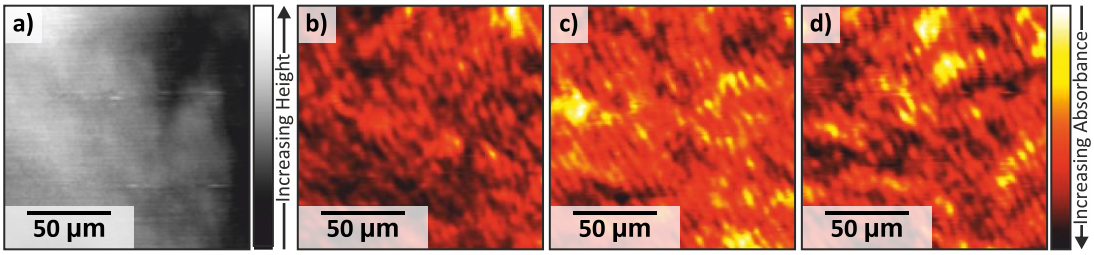

Figure 76: IR-SNOM images of a 150 µm ✕ 150 µm area of the octadecyl-functionalised (C_{18}) gold substrate with human insulin (10 mg/mL, HI) adsorbed at neutral conditions (pH 7); (a) shear-force topography, (b) 1689 cm^{-1}, (c) 1651 cm^{-1} and (d) 1626 cm^{-1}.

The IR-SNOM images of the C_{18} functionalised surface at pH 7 (Figure 76), shows an uneven flat topography (Figure 76a). The IR-SNOM images (Figure 76b – d) show similar variation, particularly with 1651 cm^{-1} and 1626 cm^{-1} (Figure 76c and d) which showed the same trend; where α-helices absorbance increases, β-sheets absorbance decreases. However, the 1689 cm^{-1} (Figure 76b) shows a larger colour contrast with an increased absorbance, which implies that the C_{18} functionalised surface at pH 7 consists of anti-parallel β-sheet structure. This observation correlates with the assumption that at pH 7 the adsorbed species is predominantly oligomeric, as dimerization of monomeric HI results in anti-parallel β-sheets,[36] therefore the image (Figure 76a) shows areas of high oligomeric content.

Overall, the IR-SNOM images acquired of the samples show that the secondary structure of the adsorbed HI layer is not entirely consistent across the hydrophobically functionalised gold surfaces at either pH 2 or pH 7. The IR-SNOM images also show, the inhomogeneity of the C_6 functionalised surface at pH 2, which was observed from QCM-D and Raman analysis in Chapter 5. The effect of pH is visually observed in IR-SNOM, where there are larger areas of α-helical content present at pH 2 compared to pH 7. However, the IR-SNOM has shown that the discrete wavelengths used show areas of high α-helical content contrasted with low β-sheet content.

6.3.3.3. Quantification of the IR-SNOM data

The acquired IR-SNOM data shows variation between the three wavelengths, corresponding to the secondary structure of HI; (1689 cm^{-1}) anti-parallel β-sheets, (1651 cm^{-1}) α-helices and (1626 cm^{-1}) parallel β-sheets. These images were

processed into histograms (6.2.2.3. Histogram Processing, page 204), as shown in Figure 77 with the non-scaled histogram in Figure S20.

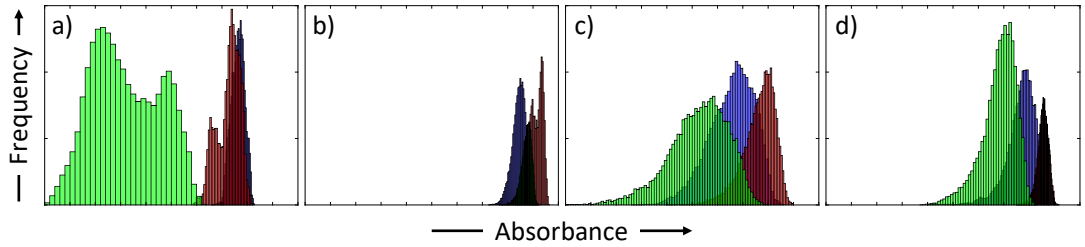

Figure 77: Histograms of the IR-SNOM images of the (blue) 1689 cm^{-1} (anti-parallel ß-sheets), (red) 1651 cm^{-1} (α-helices) and (green) 1626 cm^{-1} (parallel ß-sheets) wavelengths. The samples represented are human insulin (HI) adsorbed to; (a) C_6 functionalised at pH 2, (b) C_6 functionalised at pH 7, (c) C_{18} functionalised at pH 2 and (d) C_{18} functionalised at pH 7. Figure courtesy of Conor Whitley.

Histogramming the IR-SNOM images of the four samples (Figure 77) for the three wavelengths used; 1689 cm^{-1} (blue), 1651 cm^{-1} (red) and 1626 cm^{-1} (green), resulted in an attempted quantification of the amount of HI secondary structure present in each image obtained. The main trend observed is that both pH 7 for C_6 and C_{18} functionalised surfaces (Figure 77b and d) result in higher mean absorbance values for the three wavelengths compared to pH 2, which implies that there is more HI content at pH 7 compared to pH 2. Increased HI content at pH 7 compared to pH 2 on either C_6 or C_{18} surface was also observed in Chapter 5, as shown with an increased adsorbed HI layer thickness. There is a sizeable overlap in the histograms for all the wavelengths, for all samples except the C_6 functionalised in pH 2 (Figure 77a), which implies that there are similar amounts of structural features present on the surface.

The C_6 functionalised surface at pH 2 (Figure 77a) exhibits the lowest overall absorbance which implies the least HI content adsorbed to the surface. The mean value for the α-helices is less than the other three samples, implying that there is some α-helical structure present on the surface. The mean value for the anti-parallel β-sheets exhibits the least absorbance value, which implies that there is minimal anti-parallel β-sheet structure on the surface. This is contradicted by the mean value for the parallel β-sheets which has the absorbance of the three wavenumbers, which suggests that there is predominantly parallel β-sheet structure absorbed on the

surface. A possible explanation is that for this surface, there is a higher contribution of disordered structure than the typical parallel β-sheets maxima (Figure 65), which is plausible since for the other samples the histograms of both wavenumbers (1689 cm^{-1} and 1626 cm^{-1}) overlap whereas they do not here (Figure 77a). If there was a higher contribution of disordered structure as opposed to β-sheet, this would correspond with the implication that the C_6 functionalisation is unstable resulting in regions of C_6 functionalisation and bare gold across the surface, as shown in the IR-SNOM images (Figure 73) which showed a phase transition. This observation and quantification of HI secondary structure across the surface, correlates with the data acquired in Chapter 5 from QCM-D and Raman spectroscopy which showed the distortion of HI monomers on the exposed gold surface.

Conversely the C_6 functionalised surface at pH 7 (Figure 77b) resulted in the three wavenumbers exhibiting similar mean absorbance values which were overall highest across all the samples studied, implying the most HI content adsorbed to the surface. The 1651 cm^{-1} (α-helices) wavenumber exhibited the highest absorbance value, followed by 1626 cm^{-1} (parallel β-sheets) then 1689 cm^{-1} (anti-parallel β-sheets) with the smallest distribution range between histograms. The highest absorbance and similar histogram distributions implies that the adsorbed HI consists of comparable quantities of secondary structure in various states which correlates to adsorbed HI oligomeric states. Similar high absorbance values were observed for the C_{18} samples also.

The C_{18} functionalisation at pH 2 (Figure 77c) exhibited similar histograms to pH 7 (Figure 77d), with increased absorbance for pH 7 compared to pH 2. The individual wavenumber trend differed to that of C_6 functionalisation at pH 2, with the 1651 cm^{-1} (α-helices) wavenumber exhibiting the highest absorbance value, followed by 1689 cm^{-1} (anti-parallel β-sheets) and then 1626 cm^{-1} (parallel β-sheets). These trends suggest that although there is a higher adsorbed HI species at pH 7 compared to pH 2, both exhibit similar structural composition by IR-SNOM.

Overall histogramming has shown that there are trends present in the IR-SNOM data acquired, which support data obtained by QCM-D and Raman in

Chapter 5. The results show that surface functionalisation and pH conditions affect the adsorption of HI onto the hydrophobic interface, with the C_6 functionalised surface at pH 2 highlighting possible issues with the functionalisation process. There is a noticeable increase in secondary structure content on both C_6 and C_{18} functionalisation which corresponds with a change in pH from pH 2 to pH 7, which is likely attributed to oligomeric adsorption as discussed further in Chapter 5. Quantitative assessment of the IR-SNOM images by histogramming allows for a better interpretation of the IR-SNOM images, without the challenge of biased imaging or scaling, however further improvements are possible to increase the reliability of this technique.

6.3.3.4. Optical microscopy of the adsorbed surfaces

In addition to the IR-SNOM, optical microscopy images of the samples were acquired (Figure 78) although these regions do not correspond to the regions studied by IR-SNOM, they are representative of the surface.

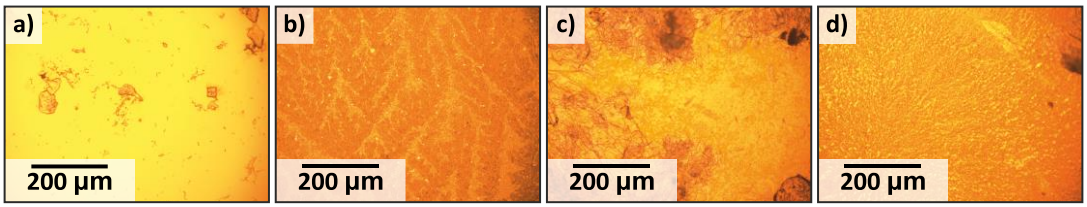

Figure 78: Optical microscopy images acquired at x20 magnification of the samples studied within the IR-SNOM; (a) C_6 pH 2, (b) C_{18} pH 2, (c) C_6 pH 7 and (d) C_{18} pH 7.

The optical microscopy images (Figure 78a) clearly indicate visual differences in the adsorbed HI between the four samples. A discrete adsorbed species for the HI adsorbed on the C_6 functionalised surface at pH 2 (Figure 78a), in contrast to the other three images which show crystalline structures (Figure 78b and d) or an amalgamated species (Figure 78c). The visually different adsorbed layer on the C_6 functionalised surface at pH 2 (Figure 78a) provides a possible explanation as to the differences observed in the IR-SNOM images, since there does not appear to be continuous adsorbed layer present.

6.3.4. Induction of fibrillation orientation as a result of structural morphology?

In addition to the optical images acquired, polarisation optical microscopy was used on the four samples to provide a preliminary observation into whether anisotropy was present,[37] as shown in Figure 79.

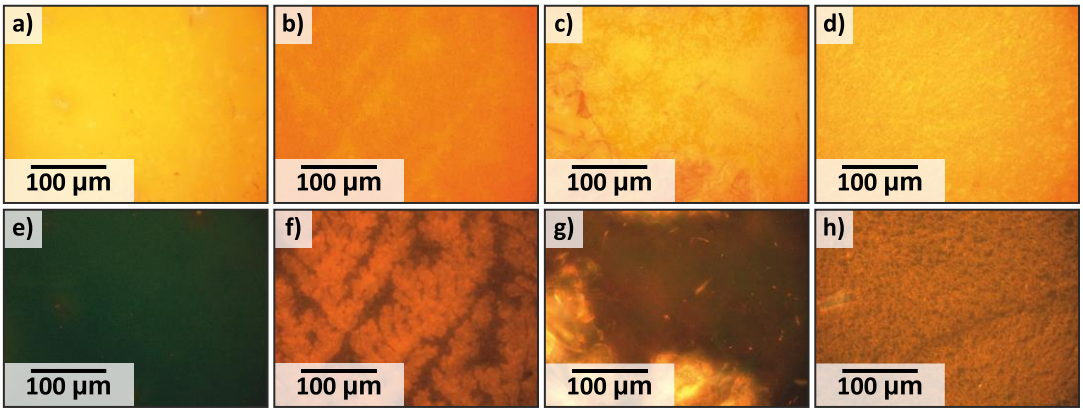

Figure 79: Comparison of the (a – d) optical microscopy images and the corresponding (e – h) polarised images, acquired at x40 magnification, for the samples studied within the IR-SNOM; (a, e) C_6 pH 2, (b, f) C_{18} pH 2, (c, g) C_6 pH 7 and (d, h) C_{18} pH 7.

Optical images (Figure 79a – d) were acquired of the samples, with polarised images (Figure 79e – h) captured at the same location. The polarised microscopy resulted in structural features of the surfaces, which was previously not observed. This polarisation effect demonstrates that there is surface anisotropy present on the surfaces, attributed to the orientation of the adsorbed HI layer. These results provide a possible application for studying these samples in Reflection Anisotropy Spectroscopy (RAS), to investigate whether the hydrophobic functionalisation facilitates the specific orientation of HI adsorption.

6.4. Conclusion

This chapter uses the novel technique of infrared scanning near-field optical microscopy (IR-SNOM) in a preliminary investigation to determine the effect of hydrophobic functionalised gold surfaces on the secondary structure of HI. The optics of the SNOM were changed in order to use the QCL as the Mid-IR light source enabling the reflection mode to be utilised.

IR-SNOM images have shown variations in the secondary structure of the adsorbed HI layer across the hydrophobically functionalised surfaces at both pH 2 and pH 7. The effect of pH is observed in the IR-SNOM images, which resulted in high α-helical content contrasted with low β-sheet content for pH 2 compared to pH 7. Quantitative assessment of the IR-SNOM images by histogramming removed the bias of image visualisation, however further improvements are possible to increase the reliability of this technique.

Promisingly the IR-SNOM results are consistent with the results obtained in Chapter 5, from conventional techniques, thereby validating this methodology.

6.5. Supplementary

Figure S19: Representative images of the samples used for contact angle measurement, (a) piranha cleaned gold, (b) C_6 functionalised and (c) C_{18} functionalised.

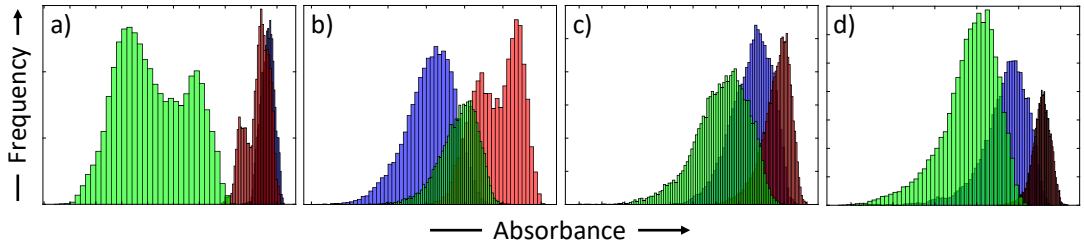

Figure S20: Non-scaled histograms of the IR-SNOM images of the (blue) 1689 cm^{-1} (anti-parallel β-sheets), (red) 1651 cm^{-1} (α-helices) and (green) 1626 cm^{-1} (parallel β-sheets) wavelengths. The samples represented are human insulin (HI) adsorbed to; (a) C_6 functionalised at pH 2, (b) C_6 functionalised at pH 7, (c) C_{18} functionalised at pH 2 and (d) C_{18} functionalised at pH 7. Figure courtesy of Conor Whitley.

Bibliography

1. Chen, X., Zheng, B. & Liu, H. Optical and digital microscopic imaging techniques and applications in pathology. *Analytical Cellular Pathology* **34**, 5–18 (2011).

2. Abbe, E. Beiträge zur Theorie des Mikroskops und der mikroskopischen Wahrnehmung. *Arch. für Mikroskopische Anat.* **9**, 413–468 (1873).

3. Heintzmann, R. & Ficz, G. Breaking the resolution limit in light microscopy. *Methods Cell Biol.* **114**, 525–544 (2013).

4. POHL, D. W. Scanning Near-field Optical Microscopy (SNOM). in 243–312 (1991). doi:10.1016/B978-0-12-029912-6.50009-9

5. Bachelot, R., Gleyzes, P. & Boccara, A. C. Reflection-mode scanning near-field optical microscopy using an apertureless metallic tip. *Appl. Opt.* **36**, 2160 (1997).

6. Amenabar, I. *et al.* Structural analysis and mapping of individual protein complexes by infrared nanospectroscopy. *Nat. Commun.* **4**, 2890 (2013).

7. Ingham, J. *et al.* An evaluation of the application of the aperture infrared SNOM technique to biomedical imaging. *Biomed. Phys. Eng. Express* **4**, 025011 (2018).

8. Cricenti, A. *et al.* Chemically Resolved Imaging of Biological Cells and Thin Films by Infrared Scanning Near-Field Optical Microscopy. *Biophys. J.* **85**, 2705–2710 (2003).

9. Rieti, S. *et al.* SNOM and AFM microscopy techniques to study the effect of non-ionizing radiation on the morphological and biochemical properties of human keratinocytes cell line (HaCaT). *J. Microsc.* **213**, 20–28 (2004).

10. Vobornik, D. *et al.* Spectroscopic infrared scanning near-field optical microscopy (IR-SNOM). *J. Alloys Compd.* **401**, 80–85 (2005).

11. Cricenti, A. *et al.* Low-frequency electromagnetic field effects on functional groups in human skin keratinocytes cells revealed by IR-SNOM. *J. Microsc.* **229**, 551–554 (2008).

12. Vobornik, D. *et al.* Very high resolution chemical imaging with Infrared Scanning Near-field Optical Microscopy (IR-SNOM). *Bosn. J. Basic Med. Sci.* **4**, 17–21 (2004).

13. Smith, A. D. *et al.* Near-field optical microscopy with an infra-red free electron laser applied to cancer diagnosis. *Appl. Phys. Lett.* **102**, 053701 (2013).

14. Halliwell, D. E. *et al.* Imaging cervical cytology with scanning near-field optical microscopy (SNOM) coupled with an IR-FEL. *Sci. Rep.* **6**, 29494 (2016).

15. Smith, C. I. *et al.* Application of a quantum cascade laser aperture scanning near-field optical microscope to the study of a cancer cell. *Analyst* **143**, 5912–5917 (2018).

16. Ingham, J. *et al.* Submicron infrared imaging of an oesophageal cancer cell with chemical specificity using an IR-FEL. *Biomed. Phys. Eng. Express* **5**, (2019).

17. Capasso, F. *et al.* New frontiers in quantum cascade lasers and applications. *IEEE J. Sel. Top. Quantum Electron.* **6**, 931–947 (2000).

18. Gmachl, C., Capasso, F., Sivco, D. L. & Cho, A. Y. Recent progress in quantum cascade lasers and applications. *Reports Prog. Phys.* **64**, 1533–1601 (2001).

19. Yao, Y., Hoffman, A. J. & Gmachl, C. F. Mid-infrared quantum cascade lasers. *Nat. Publ. Gr.* **6**, (2012).

20. Kole, M. R., Reddy, R. K., Schulmerich, M. V, Gelber, M. K. & Bhargava, R. Discrete Frequency Infrared Microspectroscopy and Imaging with a Tunable Quantum Cascade Laser. *Anal. Chem.* **84**, 10366–10372 (2012).

21. Yeh, K. & Bhargava, R. Discrete frequency infrared imaging using quantum cascade lasers for biological tissue analysis. in *Biomedical Vibrational Spectroscopy 2016: Advances in Research and Industry* (eds. Mahadevan-Jansen, A. & Petrich, W.) **9704**, 970406 (2016).

22. Bird, B. & Baker, M. J. Quantum Cascade Lasers in Biomedical Infrared Imaging. *Trends Biotechnol.* **33**, 557–558 (2015).

23. Yeh, K., Kenkel, S., Liu, J. & Bhargava, R. Fast Infrared Chemical Imaging with a Quantum Cascade Laser. *Anal. Chem.* **87**, 485–493 (2015).

24. Dean, P. *et al.* Terahertz imaging using quantum cascade lasers—a review of systems and applications. *J. Phys. D. Appl. Phys.* **47**, 374008 (2014).

25. Schwaighofer, A., Brandstetter, M. & Lendl, B. Quantum cascade lasers (QCLs) in biomedical spectroscopy. *Chem. Soc. Rev.* **46**, 5903–5924 (2017).

26. Susi, H. & Byler, D. M. [13] Resolution-enhanced fourier transform infrared spectroscopy of enzymes. in *Methods in Enzymology* **130**, 290–311 (1986).

27. Byler, D. M. & Susi, H. Examination of the secondary structure of proteins by deconvolved FTIR spectra. *Biopolymers* **25**, 469–487 (1986).

28. Jabs, A. Determination of secondary structure in proteins by fourier transform infrared spectroscopy. (2019). Available at: http://jenalib.leibniz-fli.de/ImgLibDoc/ftir/IMAGE_FTIR.html.

29. Barth, A. Infrared spectroscopy of proteins. *Biochim. Biophys. Acta - Bioenerg.* **1767**, 1073–1101 (2007).

30. Convery, J. *Reflection anisotropy spectroscopy as a potential new tool for linking macromolecular conformation to biological function (PhD thesis)*. (University of Liverpool, 2012).

31. Rueden, C. T. *et al.* ImageJ2: ImageJ for the next generation of scientific image data. *BMC Bioinformatics* **18**, 529 (2017).

32. Craig, T. *The Development of Infrared Scanning Near-Field Optical Microscopy for the Study of Cancer and Other Biological Problems (PhD thesis)*. (2016).

33. Barrett, S. *private communication*.

34. Weightman, P. *private communication*.

35. Welinder, A. C., Zhang, J., Steensgaard, D. B. & Ulstrup, J. Adsorption of human insulin on single-crystal gold surfaces investigated by in situ scanning tunnelling microscopy and electrochemistry. *Phys. Chem. Chem. Phys.* **12**, 9999–10011 (2010).

36. Weiss, M., Steiner, D. F. & Philipson, L. H. *Insulin Biosynthesis, Secretion, Structure, and Structure-Activity Relationships*. *Endotext* (2000).

37. Wolman, M. Polarized light microscopy as a tool of diagnostic pathology. A review. *J. Histochem. Cytochem.* **23**, 21–50 (1975).

38. Jorgensen, L. *et al.* Adsorption of insulin with varying self-association profiles to a solid Teflon surface—Influence on protein structure, fibrillation tendency and thermal stability. *Eur. J. Pharm. Sci.* **42**, 509–516 (2011).

39. Banerjee, P., Mondal, S. & Bagchi, B. Effect of ethanol on insulin dimer dissociation. *J. Chem. Phys.* **150**, (2019).

40. Nilsson, P., Nylander, T. & Havelund, S. Adsorption of insulin on solid surfaces in relation to the surface properties of the monomeric and oligomeric forms. *J. Colloid Interface Sci.* **144**, 145–152 (1991).

Chapter 7: Utilising Intrinsic Fluorescence to Probe a Potential Amyloid-like Signature

7.1. Introduction

In Chapter 2, Reflection Anisotropy Spectroscopy (RAS) showed that a large amount of inhomogeneous protein adsorption had occurred on the silicon (Si) surface, which resulted in the adsorbed protein exhibiting a blue colouration. The blue haze-like colouration led to an investigation to determine the cause for this colouration. A literature search revealed a widely debated phenomenon for the aggregation of proteins exhibiting a fluorescence signature in the blue visible region.[1] This phenomenon is termed; deep-blue autofluorescence (dbAF) which has been reported to originate from protein amyloidogenicity,[1–4] although there has been no consensus for where this phenomenon originates with various suggestions from aggregation state,[2,5] carbonyl interactions[6] and labile hydrogen bonding.[7] This provides a potential application of this phenomenon, as a tool to detect pre-fibrillar aggregates before fibrillation is apparent.

The fibrillation of proteins in bulk solution is an important factor in industrial processing or clinical drug delivery system because of the unintentional consequences resulting from fibrillation such as; decreased drug stability[8,9] or adverse aggregation.[10,11] There is a significant need to develop a non-invasive diagnostic technique for the detection of pre-fibrillar aggregates, to reduce inadvertent fibrillation within these scenarios. The use of fluorescence spectroscopy is advantageous because it provides a typically non-destructive and widely used highly sensitive biophysical technique, to probe species of biological or chemical interest.

The experimental change for this chapter was because of the synergy between bulk protein solutions and adsorption on substrate surfaces, as both are important for fibrillation events,[12] with the potential of dbAF to be used in both situations. The dbAF phenomenon is an exciting prospective diagnostic tool for pre-fibrillar detection, however its applicability is currently limited because of

uncertainty surrounding its origin. This chapter will use HI as a model protein and intrinsic fluorescence as a known spectroscopic technique, to investigate dbAF further.

7.1.1. Introduction to Fluorescence Spectroscopy

Fluorescence is the emission of light from electronically excited states of an aromatic species or fluorophore and is a specific type of luminescence. Luminescence is broadly defined as "the spontaneous emission of radiation from an electronically excited state or from a vibrationally excited species not in thermal equilibrium with its environment".[13] The other type of luminescence is phosphorescence, which is broadly defined as long-lived fluorescence derived from electronic transitions through a metastable excited state. Fluorescence and phosphorescence differ in the lifetime of their excited state, whether the promotion of the electron occurs to either the excited singlet (S_x) or triplet states (T_x), respectively. Fluorescence, singlet-excited state only, retains the same spin of its paired ground state, whereas phosphorescence, triplet-excited state only, has the same spin as that of the unpaired ground state electron. The process of luminescence can be fundamentally explained by using a simplified Jablonski-Perrin diagram (Figure 80) to describe these electronic transitions.[14]

As shown in the Jablonksi-Perrin diagram (Figure 80), when a photon is absorbed by an aromatic species or fluorophore, an absorption event occurs, which leads to an electron being promoted to an excited state. This excited state is unstable thus a rapid non-radiative energy decay of the electron occurs, which is typically vibrational relaxation and leads to energy dissipation from the electron as kinetic energy, either within the molecule or via neighbouring molecules between vibrational levels. In Figure 80 at the lowest energy level of the excited state (S_2), there are two possible non-radiative decay process which can occur, either internal conversion or intersystem crossing. Internal conversion is where an electron can only transfer between vibrational energy states from a higher energy state to a lower energy state, for example between singlet-excited states (S_2 to S_1). Intersystem crossing, a reversible process, is where an electron changes spin multiplicity from an excited singlet (S_x) to an excited triplet state (T_x), this process is usually slow.

Emission of a photon from the singlet-excited (S_1) or triplet-excited state (T_1) to ground electronic state (S_0) results in either fluorescence or phosphorescence respectively.

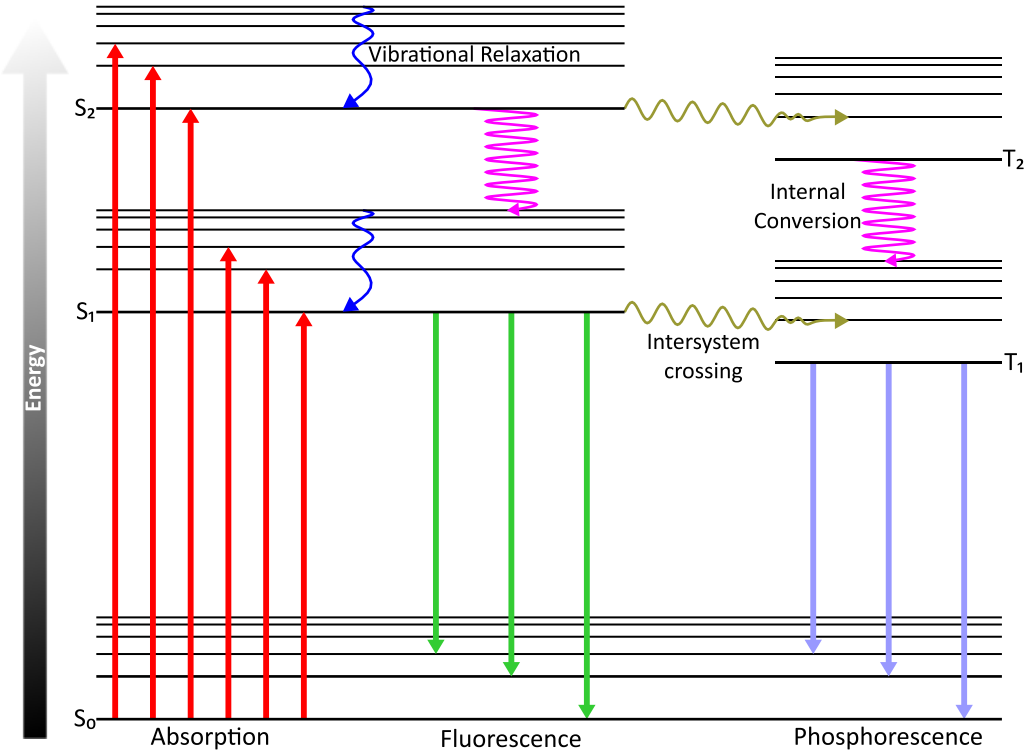

Figure 80: Simplified Jablonski-Perrin Diagram; (red arrows) photon absorption promotes the electron from the (S_0) ground electronic state to a (S_1 or S_2) singlet-excited state, followed by non-radiative decay either; (blue arrows) vibrational relaxation or (magenta arrows) internal conversion. Emission of a photon from the (S_1) singlet-excited state to (S_0) ground electronic state, results in (green arrows) fluorescence. Alternatively, (gold arrows) a change in electronic spin multiplicity leads to intersystem crossing, emission of a photon from the (T_1 or T_2) triplet-excited state to (S_0) ground electronic state resulting in (lilac arrows) phosphorescence. Adapted from Valeur et al.[15]

Steady state fluorescence spectroscopy probes fluorescence intensity as a function of wavelength, whereby the fluorophore can be located external or internal to the system of interest. The addition of a dye molecule or fluorophores (known as extrinsic fluorescence) can be used to enhance the fluorescence signal. Alternatively, the use of specific molecules internal to the system of interest (known as intrinsic fluorescence, IF) such as; aromatic amino acids,[14] neurotransmitters,[16] porphyrins[17] and green fluorescent protein have been used.[18]

7.1.1.1. Detection of aggregation using small molecule dyes

Extrinsic fluorescence occurs externally to the system or molecule, by the addition of dyes or fluorophores to enhance the fluorescence signal and observation of wavelength or intensity changes. The amyloidogenic fibrillation pathway is measured using extrinsic fluorescence techniques, notably the addition of two amyloid-specific dyes; Congo-Red (CR) and Thioflavin-T (ThT), shown in Figure 81.

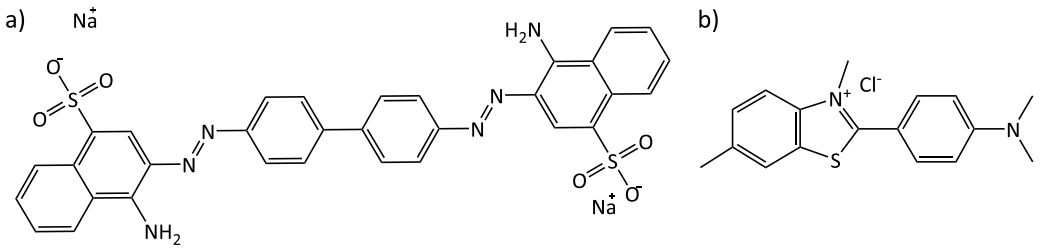

Figure 81: Chemical structures for (a) Congo-Red (CR) and (b) Thioflavin-T (ThT).

CR is used as the gold-standard for amyloid diagnosis. For a protein to be defined as amyloidogenic, suspected amyloid fibrils are stained with CR, identification is then confirmed if apple-green birefringence is observed under polarised light.[19] In ThT assays a characteristic blue-shift of emission maxima from 510 nm as a free dye molecule to 480 nm when bound to amyloid fibrils is observed.[20]

Extrinsic fluorescence is a powerful technique because consecutive readings on a multi-well plate, with an increase in sample size, can be acquired within a short-time frame. Although a powerful technique for reducing the likelihood of further fibrillation events occurring between reads, extrinsic fluorescence does have some disadvantages. The major issue with the use of these dyes for amyloid-research is their potential to affect the fibrillation pathway. This issue is compounded by the currently unknown mechanism by which ThT binds. Recent literature stresses the need to control the ThT concentrations, as delayed fibrillation has been reported due to ThT.[21,22] The use of extrinsic fluorescence provides many benefits, however the addition of dye fluorophores produce an additional variable to consider, therefore it would be desirable to utilise an alternative non-invasive fluorescence method which acquires analogous information.

7.1.1.2. Detection of aggregation using structural-specific fluorescence

Intrinsic fluorescence (IF) is a specific property of the protein originating from the aromatic amino acid residues present within the peptide primary sequence. The aromatic amino acid residues responsible for IF are; tryptophan (Trp, W), tyrosine (Tyr, Y) and phenylalanine (Phe, F) as illustrated in Figure 82. IF is highly sensitive to the local environment of the residue that gives rise to the fluorescence, which can yield structural data for the protein without introducing an external fluorophore as a probe.

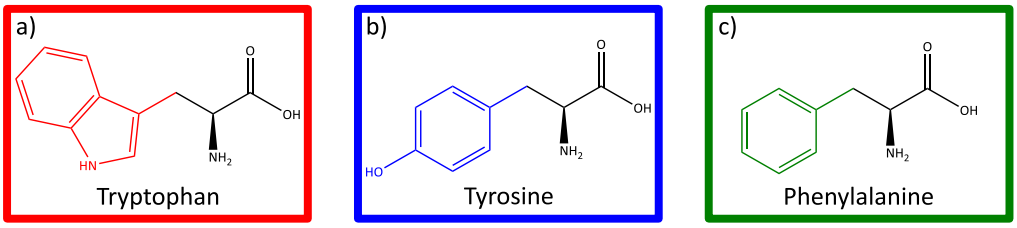

Figure 82: The chemical structures of intrinsic fluorescence (IF) active aromatic amino acids; (a) L-tryptophan, (b) L-tyrosine and (c) L-phenylalanine. The colours correspond to the (black) amino-carboxy groups and the R-groups for; (red) tryptophan, (blue) tyrosine and (green) phenylalanine.

Tryptophan is typically used as a probe to monitor the aggregation state of the protein because it has the highest quantum yield as shown in Table 5,[23] but the use of tyrosine has also been reported.[24] The strong fluorescence profile of tryptophan arises from delocalisation in the indole group,[25] and becomes blue-shifted to shorter wavelengths when buried compared to the longer wavelengths when unfolded. This blue-shift can be approximately 35 nm, dependent upon the solvent and protein studied,[26] although the intensity may be affected through the quenching mechanisms related to the protein or solvent system. This blue-shift can be utilised for studying the local environmental change, whereby the solvent accessible residue becomes buried within the hydrophobic core thus resulting in lower wavelength emission.[27] Giancotti *et al*[28] observed that histone emission blue-shifted from 360 nm to 345 nm as the residue becomes buried within the folded structure. This effect is also observed with changes in pH, since the amino acids are subject to protonation events and thus can exhibit an analogous effect.[29]

Table 5: Spectroscopic properties of the intrinsic amino acid residues, dissolved in water. The (Φ_F) quantum yield is defined as the ratio of the emitted to adsorbed photons. Adapted from Ghisaidoobe et al[30] and Wurth et al.[31]

	Fluorescence (λ_{max}, nm)	Quantum Yield (Φ_F)	Absorbance (λ_{max}, nm)	Extinction coefficient (ε, $M^{-1}cm^{-1}$)
Tryptophan	348	0.2	280	5600
Tyrosine	303	0.14	274	1400
Phenylalanine	282	0.04	257	200

The fluorescence intensity is proportional to the product of fluorescence quantum yield and extinction coefficient, thereby resulting in tryptophan having approximately five times higher fluorescence than tyrosine. This intensity difference leads to the preferential use of tryptophan for IF, although the other aromatic residues will still contribute if present, as the overall IF is an ensemble effect making disentanglement of residues often difficult unless restrictions are in-place. Overall the IF in general is significantly far less intense than extrinsic fluorescence, and therefore requires instrumentation fitted with detectors capable of higher sensitivity to distinguish the IF from the background noise.

Typically increasing the species concentration results in higher fluorescence intensity, however this is compounded by both a fundamental fluorescence principle and a physical property; the inner filter and scattering effects respectively. The inner filter effect (IFE) is where the excitation beam enters the media, exciting a higher proportion of fluorophores which decreases across the beam pathlength, therefore resulting in a graduated fluorescence emission.[14] In the scattering effect, increasing concentrations leads to reduced transparency of the solution. At extreme concentrations it becomes optically dense and opaque thereby preventing the beam from penetrating the media and thus resulting in lack of fluorescence.[32]

A major limitation for intrinsic fluorescence is the pre-requisite for aromatic residues to be present in the analyte, therefore reducing the universal applicability of this technique. A technique of similar sensitivity and specificity to IF, which delivers comparable results, is necessary.

7.1.1.3. Deep-blue autofluorescence

Deep-blue autofluorescence (dbAF) is a recently discovered phenomenon, whereby excitation (Ex) occurs in the ultraviolet (UV) region (λ_{Ex} ~350 nm) and emits (Em) in the visible blue region (λ_{Em} ~450 nm).[33] This phenomenon was first discovered by Shukla *et al*[33] in 2004, by probing protein crystals using a UV laser (λ_{Ex} 341 or 364 nm) which resulted in visible fluorescence (λ_{Em} 400 – 500 nm). The origins of this phenomenon were initially proposed to be a property of protein aggregation, which was attributed to the amyloid fibrillar state because of the increasing fluorescence intensity as aggregation proceeded,[34,35] however the phenomenon origins are still widely debated.

There have been various potential origins proposed recently for this intrinsic-type fluorescence such as; hydrogen lability,[4,7,36] carbonyl interactions,[6] fibril size.[37], charge and pH[3,38]. This phenomenon has been recently reported to exist for other molecules such as; for amyloid-β peptide (Aβ40 and Aβ42),[34] β-lactoglobulin (BLG),[6] bovine serum albumin (BSA),[6] hen egg white lysozyme (HEWL),[6] human lysozyme,[34] insulin,[39] phenylalanine di-peptide[39] and protein Tau K18.[1] The observation of this intrinsic-type phenomenon in the various molecules studied, has led to variations on the terminology proposed namely; Non-Traditional Intrinsic Luminescence (NTIL),[40] autofluorescence,[6] intrinsic amyloid fluorescence[34] and Protein Charge Transfer Spectra.[41] For this thesis, the phenomenon will be referred to as deep-blue autofluorescence.

The aim of this chapter is to utilise IF and dbAF to probe amyloid-like fibrillation of HI, α-synuclein (αS) and several small molecules. This dbAF phenomenon has the potential to be used as a non-invasive fluorescence technique to assess pre-fibrillar aggregation state, which has the possibility for use in industrial processes as a first line detection tool for situations where aggregation is to be avoided. As the origins of dbAF are widely debated with various factors proposed, this study will investigate whether; increasing oligomeric size, single-point mutations, protein oxidation and nitration, or homogeneous fibrillation affect the dbAF and whether they are the cause of the phenomenon.

7.1.2. α-Synuclein (αS)

In addition to investigating the HI fibrillation pathway by IF, this chapter also includes another physiologically important protein of interest, α-synuclein (αS). αS, a 140 amino acid (17 kDa) unstructured single chain polypeptide (Figure 83), is an intrinsically disordered protein (IDP)[42] and its aggregation pathway is a hallmark of α-synucleinopathies; Parkinson's disease (PD)[43] and dementia with Lewy bodies.[44] IDPs are functional and highly water-soluble proteins but lack an absolute fixed spatial structure.[45] Intrinsic disorder is attributed to a completely unstructured protein or more likely one which contains partial structural architecture.[46]

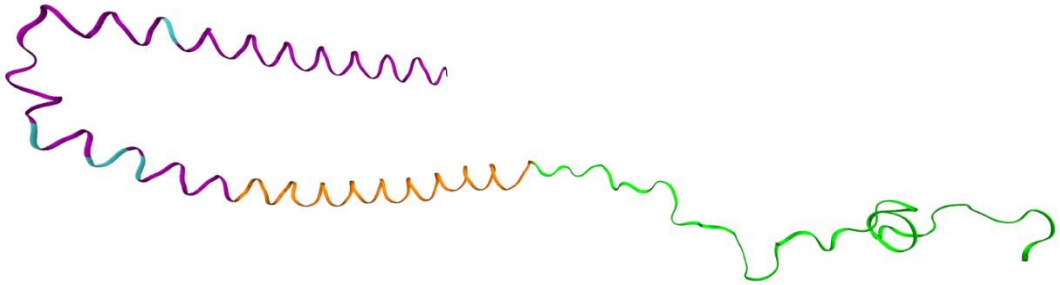

Figure 83: A visual molecular dynamics (VMD)[47] representation of α-synuclein (PDB: 1XQ8)[48], illustrating; (purple) amphipathic region, (orange) non-amyloid-ß component, (green) acidic tail and (cyan) the single-point mutation sites.

The visual molecular dynamics (VMD)[47] representation shown in Figure 83, was micelle-bound to resolve the non-mutated (wild-type, WT) αS structure by nuclear magnetic resonance (NMR) spectroscopy.[48] αS is comprised of three distinct regions (Figure 83); the amphipathic region (purple) is a long helical structure critical for membrane binding, the non-amyloid-β component (NAC, orange) which is vital for fibrillation events, and the acidic tail (green) situated at the C-terminus.[43,49–51] The cyan coloured segments shown within the amphipathic region, denote the single-point mutation sites in WT αS which gives rise to the six familial mutations (A30P, A53E, A53T, E46K, G51D and H50Q) investigated in this chapter. The difference in amino acids between the WT αS and the corresponding site within the mutation are shown in Figure 84, with the entire WT αS primary sequence provided in Figure S21.

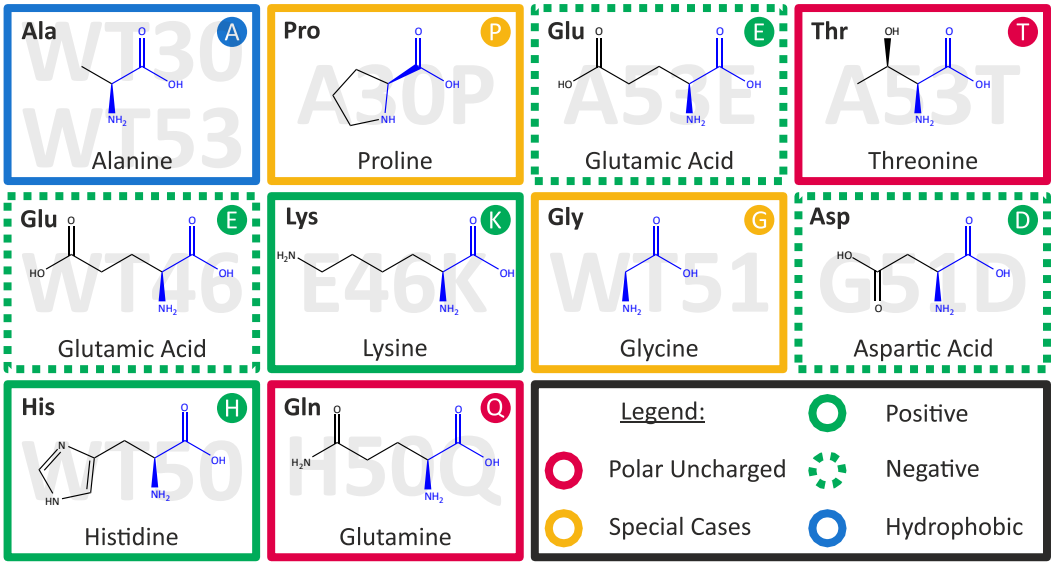

Figure 84: The various biophysical property differences between the wild-type α-synuclein (WT αS) and the six familial αS mutations; A30P, A53E, A53T, E46K, G51D and H50Q, where each corresponding difference is backlit with the mutation site. For example, in the WT sequence at residues 30 and 53 alanine is present, however alanine is replaced at residue 30 in A30P by proline and at residue 53 in A53E and A53T by glutamic acid and threonine, respectively.

The specific point mutations in the familial αS strains result in differing biophysical properties at the mutation sites, as shown in Figure 84. A steric effect of the mutations is observed in all cases, particularly; A30P, and A53T, where proline remains hydrophobic but sterically restricted in the five-membered ring, and threonine is a polar residue. The electronic states of αS are modified in; A53E, E46K, G51D and H50Q, whereby A53E and G51D become negatively charged, E46K switches from negative to positive polarity and H50Q loses a positive charge. These seven strains of αS are physiologically important as they differ in the severity and onset of the associated disease.[52,53] WT was first characterised, followed by the early onset mutations (A30P, A53T and E46K).[54–59] Recently additional early onset (A53E and G51D) and late onset (H50Q) mutations have been discovered.[54–59]

The age of onset differs between the various single-point mutations of αS, and is illustrated in Figure 85, for example the age of onset for G51D (yellow) is between 19 and 61 years of age. These pathologies however do not correlate with the experimental data surrounding fibrillation and oligomerisation whereby increased fibrillation rates and accelerated oligomerisation found in A53T, E46K and

H50Q do not have similar onsets.[60,61] This would suggest that other factors are affecting the varying pathologies, which may include differing aggregation pathways accounting for toxicity. In this chapter, αS has been used to further investigate the dbAF phenomenon by providing a second amyloidogenic protein of interest in addition to HI.[62]

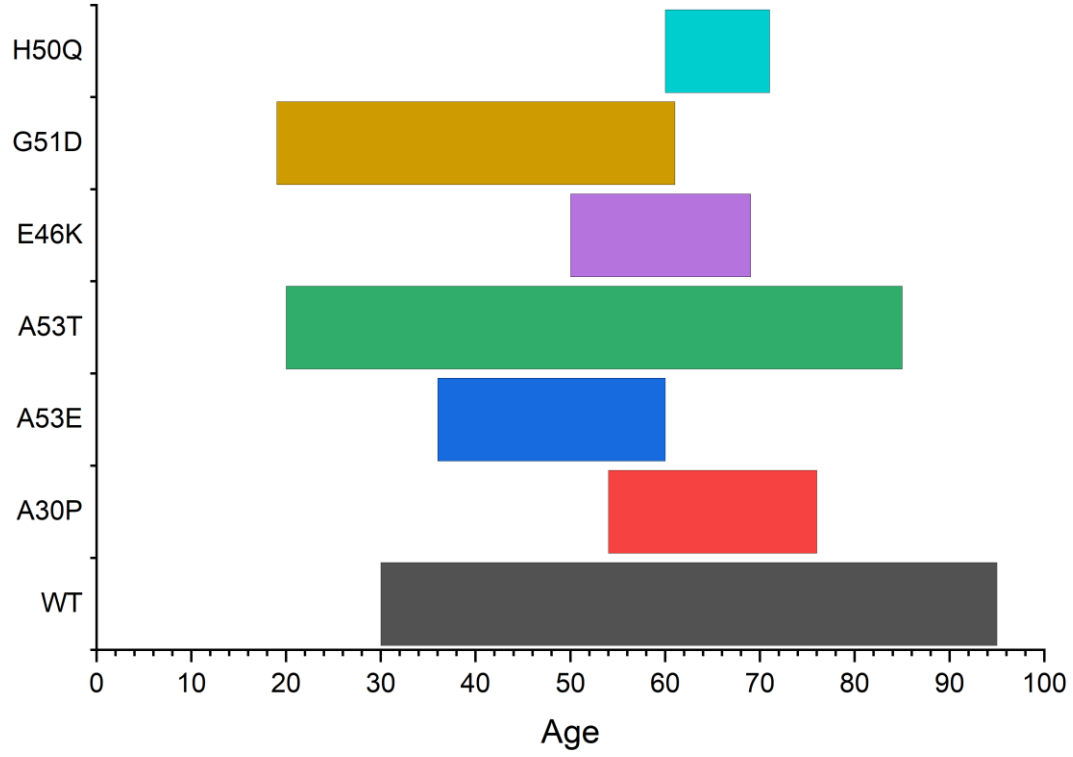

Figure 85: An illustration showing the age of onset for Parkinson's disease across the α-synuclein (αS) strains; (black) WT, (red) A30P, (blue) A53E, (green) A53T, (purple) E46K, (yellow) G51D and (teal) H50Q. Adapted from Iadanza et al[63] and Meade et al.[61]

7.1.3. Small molecules

The investigation of the six small molecules shown in Figure 86, comprised of four amino acids (purple border) and two nucleic acids (teal border), were studied to ascertain whether dbAF is present in homogeneous small molecular assemblies.

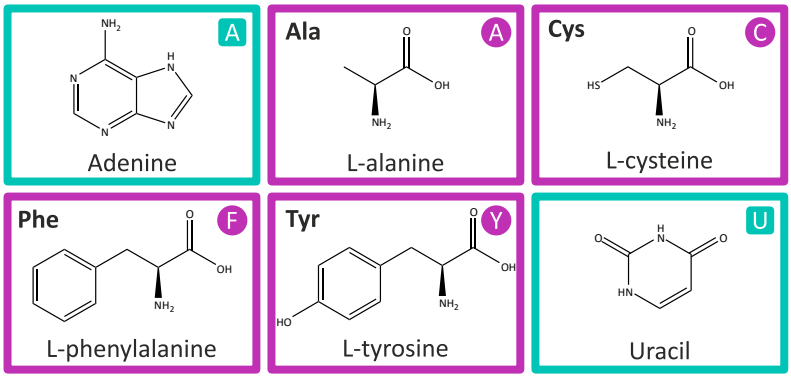

Figure 86: The small molecules, (teal) nucleic acids and (purple) amino acids, investigated in this fluorescence study, showing the one-letter and three-letter abbreviations where appropriate.

The four amino acids, which were investigated in the L-isomeric form were; L-alanine, L-cysteine, L-phenylalanine and L-tyrosine. The two nucleic acids investigated, adenine and uracil, are critical in the messenger ribonucleic acid (mRNA) transcription process, which dictates protein synthesis as determined by the deoxyribonucleic acid (DNA) sequence.[64] These six small molecules were investigated because of their ability to aggregate through amyloid-like fibrillation pathways,[65–67] and their physiological importance in metabolic diseases such as; adenine phosphoribosyltransferase deficiency,[68] cystinuria,[69] phenylketonuria,[70] tyrosinemia[71] and ornithine transcarbamylase deficiency.[72]

7.2. Materials and Methods

7.2.1. Sample Preparation

All glassware was cleaned either in an acidic Piranha solution (30% hydrogen peroxide and 70% sulfuric acid, 30 minutes) to remove any hard deposits or in a basic 10% Decon 90 overnight and then dried in an oven. The quartz cells used were thoroughly rinsed with water (Milli-Q, 18.2 MΩ cm^{-1}) and ethanol several times between measurements, air-dried before use and wiped clean using a lint-free tissue.

7.2.1.1. α-synuclein

The αS proteins used were kindly provided by James Torpey, Institute of Integrative Biology (University of Liverpool), and had been pre-suspended in either phosphate buffered saline (PBS) or nitration buffer (~100 µM peptide concentration).[73]

7.2.1.2. Human insulin

The protocol developed in Chapter 3 was followed with all reagents of analytical grade or better. HI (100 µM) was suspended in a pH 2 buffer (20% acetic acid and 139.7 mM sodium chloride) in a lo-bind Eppendorf tube (2 mL), briefly vortexed to ensure complete dissolution, and then immediately syringe-filtered (0.22 µm, polyethersulfone - PES). The HI suspensions were agitated at 37°C, after 24 hours aliquots were taken for studying the pre-fibrillar state and after 72 hours final aliquots, which were visibly cloudy, were taken for the fibrillar state. All aliquots and samples were stored in a lo-bind Eppendorf (2 mL) and immediately frozen (-20°C for short durations or -77°C for longer durations). Frozen samples were thawed back to laboratory temperature before being analysed. All peptides and proteins only underwent a maximum of one thaw cycle to reduce any potential freezing influences, as continual freeze-thaw cycles have significant effect on aggregation.[74–78]

7.2.1.3. Small molecules

The small molecules (~100 µM); adenine, L-alanine, L-cysteine, L-phenylalanine, L-tyrosine and uracil were prepared in nitration buffer, by the addition of sodium bicarbonate (25 mM) and diethylenetriaminepentaacetic acid (0.1 mM, DTPA) to a potassium phosphate buffer (100 mM). The stock potassium phosphate buffer (0.1 M, pH 7.4) was formulated by; dibasic potassium phosphate (80.2 mL, 1 M), monobasic potassium phosphate (19.8 mL, 1 M) and water (900 mL, 18.2 MΩ cm^{-1}). After the amino acids were suspended within the nitration buffer, the solutions were syringe-filtered (0.22 µm, PES) into lo-bind Eppendorf tubes (2 mL).

7.2.1.4. Oxidation

The peptides and protein samples were oxidised by addition of sub-molar quantities of hydrogen peroxide (30%) to each sample.

7.2.1.5. Nitration

The peptides and protein samples were nitrated using a peroxynitrite solution, following an adapted procedure from Beckman *et al*[79] and Hughes *et al*.[80] All solutions were cooled in ice-baths and efforts made to retain their low

temperatures until nitration was complete because of the low nitration agent lifetime (1 s). In a beaker (250 mL), sodium nitrite (50 mL, 50 mM) and hydrogen peroxide (50 mM, 30%) were rapidly agitated. Hydrochloric acid (25 mL, 1 M) was added immediately into the beaker followed by sodium hydroxide (25 mL, 1.5 M). Aliquots of the synthesised peroxynitrite solution were immediately added to the peptide/protein samples in excess, successful nitration was recognised with an observed colour change from colourless to yellow, and increased absorbance at 430 nm in the ultraviolet-visible (UV-Vis) spectra.

7.2.2. Spectroscopic Methods

7.2.2.1. Ultraviolet-visible Spectroscopy

Ultraviolet-visible (UV-Vis) spectroscopy was performed on a GENESYS UV-Vis spectrometer (ThermoFisher). Transmission spectra were acquired through the short pathlength (0.2 cm) of the micro fluorescence quartz cuvette (700 µL), and the concentration of the species calculated using the Beer-Lambert Law, which was an average of the number of scans taken.

7.2.2.2. Fluorescence Spectroscopy

The fluorescence work was carried out using a FluoroMax-4 spectrofluorometer (HORIBA), using the same micro fluorescence quartz cuvettes (700 µL) as for UV-Vis analysis.

The fluorescence measurements were acquired with the cuvette's small slit (0.2 cm) facing the incoming beam and the larger sample window (1 cm) directed towards the detector. The parameters of the Fluoromax were set at; excitation wavelengths (λ_{Ex} 245 to 600 nm), emission wavelengths (λ_{Em} 270 to 700 nm), bandpasses (5 nm for both incoming and outgoing beam path), integration time (0.1 s), Rayleigh masking slit width (12.5 nm) and measurements acquired at 5 nm intervals. The fluorimeter was programmed to acquire sample and reference channel measurements simultaneously, which allows for automatic correction of instrumental variations using a built-in algorithm. The final spectra acquired from the instrument were the corrected sample channel divided by the corrected reference channel, which were then manually buffer subtracted before further analysis was

performed. Fluorescence spectra were normalised using the probed species concentration.

7.2.2.3. Data processing

Origin (2016 64-bit) was used in the analysis of the one-dimensional (1D) fluorescence and UV-Vis spectra, and IgorPro (v6.7.3.2) was utilised for the three-dimensional (3D) fluorescence spectra. All spectra presented, unless otherwise stated, have had controls subtracted. The fluorescence is displayed using a logarithmic scale in the excitation-emission matrices (EEMs).

7.3. Results and Discussion

This objective of this chapter was to investigate whether the reported dbAF phenomenon is observed in HI, to determine the origins of this phenomenon and assess the potential application as a diagnostic tool to study the pre-fibrillar state of proteins.

7.3.1. The fluorescence profile for the human insulin fibrillation states

The IF analysis for HI was undertaken at 275 nm excitation and emission collected between 290 to 570 nm[30] as these IF parameters have previously been reported for insulin fibrillation studies.[24,81,82] The IF spectra of the oligomeric state of HI is shown in Figure 87.

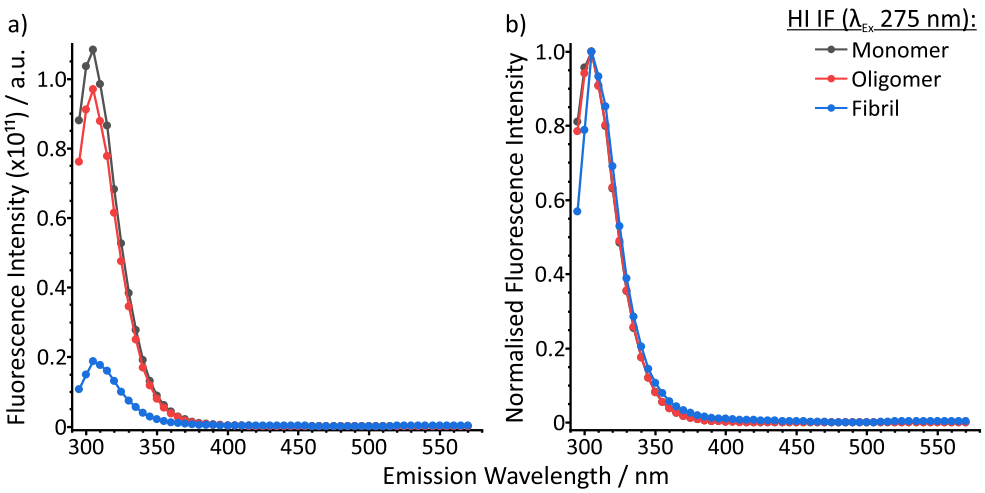

Figure 87: Fluorescence spectra of the (a) intrinsic fluorescence (IF) emission and (b) normalised IF for human insulin (HI) fibrillation showing; (black) monomer, (red) oligomer and (blue) fibril. The spectra in (b) are normalised to the maximum peak intensity in each series.

The IF for the HI fibrillation pathway as shown in Figure 87a, shows a decreasing fluorescence intensity from the HI monomer (black) to the HI fibril (blue) state. There is no apparent shift for the IF peak maxima (λ_{Em} 305 nm) as HI fibrillation proceeds, as shown in the normalised fluorescence spectra (Figure 87b). All normalised spectra for IF and dbAF, have been minimum-maximum normalised using the maximum peak intensity in each series, i.e. for Figure 87a the monomer, oligomer and fibril peak maxima are made to unity, thus allowing for peak shifts to be perceived.

Figure 88 shows the dbAF on the same samples, as a function of emission wavelength (375 – 600 nm) with an excitation wavelength fixed at 350 nm, to probe the phenomenon for the HI aggregation state.

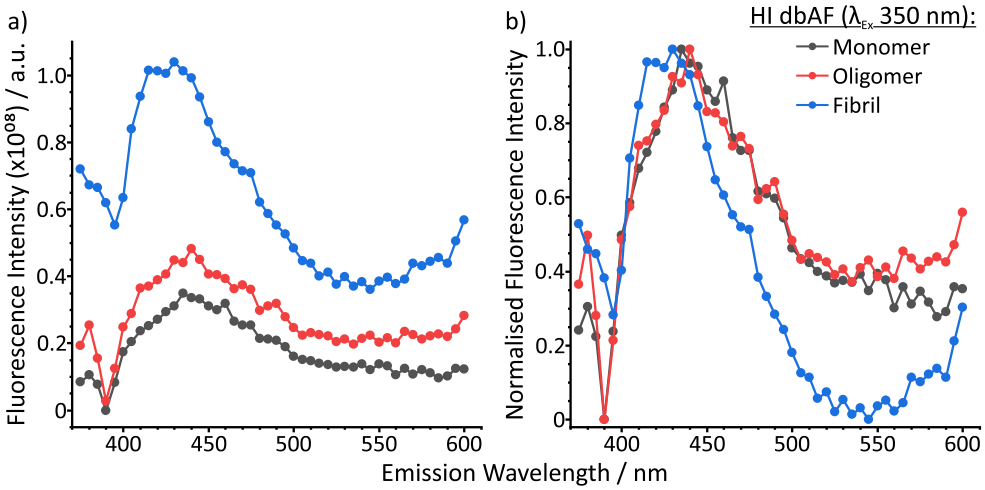

Figure 88: Fluorescence spectra of the (a) deep-blue autofluorescence (dbAF) emission and (b) normalised dbAF for human insulin (HI) fibrillation showing; (black) monomer, (red) oligomer and (blue) fibril.

The dbAF for the HI fibrillation pathway as shown in Figure 88a, shows an increasing fluorescence intensity from the HI monomer (black) to the HI fibril (blue) state. The fibrillar state has a strong fluorescence background present but there is still an overall intensity increase for the fibril. There is also a wavelength shift for the dbAF peak maxima and peak narrowing as HI fibrillation proceeds from the monomeric and oligomeric state (λ_{Em} 450 nm) to the fibril (λ_{Em} 430 nm), as shown in the normalised fluorescence spectra (Figure 88b). The shift in emission wavelength insinuates that there is a possible corresponding shift in excitation wavelength, therefore these 1D emission scans are not ideal.

7.3.1.1. Building the Excitation-Emission Matrix (EEM)

The IF and dbAF spectra (Figure 87 and Figure 88) were acquired by fixing the excitation whilst collecting the resulting fluorescence emission wavelengths, which results in a 1D emission spectrum. An emission spectrum can be used to characterise peak changes such as intensity and wavelength shifts, however the peak maxima could change in the excitation wavelength and is therefore not characterised in the emission spectra. An Excitation-Emission Matrix (EEM) is a 3D scan, which acquires both emission and excitation spectra concurrently within the same sample,[83] therefore fluorescence changes in both excitation and emission wavelengths are recorded. The use of EEMs in fluorescence studies is increasing and have previously

been reported for HI investigation of the dbAF[39] and fibril surface interactions.[84] A schematic for an acquired EEM is shown in Figure 89.

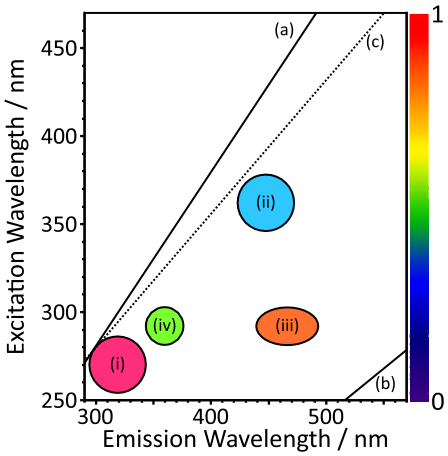

Figure 89: A schematic showing a representative excitation-emission matrix (EEM). (a – c) Lines correspond to correction features for Rayleigh and Raman scattering; (a) $\lambda_{Ex} = \lambda_{Em}$, (b) $\lambda_{Ex} = 2\lambda_{Em}$ and (c) Raman scattering. (i – iv) Coloured regions correspond to the fluorescence signatures of; (i) intrinsic fluorescence (IF), (ii) deep-blue autofluorescence (dbAF), (iii) dityrosine and (iv) tyrosinate. The colour bar is used to display the normalised fluorescence intensity in the z-axis, on a logarithmic scale.

In the EEM schematic (Figure 89), the two solid black lines (Figure 89a and b) correspond to scattering effects attributed to first and second order Rayleigh scattering. Rayleigh scattering is an elastic effect, where the electronic energy remains unchanged, and the terminology first and second order are derived from whether the emission wavelength is equal to once or twice the excitation wavelength. The Rayleigh scattering peak is broad and intense, therefore for clarity the EEMs presented in this thesis' chapter result in a smaller trapezoidal shape to remove any artefacts attributed to the broad scattering. The dashed line (Figure 89c) corresponds to water Raman scattering,[85] which is an inelastic effect where the incoming and outgoing electronic energy is different, which is termed as either Stokes (higher wavelengths) or anti-Stokes (lower wavelengths). The coloured regions (Figure 89i – iv) distinguish; IF (i), dbAF (ii), dityrosine (iii) and tyrosinate (iv). The tyrosine derivatives, including 3-nitrotyrosine which is nonfluorescent, are characteristic biomarkers of oxidation and nitration within neurodegenerative disease.[86–88] The colour scale shown for all EEMs is for the *z*-axis normalised fluorescence intensity, with the lowest (blue) to highest (red).

7.3.1.2. Investigating the human insulin fibrillation pathway by EEMs

The HI fibrillation pathway was investigated by EEMs, with excitation (250 – 470 nm) and emission (290 – 570 nm) wavelengths acquired concurrently for the three aggregation states, as shown in Figure 90.

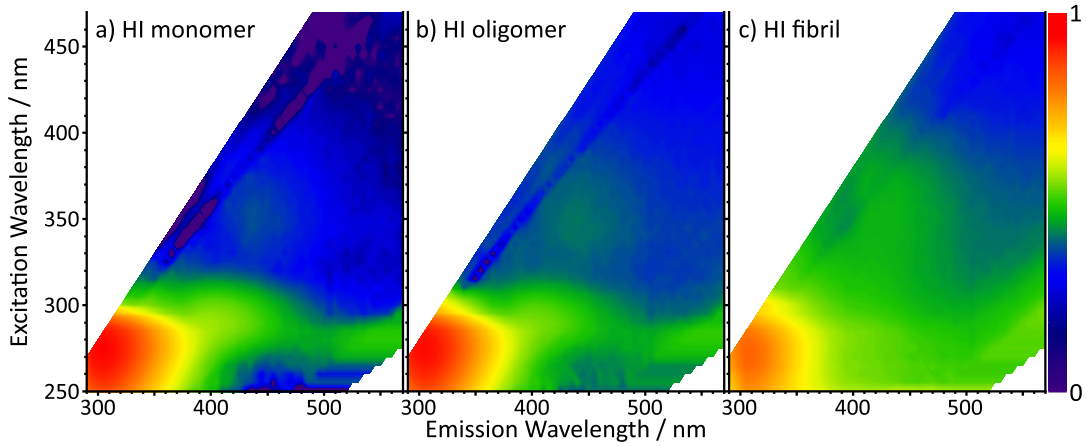

Figure 90: The human insulin (HI) EEMs, normalised to the aggregation states intrinsic fluorescence (IF) signal maxima, for the (a) monomer, (b) oligomer and (c) fibril states. The exhibited fluorescence is shown as (red) highest to (blue) lowest.

Figure 90 shows the HI aggregation states of the fibrillation pathway for the; monomer (Figure 90a), oligomer (Figure 90b) and fibril (Figure 90c), where each EEM has been normalised to the IF peak maxima to observe the relationship between IF and dbAF. The IF peak region decreases in intensity as fibrillation proceeds, which is shown by a colour change from red to orange, with a corresponding increase for the dbAF shown from blue to green. The fluorescence intensity for the HI fibrillation is low as the water Raman scattering band can be seen, in both the monomer and oligomer EEMs (Figure 90a and b).

In HI both IF and dbAF are observed but exhibit inverse fluorescence trends as fibrillation proceeds. The HI IF is an ensemble effect which is attributed to the four tyrosine (A_{14}, A_{19}, B_{16}, and B_{26}) and three phenylalanine residues (B_1, B_{24}, and B_{25}) in both chains, as there are no tryptophan residues in HI. A reduction in IF intensity was observed for the increasing aggregation states as HI fibrillation proceeds (Figure 87), which implies that the residues are quenched, however there is no change in the peak maxima (λ_{Em} 305 nm). The HI IF results are consistent with previous work that suggested the tyrosine residues are non-hydrogen bonded in the fibrillar state.[24] An

inverse fluorescence trend was shown for dbAF, where IF intensity increased as HI fibrillation proceeded (Figure 88) and a change in the emission peak maxima was observed for the fibrillar state suggesting a change in the fluorophore environment. The correlation between increased dbAF intensity and aggregation state, suggests that the phenomenon is influenced by aggregation and supports the possibility that it is a property of amyloidogenicity,[34] however because of the emission wavelength shift an associated change in the excitation wavelengths was considered, leading to the use of EEMs.

The EEMs for the HI fibrillation pathway (Figure 90) showed that the dbAF peak maxima is located at different excitation and emission wavelengths (~10 nm) than previously reported (λ_{Ex} ~350 nm, λ_{Em} ~450 nm).[39] This has a significant impact on research into this phenomenon because by fixing the excitation wavelength, the dbAF may be missed or result in biased fluorescence intensities attributed to the fluorescence slope as opposed to the peak maxima. It is therefore essential to use EEMs in the investigation of dbAF, since changes in both excitation and emission wavelengths are attained. This investigation also uses the 1D IF and dbAF spectra, with the purpose of determining the origin of the dbAF phenomenon through known and previously reported parameters.

Overall, the existence of dbAF in HI and the correlation between the increased dbAF intensity and aggregation state provides support to the theory that amyloidogenicity enhances the dbAF,[34] however the presence of dbAF in the monomeric state albeit at a reduced intensity implies other factors may also contribute. HI is a structured protein with three α-helices consisting of two chains. It is possible that the secondary structure of HI gives rise to the dbAF in the monomeric state as a result of carbonyl[6] or hydrogen bonding interactions.[89] To investigate the dbAF phenomenon further, an amyloidogenic protein lacking structure is needed to assist in the phenomenon's origins by eliminating the structural factor.

7.3.2. The fluorescence profile for the α-synuclein fibrillation states

It was established that the dbAF phenomenon was observed in the HI fibrillation pathway, however this could be attributed to the properties of the

structured protein rather than the fibrillation pathway itself. In this section, αS is studied as it also undergoes amyloid-like fibrillation but as it is an IDP, this will ascertain whether the dbAF arises from a property of protein structure or the result of fibrillation.

7.3.2.1. Investigating the wild-type α-synuclein fibrillation pathway by fluorescence

The IF for the WT αS fibrillation pathway is shown in Figure 91, and shows the same behaviour as HI with a decreasing fluorescence intensity from monomer (black) to fibril (blue) state. There is no apparent shift for the IF peak maxima (λ_{Em} 305 nm) but there is the emergence of two additional peaks (λ_{Em} 360 nm and 450 nm) as fibrillation proceeds, as shown in the normalised fluorescence spectra (Figure 91b).

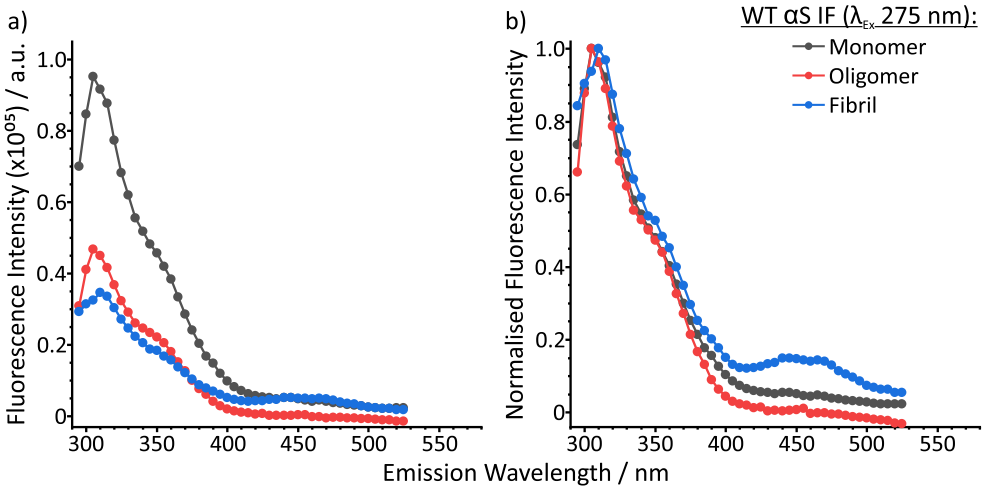

Figure 91: Fluorescence spectra of the (a) intrinsic fluorescence (IF) emission and (b) normalised IF for wild-type α-synuclein fibrillation showing the; (black) monomer, (red) oligomer and (blue) fibril states.

The investigation of the dbAF for the WT αS aggregation state, as shown in Figure 92, was undertaken using the same emission scan parameters as for HI (Figure 87).

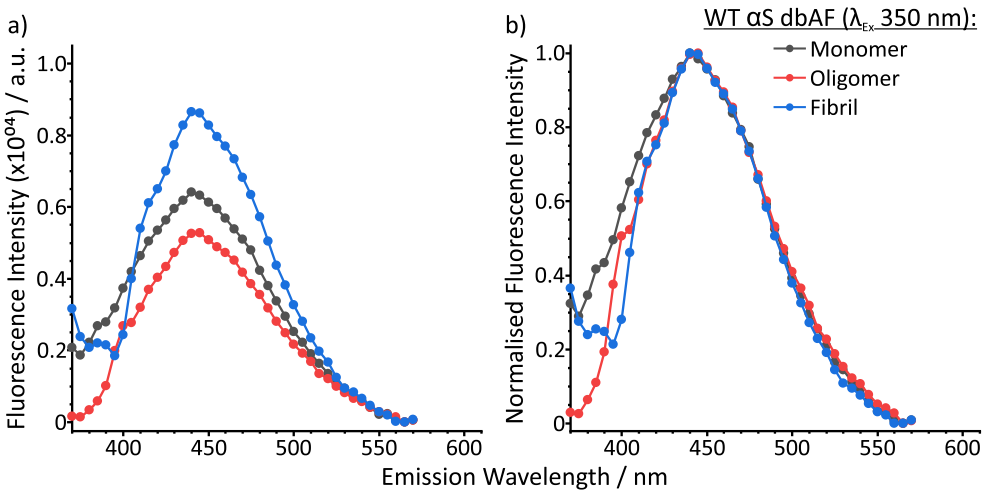

Figure 92: Fluorescence spectra of the (a) deep-blue autofluorescence (dbAF) emission and (b) normalised dbAF for wild-type α-synuclein fibrillation showing the; (black) monomer, (red) oligomer and (blue) fibril states.

The dbAF for the WT αS fibrillation pathway (Figure 92a), shows an increasing fluorescence intensity from the monomer (black) to the fibril (blue) state, with a decreased fluorescence for the oligomeric (red) state. There is no apparent wavelength shift for the dbAF peak maxima, unlike for HI, however a peak narrowing is observed at the lower wavelengths as fibrillation proceeds, as shown in the normalised fluorescence spectra (Figure 92b).

Similarly, to the HI fibrillation pathway, αS was investigated by EEMs as shown in Figure 93 with the same conditions as previously stated for HI.

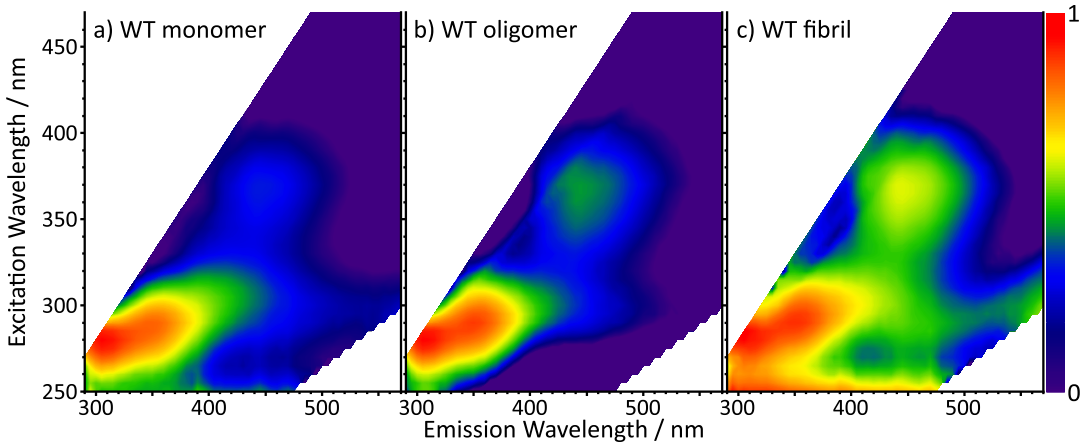

Figure 93: The wild-type α-synuclein EEMs, normalised to the intrinsic fluorescence (IF) signal maxima, for the (a) monomer, (b) oligomer and (c) fibril. The exhibited fluorescence intensity is shown as (red) highest to (blue) lowest.

Figure 93 shows the WT αS aggregation states of the fibrillation pathway for the; monomer (Figure 93a), oligomer (Figure 93b) and fibril (Figure 93c), where each EEM has been normalised to the IF peak maxima to observe the relationship between IF and dbAF. The IF peak region decreases in intensity as fibrillation proceeds, which is shown by a colour change from red to orange but is not as dramatic as previously observed for HI, whilst there is also a corresponding increase observed from blue to yellow for the dbAF. The two peaks seen in Figure 91 (λ_{Em} 360 nm and 450 nm) are further confirmed in Figure 93, as shown by the increased intensity around the tyrosine and tyrosinate spectral regions.

In WT αS both IF and dbAF are observed but exhibit differing fluorescence trends to HI, as fibrillation proceeds. The IF for the WT αS fibrillation pathway (Figure 91) was similar to HI (Figure 87), where the IF intensity decreased as aggregation increased, with no observed changes in the peak maxima (λ_{Em} 305 nm). A notable difference was the appearance of two additional peaks (λ_{Em} 360 nm and 450 nm) in the WT αS IF spectra (Figure 91b), which correlate to the fluorescence profiles of tyrosinate and dityrosine. The WT αS dbAF (Figure 92a) also showed an increase from monomer to fibril state, as shown in HI (Figure 88), however with reduced intensity for the WT αS oligomeric state. The normalised dbAF (Figure 92b) showed peak narrowing as aggregation proceeded, which suggests possible

two-dimensional (2D) peak shifts specifically shifts in the excitation wavelengths, therefore requiring EEMs to characterise the dbAF phenomenon.

The EEMs for the WT αS fibrillation pathway (Figure 93) showed a significant shift in the excitation wavelengths for the dbAF peak maxima (λ_{Ex} ~370 nm, λ_{Em} ~450 nm) than previously acquired for HI or reported. This peak shift suggests that the dbAF signature for WT αS differs from HI, which implies that the factors which govern dbAF are not equivalent in both proteins, therefore EEMs are an essential technique to investigate the origins of dbAF. In addition to measuring the dbAF peak shifts, the dityrosine and tyrosinate peaks (λ_{Em} 360 nm and 450 nm) shown in the IF spectra are observed in the WT αS fibrillar state EEM (Figure 93c). Interestingly the oligomeric state EEM (Figure 93b) showed that the dbAF intensity increased with respect to the IF, which was not apparent in the 1D spectra as the dbAF intensity decreased with respect to monomer and fibril states.

Overall the dbAF phenomenon is shown to exist for WT αS and a similar trend to that of HI was observed; dbAF intensity increased from the monomer to fibrillar state, which would suggest that aggregation influences the phenomenon. These results show that dbAF is present in all three aggregation states, albeit reduced intensities for the monomer and oligomer, therefore dbAF does not arise from the ordered protein structure. The reduced dbAF intensity for the WT αS oligomeric state, implies that the phenomenon is aggregation dependent, therefore to investigate this a chemically similar protein with a diverging fibrillation pathway is necessary.

7.3.2.2. The effect of α-synuclein single-point mutations on the fluorescence profile

It is well documented that single-point mutations of α-synuclein have a significant effect upon both the age of onset and severity of the associated disease,[63] as shown in Figure 85. These mutations are still amyloidogenic but give differing fibrillation pathways to WT and are used to investigate whether the dbAF phenomenon can detect differences in the pre-fibrillar state for each mutation, potentially providing a diagnostic application for dbAF. The fluorescence profiles of the six familial mutations (A30P, A53E, A53T, E46K, G51D, and H50Q) are compared to the WT in the following IF and dbAF spectra.

The IF for the effect of single-point mutations on monomeric WT αS are shown in Figure 94, where all the mutations have increased in IF intensity with the exception of H50Q. The three mutations with the lowest IF intensities (Figure 94a), which are WT, A30P and H50Q, all give rise to a second peak (λ_{Em} 360 nm) and for all seven strands there are no apparent IF peak maxima shifts observed in the normalised fluorescence spectra (Figure 94b).

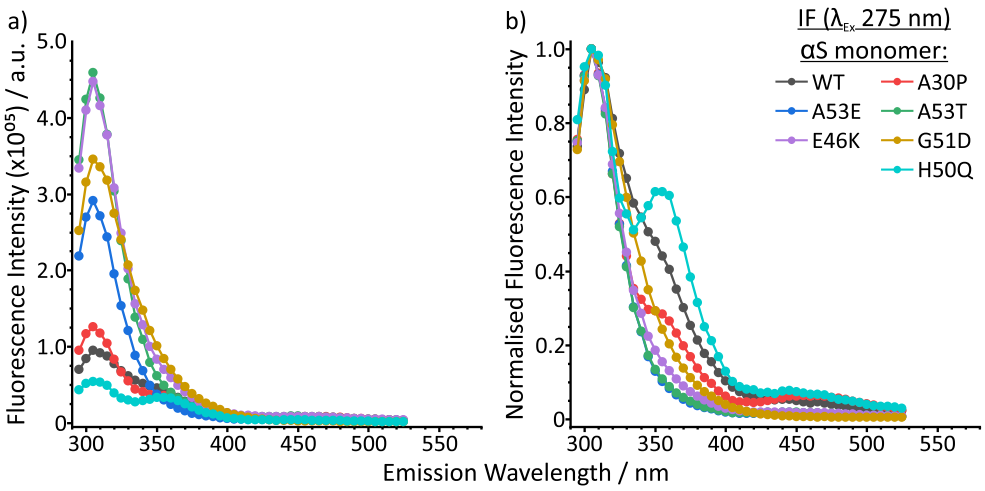

Figure 94: Fluorescence spectra of the (a) intrinsic fluorescence (IF) emission and (b) normalised IF for α-synuclein monomeric state; (black) WT, (red) A30P, (blue) A53E, (green) A53T, (purple) E46K, (yellow) G51D and (teal) H50Q.

The IF for the effect of single-point mutations on oligomeric WT αS are shown in Figure 95, where all the mutations have increased in IF. Overall the oligomeric IF has decreased in intensity compared to monomeric IF for all αS strands, except for G51D which increased and A30P which remained constant. The secondary peak (λ_{Em} 360 nm) for H50Q has increased in intensity and there is no change in intensity for WT and A30P, compared to the IF peak.

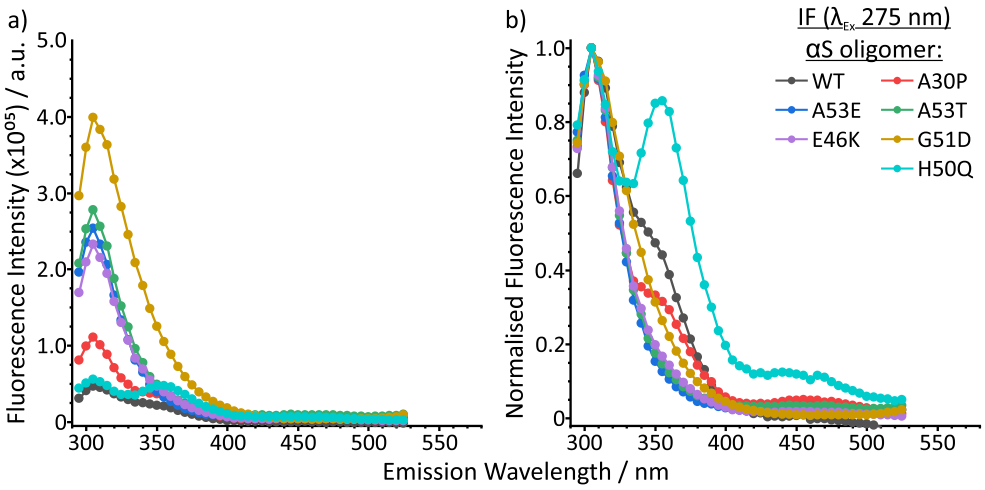

Figure 95: Fluorescence spectra of the (a) intrinsic fluorescence (IF) emission and (b) normalised IF for α-synuclein oligomeric state; (black) WT, (red) A30P, (blue) A53E, (green) A53T, (purple) E46K, (yellow) G51D and (teal) H50Q.

The IF for the effect of single-point mutations on fibril WT αS are shown in Figure 96, where all the mutations have increased in IF. Overall the fibril IF has decreased in intensity compared to both the monomeric and oligomeric IF for all αS strands, except for A53E and H50Q which have increased. The secondary peak (λ_{Em} 360 nm) has reduced in intensity, compared to the IF peak, for the three strands (WT, A30P and H50Q). A third peak (λ_{Em} 450 nm) arises for the same three strands, particularly noticeable for the WT, however due to the fibrillar scattering this could be a background artefact present for the mutations.

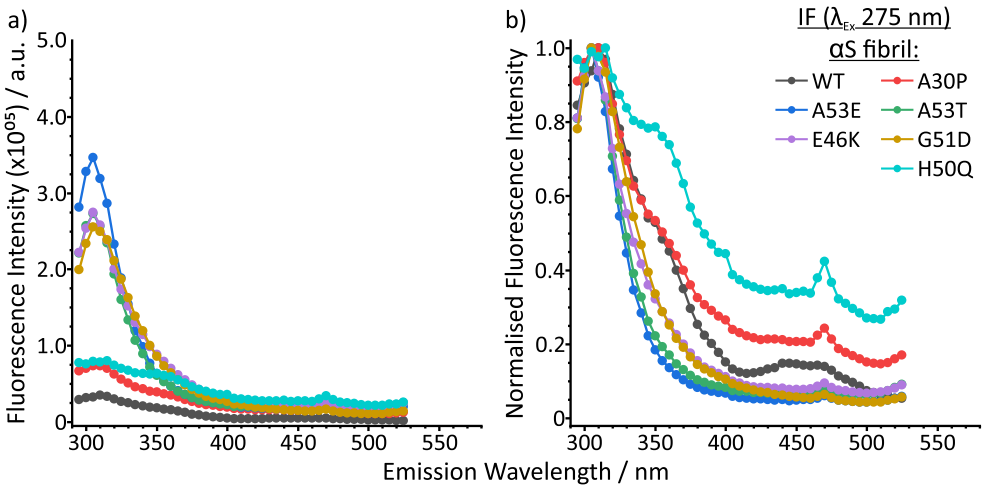

Figure 96: Fluorescence spectra of the (a) intrinsic fluorescence (IF) emission and (b) normalised IF for α-synuclein fibrillar state; (black) WT, (red) A30P, (blue) A53E, (green) A53T, (purple) E46K, (yellow) G51D and (teal) H50Q.

The dbAF for the effect of single-point mutations on monomeric WT αS (Figure 97), shows an increased fluorescence intensity for three mutations (A30P, A53T and E46K) and decreased intensity for the other three mutations (A53E, G51D and H50Q) compared to WT αS dbAF. There is a dbAF peak maxima wavelength shift for the G51D (~30 nm) to lower wavelengths, and a shift to higher wavelengths for A30P (~10 nm). All αS mutations show a narrowing of the dbAF peak compared to the WT.

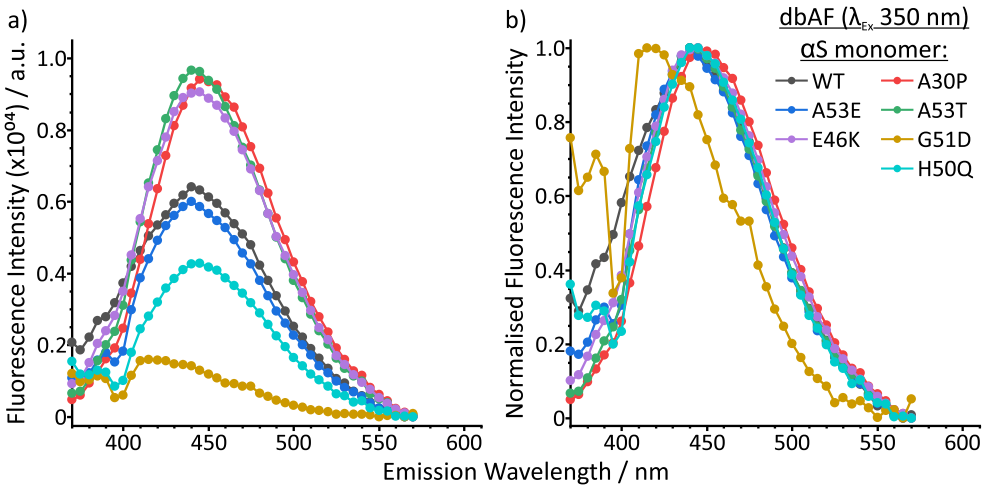

Figure 97: Fluorescence spectra of the (a) deep-blue autofluorescence (dbAF) emission and (b) normalised dbAF for α-synuclein monomeric state; (black) WT, (red) A30P, (blue) A53E, (green) A53T, (purple) E46K, (yellow) G51D and (teal) H50Q.

The dbAF for the oligomeric αS mutations (Figure 98) shows an increased fluorescence intensity for all mutations compared to WT αS dbAF. Overall the oligomeric dbAF intensity compared to monomeric varies in all αS strands; three decrease (WT, A30P and E46K), two remain similar (A53E and A53T) and two increase (G51D and H50Q). All αS mutations show a broadening of the dbAF peak compared to WT, with only G51D exhibiting a peak maxima shift.

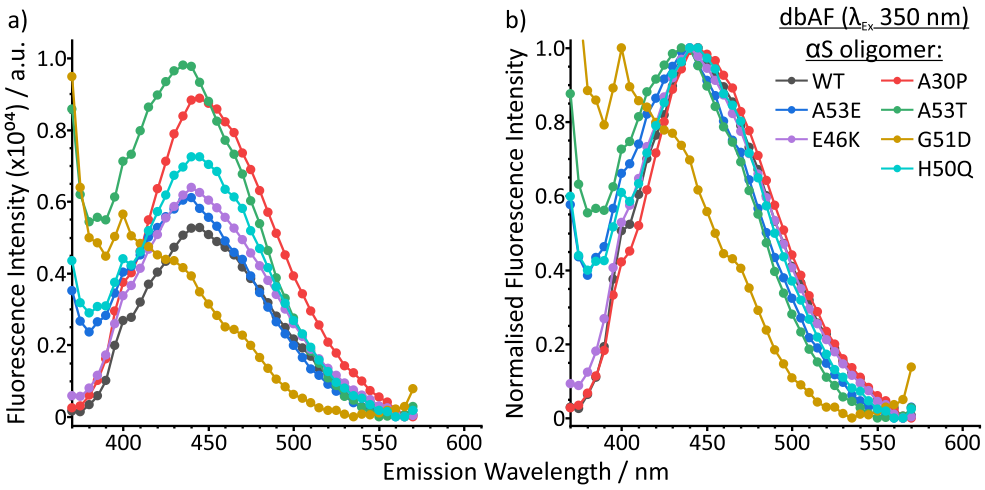

Figure 98: Fluorescence spectra of the (a) deep-blue autofluorescence (dbAF) emission and (b) normalised dbAF for α-synuclein oligomeric state; (black) WT, (red) A30P, (blue) A53E, (green) A53T, (purple) E46K, (yellow) G51D and (teal) H50Q.

The dbAF for the fibrillar αS mutations (Figure 99), shows an increased fluorescence intensity for all αS mutations compared to WT αS dbAF. Overall the fibril dbAF intensity has increased in all αS strands, however there is a strong sloping background consistent with the fibrillar physical properties. All αS mutations show a peak maxima shift with corresponding doublet (λ_{Em} ~415 nm and ~440 nm), and a new feature (λ_{Em} ~470 nm).

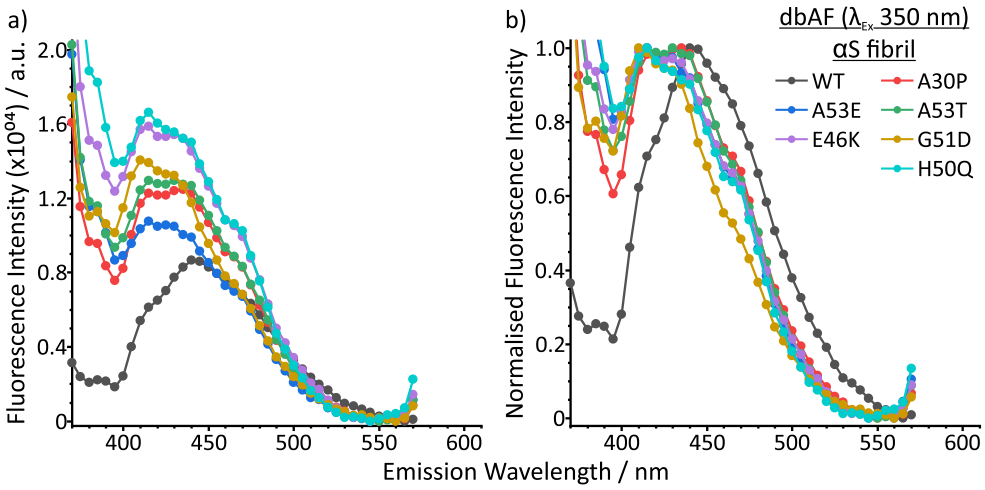

Figure 99: Fluorescence spectra of the (a) deep-blue autofluorescence (dbAF) emission and (b) normalised dbAF for α-synuclein fibrillar state; (black) WT, (red) A30P, (blue) A53E, (green) A53T, (purple) E46K, (yellow) G51D and (teal) H50Q.

The EEMs are used here to probe the effect of single-point αS mutations on the aggregation states (monomer, oligomer and fibril) for the αS fibrillation pathway. These EEMs provide context for the associated 1D peak shifts which were previously shown to highlight the effect of the mutations had on the WT αS IF and dbAF spectra as fibrillation proceeds. In each EEM presented here, the fluorescence intensity has been normalised to the IF peak maxima to observe the relationship between IF and dbAF, for each mutation.

Figure 100 shows the A30P αS aggregation states of the fibrillation pathway for the monomer (Figure 100a), oligomer (Figure 100b) and fibril (Figure 100c). In both monomer and oligomeric states, four peaks (IF, dbAF, dityrosine and tyrosinate) which correlate to those observed in the WT αS EEM (Figure 93) are observed, however interestingly, the third peak (dityrosine, λ_{Ex} ~295 nm, λ_{Em} ~455 nm) is not present in the A30P fibril EEM (Figure 100c). The IF peak is present in all the A30P aggregation states, maintaining a red colour on the intensity scale, however the dbAF peak region increases in fluorescence intensity, as shown by a colour change from blue to green, which is particularly prominent for the oligomer to fibril state. The A30P mutation exhibits a strong fluorescence scattering in the fibril EEM (Figure 100c) emanating from the lower wavelengths, which is to be expected

because of the strong scattering shown in the 1D fibril spectra (Figure 96 and Figure 99) previously shown for all the αS mutations.

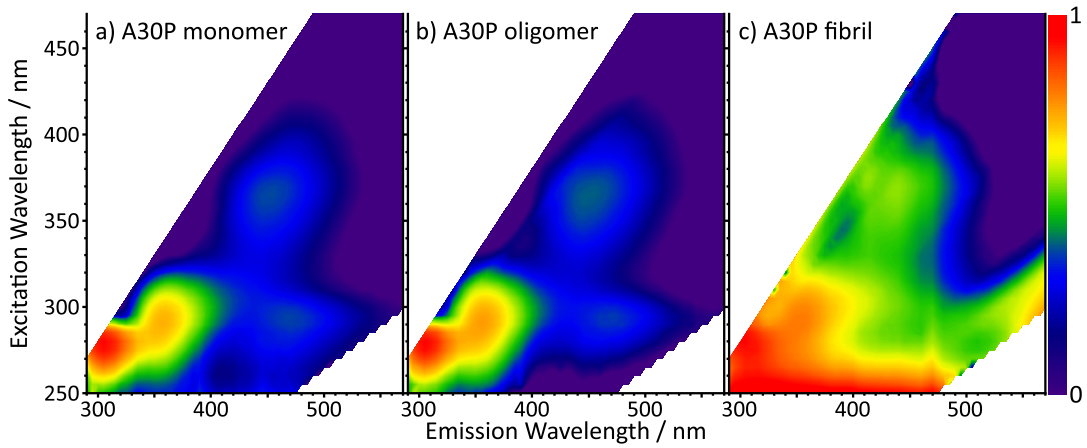

Figure 100: The A30P α-synuclein EEMs, normalised to the intrinsic fluorescence (IF) signal maxima, for the (a) monomer, (b) oligomer and (c) fibril. The exhibited fluorescence is shown as (red) highest to (blue) lowest.

Figure 101 shows the A53E αS aggregation states of the fibrillation pathway for the monomer (Figure 101a), oligomer (Figure 101b) and fibril (Figure 101c). In all three EEMs, only two peaks are observed which correspond to the IF and dbAF. The IF peak maintains a similar red colour for all states, however, becomes diffuse in the fibrillar EEM which is attributed to the fibril scattering effects. The dbAF peak is barely observed in the EEMs, as shown by the dark blue colour, which corresponds to the 1D spectra (Figure 97 and Figure 98) where the fluorescence intensity is similar for both the monomeric and oligomeric states. The intensity increases for the fibrillar state but on a sloping gradient due to the aforementioned fibril scattering effects.

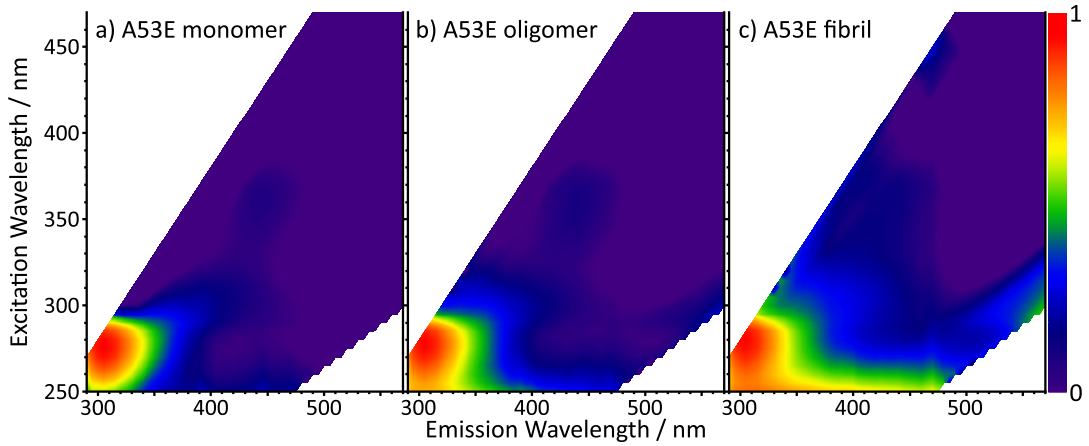

Figure 101: The A53E α-synuclein EEMs, normalised to the intrinsic fluorescence (IF) signal maxima, for the (a) monomer, (b) oligomer and (c) fibril. The exhibited fluorescence is shown as (red) highest to (blue) lowest.

Figure 102 shows the EEMs for the aggregation states of the A53T monomer (Figure 102a), oligomer (Figure 102b) and fibril (Figure 102c). Similarly to the A53E EEMs (Figure 101), only the IF and dbAF peaks are observed, whilst the IF maintains a similar red colour intensity for all three EEMs the dbAF increases in intensity from dark blue to light blue as fibrillation proceeds.

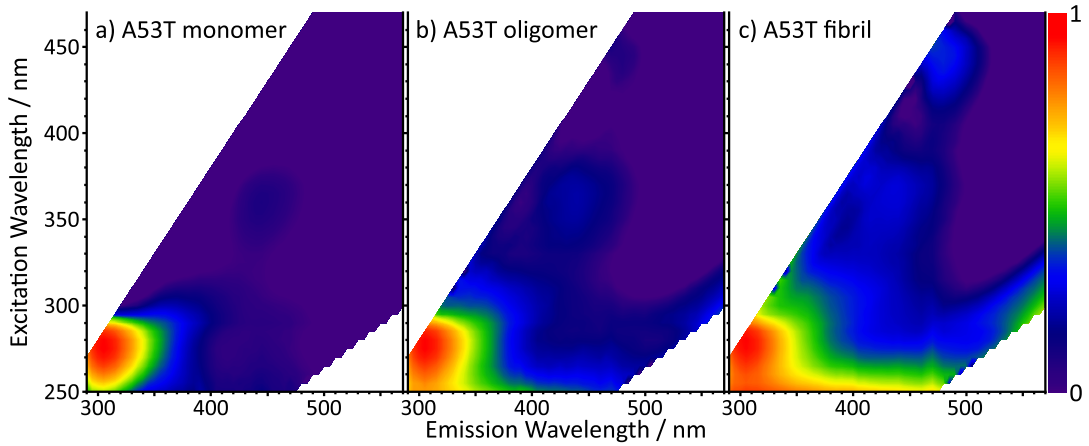

Figure 102: The A53T α-synuclein EEMs, normalised to the intrinsic fluorescence (IF) signal maxima, for the (a) monomer, (b) oligomer and (c) fibril. The exhibited fluorescence is shown as (red) highest to (blue) lowest.

Figure 103 shows the EEMs for the aggregation states of the E46K for the monomer (Figure 103a), oligomer (Figure 103b) and fibril (Figure 103c). Similarly to the A53E and A53T EEMs (Figure 101 and Figure 102), the IF and dbAF are observed with comparable intensity trends to A53T (consistent red for IF and increasing blue

for dbAF). In both the E46K monomer and oligomer states, there is a distinctly higher intensity around the dityrosine peak region which was previously observed in the A30P monomer and oligomer EEMs (Figure 100a and b).

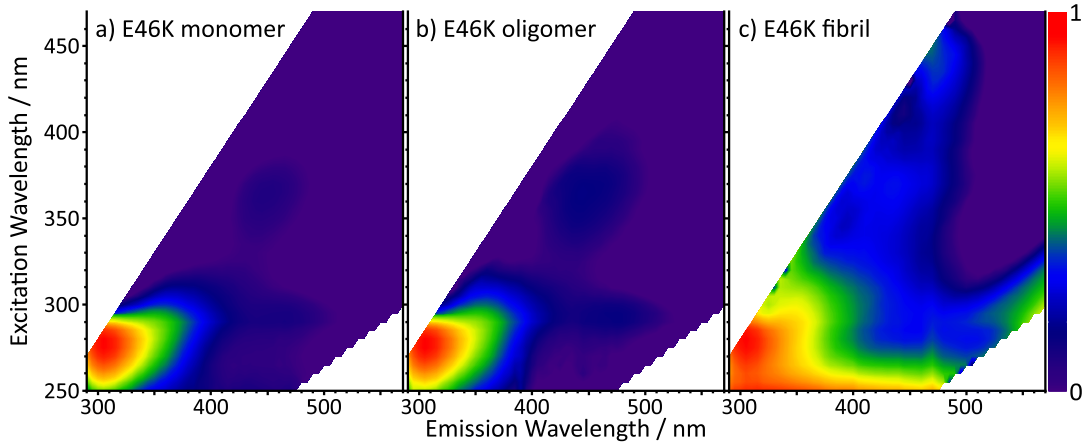

Figure 103: The E46K α-synuclein EEMs, normalised to the intrinsic fluorescence (IF) signal maxima, for the (a) monomer, (b) oligomer and (c) fibril. The exhibited fluorescence is shown as (red) highest to (blue) lowest.

Figure 104 shows the EEMs for the aggregation states of the G51D monomer (Figure 104a), oligomer (Figure 104b) and fibril (Figure 104c). As shown in the other αS mutations, the G51D IF peak also remains a consistent red colour throughout the aggregation EEMs. In contrast to the other αS mutation EEMs, G51D does not exhibit a peak in the dbAF region until the fibrillar state and the observed peak is shifted (~30 nm) in both excitation and emission wavelengths from the dbAF location observed for the other strands. In addition to the appearance of the dbAF peak, a third peak (tyrosinate, λ_{Ex} ~300 nm, λ_{Em} ~395 nm) is observed as a shoulder to the IF peak, which suffers from the physical fibril scattering effects.

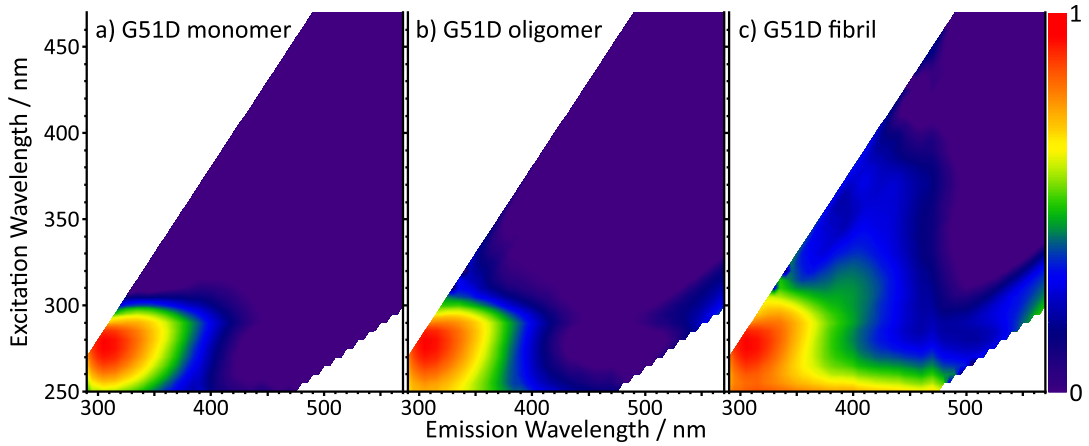

Figure 104: The G51D α-synuclein EEMs, normalised to the intrinsic fluorescence (IF) signal maxima, for the (a) monomer, (b) oligomer and (c) fibril. The exhibited fluorescence is shown as (red) highest to (blue) lowest.

Figure 105 shows the EEMs for the aggregation states of the H50Q for the monomer (Figure 105a), oligomer (Figure 105b) and fibril (Figure 105c). In all three EEMs, three peaks (IF, dbAF, and tyrosinate) can be observed which are similar to the A30P EEMs (Figure 100). The dbAF and tyrosinate peaks increase as fibrillation proceeds, which is shown by the colour changes from blue to yellow, and red to a diffused red respectively.

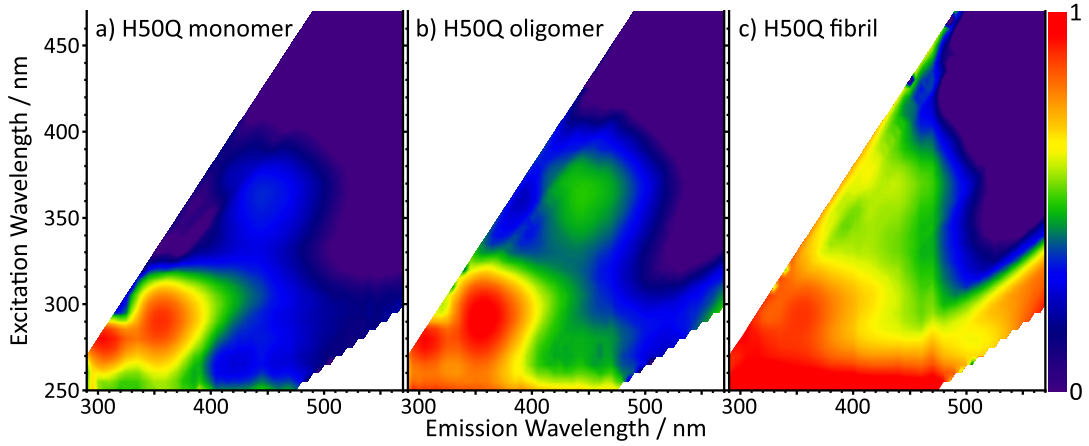

Figure 105: The H50Q α-synuclein EEMs, normalised to the intrinsic fluorescence (IF) signal maxima, for the (a) monomer, (b) oligomer and (c) fibril. The exhibited fluorescence is shown as (red) highest to (blue) lowest.

The single-point αS mutations exhibit both IF and dbAF phenomena. A similar IF trend to WT αS and HI is observed for most mutations where IF intensity decreases as fibrillation proceeds, however for the A53E and H50Q mutations an increased IF

intensity is observed for the fibrillar states (Figure 96). The A30P and H50Q mutations are of similar intensities to WT αS (Figure 91) and give rise to the two additional peaks (λ_{Em} 360 nm and 450 nm), which were identified previously as tyrosinate and dityrosine. The dbAF intensity trend correlates with both HI and WT αS, where an increased dbAF intensity is observed for all αS mutations from the monomeric to fibrillar states. Similarly, to the WT αS, the oligomeric state intensity (Figure 98) varies for the mutations; two decrease (A30P and E46K) which is comparable to WT (Figure 92), two remain similar (A53E and A53T) and the final two increase (G51D and H50Q). In the case of both A53E and A53T mutations, a broadening of the dbAF peak is observed (Figure 98b). There is no apparent dbAF peak maxima shift observed, until the fibrillar state where all the αS mutations are shifted to lower wavelengths, which corresponds with a significant fibril scattering which is not as apparent for WT αS.

The six familial αS mutations showed diversity in the fibrillation pathway EEMs, however in all fibrillar states a dispersed fluorescence emanating from lower wavelengths was observed which is attributed to the physical scattering effects for fibrils. In both A30P and H50Q EEMs (Figure 100 and Figure 105) the four fluorescence regions were observed, with the dbAF region becoming defined as fibrillation proceeds; H50Q appears linearly proportional, whereas for A30P both the monomeric and oligomeric EEMs appeared similar before a step change resulted in a defined dbAF peak in the fibril EEM. The A53T and E46K EEMs (Figure 102 and Figure 103) also exhibited an increased dbAF intensity as fibrillation proceeds, however in both cases the fluorescence signal was weak compared to the IF peak; small intensity increases were observed for A53T, whilst for E46K the region appeared more diffuse before an observed intensity increase in the fibrillar state. In the A53E EEM (Figure 101) dbAF was observed in all three aggregation states, however the intensity changes were negligible as fibrillation proceeded. In contrast, the G51D EEM (Figure 104) showed no dbAF for either monomeric or oligomeric states, however a dbAF signal was observed in the fibril state. The EEMs showed that all six familial mutations give rise to differing dbAF signatures, therefore the factors which govern the phenomenon must be affected by the differing fibrillation

pathways, however the fibril state which exhibits dbAF implies that the resultant fibrillar structure is key.

Overall the dbAF phenomenon is shown to exist for all the αS mutations, with a comparable trend to HI and WT αS; dbAF intensity increased from monomeric to fibrillar state. These results have indicated that the dbAF is affected by the fibrillation pathway, as shown by the three variations in oligomeric state for the six familial mutations, however further work is necessary to ascertain the clinical significance of dbAF as a potential diagnostic tool to probe pre-fibrillar state. The ability to probe single-point mutational differences of αS using IF and dbAF techniques, suggests it is possible to probe the effect of oxidation and nitration on WT αS. Current research has attributed toxicity of α-synucleinopathies to oxidative and nitrative damage,[90] due to the associated progression of αS oligomerisation and / or fibrillation.[91,92]

7.3.2.3. Investigating the effect of nitration on wild-type α-synuclein fibrillation

The nitration and oxidative stress of proteins are an important hallmark of neurodegenerative disease.[93,94] Protein nitration is whereby a nitro group (-NO_2) is chemically inserted into a protein, usually through nitrating agents such as peroxynitrite, which can both nitrate and oxidise the species.[95] Importantly for species containing tyrosine, this process can lead to residue modification forming nitrotyrosine, which is often associated with cellular damage.[96] The nitrated components are critical for amyloid research, since it is this process that often enhances protein aggregation[97,98] whilst also preferentially stabilising amyloid oligomers, which are suggested to be the physiologically toxic species.[99,100]

The αS was synthetically oxidised and nitrated by hydrogen peroxide and peroxynitrite respectively, to investigate whether the structural modifications resulting from nitration can be observed through fluorescence, specifically the effect upon dbAF. It is known that solvent accessible tyrosine is susceptible to both effects, resulting in the formation of; dityrosine,[101,102] tyrosinate,[103] or 3-nitrotyrosine.[104]

The IF for the effect of nitration on WT αS is shown in Figure 106, which exhibits a similar behaviour to the WT αS fibrillation pathway with decreasing fluorescence intensity from the control (black) to the oxidised (red) and

nitrated (blue) species. It should be noted that the control is not the same WT αS as previously shown, since all nitration experiments were studied in a nitration buffer and not PBS. There is a significant peak shift for the IF peak maxima (control, λ_{Em} ~305 nm) across the oxidised and nitrated species, in addition to the emergence of a large secondary peak (λ_{Em} ~455 nm) for the nitrated species, as shown in the normalised fluorescence spectra (Figure 106b).

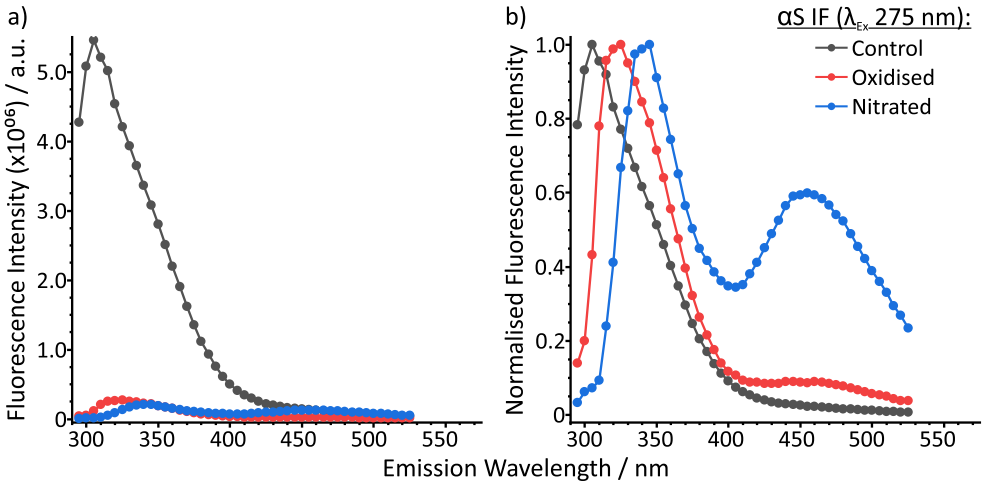

Figure 106: Fluorescence spectra of the (a) intrinsic fluorescence (IF) emission and (b) normalised IF for wild-type α-synuclein fibrillation showing; (black) control, (red) oxidised and (blue) nitrated states in a nitration buffer.

The dbAF for the effect of nitration on WT αS (Figure 107), shows an increasing fluorescence intensity from the control (black) to the nitrated (blue) state, whilst the oxidised species displays a reduced fluorescence. Similarly, to the WT αS fibrillation pathway, there is no apparent wavelength shift for the dbAF peak maxima as shown in the normalised fluorescence spectra (Figure 107b).

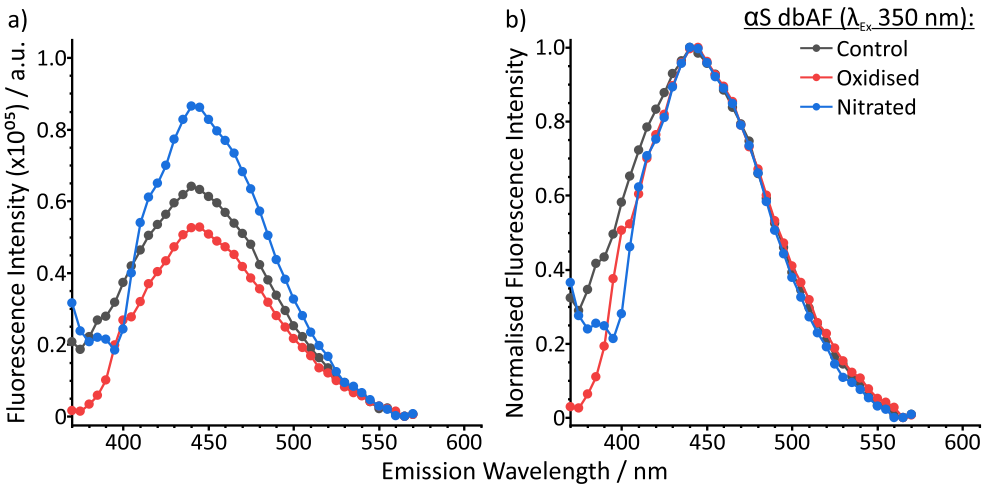

Figure 107: Fluorescence spectra of the (a) deep-blue autofluorescence (dbAF) emission and (b) normalised dbAF for WT α-synuclein fibrillation showing; (black) control, (red) oxidised and (blue) nitrated states in a nitration buffer.

Figure 108 shows the effect of nitration on the WT αS for the control (Figure 108a), oxidised (Figure 108b) and nitrated (Figure 108c) species. The IF peak region is present across all three EEMs, however as shown in Figure 106 the IF intensity has decreased. In contrast to the IF, the dbAF peak region has increased across the EEMs as shown by the observed colour change from blue to orange. There are four additional peak regions in the oxidised and nitrated EEMs, which were not observed in the control EEM.

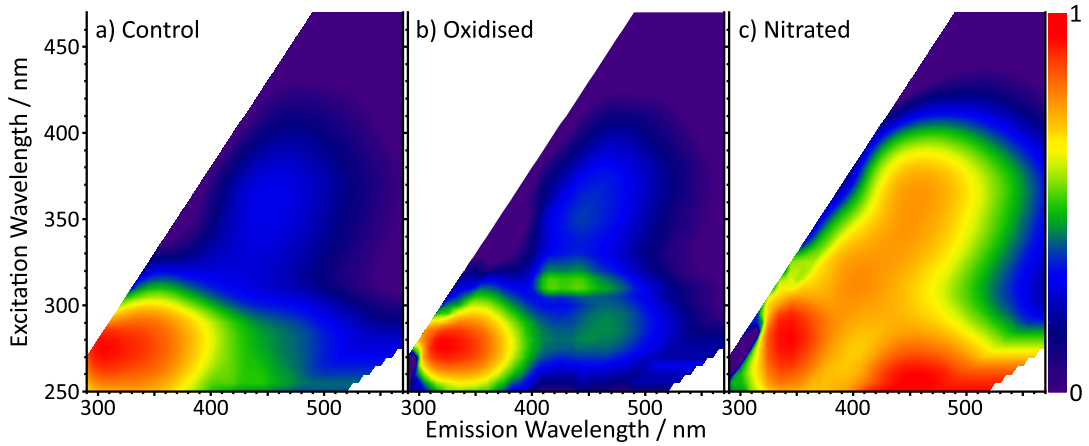

Figure 108: The effect of oxidation and nitration on wild-type (WT) α-synuclein EEMs, normalised to the intrinsic fluorescence (IF) signal maxima, showing the (a) control, (b) oxidised and (c) nitrated WT states in a nitration buffer. The exhibited fluorescence is shown as (red) highest to (blue) lowest.

The IF and dbAF phenomena are observed in both the WT αS oxidised and nitrated states with similar trends as previously observed to the aggregation states; IF intensity decreased in the nitrated and oxidised states (Figure 106) whilst dbAF intensity increased from the control to nitrated state (Figure 107). The 1D IF spectra (Figure 106) showed significant peak shifts for the control (λ_{Em} ~305 nm) to oxidised (λ_{Em} ~325 nm) to nitrated states (λ_{Em} ~345 nm), and the emergence of a second peak in the nitrated species only (λ_{Em} ~455 nm). This shift in peak maxima, which has not previously been observed, suggests a change in the environment which is potentially hydrogen bonding of the tyrosine residues, therefore this implies that the oxidised and nitrated fibrils here are different to the seven αS fibril states previously shown. The 1D dbAF spectra (Figure 107) showed an increased intensity for the nitrated state but a decreased intensity for the oxidised state, compared to the control, therefore the presence of a nitro group enhances the phenomenon, whilst oxidation reduces the propensity of the phenomenon. The resultant EEMs (Figure 108) show the emergence of the dityrosine and tyrosinate species, which is expected as both are characteristic biomarkers of oxidation and nitration processes. The effect of nitration on WT αS shows enhancement of the dbAF phenomenon and results in IF changes not previously observed. Rather than changing protein, five of the six familial mutations of αS were subjected to nitration,

with the aim to determine whether nitrated dbAF offers analogous results to the typical fibrillation EEMs.

7.3.2.4. The effect of nitration on the α-synuclein mutations

Figure 109 shows the effect of nitration on the αS mutations for A30P (Figure 109a), A53E (Figure 109b), E46K (Figure 109c), G51D (Figure 109d) and H50Q (Figure 109e). The αS mutants were nitrated with peroxynitrite, to investigate whether the mutated strands also give rise to the fluorescence features previously observed for nitrated WT αS (Figure 108).

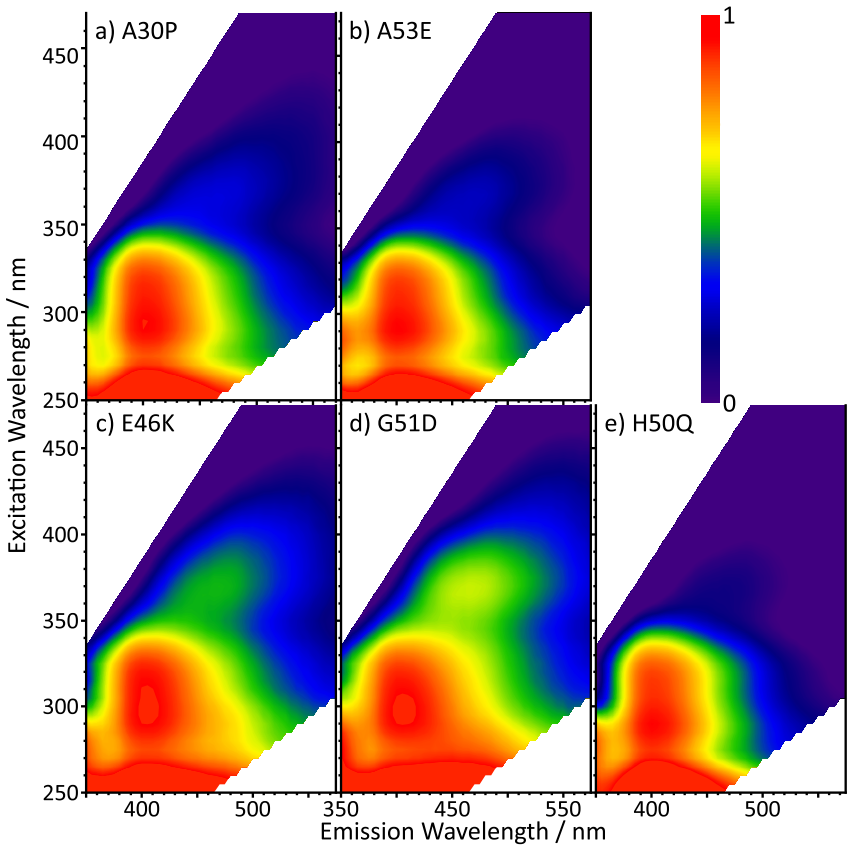

Figure 109: The effect of nitration on selected single-point mutation α-synuclein EEMs, normalised to the intrinsic fluorescence (IF) signal maxima, showing the (a) A30P, (b) A53E, (c) E46K, (d) G51D and (e) H50Q nitration states. The exhibited fluorescence is shown as (red) highest to (blue) lowest.

There are two distinct peak regions observed in all the nitrated αS mutants (Figure 109), which correspond to the dbAF and tyrosinate peak regions, with a strong fluorescence observed at the lower wavelengths attributed to the IF and fibril scattering effects. The nitrated EEMs show variable intensity for the dbAF,

from the lowest to highest; H50Q, A53E, A30P, E46K and the highest at G51D. This trend for the nitrated dbAF is the inverse of the aggregation state (Figure 99) with H50Q exhibiting the highest intensity followed by E46K, G51D, A30P and finally the lowest for A53E. The tyrosinate peak, although present in all the EEMs at a similar fluorescence intensity, appears to be elongated in the excitation wavelengths which was not previously observed in the associated aggregation EEMs but was visible in the WT αS nitrated EEM (Figure 108c).

Overall, the observation of dbAF in the HI, αS and nitrated variants implies that the phenomenon is attributed to the protein aggregation state, however the amyloidogenicity factor has not been ruled out. To investigate whether the dbAF is a characteristic of amyloidogenicity or protein structure, the amyloid-like fibrillation of homogeneous small molecules will be studied.

7.3.3. The fluorescence profile for the small molecules' fibrillation states

The six small molecules (adenine, L-alanine, L-cysteine, L-phenylalanine, L-tyrosine and uracil) were studied to ascertain whether dbAF is present in homogeneous small molecular assemblies. Figure 110 shows the fibrillar state EEMs for the small molecules after a sixteen-day incubation. The EEMs of aliquots taken during the incubation period for each molecule are provided in the supplementary (Figure S22 – Figure S27).

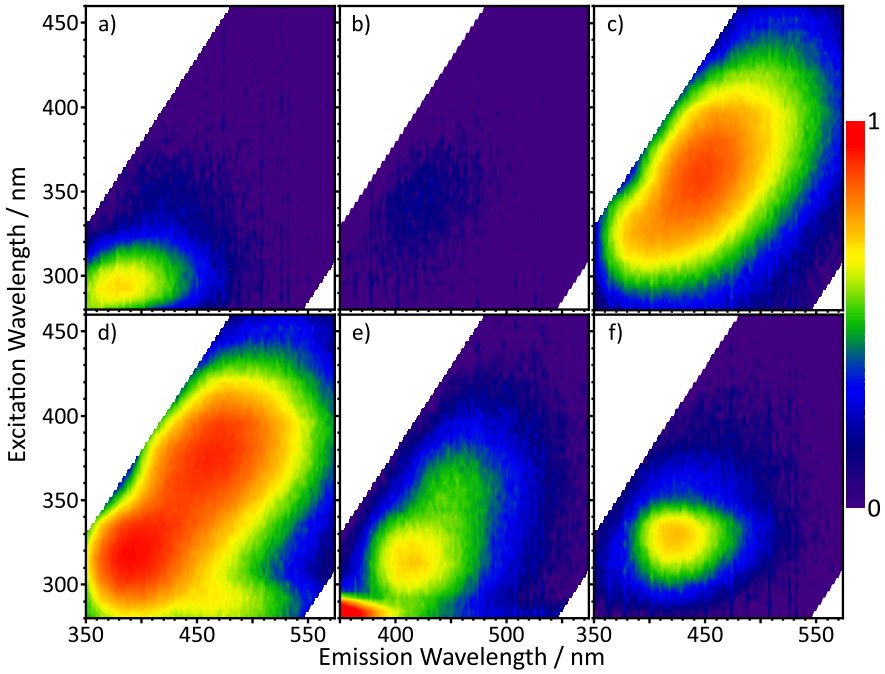

Figure 110: The deep-blue autofluorescence (dbAF) phenomenon exhibited in the EEMs for the six small molecules; (a) adenine, (b) L-alanine, (c) L-cysteine, (d) L-phenylalanine, (e) L-tyrosine and (f) uracil; in their aggregated state. The fluorescence is normalised to the maximum intensity, L-phenylalanine, which is shown as (red) highest to (blue) lowest.

Figure 110 shows the appearance of multiple fluorescence peaks, which were not previously observed for the proteins studied, however the dbAF is present in the EEMs for the aggregated; L-cysteine, L-phenylalanine, L-tyrosine and potentially in uracil due to the weak fluorescence intensity within the dbAF region.

Three of the amino acids studied exhibit the dbAF signature, which is of the highest intensity for L-phenylalanine but not observed for L-alanine, both of which are classed as hydrophobic but L-phenylalanine is aromatic due to the addition of a phenyl ring. The presence of the aromaticity in L-phenylalanine suggests that aromatic interactions in the fibrillar structure give rise to the dbAF phenomenon, which is supported by its presence in fibrillar L-tyrosine, another aromatic amino acid.

This phenomenon however is also observed in fibrillar L-cysteine, which is a non-aromatic amino acid, implying additional factors contribute to the dbAF phenomenon. Proteins with cysteine residues often include disulfide bridges as a result of disulfide bonding between two cysteine residues. The oxidation of cysteine

to cystine results in a disulfide bond,[105] between the two cysteine residues therefore providing an analogous fibrillar infrastructure to that of aromatic interactions giving rise to the dbAF phenomenon observed in Figure 110c. In regards to uracil, although there is a potential weak fluorescence intensity above the background, it is diffuse across the dbAF region and does not change as fibrillation proceeds as shown in Figure S27, therefore it is likely to be a fluorescence artefact as opposed to the dbAF phenomenon.

The small molecules study therefore, whilst disproving that the dbAF phenomenon is a characteristic of amyloidogenic proteins, does not definitively determine its origin. The lack of dbAF in three of the small molecules also implies that aggregation is not a key factor in the presence of the phenomenon, however further studies are necessary to investigate why.

7.4. Conclusions

This investigation has shown that the dbAF phenomenon is present in HI, and the use of EEMs to investigate the fluorescence profile were invaluable in this study, as they showed the relationship between IF and dbAF intensity changes as aggregation proceeded. A significant trend for HI showed that dbAF increased as fibrillation proceeds, as shown in the monomeric and fibrillar state spectra, which implies that aggregation contributes to the origin of dbAF. The presence of dbAF in the monomeric HI state, albeit at a reduced intensity, implied that a potential origin for the phenomenon was the secondary structure, therefore an IDP (αS) was studied to remove this variable.

The dbAF phenomenon was observed in αS with the same trend as shown for HI, where dbAF intensity increases as fibrillation proceeds, therefore confirming that the secondary structure of proteins was not a factor. To determine whether amyloidogenic aggregation was a factor, six small molecules which undergo amyloid-like fibrillation were studied. Three of the six molecules aggregated states exhibited the dbAF, which showed that the phenomenon was not an amyloidogenic property or the result of aggregation state. Two of the dbAF-positive molecules were aromatic amino acid residues, L-phenylalanine and L-tyrosine, where L-phenylalanine

exhibited the highest dbAF intensity of the three, which would suggest aromaticity is a factor in the phenomenon's origin. The other dbAF-positive molecule however was not aromatic, L-cysteine, and exhibited higher intensity than L-tyrosine which does not follow the aromaticity theory.

Whilst this investigation was unable to definitively determine the root cause of the dbAF phenomenon, this work has shown that an ensemble of factors likely gives rise to the phenomenon. The variation in dbAF for the single-point αS mutations, which maintains the same core fibrillar structure, implies that the phenomenon must be attributed to the side group infrastructure as opposed to the core framework. The nitration results, which showed the inverse trend for dbAF compared to the αS aggregation state, further complicates the interpretation of this phenomenon as it is implied that the origin of the dbAF is not directly associated to the fibrillar state. In summary the work in this investigation proposes that the dbAF arises as aggregation proceeds, which results in orientated stacking of side groups within the fibrillar structure, consequently generating a fluorescence effect attributed to the infrastructure interactions such as; aromatic, carbonyl and hydrogen.

The sensitivity of the dbAF phenomenon, in distinguishing differences between the various single-point mutations of αS, amplifies the potential applications for dbAF as a technique to detect pre-fibrillar state. Overall, there is further work necessary prior to widespread usage as an analytical fluorescence technique with investigations such as; pinpointing the phenomenon's origin, or studying whether there is a concentration dependence effect, or to probing mutations in HI.

7.5. Supplementary

WT α-synuclein

10	20	30	40	50
MDVFMKGLSK	AKEGVVAAAE	KTKQGVAEAA	GKTKEGVLYV	GSKTKEGVVH
60	**70**	**80**	**90**	**100**
GVATVAEKTK	EQVTNVGGAV	VTGVTAVAQK	TVEGAGSIAA	ATGFVKKDQL
110	**120**	**130**	**140**	
GKNEEGAPQE	GILEDMPVDP	DNEAYEMPSE	EGYQDYEPEA	
100	**100**	**100**	**100**	**100**

Figure S21: The primary sequence for wild-type α-synuclein, showing the regions; (purple) amphipathic, (orange) non-amyloid-ß component and (green) acidic tail regionsm and (cyan highlighted) the specific single-point mutation sites.

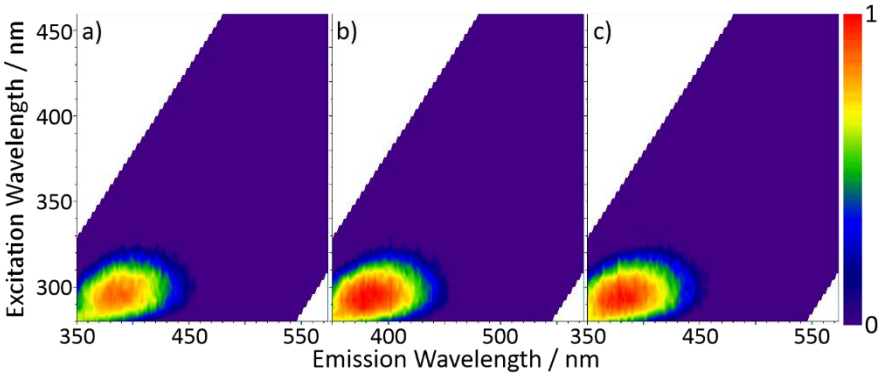

Figure S22: Adenine EEMs, showing the effect of increasing aggregation states over incubation times; (a) day 0, (b) day 4 and (c) day 16. The exhibited fluorescence, shown as (red) highest to (blue) lowest, is normalised to the maximum at day 16.

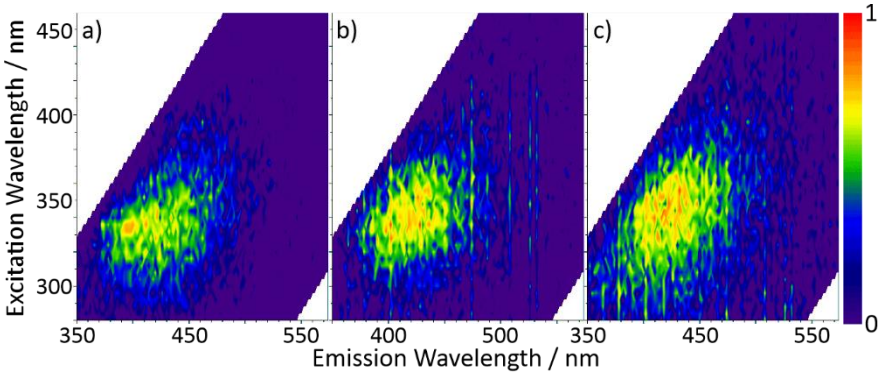

Figure S23: L-alanine EEMs, showing the effect of increasing aggregation states over incubation times; (a) day 0, (b) day 4 and (c) day 16. The exhibited fluorescence, shown as (red) highest to (blue) lowest, is normalised to the maximum at day 16.

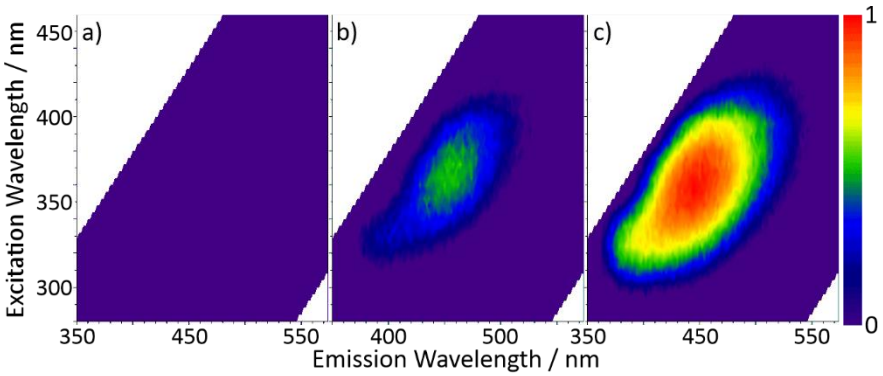

Figure S24: L-cysteine EEMs, showing the effect of increasing aggregation states over incubation times; (a) day 0, (b) day 4 and (c) day 16. The exhibited fluorescence, shown as (red) highest to (blue) lowest, is normalised to the maximum at day 16.

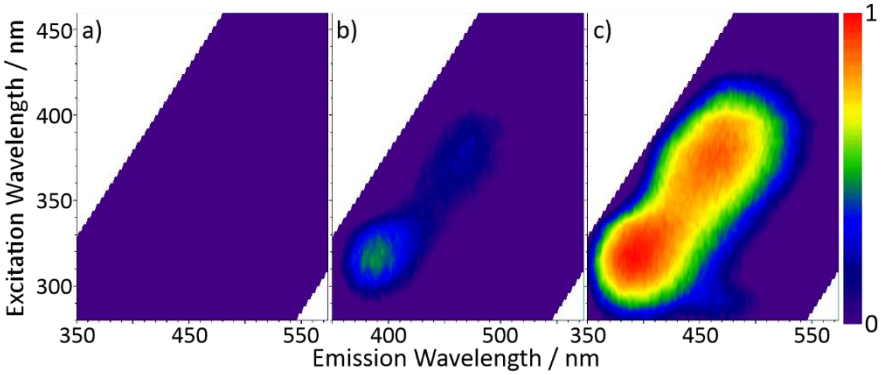

Figure S25: L-phenylalanine EEMs, showing the effect of increasing aggregation states over incubation times; (a) day 0, (b) day 4 and (c) day 16. The exhibited fluorescence, shown as (red) highest to (blue) lowest, is normalised to the maximum at day 16.

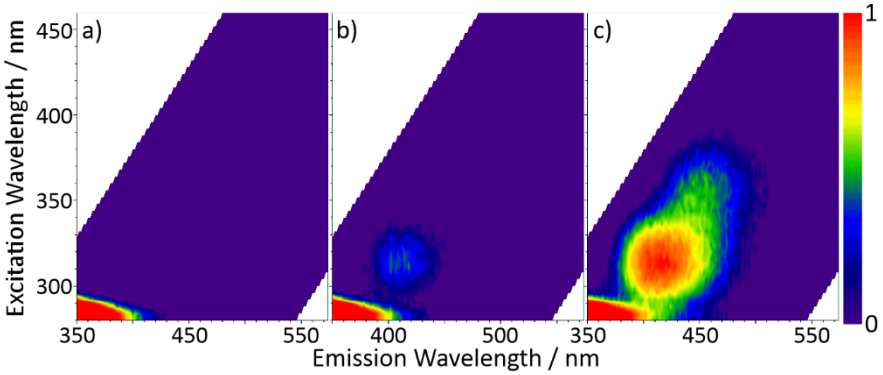

Figure S26: L-tyrosine EEMs, showing the effect of increasing aggregation states over incubation times; (a) day 0, (b) day 4 and (c) day 16. The exhibited fluorescence, shown as (red) highest to (blue) lowest, is normalised to the maximum at day 16.

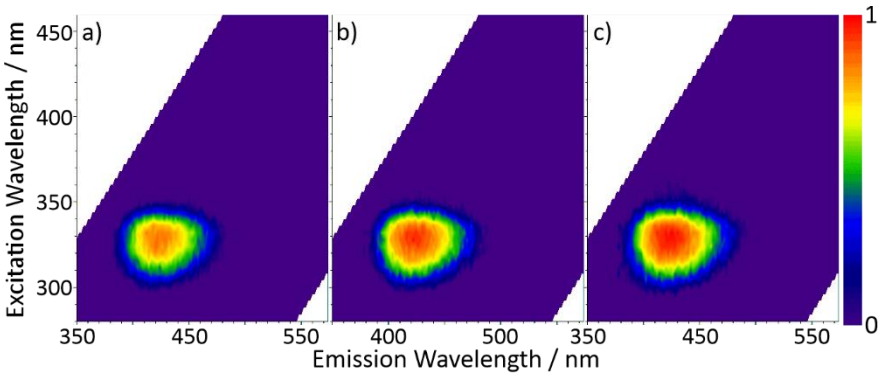

Figure S27: Uracil EEMs, showing the effect of increasing aggregation states over incubation times; (a) day 0, (b) day 4 and (c) day 16. The exhibited fluorescence, shown as (red) highest to (blue) lowest, is normalised to the maximum at day 16.

Bibliography

1. Chan, F. T. S. *et al.* Protein amyloids develop an intrinsic fluorescence signature during aggregation. *Analyst* **138**, 2156 (2013).

2. Tcherkasskaya, O. Photo-activity induced by amyloidogenesis. *Protein Sci.* **16**, 561–571 (2007).

3. del Mercato, L. L. *et al.* Charge transport and intrinsic fluorescence in amyloid-like fibrils. *Proc. Natl. Acad. Sci.* **104**, 18019–18024 (2007).

4. Pinotsi, D., Buell, A. K., Dobson, C. M., Kaminski Schierle, G. S. & Kaminski, C. F. A Label-Free, Quantitative Assay of Amyloid Fibril Growth Based on Intrinsic Fluorescence. *ChemBioChem* **14**, 846–850 (2013).

5. Johansson, P. K. & Koelsch, P. Label-free imaging of amyloids using their intrinsic linear and nonlinear optical properties. *Biomed. Opt. Express* **8**, 743 (2017).

6. Niyangoda, C., Miti, T., Breydo, L., Uversky, V. & Muschol, M. Carbonyl-based blue autofluorescence of proteins and amino acids. *PLoS One* **12**, e0176983 (2017).

7. Grisanti, L., Pinotsi, D., Gebauer, R., Kaminski Schierle, G. S. & Hassanali, A. A. A computational study on how structure influences the optical properties in model crystal structures of amyloid fibrils. *Phys. Chem. Chem. Phys.* **19**, 4030–4040 (2017).

8. Brange, J. & Langkjœr, L. Insulin Structure and Stability. in *Stability and Characterization of Protein and Peptide Drugs* 315–350 (1993). doi:10.1007/978-1-4899-1236-7_11

9. Frokjaer, S. & Otzen, D. E. Protein drug stability: a formulation challenge. *Nat. Rev. Drug Discov.* **4**, 298–306 (2005).

10. Majors, R. E. The role of the column in preparative HPLC. *LC-GC North Am.* **22**, 416–428 (2004).

11. Gusarov, D., Lasman, V. & Bayramashvili, D. Methods for protecting silica sorbents used in high-performance liquid chromatography from strongly adsorbed impurities during purification of human recombinant insulin. *J. Chromatogr. B* **853**, 354–359 (2007).

12. Hammarström, P. *et al.* An Auto-Catalytic Surface for Conformational Replication of Amyloid Fibrils—Genesis of an Amyloid World? *Orig. Life Evol. Biosph.* **41**, 373–383 (2011).

13. Braslavsky, S. E. Glossary of terms used in photochemistry, 3rd edition (IUPAC Recommendations 2006). *Pure Appl. Chem.* **79**, 293–465 (2007).

14. Lakowicz, J. R. *Principles of Fluorescence Spectroscopy*. *Principles of Fluorescence Spectroscopy* (Springer US, 2006). doi:10.1007/978-0-387-46312-4

15. Valeur, B. & Berberan-Santos, M. N. *Molecular Fluorescence*. *Wiley-VCH Verlag & Co. KGaA, Boschstr. 12, 69469 Weinheim, Germany* (Wiley-VCH Verlag GmbH & Co. KGaA, 2012). doi:10.1002/9783527650002

16. Chattopadhyay, A., Rukmini, R. & Mukherjee, S. Photophysics of a neurotransmitter: ionization and spectroscopic properties of serotonin. *Biophys. J.* **71**, 1952–1960 (1996).

17. de Oliveira Silva, F. R. *et al.* Intrinsic Fluorescence of Protoporphyrin IX from Blood Samples Can Yield Information on the Growth of Prostate Tumours. *J. Fluoresc.* **20**, 1159–1165 (2010).

18. Svendsen, A., Kiefer, H. V., Pedersen, H. B., Bochenkova, A. V. & Andersen, L. H. Origin of the Intrinsic Fluorescence of the Green Fluorescent Protein. *J. Am. Chem. Soc.* **139**, 8766–8771 (2017).

19. Marcus, A., Sadimin, E., Richardson, M., Goodell, L. & Fyfe, B. Fluorescence Microscopy Is Superior to Polarized Microscopy for Detecting Amyloid Deposits in Congo Red–Stained Trephine Bone Marrow Biopsy Specimens. *Am. J. Clin. Pathol.* **138**, 590–593 (2012).

20. Gade Malmos, K. *et al.* ThT 101: a primer on the use of thioflavin T to investigate amyloid formation. *Amyloid* **24**, 1–16 (2017).

21. Mauro, M. *et al.* Kinetics of Different Processes in Human Insulin Amyloid Formation. *J. Mol. Biol.* **366**, 258–274 (2007).

22. Foderà, V. *et al.* Thioflavin T hydroxylation at basic pH and its effect on amyloid fibril detection. *J. Phys. Chem. B* **112**, 15174–15181 (2008).

23. Vivian, J. T. & Callis, P. R. Mechanisms of Tryptophan Fluorescence Shifts in Proteins. *Biophys. J.* **80**, 2093–2109 (2001).

24. Bekard, I. B. & Dunstan, D. E. Tyrosine Autofluorescence as a Measure of Bovine Insulin Fibrillation. *Biophys. J.* **97**, 2521–2531 (2009).

25. Liu, T. *et al.* Ionization Potentials of Fluoroindoles and the Origin of Nonexponential Tryptophan Fluorescence Decay in Proteins ⊥. *J. Am. Chem. Soc.* **127**, 4104–4113 (2005).

26. Gill, H. S. Evaluating the efficacy of tryptophan fluorescence and absorbance as a selection tool for identifying protein crystals. *Acta Crystallogr. Sect. F Struct. Biol. Cryst. Commun.* **66**, 364–372 (2010).

27. Zhdanova, N. G., Maksimov, E. G., Arutyunyan, A. M., Fadeev, V. V. & Shirshin, E. A. Tyrosine fluorescence probing of conformational changes in tryptophan-lacking domain of albumins. *Spectrochim. Acta Part A Mol. Biomol. Spectrosc.* **174**, 223–229 (2017).

28. Giancotti, V., Quadrifoglio, F., Lancieri, M. & Geraci, G. Separation and properties of an H2B histone variant from the sperm chromatin of the sea urchin Sphaerechinus granularis. *Int. J. Biol. Macromol.* **2**, 309–312 (1980).

29. White, A. Effect of pH on fluorescence of tyrosine, tryptophan and related compounds. *Biochem. J.* **71**, 217–220 (1959).

30. Ghisaidoobe, A. & Chung, S. Intrinsic Tryptophan Fluorescence in the Detection and Analysis of Proteins: A Focus on Förster Resonance Energy Transfer Techniques. *Int. J. Mol. Sci.* **15**, 22518–22538 (2014).

31. Würth, C., Grabolle, M., Pauli, J., Spieles, M. & Resch-Genger, U. Relative and absolute determination of fluorescence quantum yields of transparent samples. *Nat. Protoc.* **8**, 1535–1550 (2013).

32. Itagaki, H. *Fluorescence Spectroscopy*. *Experimental Methods in Polymer Science* (Elsevier, 2000).

33. Shukla, A. *et al.* A novel UV laser-induced visible blue radiation from protein crystals and aggregates: scattering artifacts or fluorescence transitions of peptide electrons delocalized through hydrogen bonding? *Arch. Biochem. Biophys.* **428**, 144–153 (2004).

34. Chan, F. T. S. *et al.* Protein amyloids develop an intrinsic fluorescence signature during aggregation. *Analyst* **138**, 2156 (2013).

35. Chan, F. T. S., Pinotsi, D., Gabriele, S., Schierle, K. & Kaminski, C. F. Structure-Specific Intrinsic Fluorescence of Protein Amyloids Used to Study their Kinetics of Aggregation. in *Bio-nanoimaging* 147–155 (Elsevier, 2014). doi:10.1016/B978-0-12-394431-3.00013-4

36. Chan, F. T. S., Pinotsi, D., Gabriele, S., Schierle, K. & Kaminski, C. F. Structure-Specific Intrinsic Fluorescence of Protein Amyloids Used to Study their Kinetics of Aggregation. in *Bio-nanoimaging* 147–155 (Elsevier, 2014). doi:10.1016/B978-0-12-394431-3.00013-4

37. Ziaunys, M., Sneideris, T. & Smirnovas, V. Exploring the potential of deep-blue autofluorescence for monitoring amyloid fibril formation and dissociation. *PeerJ* **7**, e7554 (2019).

38. Prasad, S. *et al.* Near UV-Visible electronic absorption originating from charged amino acids in a monomeric protein. *Chem. Sci.* **8**, 5416–5433 (2017).

39. Tikhonova, T. N. *et al.* Dissection of the deep-blue autofluorescence changes accompanying amyloid fibrillation. *Arch. Biochem. Biophys.* **651**, 13–20 (2018).

40. Tomalia, D. A. *et al.* Non-traditional intrinsic luminescence: inexplicable blue fluorescence observed for dendrimers, macromolecules and small molecular structures lacking traditional/conventional luminophores. *Prog. Polym. Sci.* **90**, 35–117 (2019).

41. Prasad, S. *et al.* Near UV-Visible electronic absorption originating from charged amino acids in a monomeric protein. *Chem. Sci.* **8**, 5416–5433 (2017).

42. Alderson, T. R. & Markley, J. L. Biophysical characterization of α-synuclein and its controversial structure. *Intrinsically Disord. Proteins* **1**, e26255 (2013).

43. Stefanis, L. A-Synuclein in Parkinson's Disease. *Cold Spring Harb. Perspect. Med.* **2**, a009399–a009399 (2012).

44. Spillantini, M. G. *et al.* α-Synuclein in Lewy bodies. *Nature* **388**, 839–840 (1997).

45. Uversky, V. N. Intrinsically disordered proteins from A to Z. *Int. J. Biochem. Cell Biol.* **43**, 1090–1103 (2011).

46. Charlier, C. *et al.* Structure and Dynamics of an Intrinsically Disordered Protein Region That Partially Folds upon Binding by Chemical-Exchange NMR. *J. Am. Chem. Soc.* **139**, 12219–12227 (2017).

47. Humphrey, W., Dalke, A. & Schulten, K. VMD: Visual molecular dynamics. *J. Mol. Graph.* **14**, 33–38 (1996).

48. Ulmer, T. S., Bax, A., Cole, N. B. & Nussbaum, R. L. Structure and Dynamics of Micelle-bound Human -Synuclein. *J. Biol. Chem.* **280**, 9595–9603 (2005).

49. Bisaglia, M. *et al.* Structure and topology of the non-amyloid-β component fragment of human α-synuclein bound to micelles: Implications for the aggregation process. *Protein Sci.* **15**, 1408–1416 (2006).

50. Fusco, G. *et al.* Structural basis of synaptic vesicle assembly promoted by α-synuclein. *Nat. Commun.* **7**, 12563 (2016).

51. Braun, A. R., Lacy, M. M., Ducas, V. C., Rhoades, E. & Sachs, J. N. α-Synuclein's Uniquely Long Amphipathic Helix

Enhances its Membrane Binding and Remodeling Capacity. *J. Membr. Biol.* **250**, 183–193 (2017).

52. Pawar, A. P. *et al.* Prediction of "Aggregation-prone" and "Aggregation-susceptible" Regions in Proteins Associated with Neurodegenerative Diseases. *J. Mol. Biol.* **350**, 379–392 (2005).

53. Chiti, F. & Dobson, C. M. Protein Misfolding, Amyloid Formation, and Human Disease: A Summary of Progress Over the Last Decade. *Annu. Rev. Biochem.* **86**, 27–68 (2017).

54. Proukakis, C. *et al.* A novel -synuclein missense mutation in Parkinson disease. *Neurology* **80**, 1062–1064 (2013).

55. Krüger, R. *et al.* AlaSOPro mutation in the gene encoding α-synuclein in Parkinson's disease. *Nat. Genet.* **18**, 106–108 (1998).

56. Zarranz, J. J. *et al.* The New Mutation, E46K, of α-Synuclein Causes Parkinson and Lewy Body Dementia. *Ann. Neurol.* **55**, 164–173 (2004).

57. Nishioka, K. *et al.* Clinical heterogeneity of α-synuclein gene duplication in Parkinson's disease. *Ann. Neurol.* **59**, 298–309 (2006).

58. Lesage, S. *et al.* G51D α-synuclein mutation causes a novel Parkinsonian-pyramidal syndrome. *Ann. Neurol.* **73**, 459–471 (2013).

59. Pasanen, P. *et al.* A novel α-synuclein mutation A53E associated with atypical multiple system atrophy and Parkinson's disease-type pathology. *Neurobiol. Aging* **35**, 2180.e1-2180.e5 (2014).

60. Ghosh, D., Mehra, S., Sahay, S., Singh, P. K. & Maji, S. K. A-Synuclein Aggregation and Its Modulation. *Int. J. Biol. Macromol.* **100**, 37–54 (2017).

61. Meade, R. M., Fairlie, D. P. & Mason, J. M. Alpha-synuclein structure and Parkinson's disease – lessons and emerging principles. *Mol. Neurodegener.* **14**, 29 (2019).

62. Guerrero-Ferreira, R. *et al.* Cryo-EM structure of alpha-synuclein fibrils. *Elife* **7**, (2018).

63. Iadanza, M. G., Jackson, M. P., Hewitt, E. W., Ranson, N. A. & Radford, S. E. A new era for understanding amyloid structures and disease. *Nat. Rev. Mol. Cell Biol.* **19**, 755–773 (2018).

64. Lodish, H. F. *et al. Molecular cell biology.* (Macmillan Science & Educ. USA, 2016).

65. Shaham-Niv, S., Adler-Abramovich, L., Schnaider, L. & Gazit, E. Extension of the generic amyloid hypothesis to nonproteinaceous metabolite assemblies. *Sci. Adv.* **1**, e1500137 (2015).

66. Gazit, E. Metabolite amyloids: a new paradigm for inborn error of metabolism disorders. *J. Inherit. Metab. Dis.* **39**, 483–488 (2016).

67. Gour, N. *et al.* Amyloid-like Structures Formed by Single Amino Acid Self-Assemblies of Cysteine and Methionine. *ACS Chem. Neurosci.* **10**, 1230–1239 (2019).

68. Bollée, G. *et al.* Adenine Phosphoribosyltransferase Deficiency. *Clin. J. Am. Soc. Nephrol.* **7**, 1521–1527 (2012).

69. Rosenberg, L. E., Downing, S., Durant, J. L. & Segal, S. Cystinuria: biochemical evidence for three genetically distinct diseases. *J. Clin. Invest.* **45**, 365–371 (1966).

70. Blau, N., van Spronsen, F. J. & Levy, H. L. Phenylketonuria. *Lancet* **376**, 1417–1427 (2010).

71. Russo, P. A., Mitchell, G. A. & Tanguay, R. M. Tyrosinemia: A Review. *Pediatr. Dev. Pathol.* **4**, 212–221 (2001).

72. Levin, B., Abraham, J. M., Oberholzer, V. G. & Burgess, E. A. Hyperammonaemia: a deficiency of liver ornithine transcarbamylase. Occurrence in mother and child. *Arch. Dis. Child.* **44**, 152–161 (1969).

73. Torpey, J. H. The aggregation of α-synuclein and its inhibtion (PhD thesis). (2019). doi:10.17638/03059871

74. Schoonenboom, N. S. M. *et al.* Effects of Processing and Storage Conditions on Amyloid β (1–42) and Tau Concentrations in Cerebrospinal Fluid: Implications for Use in Clinical Practice. *Clin. Chem.* **51**, 189–195 (2005).

75. Sigurdsson, E. M., Calero, M. & Gasset, M. *Amyloid proteins. methods and protocols.* (Humana Press, 2012).

76. Domigan, L. J., Healy, J. P., Meade, S. J., Blaikie, R. J. & Gerrard, J. A. Controlling the dimensions of amyloid fibrils: Toward homogenous components for bionanotechnology. *Biopolymers* **97**, 123–133 (2012).

77. Castillo-León, J. & Svendsen, W. E. *Micro and Nanofabrication Using Self-Assembled Biological Nanostructures.* (William Andrew Publishing, 2015).

78. Liu, H.-C., Chiu, M.-J., Lin, C.-H. & Yang, S.-Y. Stability of Plasma Amyloid-β 1–40, Amyloid-β 1–42, and Total Tau Protein over Repeated Freeze/Thaw Cycles. *Dement. Geriatr. Cogn. Dis. Extra* **10**, 46–55 (2020).

79. Beckman, J. S., Chen, J., Ischiropoulos, H. & Crow, J. P. [23] Oxidative chemistry of peroxynitrite. in *Methods in*

Enzymology 229–240 (1994). doi:10.1016/S0076-6879(94)33026-3

80. Hughes, M. N. & Nicklin, H. G. The chemistry of peroxonitrites. Part II. Copper(II)-catalysed reaction between hydroxylamine and peroxonitrite in alkali. *J. Chem. Soc. A Inorganic, Phys. Theor.* 925 (1970). doi:10.1039/j19700000925

81. Nielsen, L., Frokjaer, S., Brange, J., Uversky, V. N. & Fink, A. L. Probing the mechanism of insulin fibril formation with insulin mutants. *Biochemistry* **40**, 8397–8409 (2001).

82. Uversky, V. N. *et al.* Prediction of the association state of insulin using spectral parameters. *J. Pharm. Sci.* **92**, 847–858 (2003).

83. Koller, E., Quehenberger, O., Jürgens, G., Wolfbeis, O. S. & Esterbauer, H. Investigation of human plasma low density lipoprotein by three-dimensional flourescence spectroscopy. *FEBS Lett.* **198**, 229–234 (1986).

84. Ziaunys, M., Mikalauskaite, K. & Smirnovas, V. Amyloidophilic Molecule Interactions on the Surface of Insulin Fibrils: Cooperative Binding and Fluorescence Quenching. *Sci. Rep.* **9**, 20303 (2019).

85. Lawaetz, A. J. & Stedmon, C. A. Fluorescence Intensity Calibration Using the Raman Scatter Peak of Water. *Appl. Spectrosc.* **63**, 936–940 (2009).

86. Reynolds, M. R., Berry, R. W. & Binder, L. I. Site-Specific Nitration and Oxidative Dityrosine Bridging of the τ Protein by Peroxynitrite: Implications for Alzheimer's Disease †. *Biochemistry* **44**, 1690–1700 (2005).

87. De Filippis, V., Frasson, R. & Fontana, A. 3-Nitrotyrosine as a spectroscopic probe for investigating protein-protein interactions. *Protein Sci.* **15**, 976–986 (2006).

88. Bandookwala, M. & Sengupta, P. 3-Nitrotyrosine: a versatile oxidative stress biomarker for major neurodegenerative diseases. *Int. J. Neurosci.* **130**, 1047–1062 (2020).

89. Pinotsi, D. *et al.* Proton Transfer and Structure-Specific Fluorescence in Hydrogen Bond-Rich Protein Structures. *J. Am. Chem. Soc.* **138**, 3046–3057 (2016).

90. Giasson, B. I. Oxidative Damage Linked to Neurodegeneration by Selective alpha -Synuclein Nitration in Synucleinopathy Lesions. *Science* **290**, 985–989 (2000).

91. Chavarría, C. & Souza, J. M. Oxidation and nitration of α-synuclein and their implications in neurodegenerative diseases. *Arch. Biochem. Biophys.* **533**, 25–32 (2013).

92. Burai, R., Ait-Bouziad, N., Chiki, A. & Lashuel, H. A. Elucidating the Role of Site-Specific Nitration of α-Synuclein in the Pathogenesis of Parkinson's Disease via Protein Semisynthesis and Mutagenesis. *J. Am. Chem. Soc.* **137**, 5041–5052 (2015).

93. Ischiropoulos, H. Biological selectivity and functional aspects of protein tyrosine nitration. *Biochem. Biophys. Res. Commun.* **305**, 776–783 (2003).

94. Cheignon, C. *et al.* Oxidative stress and the amyloid beta peptide in Alzheimer's disease. *Redox Biol.* **14**, 450–464 (2018).

95. Koppenol, W. H. 100 Years of peroxynitrite chemistry and 11 years of peroxynitrite biochemistry. *Redox Rep.* **6**, 339–341 (2001).

96. Murata, M. & Kawanishi, S. Oxidative DNA damage induced by nitrotyrosine, a biomarker of inflammation. *Biochem. Biophys. Res. Commun.* **316**, 123–128 (2004).

97. Uversky, V. N. *et al.* Effects of nitration on the structure and aggregation of α-synuclein. *Mol. Brain Res.* **134**, 84–102 (2005).

98. Abdelmegeed, M. A. & Song, B.-J. Functional Roles of Protein Nitration in Acute and Chronic Liver Diseases. *Oxid. Med. Cell. Longev.* **2014**, 1–21 (2014).

99. Stefani, M. & Dobson, C. M. Protein aggregation and aggregate toxicity: new insights into protein folding, misfolding diseases and biological evolution. *J. Mol. Med.* **81**, 678–699 (2003).

100. Glabe, C. G. Structural classification of toxic amyloid oligomers. *Journal of Biological Chemistry* (2008). doi:10.1074/jbc.R800016200

101. Aeschbach, R., Amadoò, R. & Neukom, H. Formation of dityrosine cross-links in proteins by oxidation of tyrosine residues. *Biochim. Biophys. Acta - Protein Struct.* **439**, 292–301 (1976).

102. Radi, R. Nitric oxide, oxidants, and protein tyrosine nitration. *Proc. Natl. Acad. Sci.* **101**, 4003–4008 (2004).

103. Antosiewicz, J. M. & Shugar, D. UV–Vis spectroscopy of tyrosine side-groups in studies of protein structure. Part 2: selected applications. *Biophys. Rev.* **8**, 163–177 (2016).

104. Souza, J. M., Castro, L., Cassina, A. M., Batthyány, C. & Radi, R. Nitrocytochrome c: Synthesis, Purification, and Functional Studies. in *Nitric Oxide, Part G Oxidative and Nitrosative Stress in Redox Regulation of Cell Signaling* (eds. Cadenas, E. & Packer, L. B. T.-M. in E.) **441**, 197–215 (Academic Press, 2008).

105. Di Felice, R. & Selloni, A. Adsorption modes of cysteine on Au(111): Thiolate, amino-thiolate, disulfide. *J. Chem. Phys.* **120**, 4906–4914 (2004).

Chapter 8: Conclusions and Future Work

This research programme has pioneered several new techniques and methodologies in its pursuit of studying human insulin (HI) amyloid-like fibrillation at a hydrophobic interface. The work has come full circle from initially working on surface-specific techniques using reflection anisotropy spectroscopy (RAS) on hydrophobically functionalised silicon (Si) surfaces, through to observing anisotropy in adsorbed HI on hydrophobically functionalised gold surfaces.

In Chapter 2 with the aim to study how HI fibrillation is induced by surface architecture was affected by sample reproducibility challenges raised, which were investigated in Chapter 3 and determined to be associated with HI treatment issues. Having solved the protein handling concerns in Chapter 3, Chapter 4 investigated how mobile hydrophobic interfaces affected the HI amyloid-like fibrillation, using conventional bulk spectroscopic techniques. Chapter 5 investigated the changes in mass and structure of adsorbed HI to hydrophobic interfaces. Chapter 6 used the novel infrared scanning near-field optical microscopy technique to determine the relative amounts of secondary structure in the adsorbed HI layer. Chapter 7 studied the deep-blue autofluorescence phenomenon to ascertain its origin, thus applicability to protein and peptide fibrillation studies.

Chapter 2

Chapter 2 used reflection anisotropy spectroscopy to determine the fibrillar orientation of human insulin (HI), which was abandoned because of irreproducible samples. The issue of reproducible samples was solved in Chapter 3, by developing a standard HI handling protocol. Implementation of the standard HI protocol with this pioneering technique, would be able to follow the HI fibrillation *in situ*, therefore allowing for the fibrillation kinetics to be measured as the Si sample will then be aligned to the principle axes to follow the changes thereof.

Chapter 4

Chapter 4 used mobile hydrophobically functionalised mesoporous silica microparticles to study the HI fibrillation. The results showed that HI incubation with

particles at pH 2 inhibited whilst at pH 7 enhancement of the typical sigmoidal curve occurred and these results were correlated to the transmission electron microscopy (TEM) images of the fibrils. This study could be improved by using different analytical techniques, which are not as sensitive to environmental variables, to determine the adsorbed HI content on the microparticles. Improvements could also be made regarding the microparticles, such as; a different supplier to directly compare with these results, monodisperse microparticles to investigate whether polydispersity is a factor, and microparticle functionalisation to study other hydrophobic interfaces whether they provide any effect on HI-fibrillation. Other possibilities also include; change of particle size to investigate the effects of sedimentation and surface area, and the use of non-alkyl groups to study other stabilisation effects such as aromaticity.

Chapter 5

Chapter 5 showed that the increasing alkyl chain on the hydrophobic interface resulted in an increased HI adsorbed layer, which implies that hydrophobicity is affected by alkyl length. Further work should consider the use of other functionalisation groups, specifically whether there is a relationship between the layer thickness and alkyl chain length, or the use of non-alkyl groups to study the stabilisation between the HI and the functionalised interface. The potential application for increased stability may lead to advancements in coatings to reduce amyloid-like fibrillation within drug delivery systems.

A probe-based Raman system was used for this work, however the use of a confocal microscope may provide depth information, particularly whether adsorbed layers result in structural rearrangement inducing auto-catalytic fibrillation. The use of a microscope would also provide mapping capability in the *x*-*y* plane, over a large area, which provides insight into whether adsorption is consistent. Furthermore, the use of a different Raman excitation wavelength would be beneficial as this will allow for a reduction in the fluorescence background therefore reducing reliance on baseline correction techniques to elucidate structural information. An additional benefit of a lower wavelength, such as 532 nm, is the increased power thus higher Raman intensity to be able to define subtle changes in the HI structure.

Chapter 6

Chapter 6 used the infrared scanning near-field optical microscopy (IR-SNOM) to determine the effect of hydrophobic functionalised gold surfaces on the secondary structure of HI. The results showed that there was a higher α-helical content at pH 2, compared to pH 7, which correlated with the results obtained with QCM-D and Raman in Chapter 5. Improvements to the instrumentation such as; new software that would allow multiple images to be acquired simultaneously, collecting the equivalent of IR spectra at each pixel as opposed to one wavelength at a time, and the use of an etched aluminium coated fibre with an aperture of less than 100 nm to enable fine detail acquisition. Having established that IR-SNOM is consistent with the other conventional techniques, the next steps would be to probe the HI fibrillation pathway from pre-fibrillar to proto-fibril through to mature fibril.

Chapter 7

Chapter 7 investigated the deep-blue autofluorescence (dbAF) phenomenon and attempted to determine the origin compared with conventional intrinsic fluorescence techniques by excitation-emission matrices. The results of this investigation did not determine the origin, however did provide additional evidence to support that it was not an amyloidogenic property due to the presence of dbAF within amino acids. Future investigations would be to; involve computational modelling which may provide insight into whether this effect is related to the chemical bonding, or study other mutations of the peptide which would provide information on whether this phenomenon was site-specific.